CALIOPE, A SEARCH FOR CPT-VIOLATION IN POSITRONIUM

Chelsea Lynn Bartram

A dissertation submitted to the faculty at the University of North Carolina at Chapel Hill in partial fulfillment of the requirements for the degree of Doctor of Philosophy in the Department of Physics.

Chapel Hill
2019

Approved by:

Reyco Henning

John Wilkerson

Chuck Evans

Jonathan Engel

Art Champagne

ABSTRACT

Chelsea Lynn Bartram: CALIOPE, A Search for CPT-Violation in Positronium
(Under the direction of Reyco Henning)

We present the results of a search for CPT-violation in the charged lepton sector by studying ortho-positronium decays with CALIOPE, or CPT Aberrant Leptons in Ortho-Positronium Experiment. Positronium, a bound state of an electron and positron, occurs in both a singlet and triplet state. The triplet state, ortho-positronium, decays primarily into three gamma rays. CPT-violation could potentially manifest itself in angular correlations between the directions of the three photons and the spin of the ortho-positronium (o-Ps). The APEX annular array consists of 24 NaI(Tl) bars arranged cylindrically and provides 75% angular coverage with a source placed at its center. We used the APEX array at Triangle Universities Nuclear Laboratory (TUNL) to acquire data for CALIOPE continuously for several months. We present the results of 16 weeks of data-taking, in addition to a comprehensive systematics study. We suggest improvements that would make such a search competitive with the most sensitive CPT-violation searches in o-Ps performed to date.

ACKNOWLEDGEMENTS

This thesis would not have been possible without the help of many people to whom I am extremely grateful.

First, I would like to thank my thesis advisor, Reyco Henning, for providing me with the opportunity to work on CALIOPE. In addition to benefitting from his mentorship, I have been touched deeply by his sincerity and kindness. His ability to communicate honestly and without pretense was critical to moving this project along. I feel extremely fortunate to have found an advisor with whom I could work so well.

I would also like to thank the other ENAP group members and my peers at TUNL, for their camaraderie and support. In particular, I would like to thank John Wilkerson for his insight and tireless dedication to excellence for ENAP, which I truly admire. Thanks also to Mark Howe for his assistance in the early days of CALIOPE. Additionally, I would like to thank all the technicians and engineers at TUNL for their assistance. Specials thanks go to Matthew Busch and Brogan Thomas for their help in the design of the support stand for the source holder. I owe a debt to Mohammad Ahmed, who was critical in the late stage implementations of various DAQ-related hardware and software. At UNC, I am grateful to Jeannie Cox and Maggie Jensen for all their administrative help and cheerfulness.

This thesis also hinged largely on a support network of scientists scattered throughout the world. I am thankful to live in a time when it is possible to communicate so quickly, so that, even if at times I felt isolated, I knew I wasn't really alone. Thanks to Michelle Perry-Kuchera and Lauren Heilborn, JoEllen McBride, Ashley Rubinstein, Andrea Welsh, Caitlin Dawson, Katherine Hill, Elim Cheung, Julie Moreau, Hally Bissell-Stone, and Ace Metivier. Thanks especially to Erin Hansen and Jack Silano for their extremely valuable commentary during those last few discouraging months. I also owe a debt to my best friend

and college roommate, Janice Yong, who was always able to put things in perspective and keep me grounded. Her support has been absolutely invaluable. I would be remiss to not also thank my sister Chloe and our conversations about the meaning of life, the universe and everything. I'm lucky to have a sister who also appreciates nature and science via the great outdoors. I would like to attribute much of my growth in the early years of graduate school to the memory of Karen Thompson (1958-2016), who taught me so much about gratitude and resilience.

I cannot thank my parents enough for their love and support throughout graduate school. I could not have done this without either of them. I am especially grateful to my mom, to whom I attribute my persistence as an experimentalist (*Nevertheless she persisted!*), and and my dad who encouraged my curiosity about science and desire to build things from a young age. This thesis is dedicated to my mom, Lynn Smith-Bartram, who always reminded me to ignore societal pressures to abandon my dreams for more conventional paths. Words cannot express how grateful I am for her love and support. She provided me with the encouragement that she did not have at the same age. Despite the fact that, characteristic of her generation and circumstances, she did not have any financial or social support to pursue a degree, she put herself through college anyway. This experiment and thesis would not have been possible without her, or any women that came before me. I am eternally grateful to them, and their courage.

Break a vase, and the love that reassembles the fragments is stronger than that love which took its symmetry for granted when it was whole.

-Derek Walcott

Ar scáth a chéile a mhaireann na daoine.

-Irish Proverb

In memory of

Lynn Smith-Bartram

April 1956-June 2018

TABLE OF CONTENTS

LIST OF TABLES

LIST OF FIGURES

LIST OF ABBREVIATIONS AND SYMBOLS

CALIOPE	CP(T)-Aberrant Leptons in Ortho-Positronium Experiment
Ps	Positronium
o-Ps	Ortho-Positronium
p-Ps	Para-Positronium
JLab	Jefferson Lab
QDC	Charge-to-Digital Converter
CFD	Constant Fraction Discriminator
TDC	Time-to-Digital Converter
SBC	Single Board Computer
DRDY	Data Ready
BSY	Busy
PMT	Photomultiplier Tube
APEX	ATLAS Positron Experiment
Flg	Front Low Gain (Channel)
Blg	Back Low Gain (Channel)
Fhg	Front High Gain (Channel)
Bhg	Back High Gain (Channel)

CHAPTER 1: Introduction

1.1 Overview of Fundamental Symmetries

Notions of symmetry, appealing perhaps to an innate desire for simplicity and aesthetics, pervade much of human civilization. Though colloquially there is an association of 'symmetry' with beauty and harmony dating back to ancient cultures, the physical definition of symmetry is invariance of a physical law under transformation. In quantum mechanics, three discrete fundamental symmetries emerge: *charge*, *parity* and *time*. Their respective operators are C, which stands for "Charge", P, which stands for "Parity", and T, which stands for "Time". Charge symmetry implies that a physical process will remain the same if all particles are changed into antiparticles and vice versa. Parity symmetry dictates that a physical process is unaltered by a spatial inversion, which is equivalent to saying that the physical laws do not differentiate between left-handedness and right-handedness. Contrary to a popular misconception that parity inversion is synonymous with a 'mirror inversion', application of the parity operator to any physical system will flip all of the coordinates ($\vec{r} \rightarrow -\vec{r}$), whereas a mirror will flip only those coordinates perpendicular to its surface. A mirror rotation is equivalent to a parity inversion times a rotation. Time symmetry means that a physical process will be indistinguishable when the flow of time is reversed. Parity symmetry was introduced in the context of quantum mechanics by Wigner in 1927 [3], followed by time reversal symmetry, also by Wigner in 1932 [4]. Charge conjugation symmetry was proposed by Paul Dirac in 1931 [5]. All three symmetries combined are connected via the CPT-Theorem, developed by Lüders and Pauli in the 1950s [6, 7]. This theorem established that CPT is a 'general symmetry of physical laws' and inseparable from Lorentz invariance, which demands that the laws of physics are immutable under relativistic trans-

formations to rotated or velocity-boosted frames. The CPT-Theorem states that, for any Lorentz-invariant quantum field theory, any permutation of all three combined symmetry operators, C, P, and T, must be an exact symmetry. One corollary of the CPT-Theorem is that a particle has the same mass and lifetime as its antiparticle. Similar consequences hold true for other properties of particles and antiparticles; for example, the magnitudes of their magnetic moments must be the same. CPT-symmetry is a robust symmetry that has stood the tests of time: every experiment performed to date has confirmed CPT-symmetry [8–24].

That said, there are a number of unresolved issues with the Standard Model of particle physics like the nature of dark matter, the hierarchy problem, the existence of the neutrino mass, and the matter-antimatter asymmetry. The CPT theorem also emerges from the success of quantum field theories, but gravity is still incompatible with quantum field theory, and so it is possible still that CPT is not universal. With many as-yet unfilled holes, questioning the foundations of our knowledge may yield clues to new physics. Interrogating our assumptions about fundamental symmetries is one way to obtain answers to these open questions.

1.2 Discoveries of Symmetry Violations

The discovery of parity violation was prompted by a perplexing phenomenon: two otherwise indistinguishable particles were observed to decay into products with differing parities. The first particle, referred to as tau, was discovered in a cloud chamber experiment by C.F. Powell in 1949 [25]. The second, seemingly distinct, particle, referred to as theta, was discovered shortly thereafter. Experiments performed at the Bevatron [26] confirmed that the particles had identical masses before others determined that their lifetimes were the same as well [27]. The tau, however,disintegrated into three pions, whereas the theta disintegrated into two pions. Termed the 'theta-tau' puzzle, it implied the possibility of parity violation because the theta and tau were identical in every way, except for their parities; the tau parti-

cle had positive parity (+1), and the theta, negative parity (-1). That two particles in nature would be identical in all of their properties except one seemed, at the time, highly improbable. The idea that parity may not be an exact symmetry of nature was proposed by theorists T.D. Lee and C. N. Yang when, in 1956, they sought experimental evidence for parity symmetry in weak interactions between quarks and came up empty-handed [28]. Chien-Shiung Wu consequently demonstrated the existence of parity violation with her famous cobalt-60 experiment, in which electrons from beta decay were emitted in a preferential direction relative to the spin orientation of the cobalt nuclei [29]. She discovered that parity was violated, maximally. The theta and tau particles were re-identified as what we now call kaons. Wu's discovery of parity violation in the winter of 1956 launched an era of investigations into our assumptions about fundamental symmetries.

The prevailing assumptions about symmetries proved hard to displace. For example, the belief in the validity of combined symmetry operators, specifically CP-symmetry, persisted until 1964, when Cronin and Fitch discovered CP-violation in the decay of kaons [30]. Their experiment involved the study of two kaon species with identical masses but unique lifetimes and different decay modes. While measuring the decay of these kaons at the end of a 57 foot beamline, they observed an unexpected excess of the short-lived species. This confirmed that one kaon species could flip into the other, thus flipping the CP of the particles from -1 to +1. These short and long-lived particles were thus shown not to be eigenstates of CP. This was sufficient to demonstrate CP-violation in weak interactions. The discovery of CP-violation has since prompted physicists to search for other symmetry violating effects, resulting in the discovery of CP-violation in both D and B meson oscillations [31]. To date, CP-violation has only been observed in the weak interactions of the quark sector.

Such discoveries proved fortuitous in explaining other natural phenomena. For example, in 1967, Andrei Sakharov pointed out that CP- and C-symmetry violation is necessary to explain the existing baryon asymmetry in the universe [32]. CP-violation is one of the three so-called Sakharov conditions required in the early universe in order to produce the

predominance of matter over antimatter (the other two being interactions out of thermal equilibrium and baryon number violation). Currently, there are not enough known sources of CP-violation to account for the observed matter-antimatter asymmetry [33] [34]. The baryon asymmetry can be quantified by the term η:

$$\eta = \frac{n_b - n_{\bar{b}}}{n_\gamma}, \tag{1.1}$$

where n_b is the baryon number density, $n_{\bar{b}}$ is the antibaryon number density and n_γ is the photon number density. The current, best measurement of η is [35]

$$4(3)\times10^{-10} \lesssim \eta \lesssim 7(10)\times10^{-10}. \tag{1.2}$$

CP-violation in the Standard Model falls short of the amount required to explain the baryon asymmetry by a factor between 10^5 and 10^7 [36].

CP-violation in the lepton sector, though postulated, has not been confirmed experimentally. A number of ongoing experiments are pursuing this search today. Two evolving efforts to detect hints of CP-violation include the T2K and NOνA experiments. The T2K experiment has been searching for CP-violation in neutrino oscillation using a neutrino beam originating in Tokai and traveling 295 km to the 22.5 kTon Super-Kamiokande (Super-K) detector underground in Kamioka [37] [38]. Similarly, NOνA (NuMI Off-axis ν_e Appearance) operates a far detector in Minnesota which is exposed to a neutrino beam originating 500 miles away at Fermilab [39].

Additionally, long-baseline neutrino experiments are being constructed to look for CP-violation in the neutrinos. Experiments such as DUNE (Deep Underground Neutrino Experiment) require a baseline which runs from Fermilab in Illinois to South Dakota and a collaboration of more than 525 scientists and engineers [40]. Furthermore, an experiment called Hyper-K has been proposed [41], which calls for the construction of two identical water Cherenkov detectors, which, when combined, would be larger in fiducial volume than Super-

K by a factor of 16.8. Installing the near detector close to Super-K and the far detector in Korea, this experiment would further expand the search for CP-violation in neutrinos.

Other groups have been searching for CP-violation in the charged lepton sector as well. For example, if the electron has a permanent electric dipole moment, this would be a sign of T violation, which is equivalent to CP-violation, provided CPT is conserved [42]. To understand why a permanent electric dipole moment is indicative of T-violation in a system, one must consider the effect of P and T operators on the electric and magnetic dipole moments of that particle. A permanent electric dipole moment would flip under P, but not T, whereas a magnetic dipole moment would flip under T and not P. Thus, if T-symmetry (and therefore P-symmetry) is conserved, one of these must be zero. Since the electron has a measured magnetic dipole moment, the existence of an e-EDM would imply the existence of T and P violating interaction involving the electron. Accelerator-based searches have probed muons and taus for a permanent electric dipole moment as well. The Muon (g-2) collaboration [43] obtained the best limit so far on the muon electric dipole moment as

$$|d_\mu| < 1.9\times10^{-19}\text{e}\cdot\text{cm}. \tag{1.3}$$

Likewise, the Belle collaboration performed a search for the electric dipole moment of the tau [44], obtaining the following result, also consistent with zero:

$$-2.2\times10^{-17} < \text{Re}(d_\tau) < 4.5\times10^{-17}\text{e}\cdot\text{cm}. \tag{1.4}$$

It is worth noting that non-zero EDMs are expected for these particles from higher order Standard Model diagrams involving quarks, but these would be far beneath the current experimental sensitivity. The small scale of the EDMs predicted by the Standard Model makes EDM searches promising probes for BSM physics.

1.3 History of CPT-Violation Searches

Unlike CP-symmetry, the combination of all three symmetry operators, or CPT, has so far held up to intense scrutiny on a number of fronts. CPT-violation, if it exists, could manifest itself in differences between the masses of matter and antimatter particles, the magnetic moments of particles and antiparticles, the charge to mass ratio of particles to antiparticles, and the mean lifetime of particles and antiparticles [45]. CPT-symmetry is a deep requirement of Lorentz-invariant quantum field theories on which our models of particle interactions, such as the Standard Model, are based. Still, the fact that gravity has not yet been adequately described by a quantum field theory leaves room for the possibility of CPT-violation. If there is anything to be learned from the history of fundamental symmetries, it is that sometimes even the most well-established of our assumptions can prove false. In light of all this, a discovery of CPT-violation would perhaps be all the more profound and point to new physics beyond the Standard Model.

A number of searches for CPT-violation have been undertaken. The experiment which set the tightest limit on CPT-violation in any system was performed on kaons. Ref [8] compared the masses of the neutral kaon with the neutral anti-kaon, obtaining the following results:

$$r_K = |(m_K - m_{\bar{K}})| \lesssim 6{\times}10^{-19}. \tag{1.5}$$

where m is the mass of the kaon.

Another experiment set the best limit on CPT-violation in baryon systems:

$$r^p_{q/m} \equiv |[(q_p/m_p) - (q_{\bar{p}}/m_{\bar{p}})]/(q/m)_{av}| \lesssim 9{\times}10^{-11}, \tag{1.6}$$

where q is the charge and m is the mass of the proton or antiproton [46].

The most stringent test to date in the lepton sector is the comparison of the electron and positron magnetic moments. This experiment worked by observing the cyclotron motion of

electrons and positrons in a Penning trap. The g-factor anomaly was attained by using the spin-cyclotron difference frequency and the cyclotron frequency [9] and the following limit on CPT-violation was obtained:

$$r_g = |(g_- - g_+)/g_{av}| \lesssim 2.1{\times}10^{-12} \tag{1.7}$$

Attempts to improve upon this measurement have so far been hindered by positron loading rate into the Penning trap [45].

1.3.1 CPT-violation in the Positronium Decay Process

Some proposed Standard Model extensions such as string theory suggest that CPT symmetry or Lorentz invariance violations might be present in certain nonlocal interactions [47] [48]. The assumptions required to prove the CPT theorem are not valid for string theory [47]. Thus, Colladay and Kostelecký [47] were able to devise a framework to treat spontaneous CPT and Lorentz breaking within conventional effective field theory. In doing so, they incentivized more searches for CPT-violation in the lepton sector. Positronium, or Ps, is a convenient lab for such experiments.

1.4 Positronium: History and Properties

In 1930, P.A.M. Dirac modified Schrodinger's equations to obtain a relativistic expression which predicted negative energy solutions, otherwise known as antiparticles, for the first time [5]. Specifically, Dirac postulated a particle that was identical to the electron but with positive charge. At the time, no such particles had ever been detected. In 1932, however, the existence of such a particle was confirmed by Carl Anderson with a cloud chamber he was using to study cosmic rays [49]. Shortly thereafter, Mohorovič predicted the existence of this particle in a bound state with the electron [50]. This was followed by more detailed

predictions about positronium, including the spectroscopic structure by Ruark in 1945 [51] and the prediction of the decay rate by Wheeler [52] and Pirenne [53] [54].

Positronium was first discovered by Martin Deutsch in Freon gas at MIT in 1951 [55]. He was able to show that the time it took for gamma rays emitted from the positronium source to reach in the detector was longer than would be expected from ordinary annihilation, implying the existence of a long-lived bound state. The discovery was followed by a measurement of the long-lived state's lifetime, which happened to match, within about $\pm 10\%$ with calculations set forth by Ore and Powell in 1949 [56]. Ore and Powell predicted that the decay rate of the long-lived state of positronium, ortho-positronium, is

$$\Gamma^0_{3\gamma} = \frac{2}{9}(\pi^2 - 9)\frac{\alpha^6 m_e}{\pi} = 7.2{\times}10^6 s^{-1}, \tag{1.8}$$

where α is the fine structure constant and m_e is the electron mass. Martin Deutsch measured the decay rate to be $\Gamma^0_{3\gamma} = (6.8){\times}10^6 \mathrm{s}^{-1} \pm 10\%$ [55].

In the simplest model, positronium's energy levels can be obtained by treating it like the hydrogen atom in non-relativistic quantum mechanics, but replacing the mass of the proton with the reduced mass of the electron and positron. Unlike the hydrogen atom, however, positronium is unstable and eventually decays into gamma rays. Positronium exists in both a triplet (S= 1) and singlet (S = 0) state. For this experiment, we are only concerned with positronium in its ground state where $n = 1$. The number of gamma rays emitted during annihilation is determined by the charge conjugation invariance of QED. C-parity in positronium is given as $C = (-1)^{s+l}$, where s is the spin quantum number and l is the orbital angular momentum number. In our system, positronium decays from the $l = 0$ state, so the C parity is -1 (odd) for the triplet state and 1 (even) for the singlet state. C parity is multiplicative, and the photon has odd charge conjugation parity. Therefore, the triplet state, also known as ortho-positronium (o-Ps), decays into three photons with odd charge conjugation parity and the singlet state, or para-positronium, (p-Ps), decays into two photons with even charge conjugation parity. While it is possible for o-Ps to decay into a

larger, odd number of photons (and likewise, p-Ps into a larger, even number of photons), this rarely happens because the branching ratios for these decays are greatly suppressed by a factor $1/\alpha$, where α is the fine structure constant. Number of photons aside, the triplet state and singlet state can also be easily differentiated by their lifetimes. The triplet state has a much smaller phase space and an extra vertex that contributes an extra factor of the fine structure constant. These two features extend the lifetime of the triplet state (142 ns) to nearly a factor of 1,000 greater than that of the singlet state (125 ps).

Positronium, consisting of two charged leptons, is an ideal and convenient system for fundamental symmetry searches. It can be generated in the laboratory with relative ease, requiring a material that is conducive to its formation and a positron emitting radionuclide source. Though early on it was discovered to form in silica powders, it is now known that silica aerogel is best suited to positronium creation [57] [58] [59]. Ps is formed in the solid matrix of the aerogel and reaches a pore surface via diffusion. Once in the pore, the Ps dissipates a few eV of its energy via collisions with the pore walls [60] [61] [62]. This small amount of energy loss is enough to prevent the Ps from escaping the pore back into the solid phase [63] [64]. Once inside a pore, the Ps is less likely to interact with electrons in the ambient material, and therefore can remain in its bound state for a longer time. Smaller pore sizes result in a higher chance that the Ps annihilates with an electron in the walls of the pore (known as the 'pick-off' effect), and the measured lifetime of the Ps will be shortened. It is actually this property of Ps that makes it a useful tool for measuring the porosity of different materials [65]. An SEM image of silica aerogel with its porous nature clearly evident can be found in fig 1.1.

Positronium is also purely leptonic and therefore free from complications arising from QCD effects.

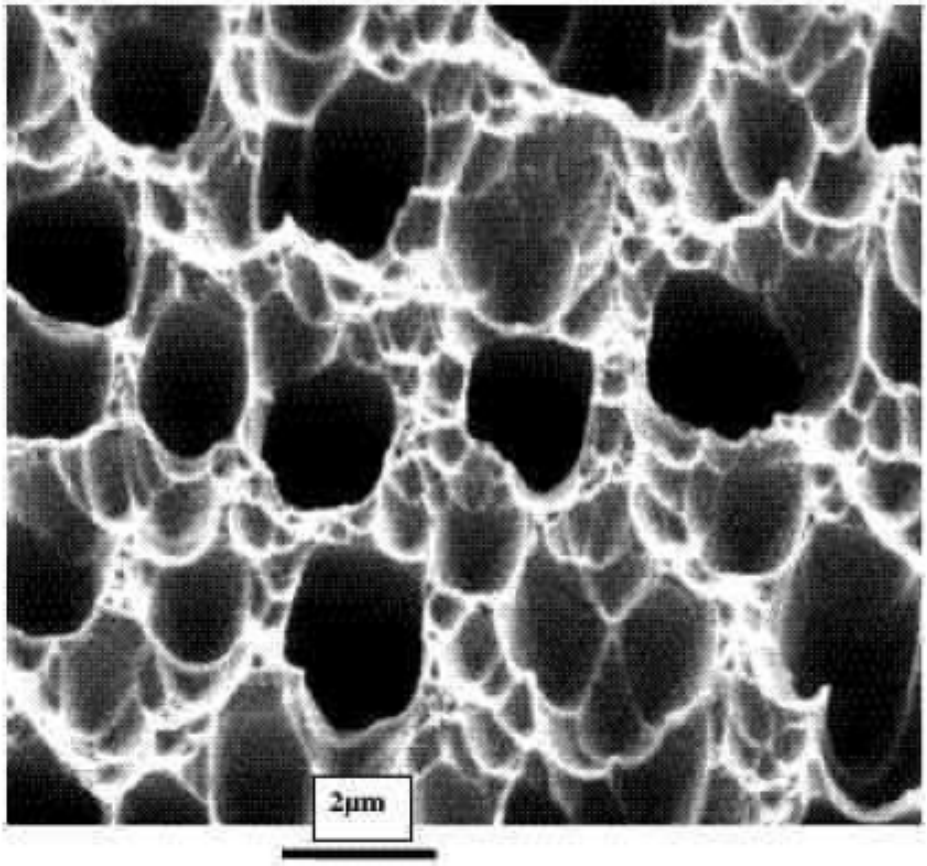

Figure 1.1: An SEM image of silica aerogel, in which the pores are highly visible, from the Moscow Micro Electronics Technology Institute [66].

1.4.1 The ortho-positronium lifetime puzzle

Most practical mechanisms of Ps formation occur in porous materials. The Ps remains trapped in the material afterwards, and, under such circumstances, corrections need to be included to the lifetime calculations due to interactions between the Ps and electrons in the material. As the precision of Ps lifetime measurements increased, so too did the challenges posed by systematics. It was not long before a discrepancy between the predicted, theoretical lifetime and the measured lifetime arose. Ps lifetime measurements typically relied on one of three techniques to generate the o-Ps; these are 1) positronium formation via collision with gas molecules at different pressures, which requires an extrapolation to zero-density to obtain the decay rate in vacuum 2) positronium formation via SiO_2 pow-

ders, as used in the original measurement by Deutsch, and 3) positronium formation via a vacuum cavity coated in MgO or SiO_2, using a slow beam of positrons. The systematics and experimental challenges vary between the different techniques, but all experiments tagged on the positron to start the clock. The first appearance of a discrepancy between the lifetime predicted by Ore and Powell and the measured lifetime was apparent in a measurement ($\Gamma^0_{3\gamma} = (0.7262\pm0.0015)\cdot10^7 s^{-1}$) by Beers and Hughes in 1968 [67], using technique 1. This was followed by two more measurement using the gas technique in which the lifetime discrepancy was still apparent [68] [69]. At the same time, theorists improved their calculation of the o-Ps lifetime ($\Gamma^0_{3\gamma} = (0.724\pm0.001)\cdot10^7 s^{-1}$) [70], reducing, but not eradicating, the discrepancy. In the late 70s, a group at Michigan performed this measurement using two different approaches: one with powder ($\Gamma^0_{3\gamma} = (0.7104\pm0.0006)\cdot10^7 s^{-1}$) [71] and one with vacuum ($\Gamma^0_{3\gamma} = (0.709\pm0.002)\cdot10^7 s^{-1}$) [72]. The results were confirmed by a novel gas measurement [73]. These results prompted yet more corrections by theorists ($(0.70379\pm0.00121)\cdot10^7 s^{-1}$) [74]. Incompatibility between theory and experiment persisted, and the Michigan group performed yet another two experiments, one in vacuum [75] and the other in gas [76]. This was followed by yet another attempt by theorists to improve their prediction ($(0.70386\pm0.00002)\cdot10^7 s^{-1}$) [77].

The Michigan group published very precise results (200 ppm uncertainty) in 1989 [78] and 1990 [79] that were again inconsistent with the theory. Eventually, however, measurements performed in powders in 1995 by a group in Tokyo claimed to have resolved the issue [80]. The Tokyo group further improved their 1995 results in 2000, accounting for time dependence of the pick-off rate in their fitting procedure [81]. The Michigan group responded by making an adjustment to their 1989 results and later ran an experiment in 2003 that finally obtained results consistent with the theory and those of the Tokyo group. The necessary improvements included use of a slow positron beam with an improved double cavity to prevent escaping positronium atoms and a means of removing fast, back-scattered positrons [82].

As experimentalists grappled with unforeseen systematic erros, it was not clear that the

o-Ps lifetime puzzle was a result of new physics or flaws in the experimental techniques. Thus, searches for new physics is the o-Ps system were undertaken as a means of explaining the problem. These experiments included searches for decays of o-Ps into two photons [83], searches for invisible decays of o-Ps [84], and searches for o-Ps decays into neutral bosons [85]. Though the o-Ps lifetime puzzle was eventually resolved, it opened the door to searches for physics beyond the Standard Model using positronium.

1.5 Positronium Kinematics

The energies and momenta of the gamma rays emitted in the decay of ortho-positronium must conserve energy and momentum, as shown below, where m is the rest mass of the electron and $\vec{k_i}$ are the momenta vectors of the gamma rays, with $\vec{k_1}$ being the highest energy gamma, $\vec{k_2}$ being the second highest energy gamma ray, and $\vec{k_3}$ being the lowest energy gamma ray:

$$|\vec{k_1}| + |\vec{k_2}| + |\vec{k_3}| = 2m \tag{1.9}$$

$$\vec{k_1} + \vec{k_2} + \vec{k_3} = \vec{0}. \tag{1.10}$$

The energy spectrum is given by the following equation, where m is the rest mass of the electron, as derived by Ore and Powell [2]:

$$F(k_1) = \int_{m-k_1}^{m} \left(\frac{m^2(m-k_1)^2}{k_2^2 k_3^2} + \frac{m^2(m-k_2)^2}{k_3^2 k_1^2} + \frac{m^2(m-k_3)^2}{k_1^2 k_2^2} \right) \frac{dk_2}{m} \tag{1.11}$$

$$= 2\left(\frac{k_1(m-k_1)}{(2m-k_1)^2} - \frac{2m(m-k_1)^2}{(2m-k_1)^3} \ln\left(\frac{m-k_1}{m} \right) \right. \tag{1.12}$$

$$\left. + \frac{2m-k_1}{k_1} + \frac{2m(m-k_1)}{k_1^2} \ln\left(\frac{m-k_1}{m} \right) \right). \tag{1.13}$$

In this equation, $\vec{k_1}$ is the highest energy gamma ray and $\vec{k_2}$ is the second highest energy gamma ray. Once an energy is picked for $\vec{k_1}$ in the distribution, that energy can be substituted back under the integral and a value for $\vec{k_2}$ can be calculated. The energy for $\vec{k_3}$ is determined by conservation of energy. Figs 1.2, 1.3 and 1.4 show the $\vec{k_1}$, $\vec{k_2}$, and $\vec{k_3}$ energy distributions, respectively.

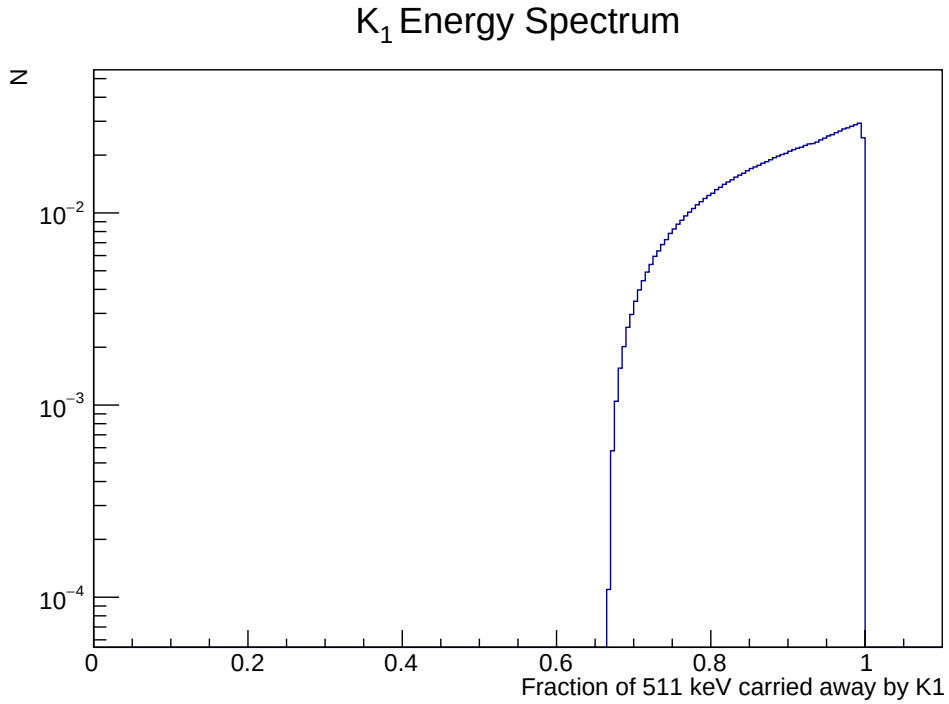

Figure 1.2:
$\vec{k_1}$ energy spectrum created with positronium generator code which simulates positronium kinematics.

In quantum mechanics, the magnetic quantum number, m, is one of the four numbers that specify the quantum state of an electron. The name 'magnetic quantum number' derives from the fact that energy levels of the electron are altered according to which m state they occupy. In an o-Ps decay, the magnetic quantum number also determines some of the decay kinematics. In particular, the normal to the o-Ps decay plane has a specific angular distribution. This distribution was determined by Bernreuther [86] and changes depending on the magnetic quantum number of the o-Ps.

For $m = 0$ states, the angle, θ, which is defined as the angle between the normal to the

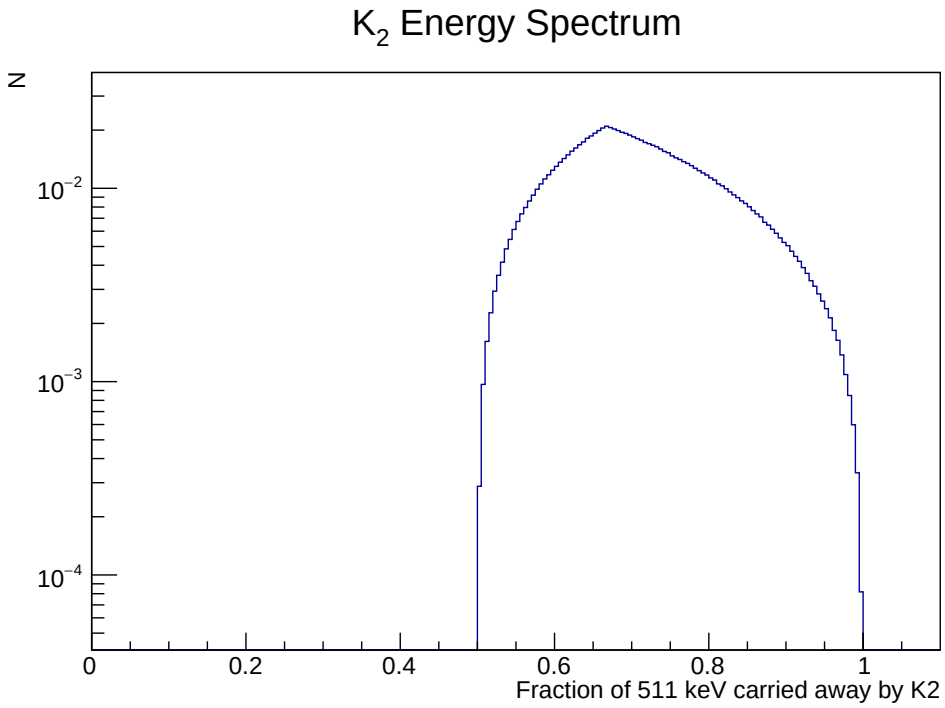

Figure 1.3: $\vec{k_2}$ energy spectrum created with positronium generator code which simulates positronium kinematics.

decay plane and the o-Ps spin, the distribution is given as $P(\theta) = 1 + \cos^2\theta$. For $m = \pm 1$, the distribution is given as $P(\theta) = \frac{3-\cos^2\theta}{2}$. This is discussed further in Section 4.2.

Additionally, the angle ψ, or the azimuthal angle, is defined as the angle between the $\vec{k_1}$ and $\vec{k_2}$ gamma rays. The angular distribution for ψ was worked out by Ore and Powell [2], and can be see in fig 1.6. One can see from this image that the angle between $\vec{k_1}$ and $\vec{k_2}$ is often close to but less than 180°.

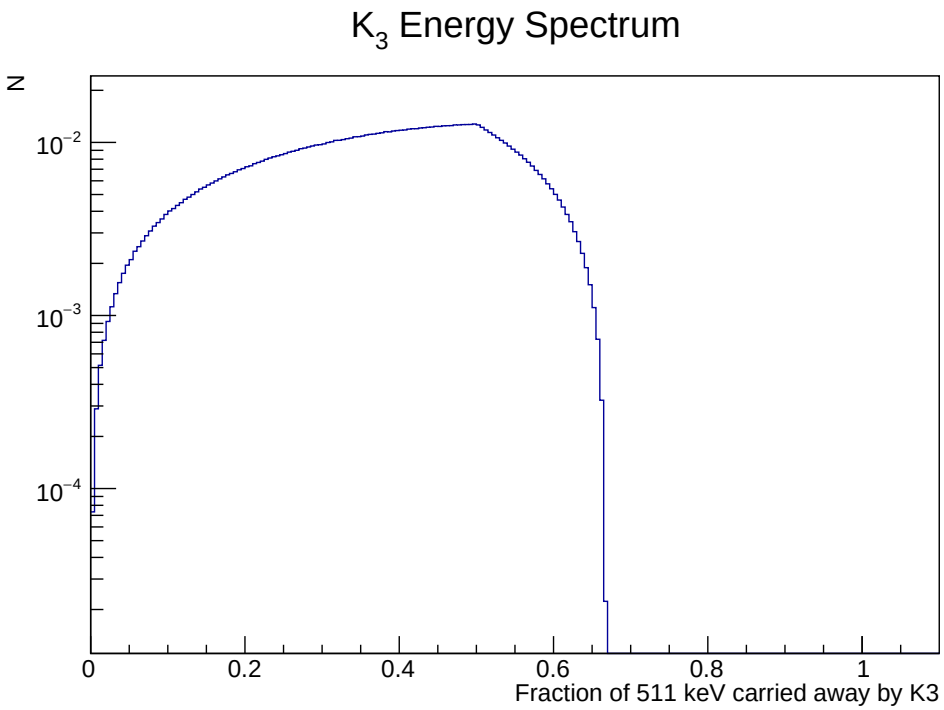

Figure 1.4: $\vec{k_3}$ energy spectrum created with positronium generator code which simulates positronium kinematics.

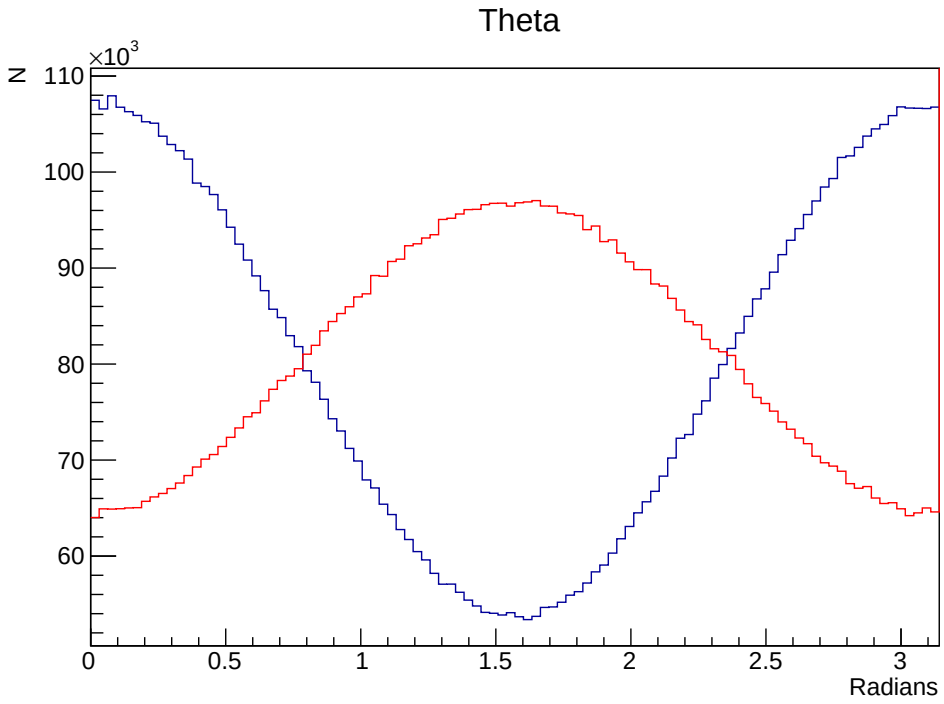

Figure 1.5: Angular distribution for θ, the angle between the spin of the o-Ps and the normal to the decay plane. The m=0 case is shown in blue and the m=1 case is shown in red.

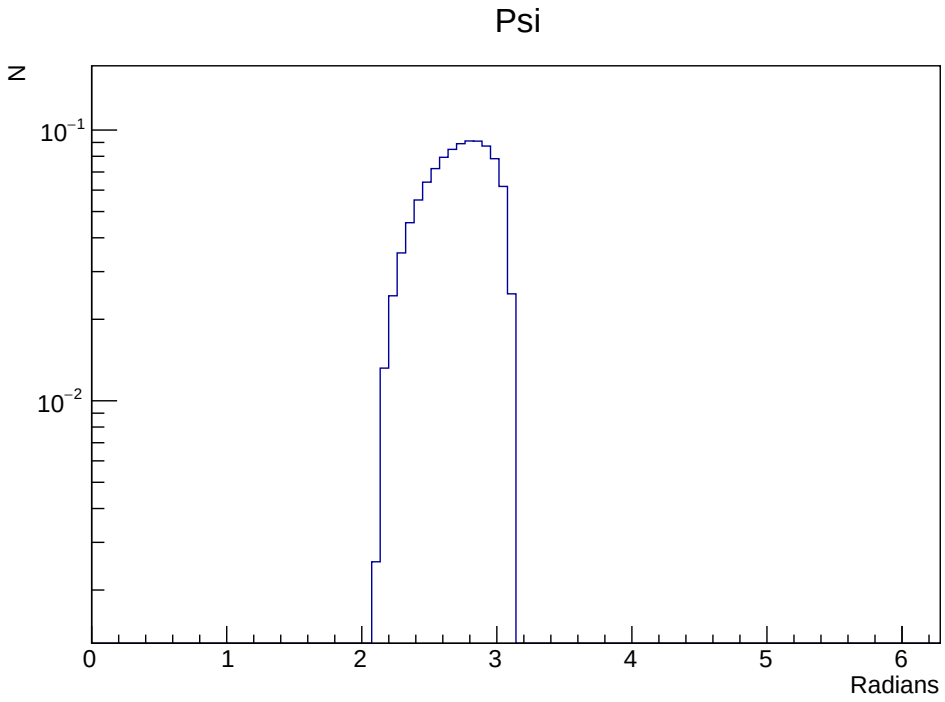

Figure 1.6: Angular distribution for ψ, the angle between the $\vec{k_1}$ and $\vec{k_2}$ gamma rays.

1.6 CPT-Violating Correlation

CPT-violation in o-Ps decay could manifest itself as a CPT-violating angular distribution of the emitted gamma rays. One such CPT-violating correlation, as introduced by Bernreuther [86], can be written in the following way:

$$\vec{S}\cdot\vec{n}, \tag{1.14}$$

where $\vec{S}$ is the spin polarization axis and $\vec{n}$ is the normal to the o-Ps decay plane, as defined by gamma rays k_1 and k_2. This can also be written in the following form:

$$\vec{S}\cdot\vec{k_1}\times\vec{k_2} = |S||n|\cos\theta, \tag{1.15}$$

where θ is the angle between the spin of the o-Ps and the normal to the decay plane.

A common principle behind searches for CPT-violation in such decay processes is to measure what is called the 'asymmetry term', defined as follows:

$$A = C_{CPT}Q(\theta) = \frac{N_+ - N_-}{N_+ + N_-}, \tag{1.16}$$

where A is the asymmetry parameter, C_{CPT} is the CPT-violation coefficient, $Q(\theta)$ is our observable, $(\vec{S}\cdot\vec{k_1}\times\vec{k_2})$ as a function of θ, N_+ is the number of events for which that term is positive, and N_- is the number of events for which that term is negative.

If A is measured to be inconsistent with zero, that would be confirmation of CPT-violation. An exaggerated version of what one would see in each case can be seen in figures 1.7 and 1.8.

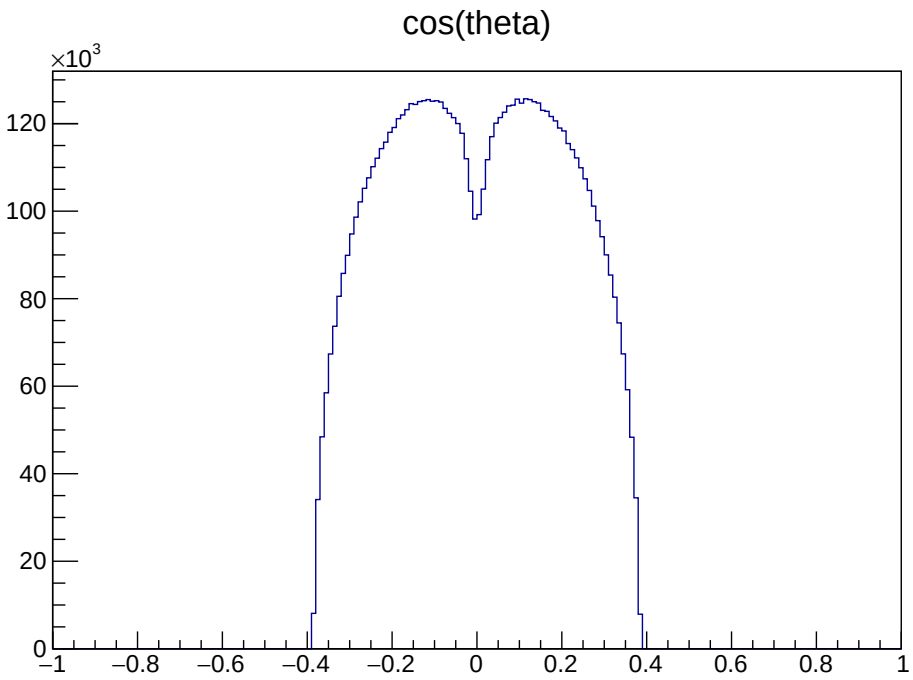

Figure 1.7: $(\vec{S}\cdot\vec{k_1}\times\vec{k_2})$ distribution in the case of no CPT-violation

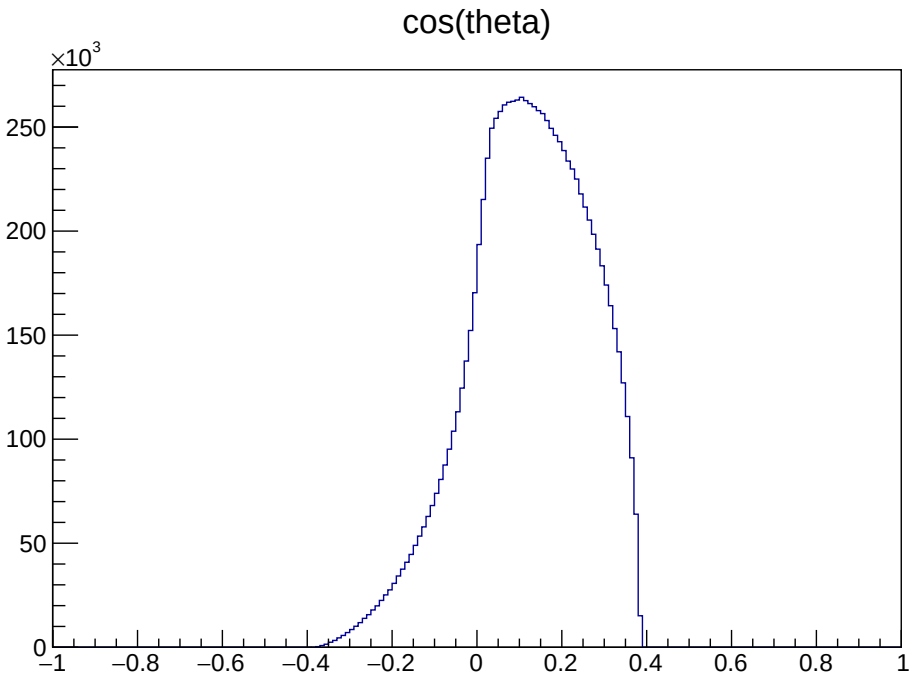

Figure 1.8: $(\vec{S}\cdot\vec{k_1}\times\vec{k_2})$ distribution in the case of CPT-violation. In this case, the energy distribution of the photons is model-dependent and therefore unknown. To generate this distribution, we therefore picked the gamma ray energies using phase space considerations as was performed in the ref [2] by Ore and Powell.

1.7 Previous CPT-violation Searches in Positronium

Previous experiments studying the angular correlations in o-Ps decay did not observe any CPT-violation. One such experiment was performed by Arbic *et al* [87], which limited this correlation to about 2%. This experiment used a positron beam and planar arrays of NaI detectors. The most recent experiment of this type was performed by Paul Vetter and Stuart Freedman using the Gammasphere array, a 4π angular array of high purity germanium (HPGe) detectors equipped with Compton Suppressors [1] [88]. The experiment used both ^{22}Na and ^{68}Ge in separate runs, with the idea that any true CPT-violating signal would scale differently with different sources. In each run, the source was set adjacent to a hemisphere of aerogel at the center of the Gammasphere. Like the o-Ps lifetime experiments, this search tagged on the positron to start the clock. To accomplish this, a thin piece of scintillator coupled to a PMT via optical fiber was placed adjacent to the source.

Vetter and Freedman calculated $(\vec{S}\cdot\vec{k_1}\times\vec{k_2})W_i(E_1, E_2)$, where $W_i(E_1, E_2)$ is a weighting function for the decay plane normal vector which depends on the energy of the gamma rays. Three such functions were used; they were:

$$W_1 = \frac{1}{|\vec{k_1}\times\vec{k_2}|}, \tag{1.17}$$

$$W_2 = 1/(E_1E_2), \tag{1.18}$$

$$W_3 = 1. \tag{1.19}$$

These weighting functions were suggested by Bernreuther [89]. They then calculated the asymmetry term in each of these cases to arrive at three different asymmetry terms, C_1, C_2, and C_3, corresponding to the three different weighting functions. The calculated CPT-violating asymmetry terms are shown in Table 1.1. In general, they were able to improve upon the previous such search by about an order of magnitude (setting a limit at about $\tilde{0}.2\%$).

Source	C_1	C_2	C_3
^{22}Na	-0.0132(57)	-0.0006(92)	0.0004(57)
^{68}Ge	0.0008(15)	0.0134(83)	0.0038(30)
Both	-0.0001(14)	0.0071(62)	0.0026(31)

Table 1.1: Table of results from [1]. The different values for C_i correspond to the different weighting factors. The error is shown in parentheses, and the combined result from both ^{68}Ge and ^{22}Na is shown at the bottom.

The Vetter experiment benefited from the advantage of using a well-characterized HPGe array with excellent energy resolution and angular coverage. On the flip side, the Gammasphere is very heavily subscribed and so the duration of their experiment lasted only a few weeks. We proposed to search for CPT-violation with a detector that could be dedicated soley to the purpose of our search over the course of many months, with the intention of boosting our statistics. We explain, in the the subsequent chapters, the design of our data acquisition system (DAQ), the inner-workings of the APEX array, simulations of our setup, and finally the analysis of our search for CPT-violation in o-Ps.

CHAPTER 2: Experimental Setup

2.1 CALIOPE: Experimental Design

CALIOPE (pronounced: k-ah-LY-oh-pee) stands for $CP(T)$ Aberrant Leptons in o-Ps Experiment. Named for the Greek muse of epic stories, the purpose of CALIOPE is to search for fundamental symmetry violations in o-Ps. The experiment is located at Triangle Universities Nuclear Laboratory (TUNL) in the LENA (Laboratory for Experimental Nuclear Astrophysics) building. CALIOPE uses the APEX (ATLAS Positron Experiment) array of NaI(Tl) bars [90] to search for CPT-violating correlations in the gamma rays emitted in decay of o-Ps. O-Ps is formed near the center of the APEX array, using aerogel next to the ^{22}Na source. The gamma rays from the o-Ps are detected with the NaI(Tl) bars (see fig 2.9). A cross section of the entire setup can be seen in fig 2.1. The positronium formation region is small relative to the scale of the detector, so an enlarged image of the source holder is also shown in fig 2.2.

2.1.1 Positronium Formation, Decay, and Detection

CALIOPE uses a 10μCi ^{22}Na source deposited on a thin layer of kapton foil adjacent to a cylinder of aerogel. The source is provided by Eckert and Ziegler Isotope Products, Inc [91]. Its physical diameter is 12.7 mm and the active diameter is 5.08 mm. The foil is composed of 7.2 mg/cm^2 polymide that is sealed with epoxy. The source and aerogel are contained in the delrin source holder that is held inside a carbon fiber tube with four retaining pins (see fig 2.4). The source holder contains vent holes to enable the flow of purge gas. One important feature of the holder is that aerogel can only be located on one

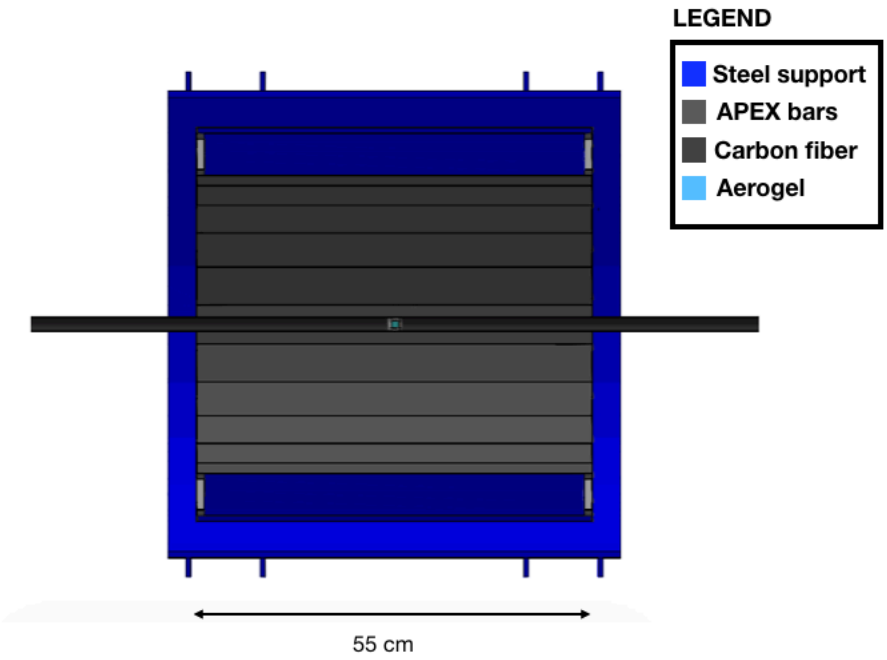

Figure 2.1: CALIOPE Cross Section (Bird's Eye View). The small, light blue cylinder in the center of the array is the aerogel. The black tube running through the center of the array is the carbon fiber tube. Everything else is the APEX array. The cross section is taken as a slice down the length of the cylindrical array. This cross section was generated using Geant4's DAWN viewer.

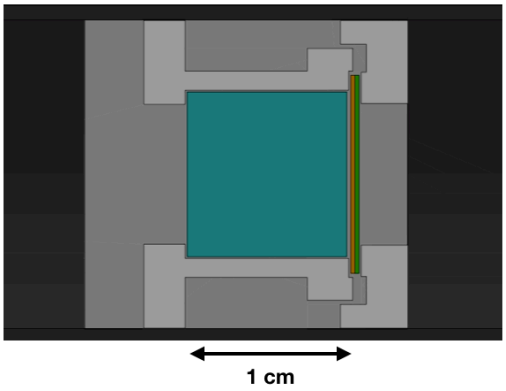

Figure 2.2: Zoomed-in cross-section of the source holder from 2.1 near the center of the array. The cyan is the aerogel, the orange is the thin film source, and the green is the aluminum back-plate. The white is the source holder. Grey is an extra air volume defined in Geant4 for simulation purposes; it does not represent anything in the actual experiment. Black is the carbon fiber tube.

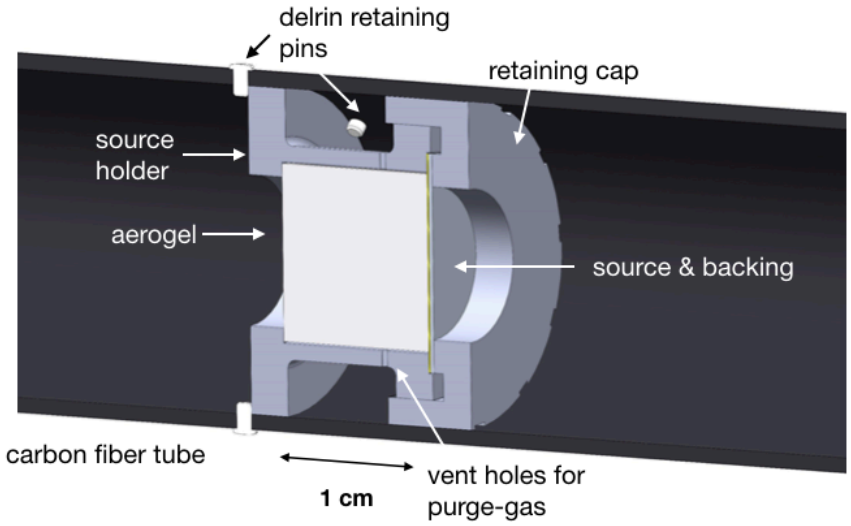

Figure 2.3: Engineering drawing by TUNL engineer Matthew Busch of source holder in carbon fiber tube.

side of the source. The other side of the source is adjacent to a thin piece of aluminum. This enables us to constrain the spin-direction of the positronium, as this is correlated with the velocity direction of β^+ particles emitted from the source. The aluminum backing provides mechanical support and stops electrons from scattering back into the aerogel. A similar design has been implemented in previous such searches [1]. The carbon fiber tube is connected via plastic tubing to a nitrogen cylinder with regulator and needle valve on one end and a bubbler, filled with mineral oil, on the other. The contents of the carbon fiber tube are flushed continuously with the 99.998% pure nitrogen. The purpose of the nitrogen purge setup is to maximize the number of 'good' events by suppressing pick-off annihilation. Pick-off occurs when the positron wavefunction overlaps with that of an electron in the ambient material. There is therefore some probability that the positron annihilates with an electron that is not its bound partner. This reaction is more likely to happen in gases containing molecules with an odd number of electrons, and effect first demonstrated by Martin Deutsch in his paper describing the discovery of positronium [55]. By adding 3% nitrous oxide to pure N_2, he was able to show that the number of o-Ps events was reduced by a factor of 3.

The aerogel serves as a positronium generator as positrons emitted in the beta decay

Figure 2.4: Photograph of delrin source holder before insertion into the carbon fiber tube.

of ^{22}Na interact with electrons in the SiO_2 to form positronium. The positronium forms in either the singlet or triplet state and subsequently decays. The singlet state decays into primarily two gamma rays due to charge conjugation, whereas the triplet state decays primarily into three gamma rays. Provided these gamma rays propagate to and interact in one of the NaI(Tl) segments of the APEX, they are detected by photomultiplier tubes (PMTs) which can sense scintillation light at either end of a single bar. Gamma rays hitting the bars interact primarily via the photoelectric effect and Compton scattering.

2.1.2 Aerogel And Source Implementation

For this experiment, we use custom, hydrophobic aerogel obtained from Marketech International [92]. The aerogel was created by Marketech in custom cylindrical molds, 5.08 cm in length and 0.5 cm in radius with a density of 0.13 g/cc. A 1 cm length cylinder was trimmed from the original piece using a razor blade cleaned with alcohol. The aerogel was further desiccated by sealing it in an evaporator and pumping down on it in vacuum for 2 hours. Afterwards, it was stored in a container that we flushed with nitrogen until it could be inserted into the carbon fiber tube.

We took precautions to keep the aerogel clean and dry. A protocol for loading the aerogel and source into the carbon fiber was generated and approved by radiation safety.

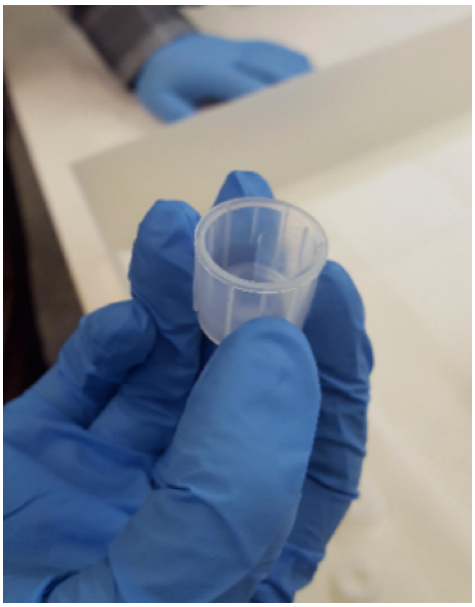

Figure 2.5: Cut aerogel cylinder held in small plastic container (left) and aerogel illuminated by external light (right, faint blue).

Using gloves, we inserted the aerogel into the holder, followed by the source and aluminum backing. We used a pair of dedicated plastic tweezers to insert the source. Next, we gently screwed on the source holder top by hand, and pushed the holder into the tube using a long metal rod. Delrin pins were inserted to hold it in place. The process was checked and monitored by radiation safety due to the fragile nature of the thin film source.

2.1.3 APEX Bars and Detector Configuration

The APEX array consists of 24 trapezoidal NaI(Tl) segments (fig 2.7). The dimensions of each segment are $55\times6\times5.5(7.0)\,\mathrm{cm}^3$, (L×W×H), with the number in parentheses indicating the longer width of the trapezoid. With a source located at the center of the APEX array, 75% of 4π angular coverage can be obtained. The inner diameter of the array is 42.8 cm and the outer diameter of the array is 56.7 cm. The APEX array uses Hamamatsu 580 PMTs for 16 of the NaI(Tl) bars and Photonis XP2012B PMTs for the remaining 8 bars. The NaI(Tl) crystals are each encapsulated in a stainless steel box with openings on either end where quartz windows are fastened. The windows, 4.4 cm in diameter and 1.1 cm thick,

Figure 2.6: Assembling the source holder. The thin orange film is the ^{22}Na source encased in kapton foil. It was delicately pushed on top of the aerogel with tweezers.

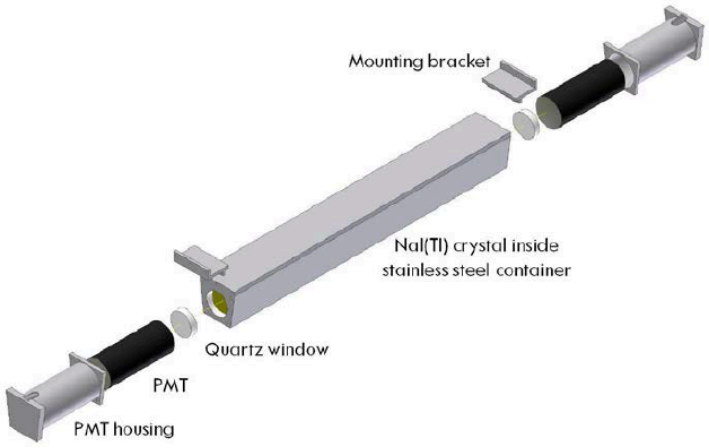

Figure 2.7: Exploded view of NaI(Tl) bar with PMTs, complete with steel encasement [93].

enable light to illuminate the PMTs that are optically coupled to them with silicone grease (Saint-Gobain BC-630). The quality of the NaI(Tl) crystals were last examined and assessed by former graduate student, Stephen Daigle [93] at some point between 2007 and 2013. An exploded view of each segment is rendered in fig 2.7. Prior to our experiment, Stephen Daigle used the array to measure the ground state transition for the $^{13}\mathrm{N}\,(\mathrm{p},\gamma)\,^{25}\mathrm{O}$ reaction. The APEX array dates back to 1993, when it was aseembled and used to detect positrons and electrons from heavy ions at Argonne National Lab [90].

2.1.4 APEX Gain-Matching

We adjusted each PMT voltage level to achieve full dynamic range of the NaI(Tl) bars. Interactions that occur at the ends of the bar have a tendency to saturate the channels corresponding to the closest PMT. Furthermore, by the time the signal is detected at the opposite (far) end of the bar, it is sometimes attenuated to the point that it does not exceed threshold settings on the CFD (constant fraction discriminator) or QDC (charge-to-digital converter). The combination of these two effects makes interactions towards the ends of the bars difficult to detect. Gain-matching the PMT voltage levels was therefore critical in optimizing the number of detectable events along the length of the bar. By gain-matching,

we could guarantee that, for an interaction of a given energy, the z positions corresponding to saturation of the nearest PMT channel were approximately equidistant from the center of the array. This effectively maximizes our total angular coverage.

We performed this optimization process using a collimated ^{22}Na source positioned at the center of the array. The collimator consists of two lead disks with a small hollow space to place a button source. The lead disks are inserted in a delrin container at the end of an aluminum rod. The rod has markings every 0.5 cm for precise placement of the source within the array. A photo of the collimator tube in use can be seen in fig 2.8. Gain-matching was accomplished using a 10 μCi ^{22}Na button source in the collimator cavity at the center of the bars. The PMT voltage levels on either end were then adjusted such that the z position of the hits, when reconstructed, appeared as close to the center as possible without losing too many low energy events. For several Photonis PMTs, perfect gain-matching was not feasible, especially without losing many low energy events. This is because many of these PMTs were biased to their maximum recommended operating voltage. Lowering the voltage levels would have resulted in a loss of a considerable amount of low energy events. The need to gain match was therefore balanced with the need to detect low energy gamma rays for these PMTs. A table of all the operating voltages for the PMTs is shown in Table 2.1. PMTs 1-8 are Photonis PMTs, and the remaining are Hamamatsu. In addition to using the collimator for gain-matching, collimated data was taken at various z positions along the bar, so that the actual physical position could be calibrated. As such, we were able to determine the attenuation for individual bars. Further explanation of the energy calibration using collimated and uncollimated data will be provided in the next chapter.

2.1.5 Source and Setup

For the actual experiment, we used ^{22}Na as our positron emitter. The ^{22}Na decays via the emission of a beta particle (fig 2.10) to an excited state of ^{22}Ne, with a 90% branching ratio. This state is short-lived (half-life of 3.7 ps), relative to the lifetime of o-Ps, and decays to

Figure 2.8: The collimator tube inserted inside the APEX array.

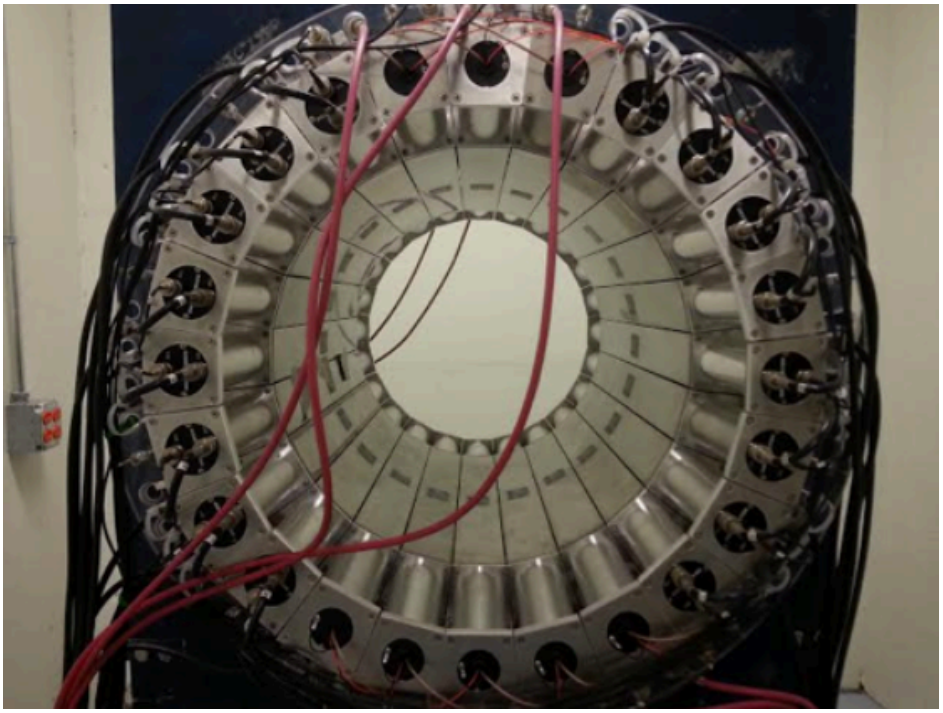

Figure 2.9: APEX Front View without any source or collimator tube.

the ground state of the ^{22}Ne via emission of a 1.274 MeV gamma ray. The interaction of the 1.274 MeV gamma ray served as our start signal for an o-Ps event. This is a novel technique that differed from previous experiments that used a thin piece of scintillator coupled to a PMT via optical fiber to tag beta particle emitted in the ^{22}Na decay as the start signal [1]. We initially estimated our total efficiency with a 10 µCi source to be about 7.91×10^{-4}. Additionally, we estimated an accidental rate of about 5% using a 10µCi source combined with a 1 µs gate.

When taking o-Ps data, the collimator tube was removed from the array and replaced with the source holder for the experiment. The source holder was mounted inside of the array via the carbon fiber tube. The location of the tube could be adjusted inside the array to within 2 mm in the x, y, and z directions. The alignment was controlled by the support stand. The carbon fiber was supported by this stand via delrin clamps on either end. These clamps were each connected to an aluminum rod, with a vertical height adjustment achieved by a threaded collar mounted on top of the channel. An image can be seen in fig 2.11.

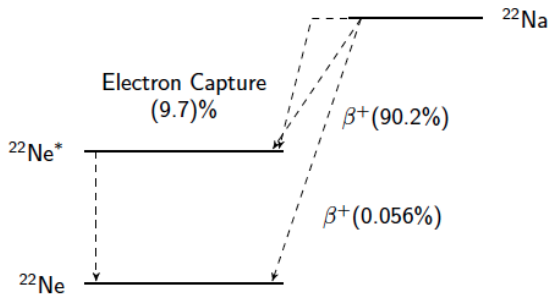

Figure 2.10: Decay Scheme for ^{22}Na [94]. In 9.7% of cases, there is no positron emitted because the ^{22}Na undergoes electron capture. The remaining ^{22}Na decays via emission of a positron, followed by the emission of a 1.27 MeV gamma ray, a few picoseconds later.

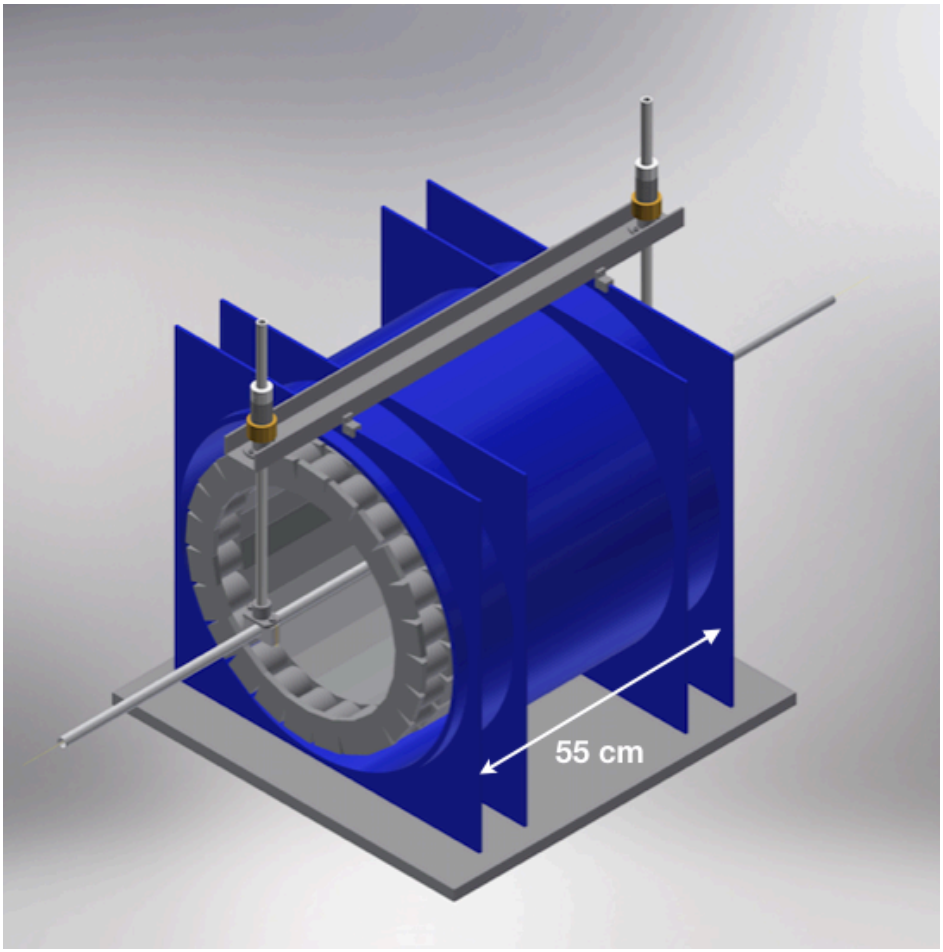

Figure 2.11: CALIOPE Autodesk Rendering by TUNL engineer Brogan Thomas. The carbon fiber tube can be seen running the length of the array, supported by two aluminum rods connected to an aluminum channel that sits on top of the detector.

2.1.6 Event Reconstruction

We calculate the position and energy of the hits in our detector by using the charge amplitudes measured by the photomultiplier tubes and a technique developed by early APEX users [90]. According to this technique, the amplitude of the signal from the first (front) photomultiplier tube can be written as follows:

$$A_1 = \frac{E_\gamma P}{E_0} \exp[-\mu(L/2 + z)], \tag{2.1}$$

where z is the position of a hit, E_γ is the energy deposited by the gamma ray, P is the quantum efficiency of the photomultiplier tubes, E_0 is the energy deposited per light photon created in the scintillator and μ is the light attenuation coefficient. The attenuation coefficients were all measured by Stephen Daigle [93]. As shown below, exact knowledge of these values is not required for reconstruction of energy and position. For the second (back) photomultiplier tube, we have a similar equation:

$$A_2 = \frac{E_\gamma P}{E_0} \exp[-\mu(L/2 - z)]. \tag{2.2}$$

We can combine these equations to find the position in the bar from the charge amplitudes:

$$z = \frac{1}{2\mu} \ln \frac{A_2}{A_1}. \tag{2.3}$$

In a similar manner, the energy can also be calculated from the charge amplitudes using the following equation:

$${E_\gamma}^2 = A_1 A_2 \left(\frac{E_0}{P}\right)^2 e^{\mu L} \tag{2.4}$$

$$E_\gamma = \sqrt{A_1 A_2} \frac{E_0}{P} e^{\mu L/2}. \tag{2.5}$$

Though we still model the amplitude of a pulse as an exponential, we took a slightly

different approach. We calculated the energy using $E \propto \sqrt{A_1 * A_2}$ and the z position using $z \propto \ln \frac{A_2}{A_1}$, however, we do not deal directly in terms of the proportionality factor, $\frac{E_\gamma P}{E_0}$, or the attenuation factor, μ. Instead, we just determined the overall proportionality constant for the z and energy reconstruction and included a constant offset. The values for the proportionality constant and offset were calculated by taking fitting collimated data; this is explained further in chapter 3.

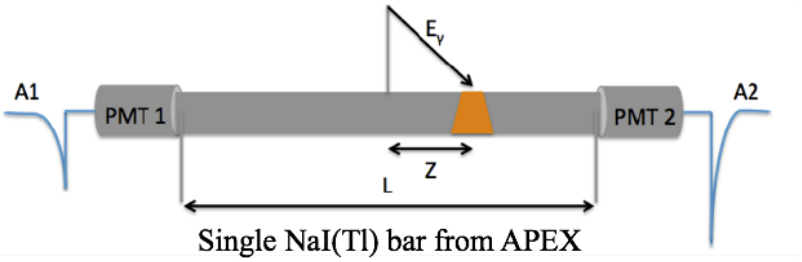

Figure 2.12: Diagram of an NaI segment. A_1 shows an example pulse amplitude from the front PMT, and A_2 shows an example pulse amplitude from the back PMT. The relative pulse amplitudes provide information about the z position and the energy of a hit.

2.1.7 Data Acquisition System

The DAQ for CALIOPE, shown in fig 2.13, uses a CAEN V775 TDC (Timing-To-Digital Converter) [95] and three CAEN V862 QDCs (Charge-To-Digital Converter) [96] to record timing and charge information, respectively. These cards were mounted in a VME crate (UEP 6021), along with the SBC or single board computer (MVME 5100) [97], Jlab Trigger Board [98], and 6 CAEN V812 CFDs (Constant Fraction Discriminator) [99]. All other electronics were NIM-based. The PMT signal is split and feeds into separate channels of an amplifier (NIM Model 776, Phillips Scientific), which amplifies the signal by a factor of 10. Each amplifier channel then produces two amplified output signals. One of these signals proceeds to the CFD and the other signal ultimately feeds into the QDC. The signal which enters the CFD triggers the CFD NIM and ECL outputs if it exceeds the threshold. The NIM output proceeds to the TDC common start and also triggers the common gate of the

QDC (1 μs in duration). The V812 CFDs were modified by CAEN for our purposes to produce ECL gates of 1 μs in duration. Two ECL signals are generated by the CFD for every input signal that exceeds the threshold settings. The first ECL signals travel through a delay chip and cable before serving as the TDC stop signal. The second ECL signal serves as an individual gate for the QDC channel of interest after passing through a delay. The attenuated PMT pulse is delayed and inverted (the V862 requires positive-going pulses) via custom-made electronics boards before entering the signal channel on the QDC.

The way the DAQ works in the case of an ideal o-Ps 'event' is as follows. The interaction of the 1.274 MeV gamma ray in a bar emitted in the decay of ^{22}Na serves as the start signal for a good event. The start signal is determined by the TDC channel that registers the shortest time duration that is characterized by the length of the delay line from the ECL output of the CFD to the stop input on the TDC. That same channel on the QDC would register at an energy of 1.274 MeV. In an ideal o-Ps event, that start signal would be followed by three bars that are hit within some time frame that is characteristic of the o-Ps lifetime. This duration would appear on three separate TDC channels. The corresponding QDC channels should measure energies that add to 1022 keV, which is twice the rest mass of the positron.

To build this DAQ, several components were designed and fabricated at TUNL. There were three types of PC boards that were custom built. The first are the PC boards that delay the signals going to the TDC. These use the TZA4-20 delay chips, made by Rhombus Industries, with a delay of 20 ns. This was not long enough to account for the minimum measurable time duration of the TDC, so an additional 10 ft of ribbon cable was added before the signal reaches the TDC. The next type of PC board are those that perform the 200 ns delay and inversion of the signal that runs straight to the QDC. These boards use the TF200-5 delay chips and included a 10 µF capacitor to remove any DC offset present in the signal. Finally, there is another set of PC boards that include a 120 ns delay (TF120-5 delay chips) for the individual gate signals running from the CFD to the QDC.

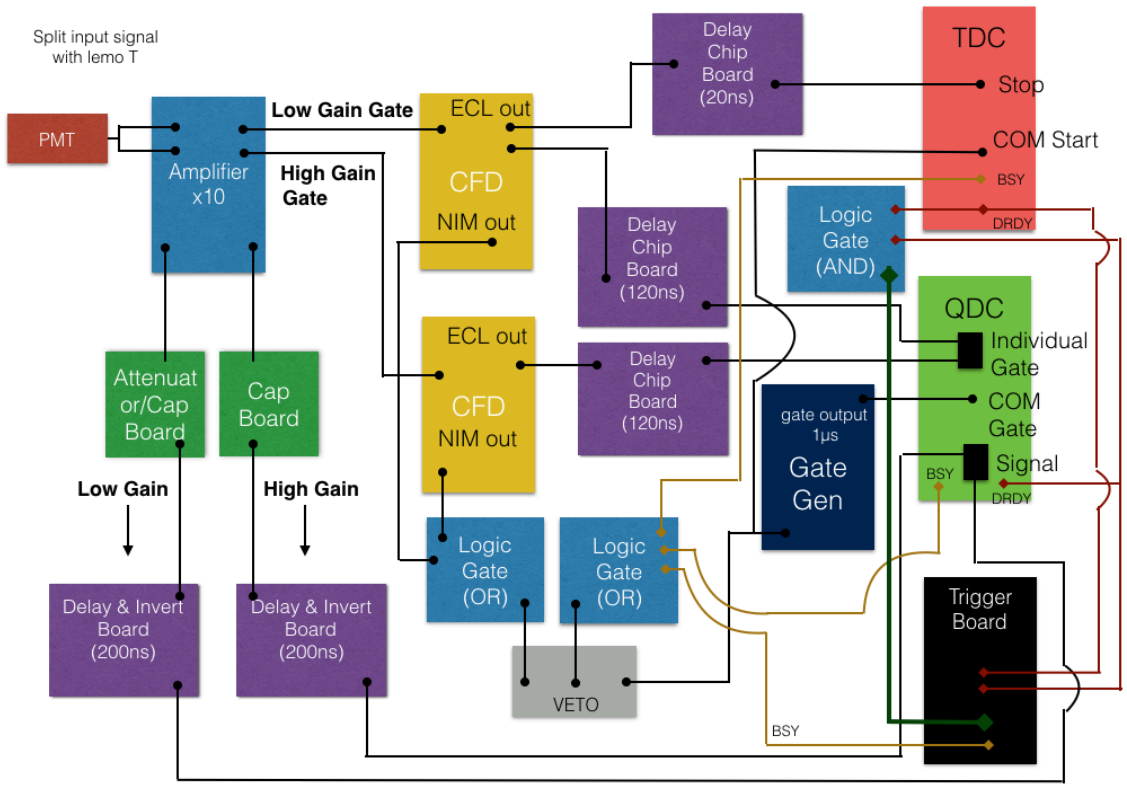

Figure 2.13: Simplified wiring diagram of the CALIOPE DAQ. Only one QDC, out of three total, and two CFDs, out of six total, are shown. There are a total of 48 PMTs, each with a corresponding high and low gain channel, for 96 QDC channels total. There is also one TDC channel per bar, which uses the front PMT. This requires a total of 120 channels overall. Black cables are either LEMO or ribbon cables. Yellow cables are the busy signals and red cables are the data ready signals coming from the individual cards. The green cable running from the QDC to the trigger board is the master trigger which initiates the readout.

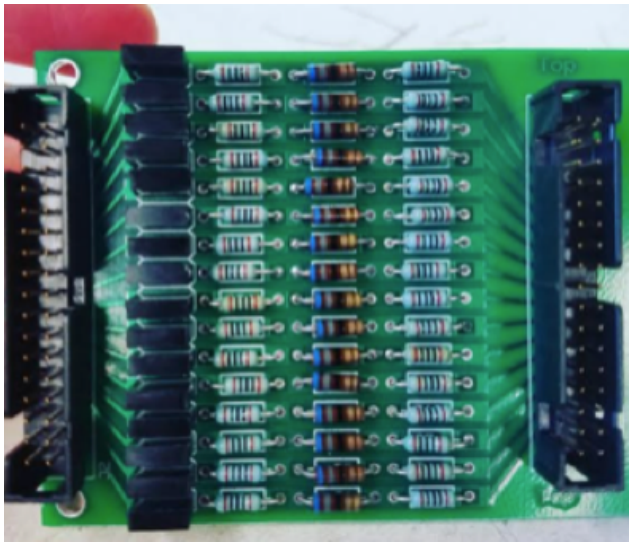

Figure 2.14: Attenuator PC Board uses Pi-Pad Attenuation. 0.1 µF capacitors remove any remaining DC offset. The shunt resistors are 71 ohms and the series resistors are 137 ohms.

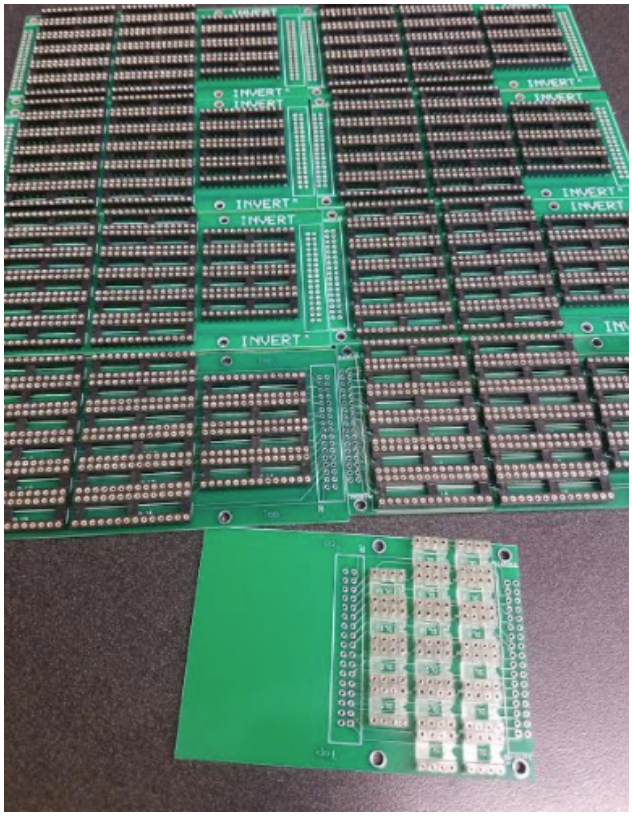

Figure 2.15: IC sockets soldered onto the PC boards, about halfway through the construction process of the delay boards.

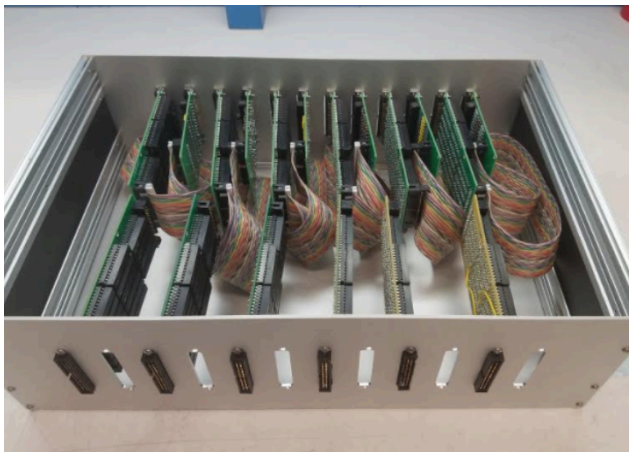

Figure 2.16: The attenuation and delay boards are shown assembled in box to be mounted in the DAQ rack. The back of the box holds 6 attenuator boards and 6 delay boards (alternating) that are used to propagate the low and high gain signals. The front of the box hold the 6 attenuator boards for the delay signals.

Our DAQ uses the Coda readout system [100], version 2.5. Raw binary files are processed using the coda2root software [101]. Our version of Coda required the usage of the Jlab trigger interface (TI) board. The trigger system worked as follows. Twisted pair cables coming from the DRDY pins on the TDC and three QDCs provided inputs on pins 5-8 (one per pin). To generate the main trigger (pin 0 on the trigger interface board), the TDC DRDY signal was AND-ed with the OR of the three QDC DRDY signals. While the signal on this pin triggered the readout, the signals on the input pins indicate to the SBC which modules actually had data available to read out. The four 'input' pins (pins 5-8) above the main trigger pin told the SBC which cards had DRDY high, and therefore, which cards to read out.

Coda uses the coda readout language (CRL). Thresholds and other settings for the cards were programmed onto the cards using a CRL file that was loaded onto the SBC. The thresholds for each QDC were set individually. The threshold for the TDC were set to zero and the full scale range was programmed to 1200 ns. The CFD thresholds were all set to 40.

2.1.8 CALIOPE Event Display

In order to guarantee the viability of our DAQ, we used an event display that showed hits in high and low gain QDC values as well as the TDC. An ideal 'o-Ps' event would have a hit in both high and low gain channels for the $\vec{k_1}$ and $\vec{k_2}$ gamma rays as well as a hit for the start signal. Each of these active bars would also have a corresponding TDC signal. The event dispay was vital for troubleshooting purposes. The event display can be seen in fig 2.17.

2.1.9 APEX Detector Usage

All bars except bar 8 were set up to be used for the experiment. Bar 8 was omitted because of bad channels on the CFDs and poor quality signals. Fig 2.18 shows the layout of APEX bars and how they are grouped according to which QDC their signals enter (there are three total). This design was chosen so as to simplify the organization of the DAQ. Two CFDs (one for high gain channels and one for low gain) correspond to a single QDC. The V862 QDC has two input connectors. The upper input connector was used for low gain channels and the lower input connector was used for high gain channels on each of the QDCs. Photos showing the construction of the DAQ, as well as the final configuration of CALIOPE, can be seen in figs 2.19 and 2.20.

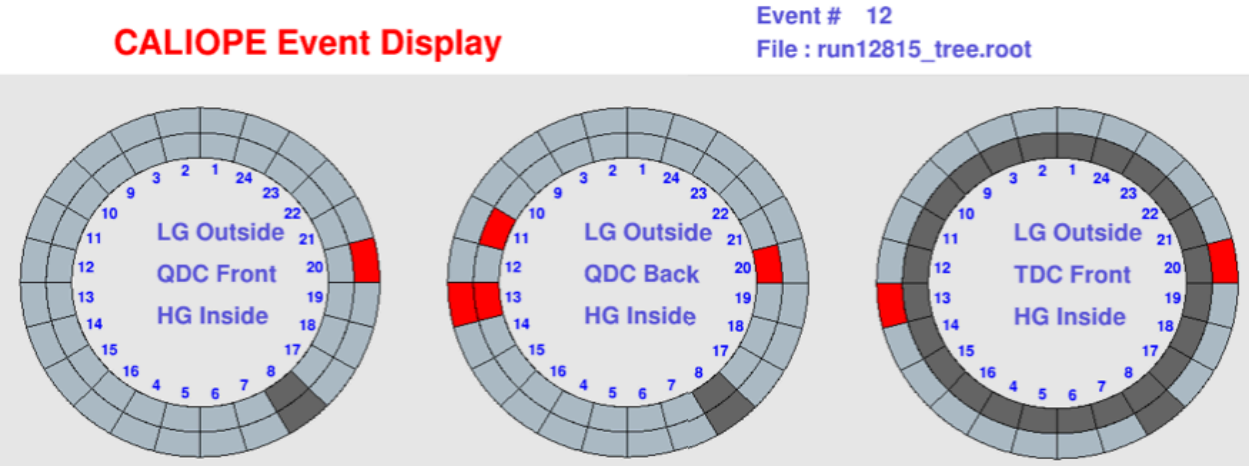

Event display showing what is likely a p-Ps event. The back-to-back gamma rays in bars 13 and 20 are indicative of this type of event.

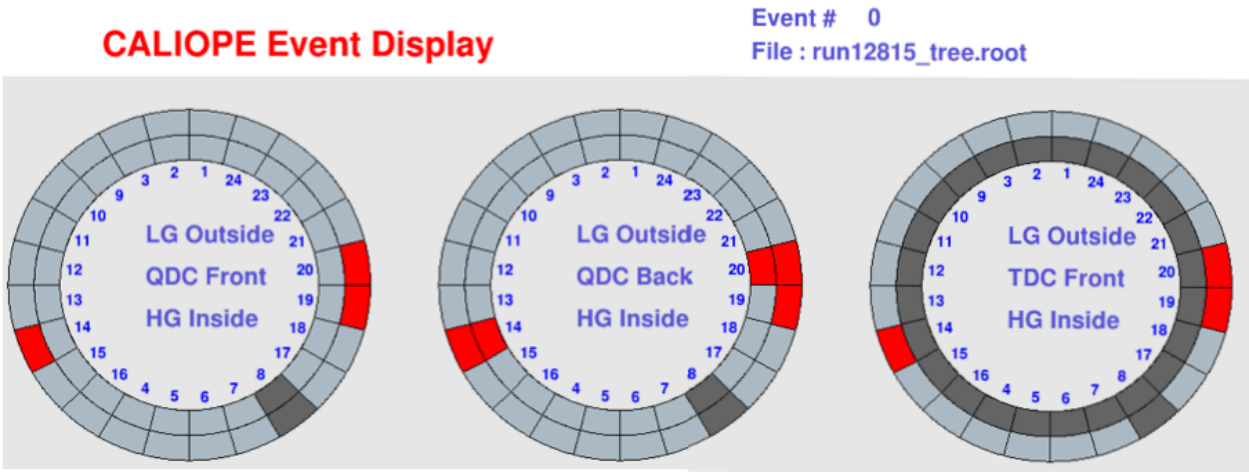

Event display showing what is likely an o-Ps event. Bar 19 likely fired because of the 1.27 MeV start signal, since only the low gain channels are red. Bars 14 and 20 are likely o-Ps gamma rays. The angular separation supports this.

Figure 2.17: An event display was created to help troubleshoot the DAQ. This enabled us to guarantee that each event had good data. The presence of data on any given channel is indicated by the color red. Dark gray segments indicate channels that were not connected. These include bar 8 and the back PMT TDC channels.

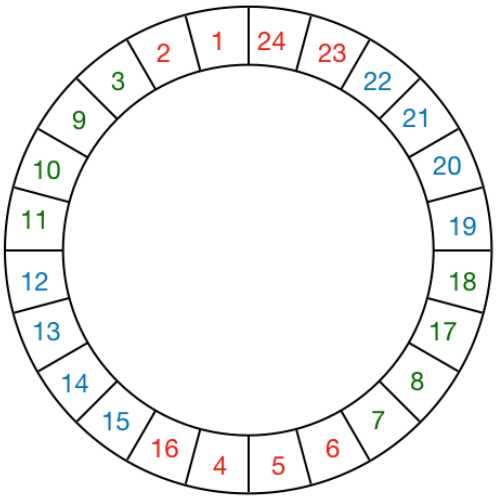

Figure 2.18: Bar numbering scheme for APEX. Colored text indicate how bars are grouped. Bars of the same color enter the same QDC. Bars 1-8 use Photonis PMTs, whereas the remaining bars are Hamamatsu PMTs.

PMT	Voltage (V)	PMT	Voltage (V)	PMT	Voltage (V)	PMT	Voltage (V)
1F	1800	1B	1724	13F	1573	13B	1524
2F	1800	2B	1800	14F	1506	14B	1499
3F	1784	3B	1800	15F	1602	15B	1524
4F	1691	4B	1663	16F	1485	16B	1643
5F	1753	5B	1800	17F	1525	17B	1502
6F	1753	6B	1800	18F	1454	18B	1485
7F	1760	7B	1800	19F	1485	19B	1645
8F	1800	8B	1800	20F	1515	20B	1515
9F	1371	9B	1468	21F	1545	21B	1661
10F	1446	10B	1499	22F	1530	22B	1530
11F	1642	11B	1656	23F	1524	23B	1499
12F	1644	12B	1657	24F	1570	24B	1506

Table 2.1: High Voltage Settings for APEX PMTs: ‘F’ indicates that the PMT was located at the front of the NaI(Tl) bar and ‘B’ indicates that the PMT was located at the back of the NaI(Tl) bar.

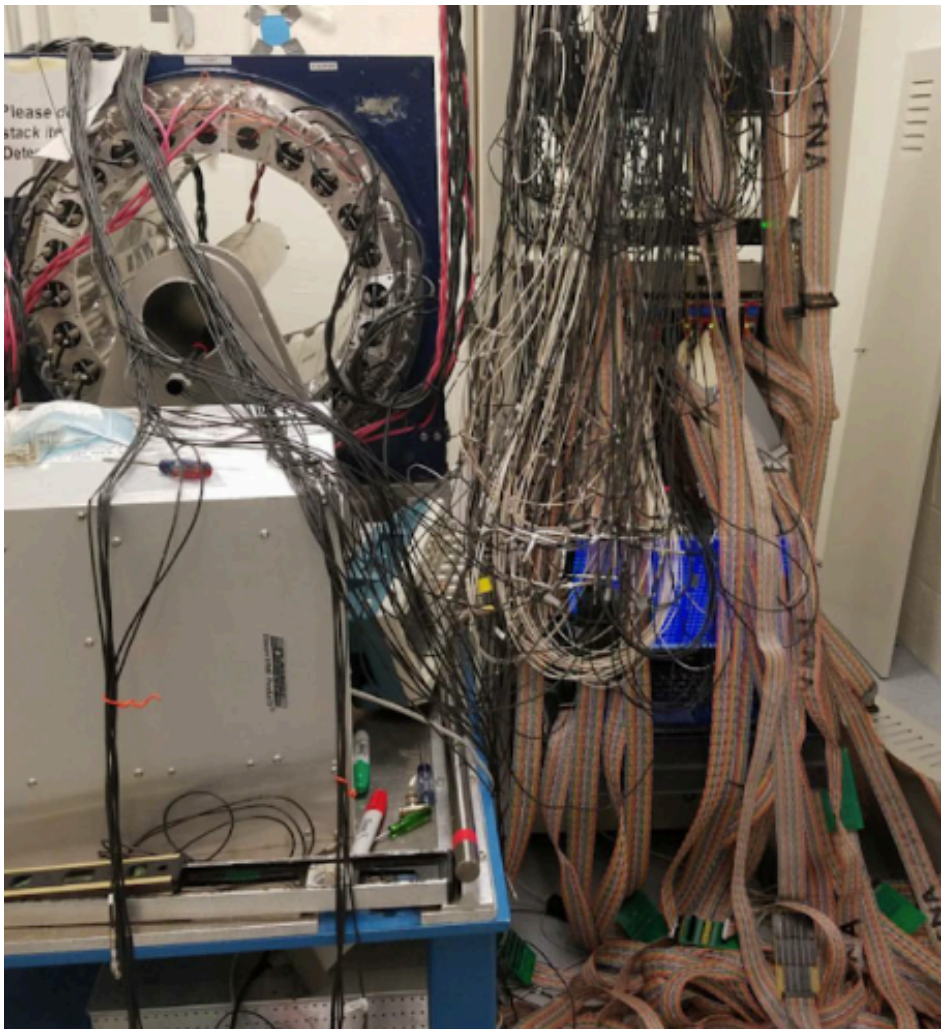

Figure 2.19: The DAQ under construction, showing just before cables and boards were arranged into boxes.

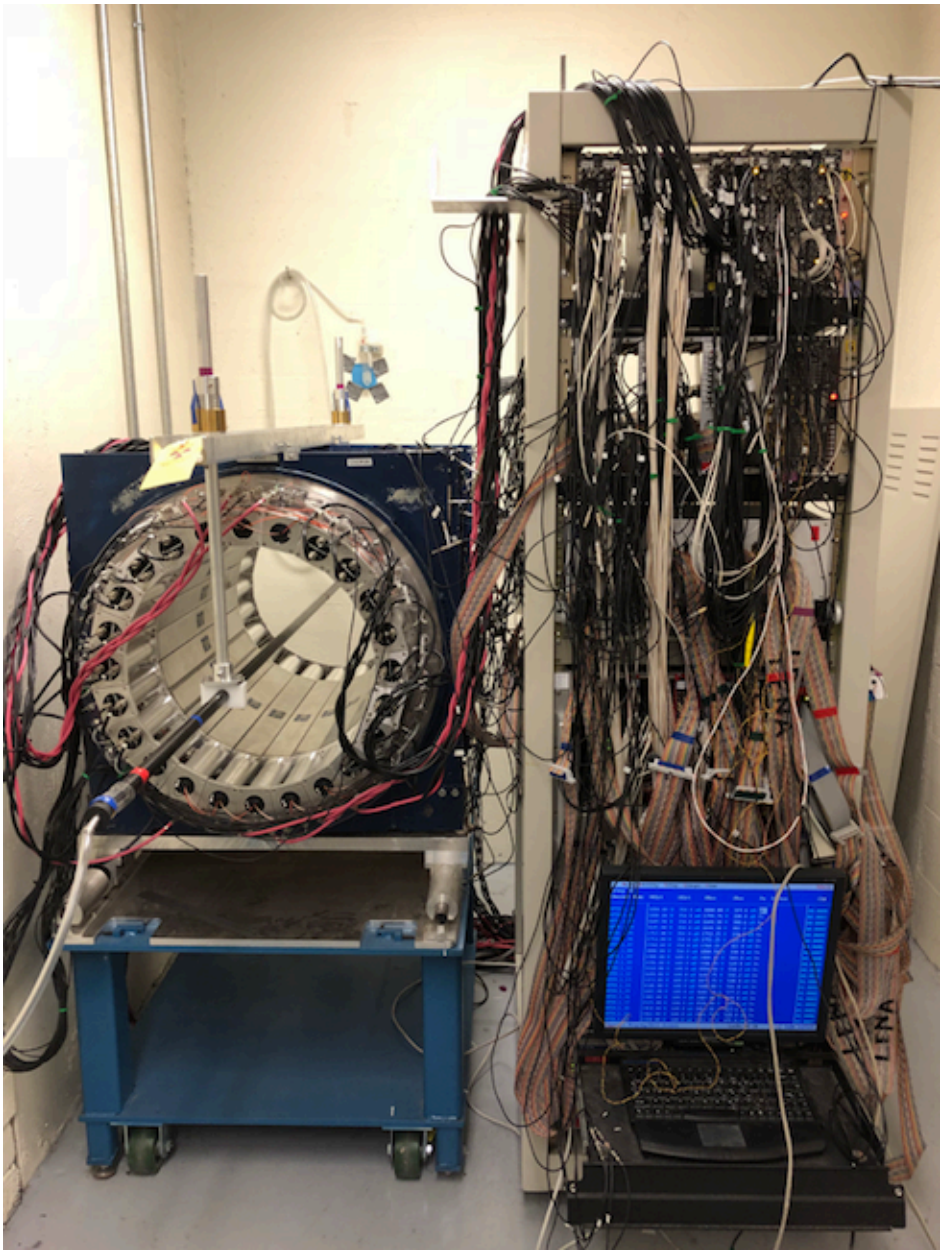

Figure 2.20: The final, working experimental configuration of CALIOPE. The APEX array, carbon fiber tube, and nitrogen gas tubing is shown on the left. The data acquisition system is shown on the right.

CHAPTER 3: Detector Calibration

3.1 Overview

A challenging aspect of working with the APEX array was attenuation of scintillation light in the bars. Additionally, gamma rays interacting at the end of the bars tended to saturate the nearest PMT channel. This made energy calibration of the bars difficult, as we needed to access a fairly broad range of energies, from several hundred keV to 1.27 MeV. To mitigate these effects, we split each signal coming from the PMT into high and low gain channels. The low gain channels provided access to high energy interactions (primarily our 1.27 MeV gamma ray start signal), whereas the high gain channels provided access to the low energy interactions (our $\vec{k_1}$, $\vec{k_2}$, and $\vec{k_3}$ gamma rays). More importantly, we were able to use different channel combinations to reconstruct events that occurred away from the center of the bar. In other words, the front PMT amplitude could be obtained from the high gain channel and the back PMT amplitude could be obtained from the low gain channel and vice versa. These combinations of high and low gain channel amplitudes enabled us to better use the full range of a NaI(Tl) crystal. Nevertheless, this approach entailed the usage of four channels per bar, and therefore increased the complexity of not only the DAQ cabling (as seen in the previous chapter), but the detector calibration process, which will be described in this chapter.

We discovered that the energy calibration was highly dependent on the z position of an interaction along the length of a given NaI(Tl) bar, where we define the z-axis as the axis which runs down the center of the cylindrical array. We explain in this chapter how we discretized the bars and calibrated the energy separately in each section. For the z position calibration, we used collimated data acquired at different locations inside the array, and for

the energy calibration, we used data acquired with different sources.

Though the performance of APEX at such low energies has been demonstrated in the past [102], its previous application at TUNL did not split the PMT signal in half [93], as we did. Splitting the signal prior to amplification increased our noise and diminished low energy sensitivity to gamma rays. The low energy reach of APEX, given our setup, was about 150 keV. This meant that we were able to detect the $\vec{k_1}$ and $\vec{k_2}$ gamma rays and some of the $\vec{k_3}$ gamma rays. We elaborate further on the energy reconstruction capabilities in the subsequent sections.

3.2 Z Position Reconstruction and Calibration

We calibrated the z position reconstruction using data acquired with a 10 µCi, collimated ^{22}Na button source. A photo of the collimator tube inside the APEX array can be seen in fig 2.8. We took data for 30 minutes at five different positions along the length of the array: at the center, 10 cm from the center towards the front of the array, 10 cm from the center towards the back of the array, 20 cm from the center towards the front of the array, and 20 cm from the center towards the back of the array. For each data set, we performed the z position reconstruction using the equation $z \propto \ln(\frac{A_1}{A_2})$, where A_1 is the QDC amplitude measured at the front of the bar and A_2 is the QDC amplitude measured at the back of the bar. We then reconstructed the z position with four different methods:

1. using the high gain channels for both A_1 (front PMT amplitude) and A_2 (back PMT amplitude)

2. using the low gain channels for both A_1 (front PMT amplitude) and A_2

3. using the high gain channel for A_1 and the low gain channel for A_2

4. using the low gain channel for A_1 and the high gain channel for A_2.

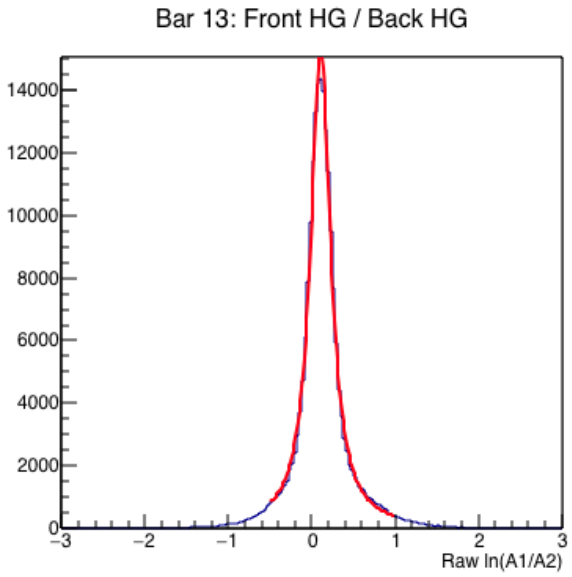

Collimated ^{22}Na source at center of array using FhgBhg channel combinations.

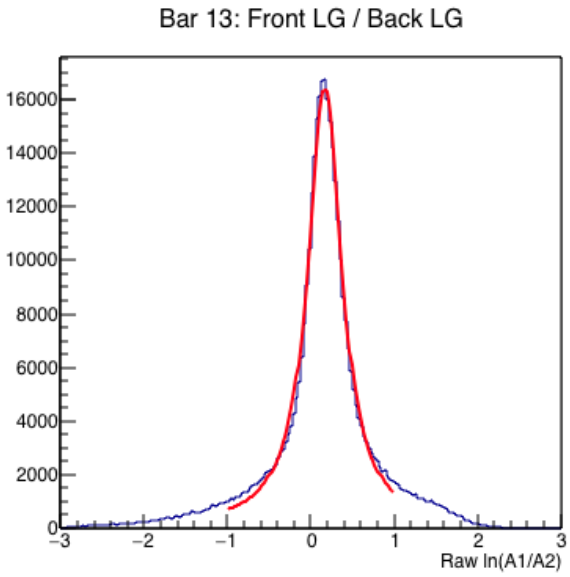

Collimated ^{22}Na source at the center of the array using FlgBlg channel combinations.

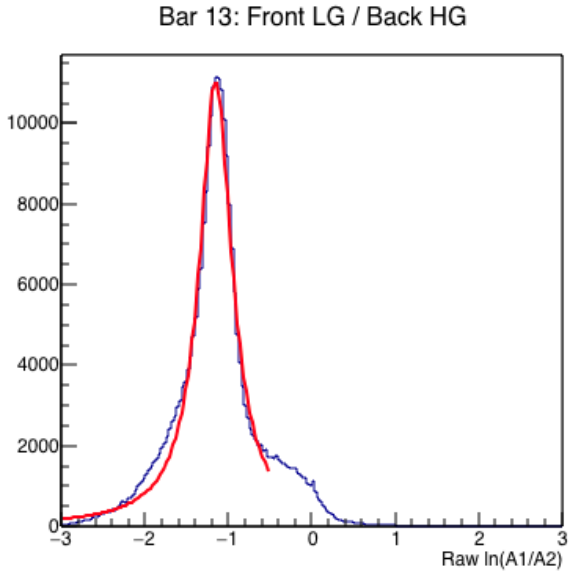

Collimated ^{22}Na source at the center of the array using FlgBhg channel combinations.

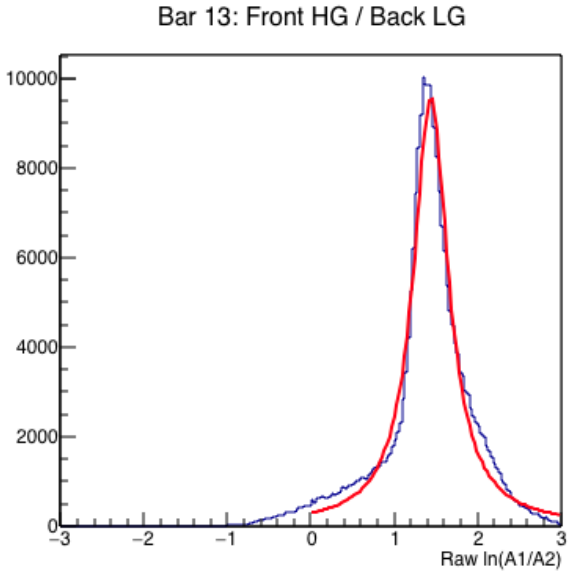

Collimated ^{22}Na source at the center of the array using FhgBlg channel combinations.

Figure 3.1: Collimated ^{22}Na data at the center of the bar using different channel combinations for bar 13. Imperfections in the Lorentzian curve fit, particularly near the base of the curve, are likely due to the scattering of gamma rays off the lead collimator. We observed similar effects with a simulation. Examining the tails of these histograms, we estimate approximately 10% of the data is not well-characterized by our fit. As the z position is not critical to determining the handedness of our o-Ps gamma rays, we believe this has a negligible effect.

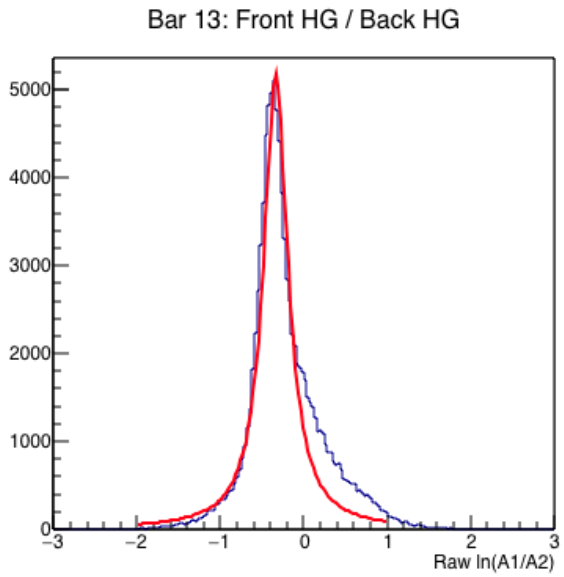

Collimated ^{22}Na source 10 cm towards the back using FhgBhg channel combinations.

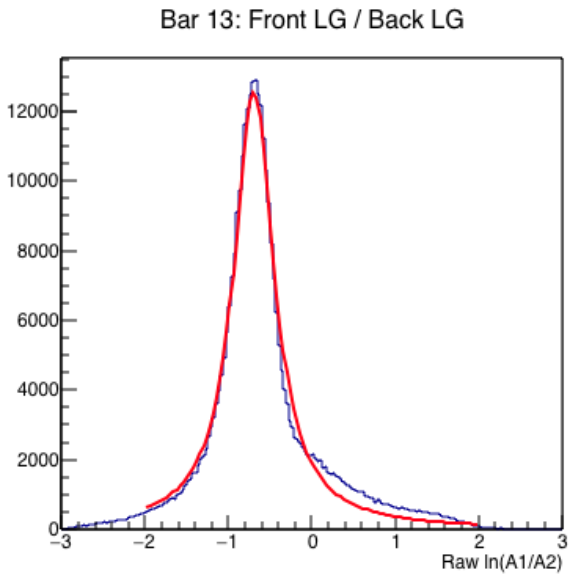

Collimated ^{22}Na source 10 cm towards the back of the array using FlgBlg channel combinations.

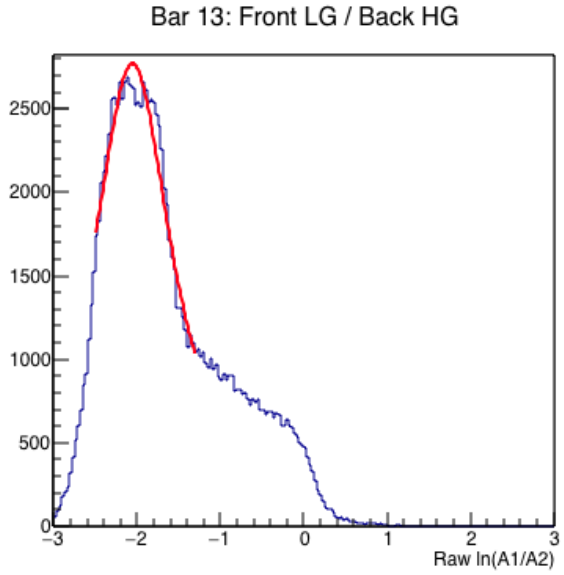

Collimated ^{22}Na source 10 cm towards the back of the array using FlgBhg channel combinations.

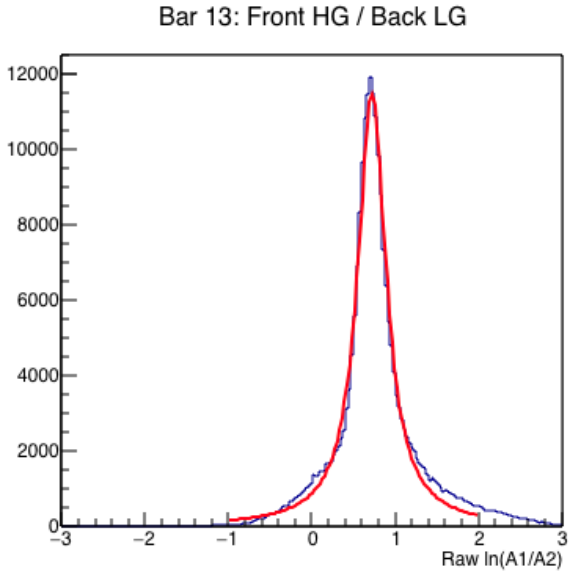

Collimated ^{22}Na source 10 cm towards the back of the array using FhgBlg channel combinations.

Figure 3.2: Collimated ^{22}Na data 10 cm from the center of the array towards the back using different channel combinations for bar 13. Imperfections in the fit, particularly near the base of the curve, are likely due to the scattering of gamma rays off the lead collimator. This impacts only a small fraction of the data, and has a negligible effect on our measurement.

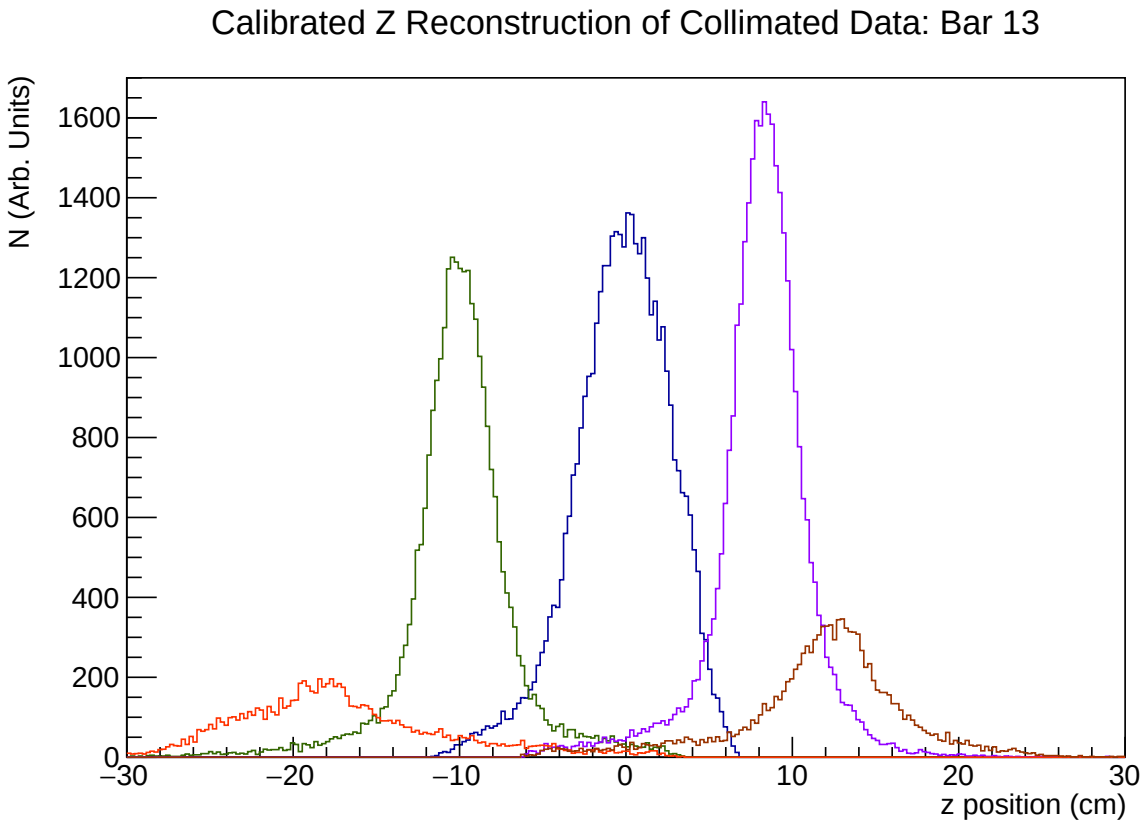

Figure 3.3: Position reconstruction with APEX array using 10 µCi collimated ^{22}Na source. Shown are data sets taken with the collimator located at different positions inside the array. Points were taken at 10 cm intervals along the array starting at -20 cm (towards the back). For this plot, a cut was made so that it includes only ±20 keV around the 511 keV gamma ray. Each curve uses a different combination of high and low gain channels. The blue data set uses exclusively high gain channels. The purple and yellow peaks to the right of the blue peak use a combination of front low gain and back high gain channels because this data was acquired towards the front of the bar. Likewise, the green and orange peaks to the left of the blue peak use a combination of back low gain and front high gain channels. The poor resolution near the back of the array (≈20 cm, shown in red) is not likely to be a serious issue as most of our data is shifted towards the front, since only this PMT was connected to the TDC. Furthermore, the z position is not necessary to determine the handedness of the $\vec{k_1}$ and $\vec{k_2}$ gamma rays.

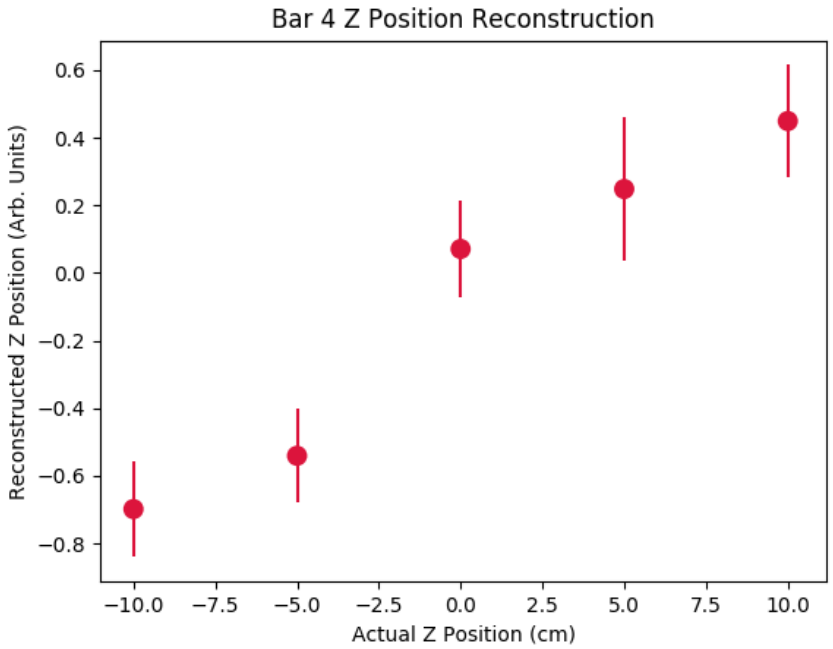

Figure 3.4: Actual z position vs uncalibrated, reconstructed z position. Collimated ^{22}Na data were used with bar 4.

We developed code that partially automated the process of fitting the reconstructed z position data from the individual bars with a Lorentzian curve, using ROOT [103]. Examples of the fits can be seen in figs 3.1 and 3.2. These figures show the calibration for all possible permutations of available channels. Most bars were calibrated using a linear fit between the raw data points at two positions within the array: the center and 10 cm towards the front. The majority of our data falls in this regions, since only the front PMT was connected to the TDC. Furthermore, we were able to show that the fit acquired with these data points is equivalent to that acquired with more data points along the length of the bar. An example of this can be seen in fig 3.4.

Fig 3.3 shows the z position calibration at different locations along the length of the bar with a cut applied to isolate the 511 keV gamma ray. The far ends of the bar cannot be accessed in this energy range using the high gain channels exclusively, and we used the combined front low gain/back high gain channels to access the 'front' end of the bar ($>$ 5 cm from the center of the array) and the front high gain/back low gain channels to access

Bar	Attenuation Coefficient (mm^{-1})	FWHM (cm)	Error (cm)
1	0.0025	2.18	0.003
2	0.0011	4.06	0.003
3	0.0023	2.27	0.003
4	0.0019	3.70	0.003
5	0.0009	5.60	0.003
6	0.0012	6.70	0.003
7	0.0054	0.91	0.003
9	0.0028	1.96	0.003
10	0.0028	2.40	0.003
11	0.0029	1.70	0.003
12	0.0021	3.03	0.003
13	0.0024	2.23	0.003
14	0.0024	2.30	0.003
15	0.0030	2.08	0.003
16	0.0002	1.41	0.003
17	0.0026	2.30	0.003
18	0.0025	2.46	0.003
19	0.0019	2.86	0.003
20	0.0027	2.52	0.004
21	0.0020	3.69	0.003
22	0.0036	2.44	0.003
23	0.0020	2.93	0.003
24	0.0020	4.31	0.002

Table 3.1: Table of attenuation coefficients for each of the bars.

the 'back' end of the bar ($<$ -5 cm from the center of the array).

In the analysis code, we used the the high gain channels to calculate the z position if they were available. If not, we used the combination of front high gain with back low gain, or back high gain with front low gain, depending on which channels were missing (either saturated or below threshold). If the only available data existed on the low gain channels, we calculated the z position using those. Calibrating the z position then enabled us to calibrate the energy spectra, which is described in the following section. A table of the attenuation coefficients, position resolution, and associated error is shown in Table **??**.

3.3 Energy Reconstruction and Calibration

3.3.1 Unsuccessful Techniques

Our initial approach to the energy reconstruction was to convert raw ADC values in the high gain channels to raw ADC values in the low gain channels before calculating the energy via $E \propto \sqrt{(A_1 * A_2)}$. We decided to abandon this approach when we realized that there was a large spread in the high gain channel data when plotted as a function of the low gain channel data. Another energy calibration approach that we considered was to use an alternative function to the square root of the product of the PMT amplitudes, $E \propto \sqrt{A_1 * A_2}$. We examined the 2D histograms of the raw ADC values for the front and back high gain channels, as well as the front and back low gain channels, to see if we could devise a better means of calculating the energy. These histograms, shown in fig 3.5 and 3.6 were generated using an uncollimated, 10 µCi ^{22}Na button source near the center of the array. In fig 3.5, the yellow band in the top right corner corresponds to the 511 keV gamma ray. In fig 3.6, the 'banana-shaped' yellow band in the middle corresponds to the 1.27 MeV gamma ray peak and the band in the bottom left corresponds to the 511 keV gamma ray peak. One approach we used was to modify the energy reconstruction equation to include a noise term for each PMT amplitude, so $E \propto \sqrt{(A_1 + N_1)(A_2 + N_2)}$, where N_1 is the noise inherent to the front PMT and N_2 is the noise inherent to the back PMT. We then performed a fit to the 511 and 1275 keV curves in 3.6 to determine N_1 and N_2. This approach was abandoned, as it yielded a composite energy spectrum with poor resolution.

3.3.2 Successful Energy Reconstruction Technique

As it was not viable to convert high gain channels to low gain channels (or vice versa), we needed to find an alternative means of deciding which channels to use in the reconstruction. We devised a method that also considered the z dependence of the energy, which can be seen

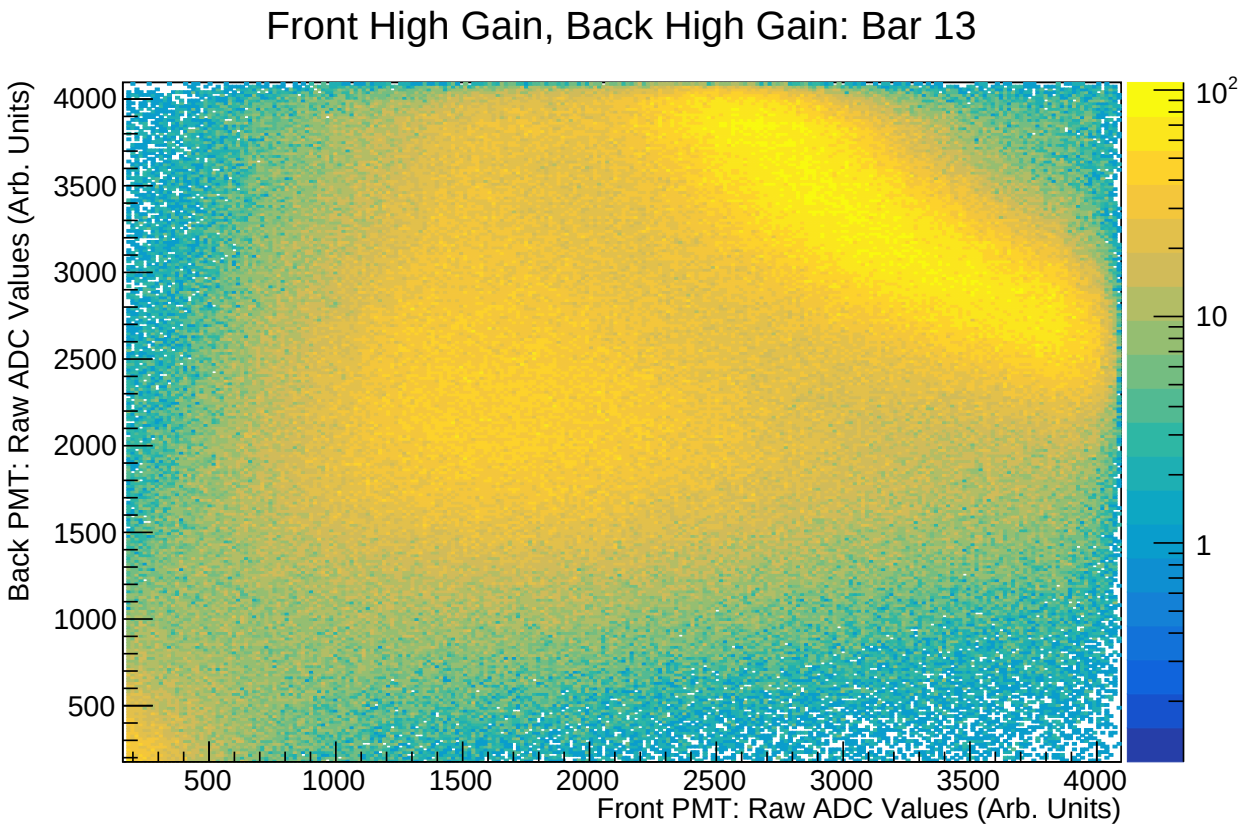

Figure 3.5: Front PMT vs Back PMT raw ADC values using high gain channels for bar 13. The data was acquired with an uncollimated, 10 µCi ^{22}Na button source. The yellow band in the top right is the 511 keV line from ^{22}Na source.

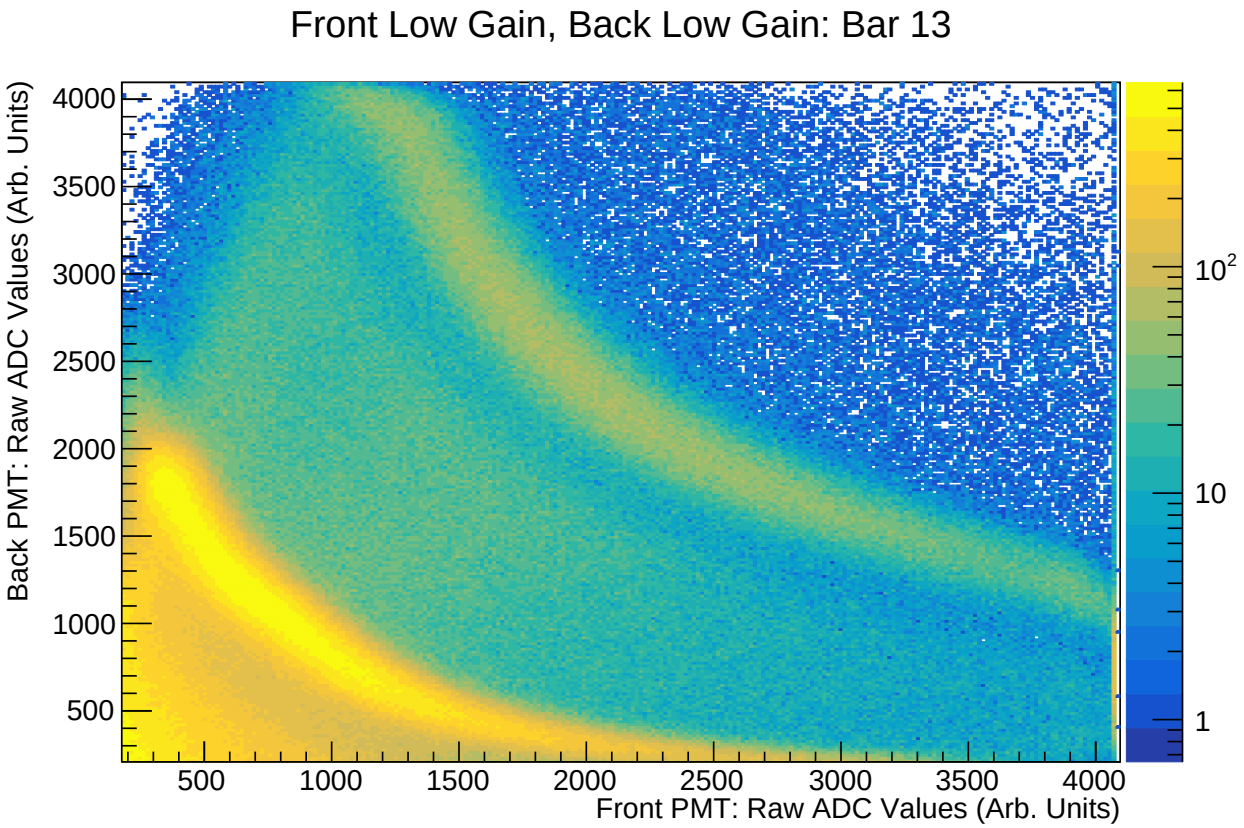

Figure 3.6: Front PMT vs Back PMT raw ADC values using low gain channels for bar 13. The data was acquired with an uncollimated, 10 µCi source. The yellow 'banana'-shaped bands are the 1.27 MeV gamma ray (middle) and the 511 keV gamma ray (bottom left).

in fig 3.7, as well as the number of channels with 'valid' data present for a given interaction. By 'valid' data, we mean raw QDC values that exceed 100 (raw QDC output) and do not saturate the channel. Less than 1% of events detected saturate a given channel. While about 20% of our valid data consists of 4 channel events, the remaining 80% of our valid data consists of events with only three or two channels. Interactions with over 2 channels presented the dilemma of which channels to use in the reconstruction. The algorithm for determining which channels to use was as follows.

If data was valid and present on all four channels, the high gain channels ('FhgBhg': see fig 3.8) were used to perform an event reconstruction, unless the interaction occurred more than 5 cm off-center. If the event occurred more than 5 cm off-center, alternative combinations of channels were used. These are described in entries 1-5 of Table 3.2. Energies of interactions in each segment were calibrated separately. We excluded all events that occurred within 2.5 cm of the ends of the bar.

In the case that valid data appeared in only three channels, a similar technique was used. There are two scenarios that occur when there is data on only three channels: either the high gain channel for one PMT is missing, or the low gain channel for one PMT is missing. Our choice of channels for the energy reconstruction was motivated by the presence of valid channel data combined with the z position of the interaction. This is cataloged in entries 6-7 in Table 3.2.

There are four cases that still allow for event reconstruction in the absence of two channels. These are:

1. valid data only for the front high gain and back high gain channels
2. valid data only for the front high gain and back low gain channels
3. valid data only for the front low gain and back high gain channels, and
4. valid data only for the front low gain and back low gain channels.

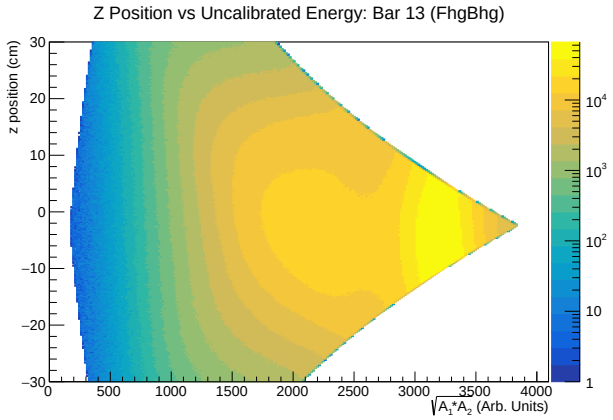

Reconstructed z vs uncalibrated energy for bar 13 using front high gain and back high gain channels. The 511 keV gamma ray can be seen on the right.

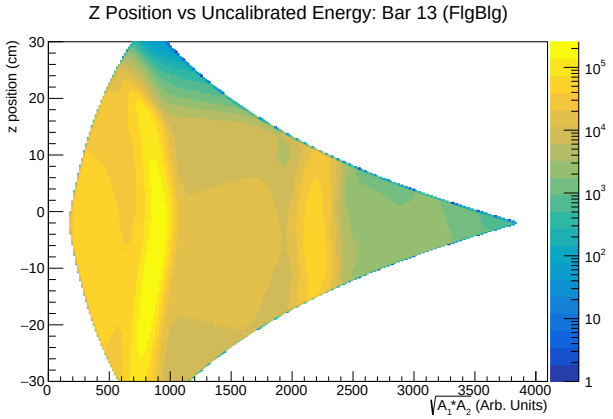

Reconstructed z vs uncalibrated energy for bar 13 using front low gain and back low gain channels. The 511 keV gamma ray can be seen on the left, and the 1.27 MeV gamma ray can be seen in the middle.

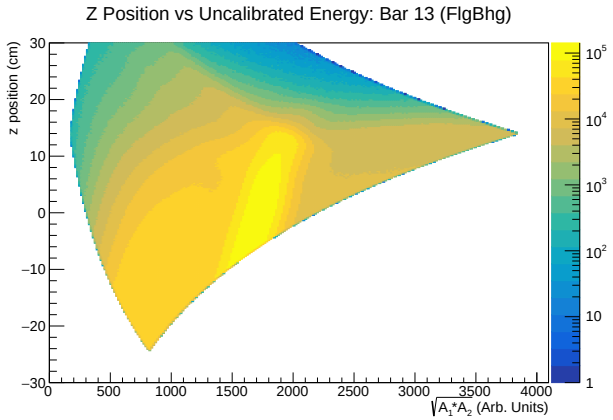

Reconstructed z vs uncalibrated energy for bar 13 using front low gain and back high gain channels. The 511 keV gamma ray can be seen in the middle.

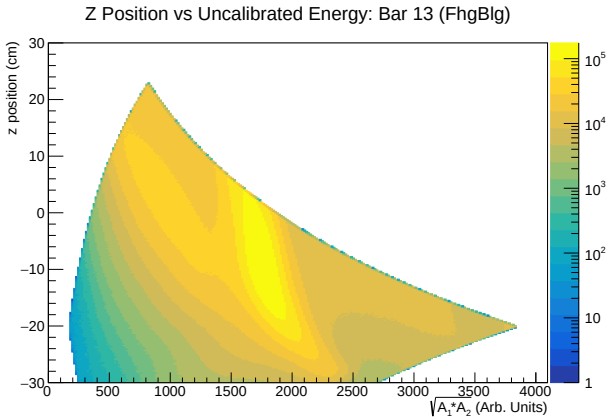

Reconstructed z vs uncalibrated energy for bar 13 using from high gain and back low gain channels. The 511 keV gamma ray can be seen in the middle.

Figure 3.7: Reconstructed z position vs uncalibrated energy using different channel combinations with uncollimated ^{22}Na for bar 13. The 'funnel' (right hand side of these plots), shows how higher energy events saturate and can no longer be detected far off center. The 'bell' (left hand side of these plots), shows how the detector threshold varies with position.

These cases are described in 3.2. Once again, the z position is also considered in the energy calibration.

For future reference, we refer to the discretized regions along the z length of the bar as 'voxels' and call the convolution of the number of channels with z position a 'calibration function'. Table 3.2 lists all possible calibration functions that were just explained in this section.

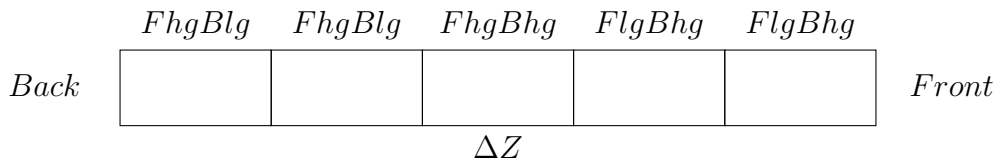

Figure 3.8: Diagram of a NaI(Tl) bar, split into sections. ΔZ is equal to 10 cm. The sections are labeled according to which channels are used to determine the energy there. The abbreviations refer to which channels were used in the energy reconstructions, for example, 'FhgBlg' refers to where the front high-gain and back low-gain channels were used. The regions where the 'FlgBhg' and 'FhgBlg' channel combinations are used are further split according to the z position along the length of the bar. High gain channels closest to the end of the bar can saturate, hence the LG channel is used.

When plotting the z position as a function of the uncalibrated energy, as in fig 3.7, a 'trumpet' shape becomes evident. The narrow 'funnel' on the right hand side reflects the fact that high energy gamma rays saturate the nearest PMT channel, especially when the gamma ray hits occur off-center. Additionally, the flared nature of the left-hand side of the plot demonstrates how the detector threshold varies with position. These features complicate the energy calibration process, as calibration peaks need to appear in all voxels. For most bars, the 'FhgBhg', 'FlgBhg', and 'FhgBlg' channel combinations could be calibrated in all voxels using the 511 keV line in ^{22}Na and the 356 keV line feature in ^{33}Ba. A few bars, however, did not have an adequate ^{133}Ba peak to fit in the 'FhgBlg'/'FlgBhg' voxels for energy calibration due to this attenuation. In these cases, the 662 keV line in ^{137}Cs was used to calibrate the energy spectrum in those segments instead. Such bars likely have a higher

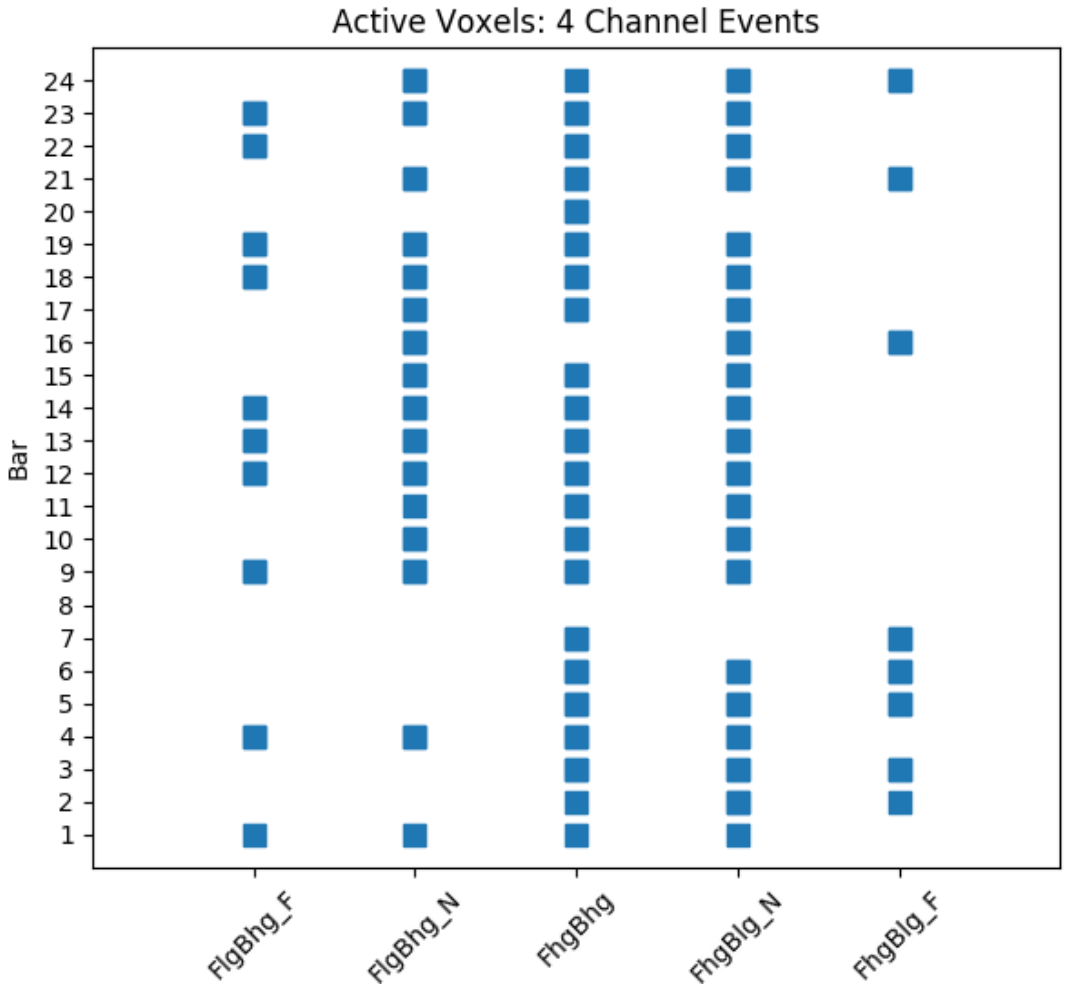

Figure 3.9: Active voxels for four channel events. 'FlgBhg_N' and 'FhgBlg_N' stand for the "near" regions of the bar that use those channels ($5 < z < 15$, or $-15 < z < -5$). 'FlgBhg_F' and 'FhgBhg_f' stand for the "far" regions of the bar that use those channels ($15 < z < 25$, or $-25 < z < -15$). These regions are labeled in fig 3.8. Missing voxels are regions that did not have two good energy peaks between the barium, cesium, or sodium spectra with which to perform a fit.

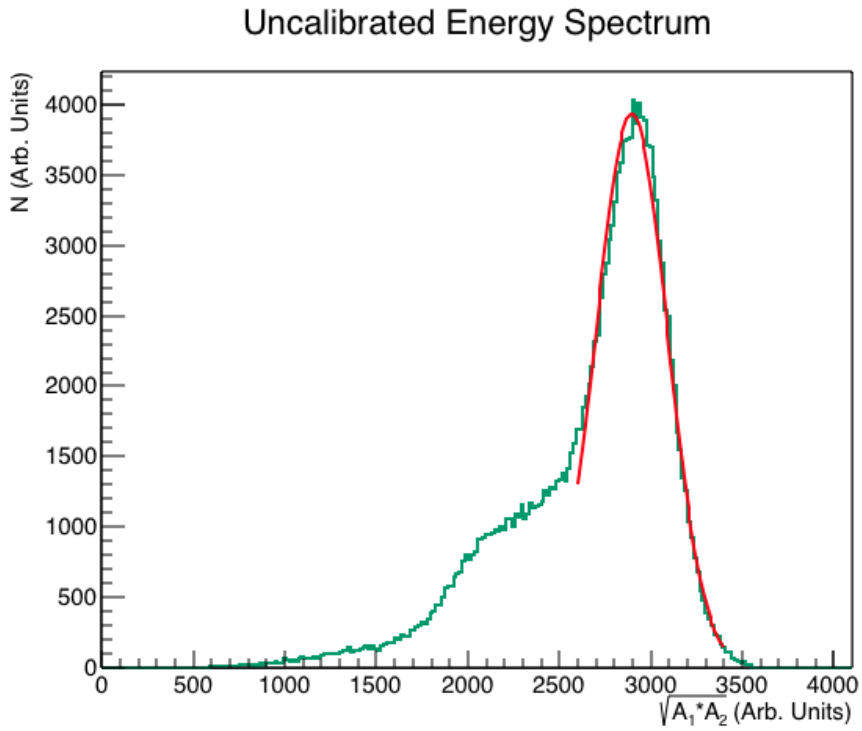

Figure 3.10: Uncalibrated energy spectrum for bar 12 using uncollimated ^{22}Na. Center voxel, 'FhgBhg' data set used, valid data on all four channels. Discrepancies between the fit and the data may be ascribed the fact that any Compton shoulder is not really accounted for in our fit. There is also more noise at low energies in our detector and electronics. Gaussian fit is shown in red.

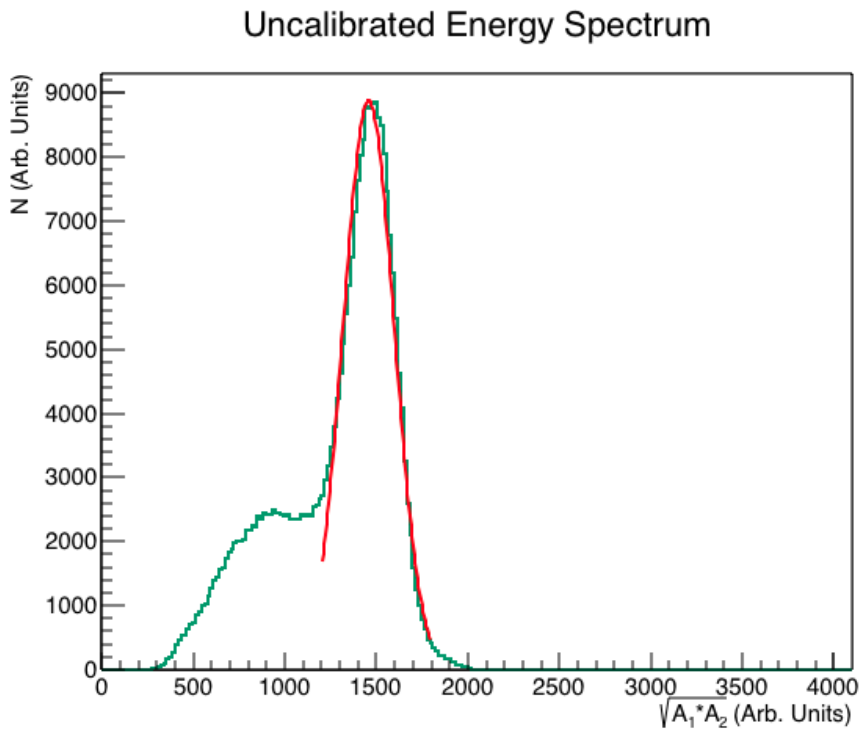

Figure 3.11: Uncalibrated energy spectrum for bar 12 using uncollimated ^{22}Na. Front 'near' voxel, 'FlgBhg' data set used, valid data on all four channels. Discrepancies between the fit and the data may be ascribed to low energy noise in our detector or electronics. Gaussian fit is shown in red.

energy threshold, and so may not be as sensitive to $\vec{k_3}$, though we still used them for the detection of our o-Ps and start signal gamma rays. We show a figure of the voxels available to us for each bar using four channel events in fig 3.9. In the case of the 'FlgBlg' channel combinations, the 511 keV and 1.27 MeV gamma ray peaks from ^{22}Na were used to perform the calibration. It is clear from fig 3.7 that the 1.27 MeV gamma ray quickly saturates the PMT as it moves towards either end of the bar. The 'FlgBlg' channel was used only to identify start signal interactions from the 1.27 MeV gamma ray.

Raw ADC values used in the energy spectra were required to fall in the range from 100 to 3840 raw ADC counts, as explained earlier. Additionally, we implemented a cut at 150 keV before generating the spectra, as we did not intend to use any data below this threshold. To calibrate the energy for each bar, we performed a unique fit to the raw energy spectrum ($\sqrt{A_1 * A_2}$) for each calibration function. We fit Gaussian curves to the barium, sodium, and occasionally, cesium peaks that appeared in these subsets of data using custom ROOT code. Examples of these fits in the case of ^{22}Na can be seen in fig 3.10 and 3.11. This code was interactive, and enabled the user to provide a range over which a given peak could be fit. The resolution and mean value of the fits were written to files that were later incorporated in the energy reconstruction portion of the analysis. We provide two examples of the finalized, composite energy spectra for individual bars. In figs 3.12, we show the energy spectra for sodium, barium and cesium, respectively, in bars 1 and 13. Bar 13 is equipped with Hamamatsu PMTs and, consequently, has one of the best energy resolutions. Bar 1 is equipped with Photonis PMTs and, consequently, has one of the worst energy resolutions.

Once in possession of the composite energy spectra, we were able to determine the overall energy resolution. A histogram of the percent energy resolution of all of the APEX bars can be seen in fig 3.13 and 3.14. For the 511 keV peak, the best resolution is around 9% and the worst resolution is about 17%. For the 356 keV peak, the best measured resolution is about 13% and the worst is around 29%. For barium our resolution is actually slightly better than measured here, since we did not account for the presence of the 302 keV peak in our fit.

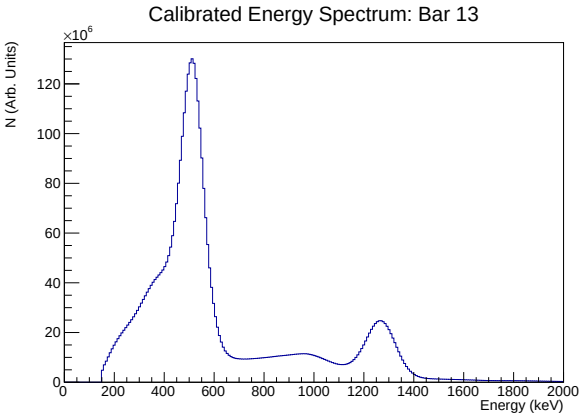

Calibrated energy spectrum for bar 13 using uncollimated ^{22}Na.

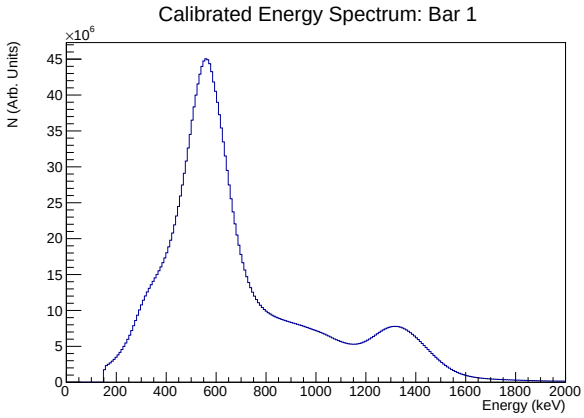

Calibrated energy spectrum for bar 1 using uncollimated ^{22}Na.

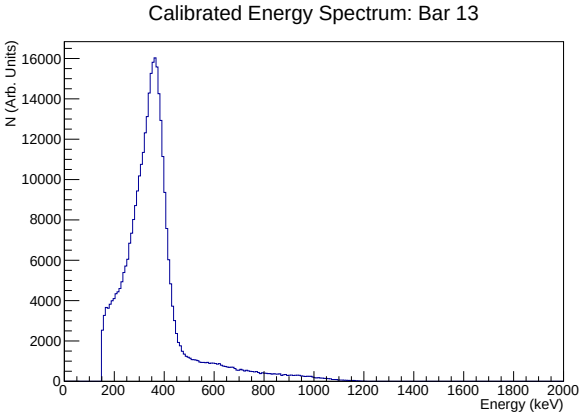

Calibrated energy spectrum for bar 13 using uncollimated ^{133}Ba.

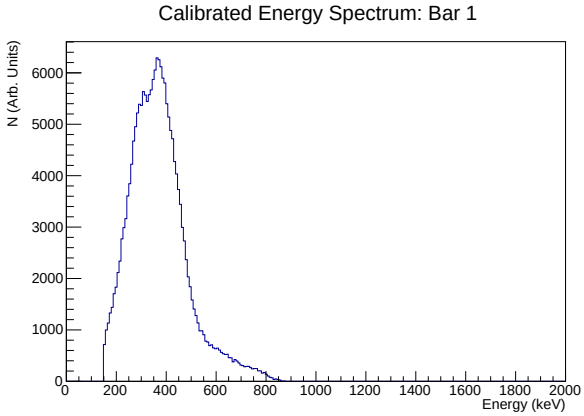

Calibrated energy spectrum for bar 1 using uncollimated ^{133}Ba.

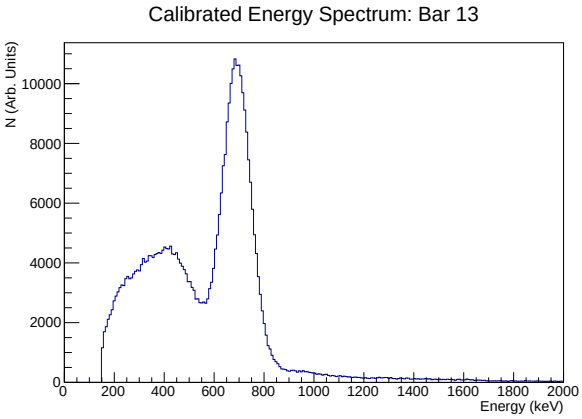

Calibrated energy spectrum for bar 13 using uncollimated ^{137}Cs.

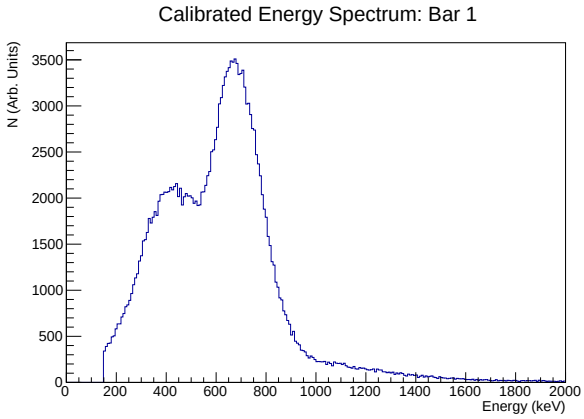

Calibrated energy spectrum for bar 1 using uncollimated ^{137}Cs.

Figure 3.12: Calibrated Energy Spectra: Bars 1 (Photonis PMTs) and 13 (Hamamatsu PMTs).

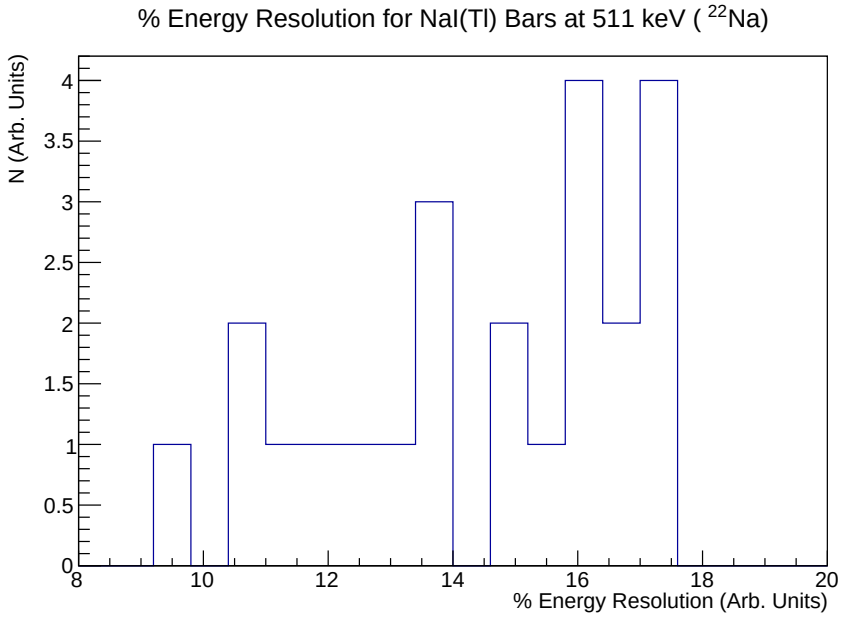

Figure 3.13: Percent energy resolution of all bars for ^{22}Na for the 511 keV line.

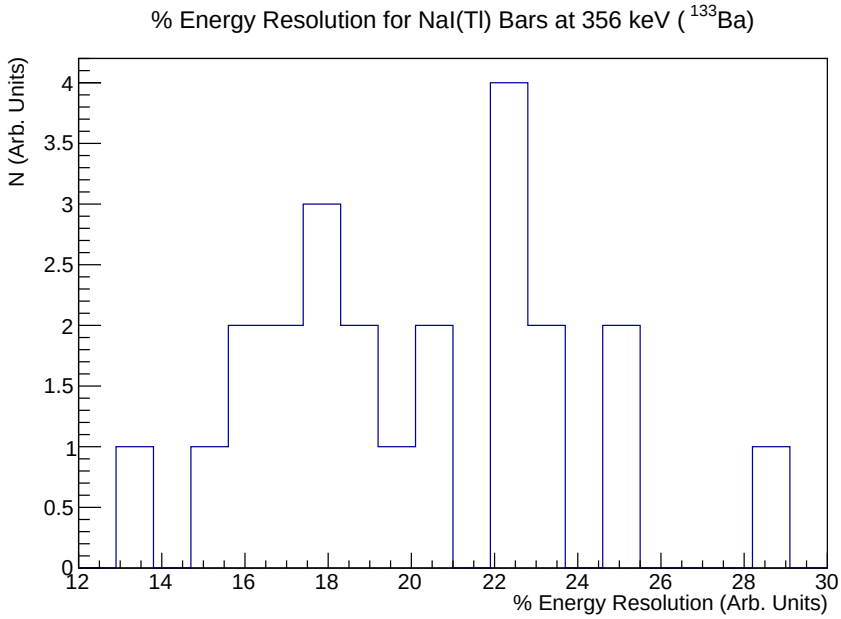

Figure 3.14: Percent energy resolution of all bars for ^{133}Ba for the 356 keV line.

The energy resolution determines our ability to distinguish the $\vec{k_1}$ and $\vec{k_2}$ gamma rays, and so determines the sensitivity of our experiment. We used the energy resolutions in figs 3.13 and 3.14 to determine the reduction in sensitivity in a process explained in section 5.6.1.

Function	Valid channels	Z Position	Channels Used	Channels Missing	Detected Gammas
1	4	-5 cm < z < +5 cm	FhgBhg	0	$\vec{k_1}$, $\vec{k_2}$, $\vec{k_3}$
2	4	+5 cm < z < +15 cm	FlgBhg	0	$\vec{k_1}$, $\vec{k_2}$, $\vec{k_3}$
3	4	+15 cm < z < +25 cm	FlgBhg	0	$\vec{k_1}$, $\vec{k_2}$, $\vec{k_3}$
4	4	-15 cm < z < -5 cm	FhgBlg	0	$\vec{k_1}$, $\vec{k_2}$, $\vec{k_3}$
5	4	-25 cm < z < -15 cm	FhgBlg	0	$\vec{k_1}$, $\vec{k_2}$, $\vec{k_3}$
6	3	-5 cm < z < +5 cm	FhgBhg	Blg	$\vec{k_1}$, $\vec{k_2}$, $\vec{k_3}$
7	3	+5 cm < z < +15 cm	FlgBhg	Blg	$\vec{k_1}$, $\vec{k_2}$, $\vec{k_3}$
8	3	+15 cm < z < +25 cm	FlgBhg	Blg	$\vec{k_1}$, $\vec{k_2}$, $\vec{k_3}$
9	3	-5 cm < z < +5 cm	FhgBlg	Flg	$\vec{k_1}$, $\vec{k_2}$, $\vec{k_3}$
10	3	-15 cm < z < -5 cm	FhgBlg	Flg	$\vec{k_1}$, $\vec{k_2}$, $\vec{k_3}$
11	3	-25 cm < z < -15 cm	FhgBlg	Flg	$\vec{k_1}$, $\vec{k_2}$, $\vec{k_3}$
12	3	-5 cm < z < +5 cm	FhgBlg	Bhg	$\vec{k_1}$, $\vec{k_2}$, $\vec{k_3}$
13	3	-15 cm < z < -15 cm	FhgBlg	Bhg	$\vec{k_1}$, $\vec{k_2}$, $\vec{k_3}$
14	3	-25 cm < z < -15 cm	FhgBlg	Bhg	$\vec{k_1}$, $\vec{k_2}$, $\vec{k_3}$
15	3	-5 cm < z < +5 cm	FlgBhg	Fhg	$\vec{k_1}$, $\vec{k_2}$, $\vec{k_3}$
16	3	+5 cm < z < +15 cm	FlgBhg	Fhg	$\vec{k_1}$, $\vec{k_2}$, $\vec{k_3}$
17	3	+15 cm < z < +25 cm	FlgBhg	Fhg	$\vec{k_1}$, $\vec{k_2}$, $\vec{k_3}$
18	2	-5 cm < z < +5 cm	FhgBhg	FlgBhg	$\vec{k_1}$, $\vec{k_2}$, $\vec{k_3}$
19	2	Entire bar	FlgBlg	FhgBhg	$\vec{k_1}$, $\vec{k_2}$, start signal
20	2	-5 cm < z < +5 cm	FhgBlg	FlgBhg	$\vec{k_1}$, $\vec{k_2}$, $\vec{k_3}$
21	2	-15 cm < z < -5 cm	FhgBlg	FlgBhg	$\vec{k_1}$, $\vec{k_2}$, $\vec{k_3}$
22	2	-25 cm < z < -15 cm	FhgBlg	FlgBhg	$\vec{k_1}$, $\vec{k_2}$, $\vec{k_3}$
23	2	-5 cm < z < +5 cm	FlgBhg	FhgBlg	$\vec{k_1}$, $\vec{k_2}$, $\vec{k_3}$
24	2	+5 cm < z < +15 cm	FlgBhg	FhgBlg	$\vec{k_1}$, $\vec{k_2}$, $\vec{k_3}$
25	2	+15 cm < z < +25 cm	FlgBhg	FhgBlg	$\vec{k_1}$, $\vec{k_2}$, $\vec{k_3}$

Table 3.2: Table showing the different subsets of events for which unique energy calibrations were performed.

CHAPTER 4: Simulation

4.1 Overview

Though it is possible to estimate our statistical uncertainty with a rough idea of our solid angle coverage and source intensity, the systematic uncertainty presents a more challenging problem. Therefore, we turned to a more sophisticated means of quantifying our systematics: simulation. In this chapter, we anticipate various systematic effects and describe simulation techniques that we used to study them. We discuss simulations of varying complexity, starting with our 'Ps generator' and working up to the full blown Geant4 [104] (GEometry ANd Tracking) Monte Carlo. All of our code is documented on Github [105].

4.2 Ps Generator Code

To lay the groundwork for our Geant4 simulation, we began with a simpler simulation that we called the 'Ps generator'. The Ps generator modeled o-Ps decays by sampling theoretically predicted distributions for the momenta of the gamma rays.

Ore and Powell [2] computed the energy distributions of the $\vec{k_1}$, $\vec{k_2}$ and $\vec{k_3}$ gamma rays in QED (eqn. 1.11 and figs 1.2- 1.4. Bernreuther [89] computed the angular distribution between the o-Ps spin and the normal to the decay plane, θ. A diagram showing the relevant decay angles can be seen in fig 4.1. We show the angular distributions as created by the Ps generator in fig 4.2 and fig 1.6. As discussed in previous chapters, the angular distribution for θ various depending on the magnetic quantum number, m, of the o-Ps. Quantum mechanics predicts that 66% of the o-Ps events are formed in the $m = 1$ and $m = -1$ states, and the remaining 33% are formed in the $m = 0$ state. The θ distributions for the $m = 1$ and

$m = -1$ states are given by

$$P_m(\theta) = \frac{1}{2}\left(3 - \cos^2\theta\right), \tag{4.1}$$

whereas the distribution for the $m = 0$ state is described by

$$\left(1 + \cos^2\theta\right). \tag{4.2}$$

We used the generator code to evaluate our CPT-violating observable, $(\vec{S}\cdot\vec{k_1}\times\vec{k_2})$ in the absence of any detector effects. This can be seen in fig 1.7. Included in the Ps generator was the ability to toggle CPT-violation on and off, so that we could compare the resulting $(\vec{S}\cdot\vec{k_1}\times\vec{k_2})$ distributions. In the CPT-violating case, the energy distribution of the photons is model-dependent; hence, we cannot know, a priori, what it will be. As one possible example, we sampled the gamma ray momenta from the phase-space distributions described in Ore and Powell's paper [2], where the matrix element is a constant. This particular example can be seen in fig 1.8.

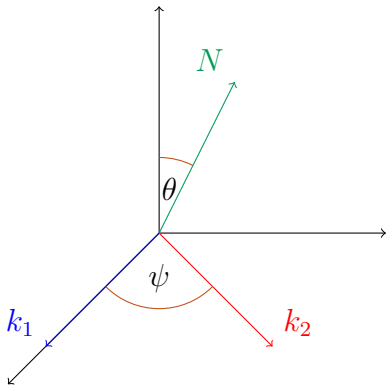

Figure 4.1: Ps decay angles, defined. ψ is the angle between $\vec{k_1}$ and $\vec{k_2}$, θ is the angle between the z-axis, or spin direction and the normal to the decay plane, N.

4.3 Geant4 Simulation

We used the Geant4 software to simulate the physics of CALIOPE in depth. Geant4 does not include positronium physics, and so we developed a separate class which generated the necessary positronium decays. In the simulation, a ^{22}Na source is placed inside the delrin source holder. The source is modeled as a disk with the same radius of our actual, physical source. Positrons are emitted in the ^{22}Na decay and travel into the aerogel moderator. Once they lose all their energy at the end of their track, the simulation inserts a positronium decay in lieu of other interactions (annihilation). To accomplish this, we modified the normal positron annihilation class (G4PlusAnnihilation) to include positronium physics. Specifically, we incorporated the Ps generator code to create the proper kinematics. At the decay vertex, the branching ratios of o-Ps and p-Ps are taken into account, and the gamma rays are generated accordingly. We did not include the drift of the positronium within the aerogel, which is on the order of a few microns [106]. While this would improve the accuracy of our model, its impact is likely sub-dominant to other effects.

Using some previously developed detector construction code from Stephen Daigle [93], we modeled the APEX array in detail. A complete rendering can be seen in fig 4.3. The simulated APEX array includes all 24 NaI(Tl) bars encased in their stainless steel housing, complete with quartz windows. We did not simulate the PMTs. The NaI(Tl) bars are enclosed in a steel structure that supports the entire array (shown in blue in fig 4.3). We modified the code to easily alter the detector and experimental setup in order to test a variety of configurations. This was facilitated with the implementation of a 'detector messenger' class, which provided a user interface with which to change the orientation of various components and swap out parts. The array could be configured to consist of NaI(Tl) crystals of varying, customizable dimensions. Likewise, the dimensions of individual steel encasement were adjustable.

To some extent, we used the simulation to iterate on the design of the source holder.

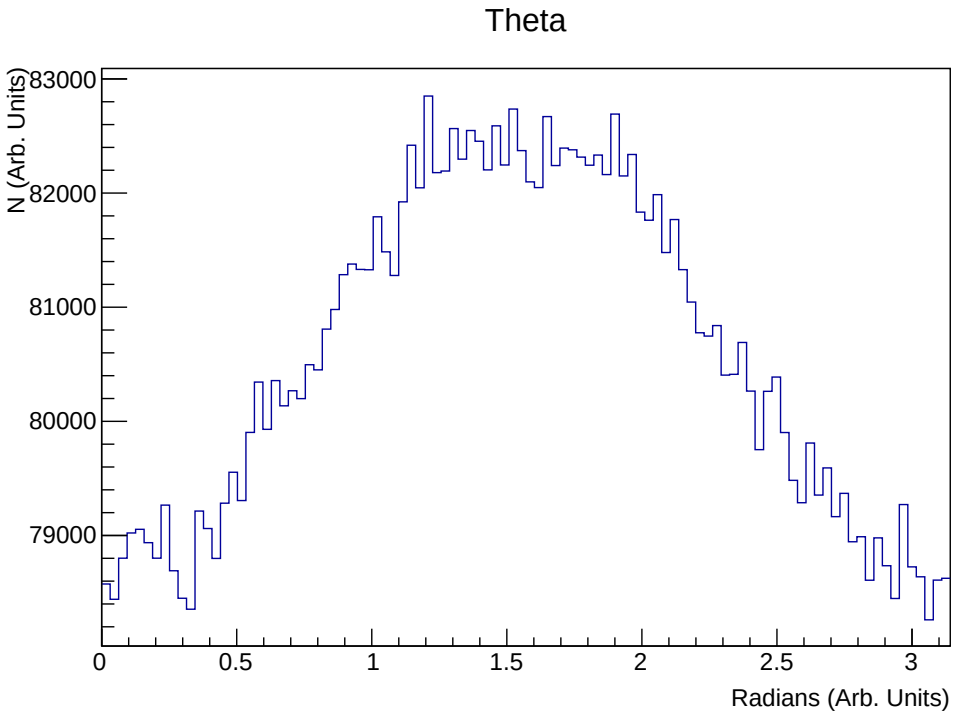

Figure 4.2: A Monte Carlo simulation of the angular distribution of θ, combining m=1 and m=0 cases in their respective fractions. This was created with the 'Ps generator'.

Ultimately, we chose a highly symmetric source holder design with the idea that this would help eliminate asymmetries in the CPT-violating observable. We also decided to pick construction materials with low density and atomic number, as we sought to minimize scattering from gamma rays emitted in positronium decay. This motivated the choice of delrin as the source holder material, and carbon fiber as the tube material. The high rigidity of carbon fiber also helped to prevent any compression or bending of the tube within the array. The final version of the simulation included the carbon fiber tube, shown in fig 4.3, to house the source and positronium moderator, as shown in fig 4.4.

The carbon fiber tube's orientation with respect to the detector could be rotated or translated via the detector messenger class. Additionally, the contents of the carbon fiber tube could be shifted along the length of the tube. Finally, different source holder designs could be swapped in and out. As explained in the following sections, we methodically altered various aspects of the detector geometry for the purpose of assessing different systematic

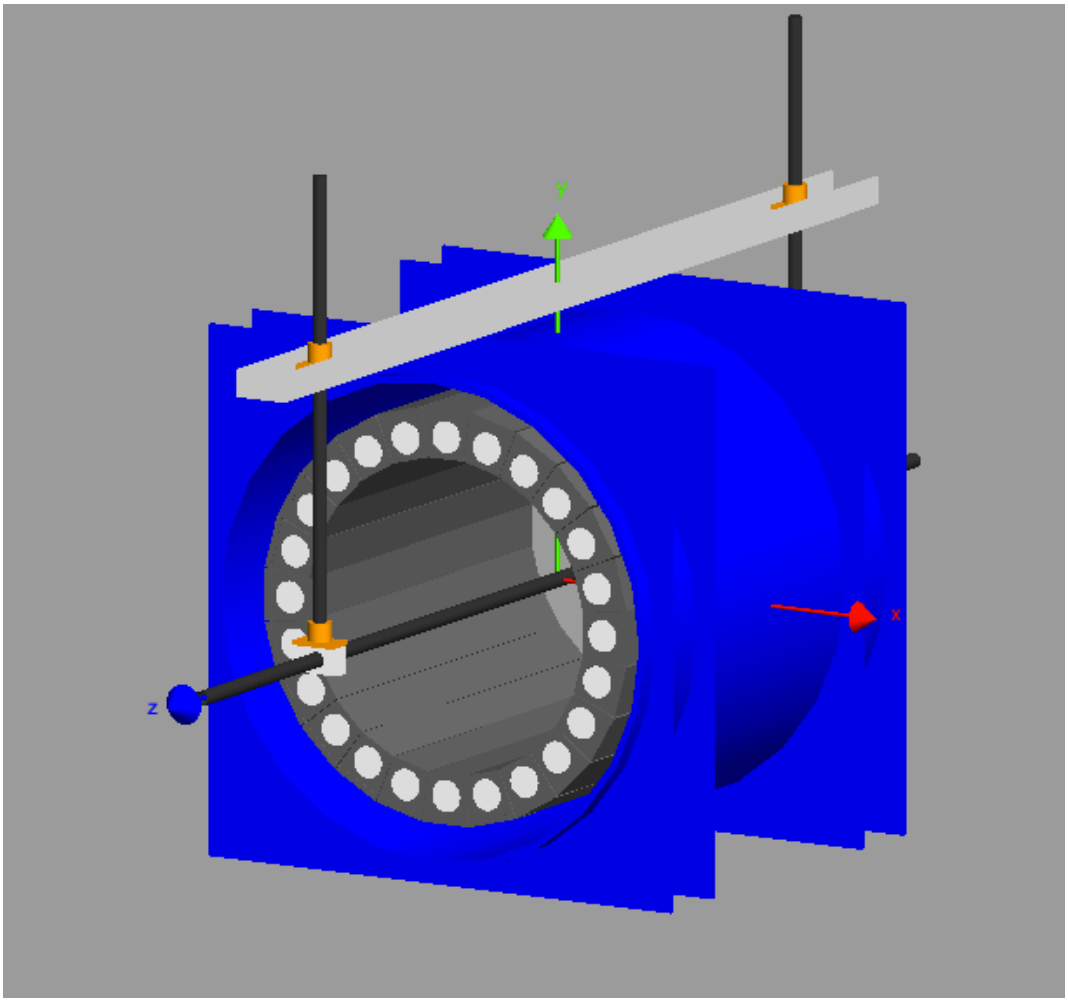

Figure 4.3: Geant4 APEX Detector Construction. Coordinate axes are shown in red (x), blue (z), and green (y). The blue structure is aluminum and serves to support the entire array. The NaI(Tl) bars are shown, encased in steel (dark gray). Circular quartz windows are shown in white on each end of the bars. The aluminum channel (light gray), brass collars (orange) and aluminum tubes (black, vertical), make up the support stand. They are shown holding the carbon fiber tube (black, passing through the array).

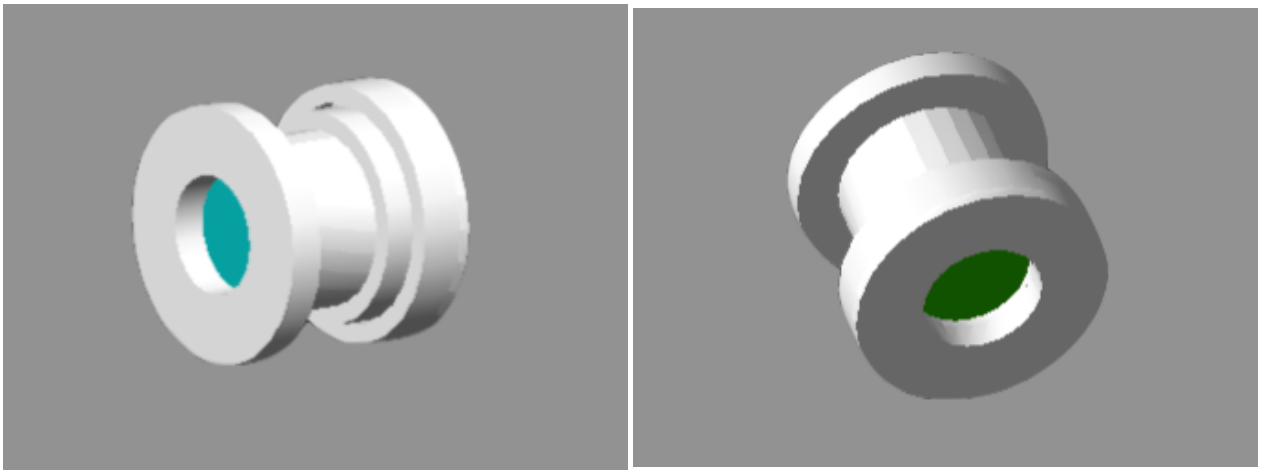

Figure 4.4: The source holder, rendered in Geant4. The image on the left shows the front of the holder, with aerogel shown in cyan. The image on the right shows the back of the holder, with the aluminum backing shown in green.

errors.

In the simulation, we generated diagnostic plots at key points throughout the duration of a single event. We established three points of interest in an event's 'life cycle': 1) the o-Ps decay vertex, 2) the point at which the gamma rays exit the carbon fiber tube, and 3) the point at which the gamma rays interact in the APEX array. This enabled us to verify that the simulation code worked as intended and also see the effect of various detector components on the $\vec{k_1}$ and $\vec{k_2}$ gamma ray energies and momenta. Figs 4.5, 4.6, and 4.7 show what the simulated gamma ray energy spectra look like after the gamma ray passes through the source holder. A slight tail can be seen at low energies, but the gamma rays are not greatly affected by passing through the delrin, as expected. Figs 4.8, 4.9, and 4.10 show what the $\vec{k_1}$, $\vec{k_2}$, and $\vec{k_3}$ energy spectra look like after the respective gamma rays are reconstructed in a NaI(Tl) bar, using our reconstruction methods. We included the energy and z position resolution of the individual bars from the actual APEX detector in the event reconstruction. We also show the angular distributions plotted at different time points throughout an event. Fig 4.11 shows two distributions for ψ, the angle between the $\vec{k_1}$ and $\vec{k_2}$ gamma rays: one at the decay vertex and one immediately after the $\vec{k_1}$ and $\vec{k_2}$ gamma rays exit the source holder. Fig 4.12 shows what the angular distribution for ψ looks like after the $\vec{k_1}$ and $\vec{k_2}$ gamma

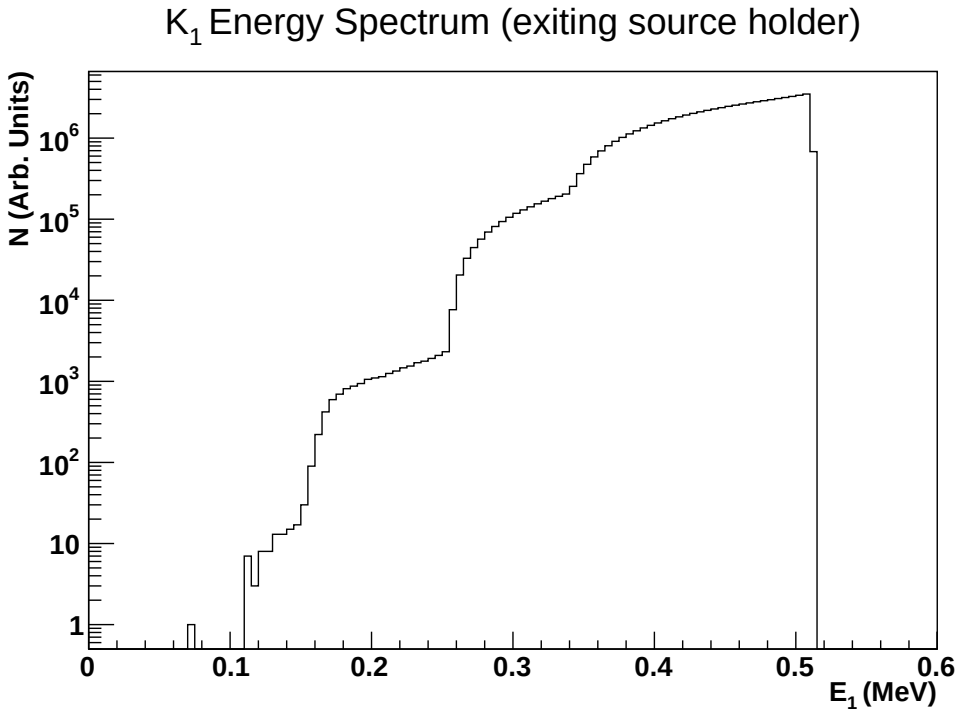

Figure 4.5: $\vec{k_1}$ energy spectrum after the $\vec{k_1}$ gamma ray passes through the source holder. The 'steps' to the left are due to gamma ray scattering in the holder.

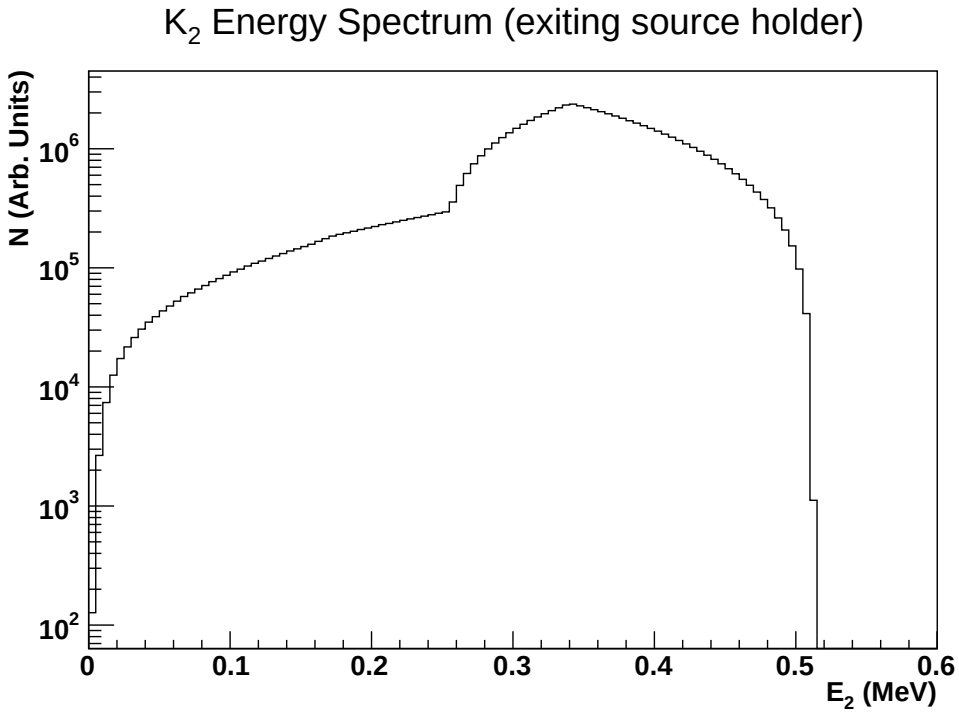

Figure 4.6: $\vec{k_2}$ energy spectrum after the $\vec{k_2}$ gamma ray passes through the source holder.

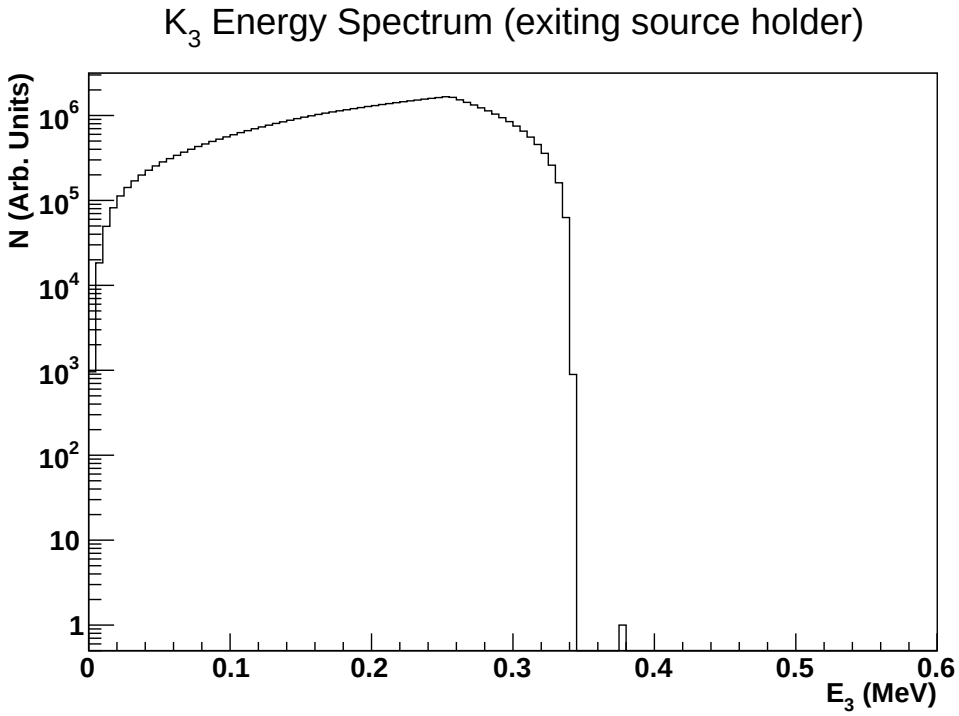

Figure 4.7: $\vec{k_3}$ energy spectrum after the $\vec{k_3}$ gamma ray passes through the source holder.

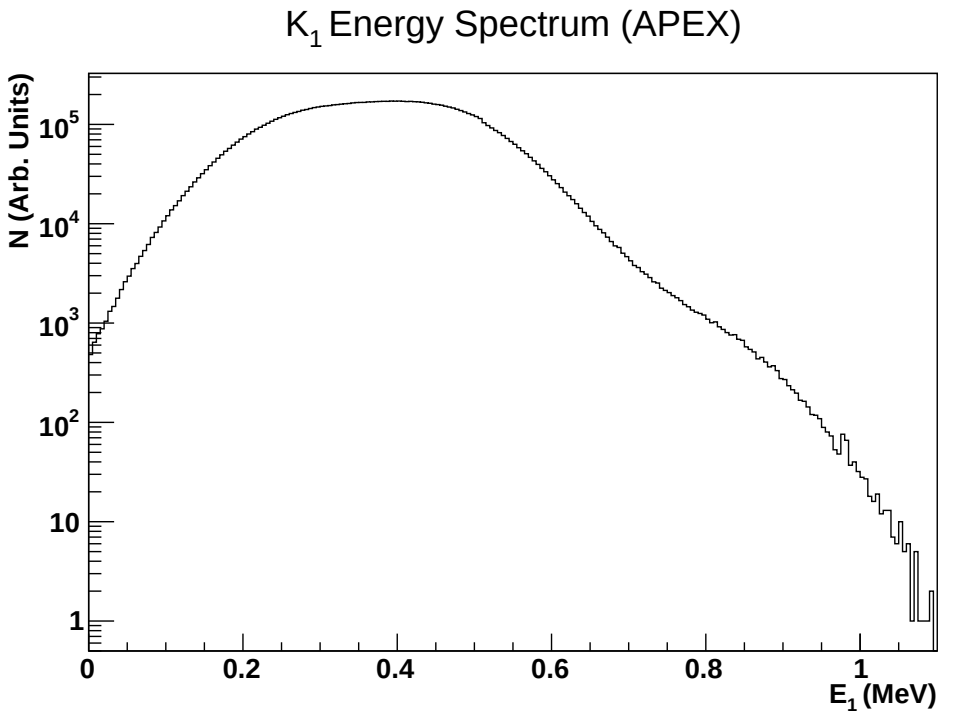

Figure 4.8: k_1 energy spectrum after the $\vec{k_1}$ gamma ray interacts in the NaI(Tl) bar of APEX.

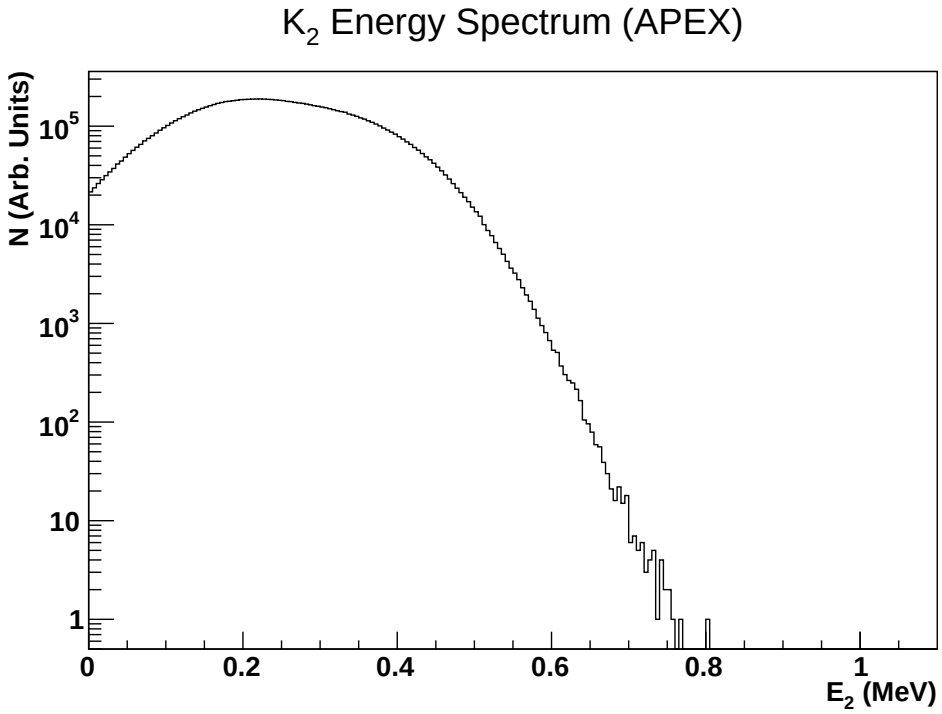

Figure 4.9: k_2 energy spectrum after the $\vec{k_2}$ gamma ray interacts in the NaI(Tl) bar of APEX.

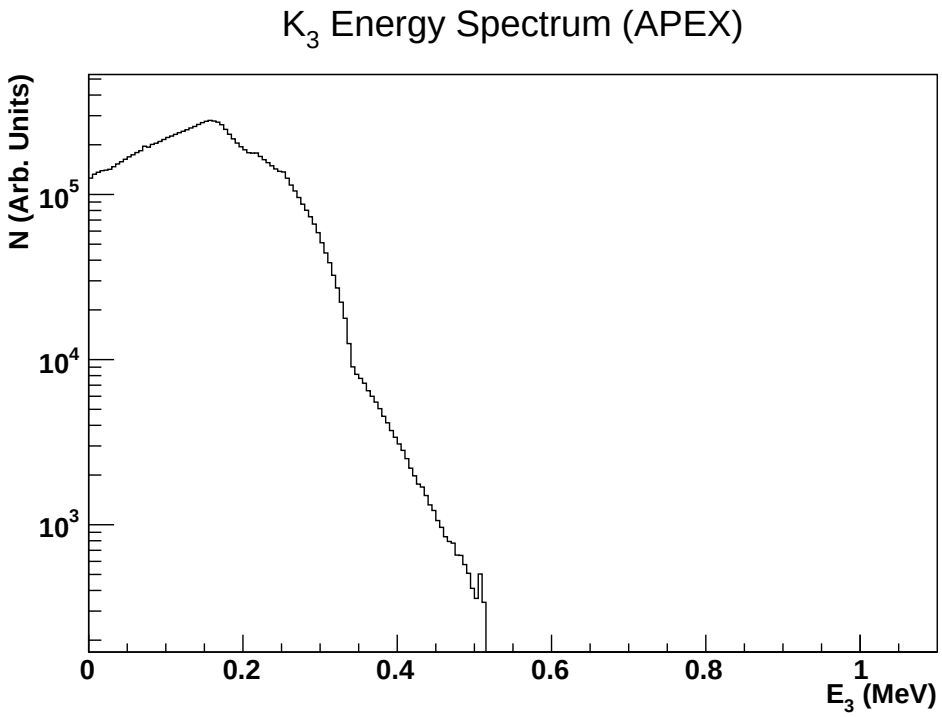

Figure 4.10: k_3 energy spectrum after the $\vec{k_3}$ gamma ray interacts in the NaI(Tl) bar of APEX.

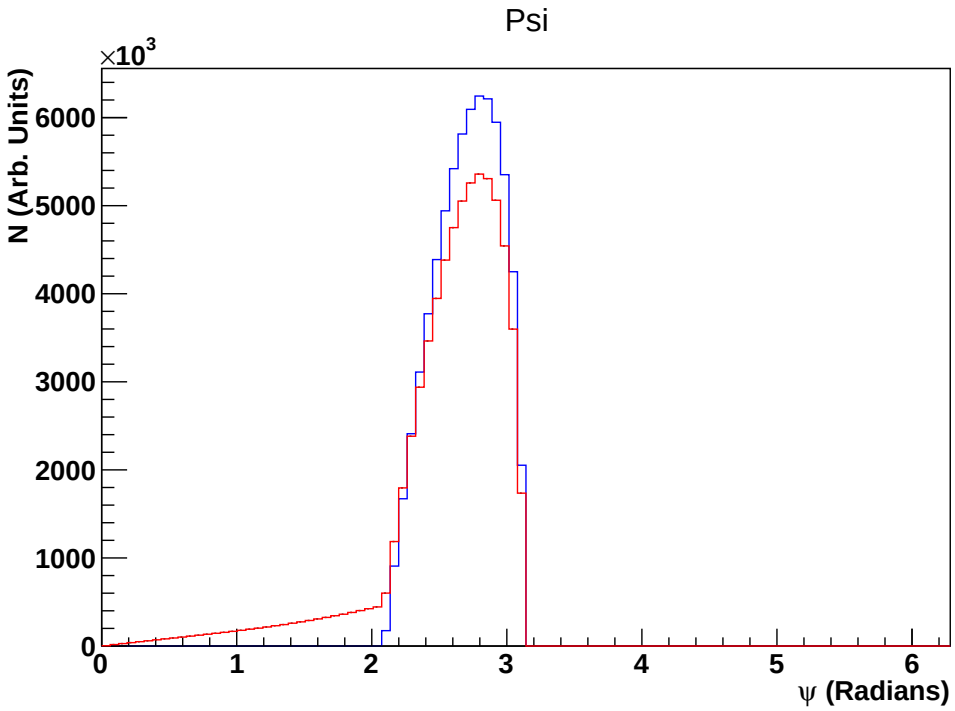

Figure 4.11: The angle ψ reconstructed just after the $\vec{k_1}$ and $\vec{k_2}$ gamma rays are generated at the decay vertex in the Geant4 Monte Carlo. Blue shows the distribution reconstructed at the o-Ps decay vertex and red shows the distribution reconstructed after the gamma rays exit the source holder.

rays are reconstructed in the APEX array, after all analysis cuts are applied. Similarly, fig 4.13 shows the angular distribution of θ at the vertex and just after the gamma rays exit the source holder. Fig 4.14 shows the angular distribution as reconstructed with the APEX array.

At the end of an event, the analysis cuts that we used were identical to those in the real analysis code, aside from any timing cuts. Geant4 does not easily include a means of inserting the Ps decay time. We did find a way to insert a delay at the end of a Ps track, but this proved to be incompatible with newer versions of Geant4.

If an event survives all of our cuts, the CPT-violating asymmetry observable is calculated and histogrammed at the end of an event. Fig 4.15 shows an example of this under ideal conditions (all detector components aligned, no systematic effects introduced). This distribution changes if, for example, one alters some of the geometrical aspects of the experiment,

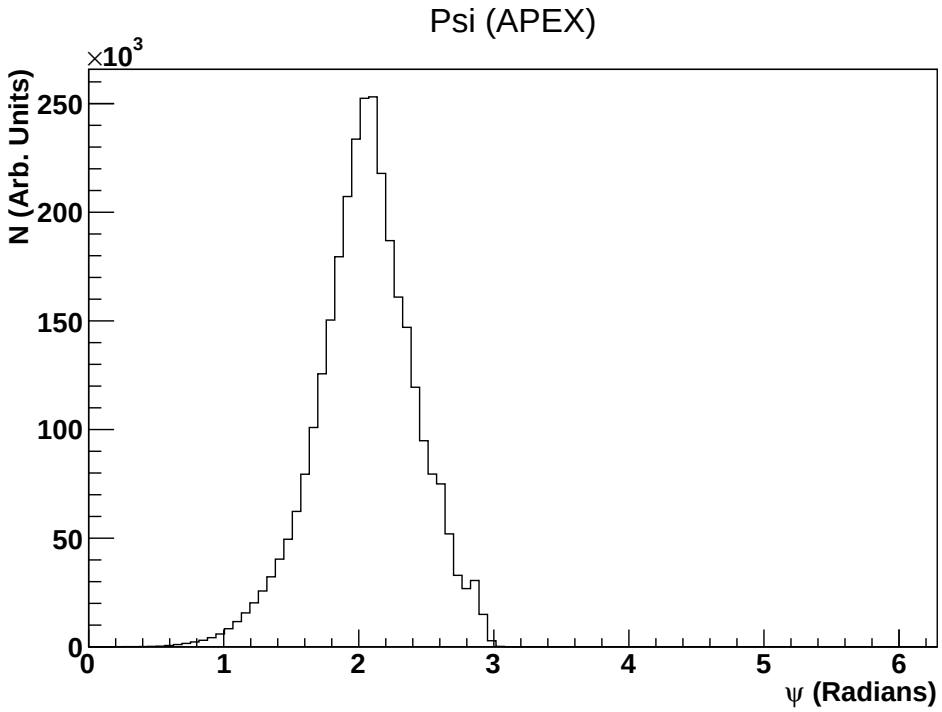

Figure 4.12: The angle ψ reconstructed after interacting with the APEX array. The distribution is skewed slightly due to cuts performed to isolate o-Ps.

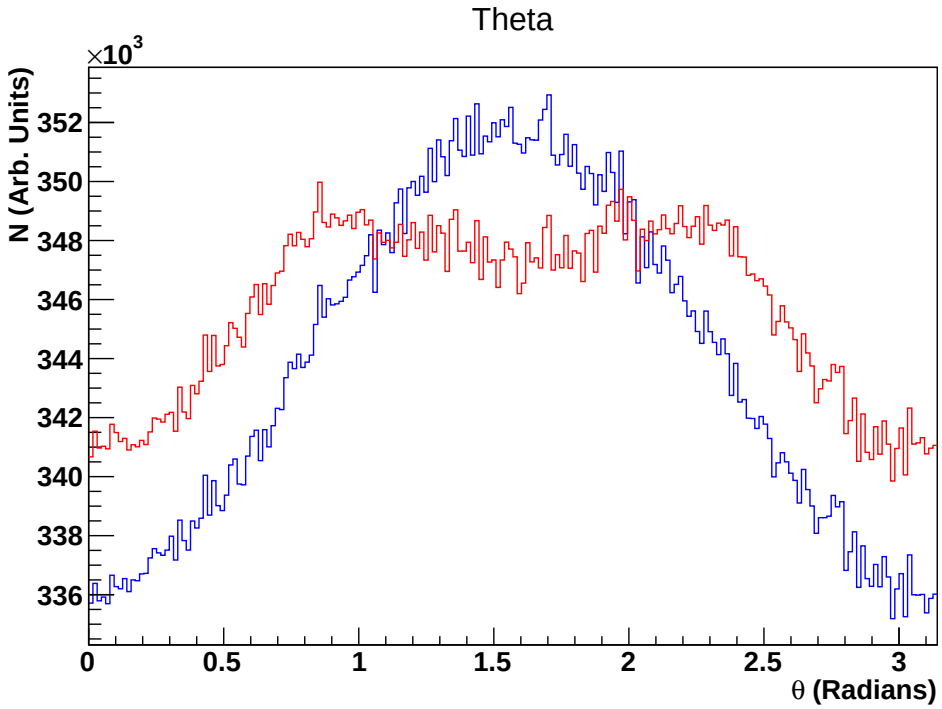

Figure 4.13: The angle θ, reconstructed just after the o-Ps decay in the Geant4 Monte Carlo, at the vertex. Blue shows the distribution reconstructed at the o-Ps decay vertex and red shows the distribution reconstructed just after the gamma rays exit the source holder.

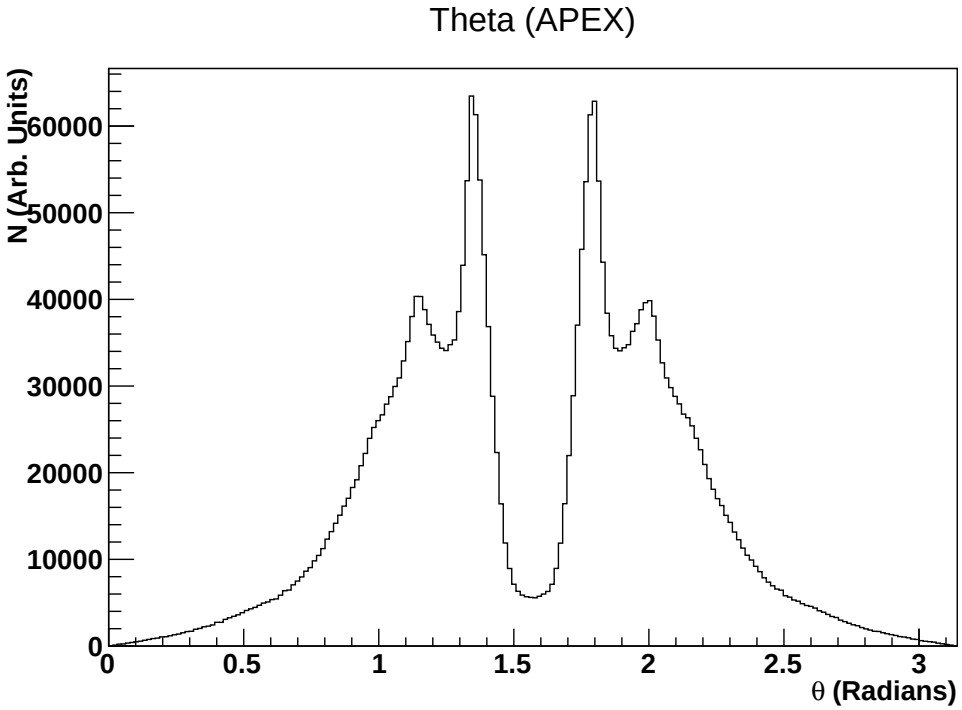

Figure 4.14: The angle θ, after reconstruction using interactions in the APEX array. At this point, the angular distribution is strongly affected by the solid angle coverage of the array.

such as translating it in the x-direction. An example of this can be seen in fig 4.16. It is important to note that a change in the distribution of $(\vec{S} \cdot \vec{k_1} \times \vec{k_2})$ does not necessarily create a change in the asymmetry (or lack thereof).

4.3.1 Systematics Study

A number of potential systematics were considered for this experiment. In order to qualify as a possible source of error, systematics would have to generate a fake asymmetry. In other words, it would have to flip the sign of $(\vec{S} \cdot \vec{k_1} \times \vec{k_2})$ from positive to negative more often than it flips it from negative to positive, or vice versa.

Most systematics, in theory, can be canceled by rotating the orientation of the source holder by 180° within the detector. This works because any true CPT-violating asymmetry would be a feature of the decay process, not the geometry of the detector. This flips the z-axis of the coordinate system, and therefore the sign of $\vec{S}$. To accomplish this systematic

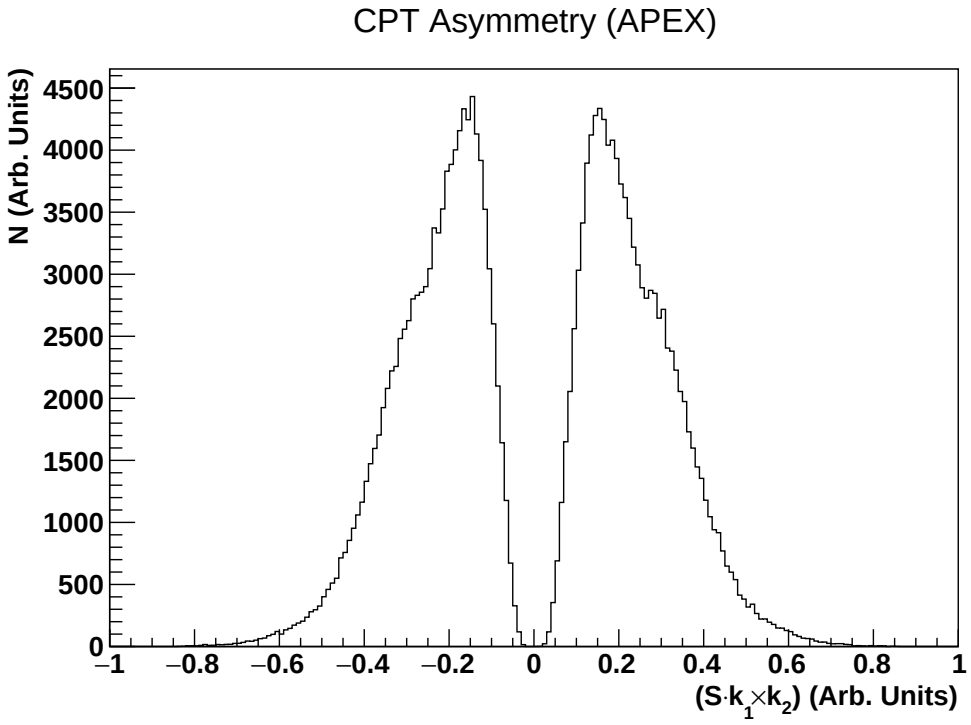

Figure 4.15: Histogram of our observable, $(\vec{S}\cdot\vec{k_1}\times\vec{k_2})$, generated using our simulation of 'normal' o-Ps decays predicted by QED. The gap in the middle is due to energy thresholds that are set to those of the real APEX array (250 keV). The tails at either end of the distribution are due to the finite energy resolution of the array.

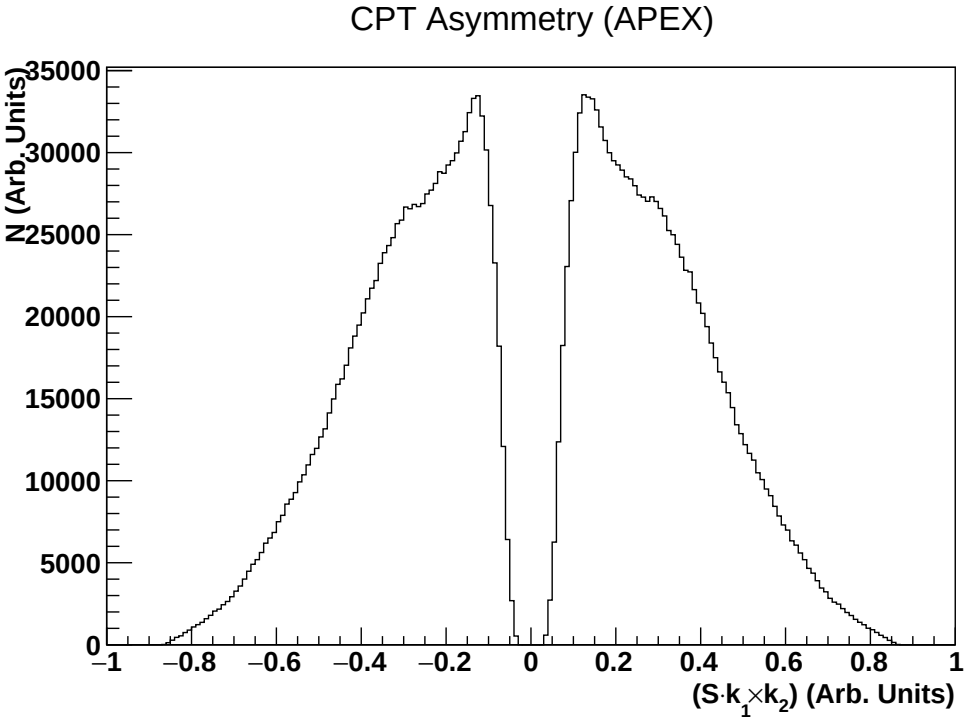

Figure 4.16: Histogram of our observable, $(\vec{S}\cdot\vec{k_1}\times\vec{k_2})$, generated using gamma ray interactions in APEX in Geant4, with the source shifted 15 cm in the positive x-direction. This alters the shape of the $(\vec{S}\cdot\vec{k_1}\times\vec{k_2})$ histogram, but it does not generate a net asymmetry.

cancellation, events acquired with the source oriented in one direction can be subtracted from those collected with the source oriented in the opposite direction.

We did not have the computing power to iterate through a large number of systematics and so we used a few approaches to optimize our resources on UNC's cluster. First, we ran the simulation with greatly exaggerated forms of the systematics, the idea being that an asymmetry would be more likely to appear under such circumstances. If a fake asymmetry appeared, we could then incrementally reduce the exaggeration until the asymmetry disappeared or apply scaling arguments to quantify its effect. This would give us an idea of how the asymmetry scales with the size of the systematic and tells us at what level the effect becomes negligible. For example, in considering how a translation of the source holder affects the asymmetry measurement, we would run the simulation with the source holder translated, say, 15 cm in the x-direction. If a fake asymmetry appears, we would then repeat the simulation with smaller translations of the source holder. The second tactic that we used to optimize our computing time was to thoroughly analyze the effects of different systematics before testing our predictions with the simulation. We outline several categories of systematics and present our analysis below. The results from the runs with exaggerated effects are summarized in Table 4.1. These effects have been scaled to more reasonable levels in Table 4.2. For this table, we assumed linear scaling for systematics in which only one parameter was altered. For effects where more than one parameter were altered (such as a combination of a rotation and a translation of the source), the asymmetry was assumed to scale with the product of the two parameters. Certain effects that combine large translations with rotations cause the overall event rate to decrease in the detector due to smaller angular coverage of the source. Hence, this causes a decrease in the statistics. This explains the smaller statistical uncertainty for entries involving correlated effects in Table 4.2.

4.3.2 Categories of Systematics

1. Translations of the source holder in the x and y direction.

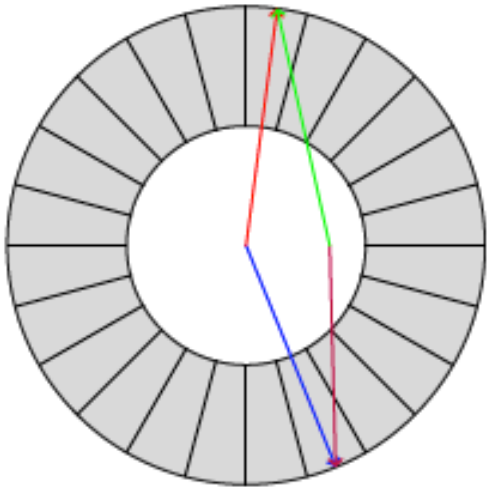

Figure 4.17: Red is the $\vec{k_1}$ gamma ray and blue is the $\vec{k_2}$ gamma ray as reconstructing assuming the source is in the center of the array. Green is the $\vec{k_1}$ gamma ray and violet is the $\vec{k_2}$ gamma ray with the decay vertex shifted off-center. One can see that when the decay vertex is shifted, this event goes from being $(\vec{S} \cdot \vec{k_1} \times \vec{k_2})$ negative to $(\vec{S} \cdot \vec{k_1} \times \vec{k_2})$ positive.

A translation of the source holder is equivalent to a shift in the average positronium decay position within the aerogel. One might think that a translation of the source holder radially would impose a fake asymmetry, but we conclude that it does not. An example can be shown in fig 4.17. In this diagram, red is the $\vec{k_1}$ gamma ray and blue is the $\vec{k_2}$ gamma ray as reconstructing assuming the source is in the center of the array. Green is the $\vec{k_1}$ gamma ray and violet is the $\vec{k_2}$ gamma ray with the decay vertex shifted off-center. One can see that when the decay vertex is shifted, this event goes from being $(\vec{S} \cdot \vec{k_1} \times \vec{k_2})$ negative to $(\vec{S} \cdot \vec{k_1} \times \vec{k_2})$ positive. It does not generate an asymmetry, however, because for every event for which $\vec{k_1}$ is the red vector, this is an event for which $\vec{k_1}$ is the blue vector. These events flip $(\vec{S} \cdot \vec{k_1} \times \vec{k_2})$ from positive to negative instead. These events cancel and there is no resulting fake asymmetry. We tested this systematic in the simulation with a translation of 15 cm and the result was consistent with zero, as predicted. Furthermore, in the actual experiment, we were able to constrain the carbon fiber tube to within about 2 mm of the center of the array.

2. Rotations of the source holder about the x or y-axis.

We considered the possibility that a rotation of the source holder about the x or y-axis

might contribute to an overall fake asymmetry as well. Such a rotation changes the proximity of the source to the NaI(Tl) bars, but it was not clear to us how this may generate a fake asymmetry. We tested this in the Geant4 simulation with rotations of 20° about the x-axis and the result was consistent with zero.

3. Energy-dependent systematic

An energy dependent systematic might cause a fake asymmetry, especially if that systematic breaks the azimuthal symmetry of the detector. One example of this would be to have a gradient in the bar thickness of the APEX array, such that the bars get thinner as one moves clockwise or counter-clockwise around the array. This example was tested in the Geant4 Monte Carlo and the result, which was consistent with zero, can be seen in Table 4.1. Another such energy dependent systematic would be if the energy thresholds increased or decreased as one travels clockwise or counter-clockwise around the APEX array. We set the energy thresholds in the simulation such that they increased clockwise around the array, starting at 50 keV and increasing by 50 keV every three bars. The highest energy threshold was 450 keV. This created a fake asymmetry of A = -0.0333±0.0025, which is shown in Table 4.1. This is similar to the actually asymmetry term that we see in our data taken with APEX, which will be explained in the following chapter. In theory, such an asymmetry can be canceled out subtracting the asymmetry acquired by rotating the source 180°. However, in reality, a perfect rotation of the source is difficult to execute. The source was likely subjected to small shifts along the radial and z direction with each rotation. Because the thresholds vary not only between bars, but along the length of the bar, small shifts could cause the asymmetry terms to not cancel between data sets taken in each orientation. We were not able to accurately quantify the individual detector thresholds and input them into the simulation. This is one change that could improve the accuracy of the simulation.

4. Correlated Systematic Effects

We also considered the fact that two or more systematic effects may be at play. These included combinations of systematics such as translating the carbon fiber tube and rotating

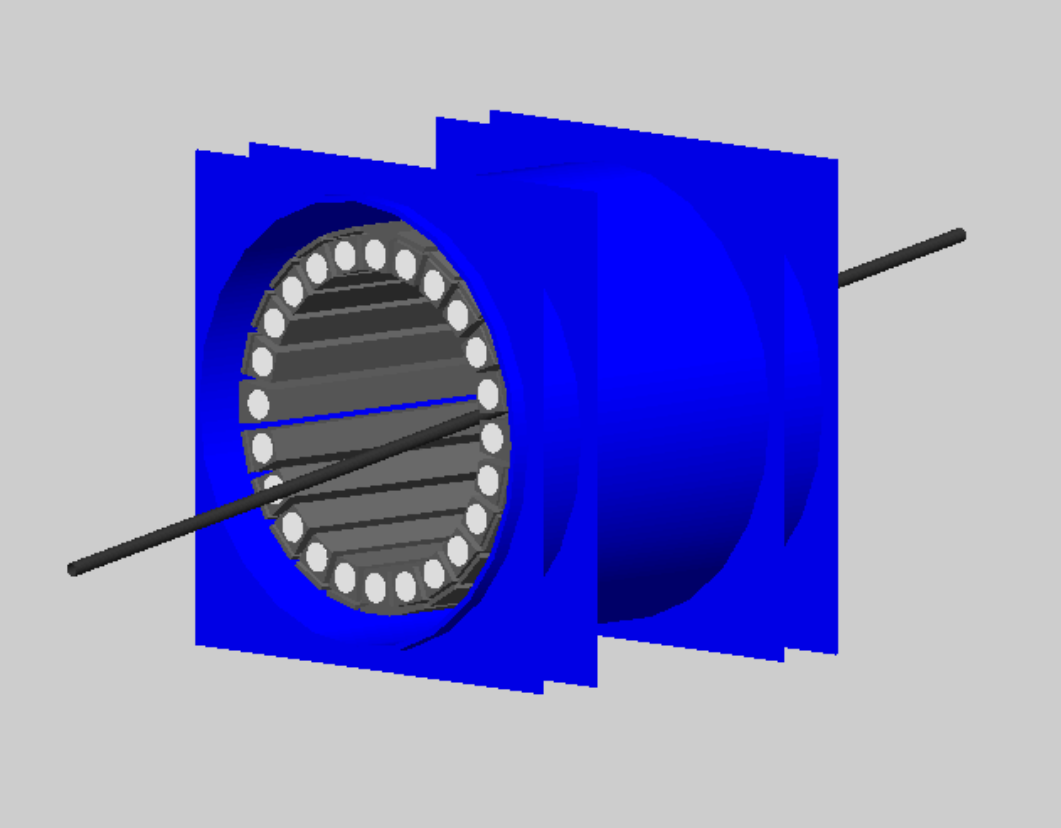

Figure 4.18: Geant4 rendering of the APEX array with the carbon fiber tube rotated about the x-axis by 10 degrees. This was one of the systematics which was tested.

it. Such effects are much harder to visualize, but the simulation results can be seen in Table 4.1.

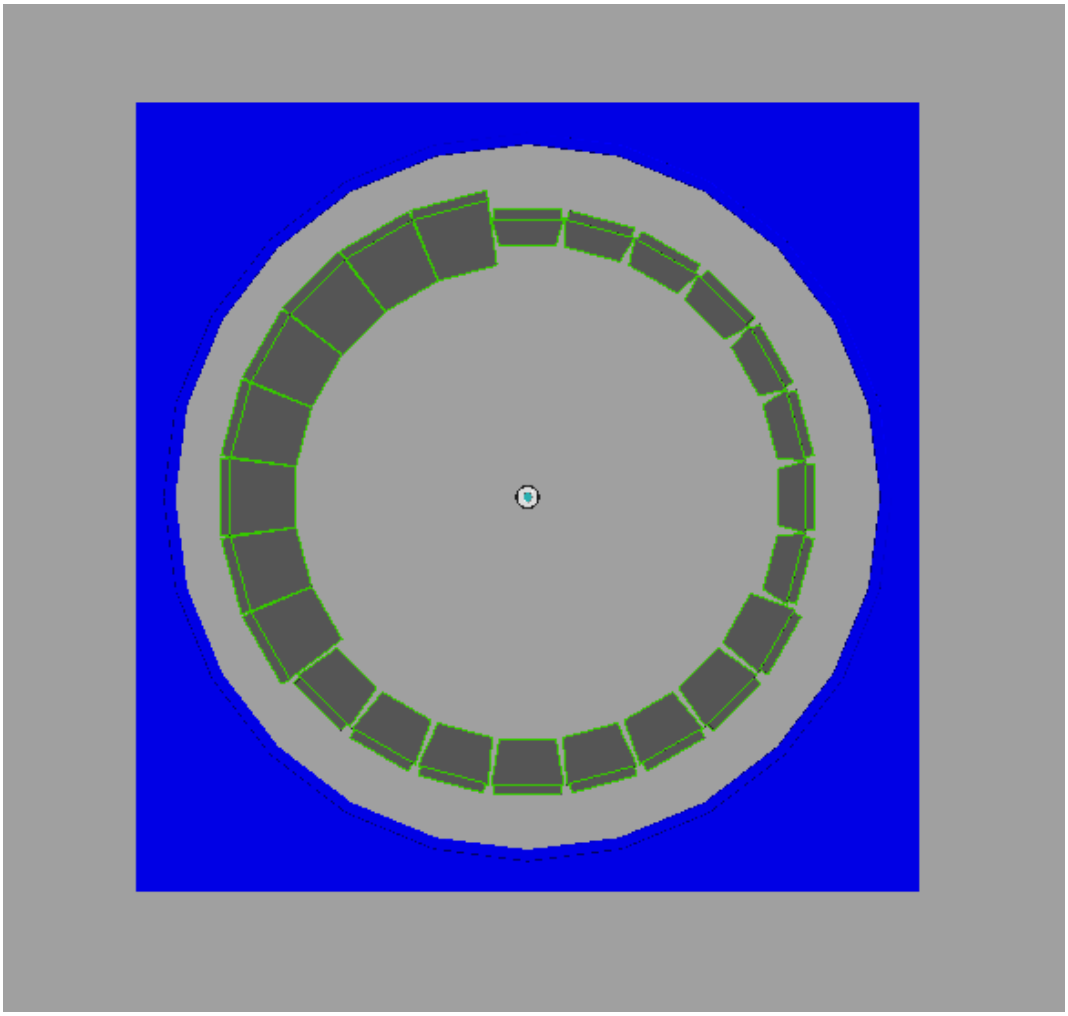

Figure 4.19: Above shows an extreme case in which there is a clockwise gradient in the NaI(Tl) bar thickness. In this case, there are three different bar thicknesses: 6 cm, 4.2 cm, and 2.4 cm. In principle, we would never see such large variations in bar thickness.

Systematics Table: Exaggerated Effects	
Exaggerated Systematic	Asymmetry Parameter
Ideal Geometry	
Perfect Setup	-0.0001 ± 0.0007
Holder Translations	
Shift in x (+15cm)	0.0014 ± 0.0006
Shift in z (+10cm)	0.0003 ± 0.0007
Holder Rotations	
Rotate around x-axis (20°)	0.0004 ± 0.0007
Holder Translation and Rotation	
Shift in x (+10 cm) & Rotate around x-axis (20°)	0.0004 ± 0.0006
Shift in x (+10 cm) & Rotate around y-axis (20°)	-0.0017 ± 0.0006
Shift in x (+5 cm) & Shift in z (+5 cm) & Rotate around x-axis (20°)	0.0020 ± 0.0013
Variations in Bar Thickness	
Reduced Bar Thickness: 8 Adjacent Bars Reduced by Uniform Thickness of 1.8 cm	0.0001 ± 0.0006
Gradient in Bar Thickness Clockwise of 1.8 cm every 8 bars	-0.0005 ± 0.0006
Gradient in Bar Thresholds Clockwise of 50 keV every three bars	-0.0333 ± 0.0025

Table 4.1: Table of systematic biases introduced by several effects as computed in Monte Carlo. The error included is statistical only.

Systematics Table: Realistic Effects	
Realistic Systematic	Asymmetry Parameter
Ideal Geometry	
Perfect Setup (Not affected by scaling)	-0.0001 ± 0.0007
Holder Translations	
Shift in x (+0.5cm)	0.00004 ± 0.00002
Shift in z (+0.5cm)	0.00002 ± 0.00004
Holder Rotations	
Rotate around x-axis (20°)	0.00001 ± 0.00002
Holder Translation and Rotation	
Shift in x (+0.5 cm) & Rotate around x-axis (0.5°)	$5 \times 10^{-7} \pm 8 \times 10^{-7}$
Shift in x (+0.5 cm) & Rotate around y-axis (0.5°)	$2 \times 10^{-6} \pm 8 \times 10^{-7}$
Shift in x (+0.5 cm) & Shift in z (+0.5 cm) & Rotate around x-axis (0.5°)	$5 \times 10^{-7} \pm 3 \times 10^{-7}$
Variations in Bar Thickness	
Reduced Bar Thickness: 8 Adjacent Bars Reduced by Uniform Thickness of 1 mm	$6 \times 10^{-6} \pm 3 \times 10^{-5}$
Gradient in Bar Thickness Clockwise of 1 mm every 8 bars	$3 \times 10^{-6} \pm 2 \times 10^{-6}$
Gradient in Bar Thresholds Clockwise of 10 keV every three bars	-0.00027 ± 0.00002

Table 4.2: Table of systematic biases introduced by several effects as computed in Monte Carlo, scaled to more realistic effects. The error included is statistical only.

4.4 Other Effects

We considered the possibility of a number of other effects on our asymmetry measurement. These include variations in the densities of the aerogel, source holder, steel encasement, as well as shifting the source off-center. We determined that such deviations from a 'perfect' experiment would have a negligible effect on the asymmetry measurement. Starting with defects in the aerogel, we offer justification as follows. A variable density in the aerogel would result in a net shift in the decay vertices of the o-Ps events, but only by a few microns. On average, the positron implantation depth is about 2µm [106]. Positronium has a diffusion length of about 2µm as well [106]. This would be comparable to moving the source holder by only a few microns, and we have seen from Monte Carlo studies that this alone has no effect on our ability to measure the asymmetry.

On the other hand, a variable density in the source holder would impact the intensity of emerging gamma radiation, I. The incident intensity, I_0, is attenuated via the exponential expression

$$I = I_0 e^{-\mu L}, \tag{4.3}$$

where μ is the attenuation coefficient and L is the absorber thickness. For our source holder, L varies on the order of a few millimeters. The attenuation coefficient for delrin is around 0.01 mm^{-1} [107]. If there is an extra millimeter of plastic, say, on one side of the holder, then it would attenuate the gamma rays by an extra 1%. The NaI(Tl) bar encasements are made of steel, and variations in their thickness would have a similar effect. The attenuation coefficient for steel depends on the alloy, but hovers around 0.1 mm^{-1}, and so an extra millimeter would attenuate the gamma rays by 10%. Any effect here could be said to be negligible. Furthermore, effects due to variations in material thickness would theoretically be canceled by rotating the source holder 180°.

If the ^{22}Na source is off-center with respect to the aerogel, then the average decay vertex of

the positronium will be shifted. If it is shifted far enough, it is possible that the positronium may start interacting more with the boundary of the aerogel on one side of the source holder, where it experiences the pick-off effect. That is, the positron in the positronium interacts with an electron at the boundary and annihilates. This would have two consequences. First, we would see a net decrease in the number of o-Ps events as their lifetime is shifted and removed by analysis cuts. Second, the average o-Ps decay vertex may shift slightly, but as explained before, we expect this to have no measurable effect.

Through the Monte Carlo simulation, we have been able to understand the impact of various features of the experiment on our observable, $(\vec{S} \cdot \vec{k_1} \times \vec{k_2})$. We have also been able to tabulate the results from simulation runs involving deliberate alterations to the detector geometry and experimental setup. Despite efforts to include many details in the Monte Carlo, the only systematic effect that we observed arose from the variations in the detector thresholds. We believe this systematic can be canceled by flipping the source and subtracting the asymmetries measured in both orientations. With large asymmetries, however, this becomes increasingly difficult, as the requirement for perfect flipping becomes more stringent. In the following chapter, we elaborate on our understanding of systematic effects using various diagnostic tests on our analysis data.

CHAPTER 5: Data-Taking and Analysis

5.1 Data-taking and run cadence

Data-taking for CALIOPE commenced in August of 2018. We used the Coda [100] software from Jefferson Lab to perform the readout of the SBC. The Coda 'catmaster' graphical user interface displays the acquisition rate, the number of events in a run, and the rate at which it writes to disk. A screenshot of our setup with the Coda GUI can be seen in fig 5.1. Acquisition rates were approximately 18 kHz throughout the course of data-taking. We devised an automated mouse-clicking script to improvise for the fact that this version of Coda did not have a way to automate the starting and ending of a run. A new run was started every half hour, resulting in raw binary files, each about 2.6 GB in size. These files were then automatically processed with the coda2root [101] software to convert them from binary files to ROOT [103] files. Processing with coda2root resulted in 1.5 GB-sized files which were copied automatically to our RAID server for storage and UNC's computing cluster, Longleaf, for analysis [108]. The Longleaf cluster is a Linux-based computing system with over 10,000 computing cores. It is optimized for large quantities of jobs that do not require parallel processing, a setup which is ideal for our analysis. Once on the cluster, we further reduced the size of the files with code that removed all zeros from the data. This resulted in files that were each about 1 GB in size. Over the course of the experiment, we acquired a data set of 4,674 files, or approximately 4.674 TB worth of data.

We equipped the DAQ computer with VNC [109] so that it could be monitored remotely. Additionally, an ethernet-enabled camera was placed in front of the nitrogen bubbler so that the status of the nitrogen could be monitored. The nitrogen tank was replaced approximately on a monthly basis, and the flow rate stayed at approximately 4 cc/s.

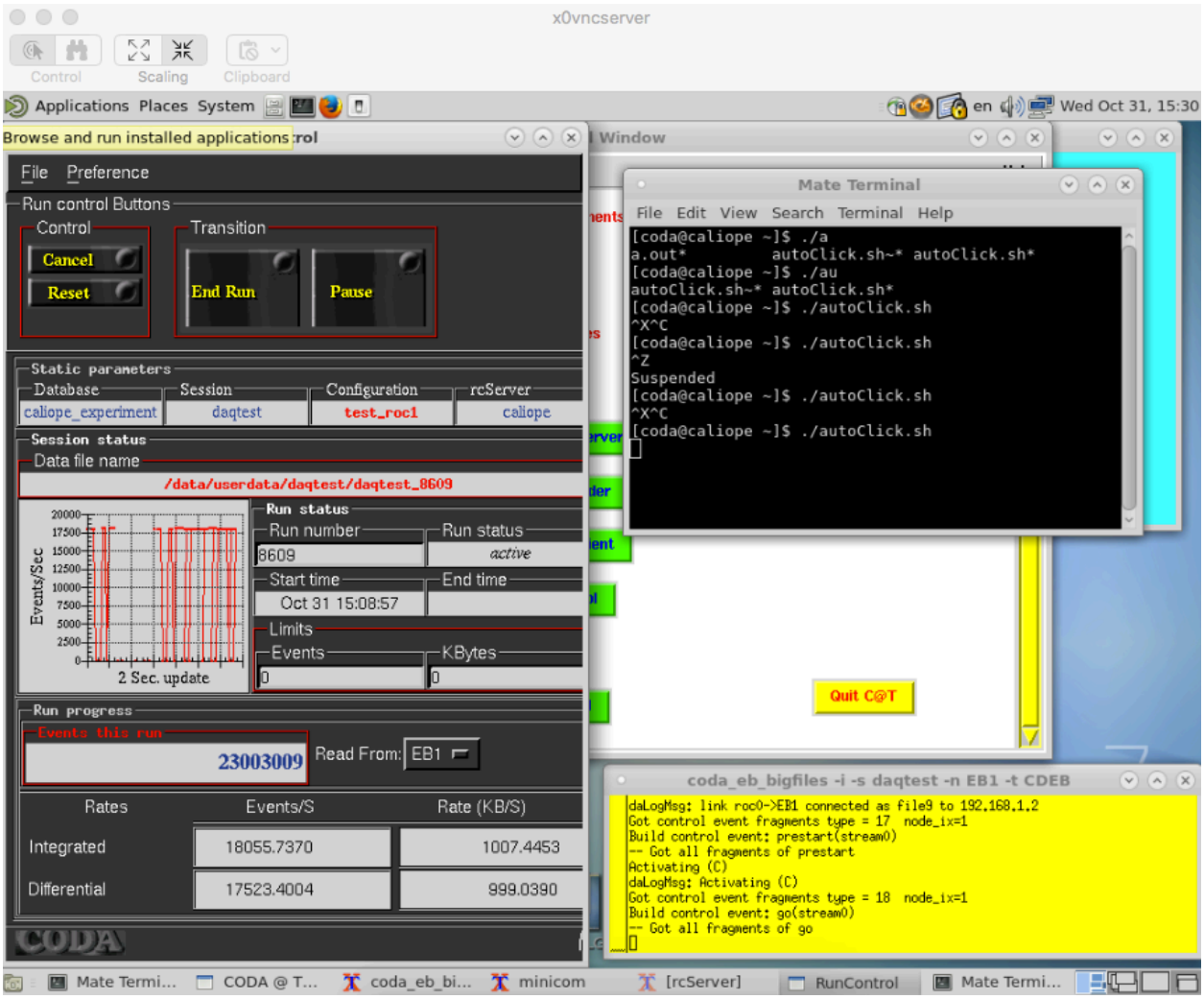

Figure 5.1: Screen shot of the Coda setup while taking data for CALIOPE. On the left is the run control GUI, showing the event rate, number of events, run number, start time and the rate at which it writes data to the disk. The plot of the event rate (in red) appears to jump because it only samples the rate every two seconds.

We acquired data in two different configurations. In the first configuration, the carbon fiber tube was aligned such that the aerogel was at the center of the array. In the second configuration, the carbon fiber tube was aligned such that the aerogel was 14 cm from the center towards the front of the array. We took data in the second configuration because only the front PMTs were hooked up to the TDC. We suspected that our event rate might therefore increase in this configuration, though this turned out not to be the case. Ultimately, we took 6 weeks of data in the first configuration and 10 weeks of data in the second configuration.

In addition to taking data in these two configurations, we flipped the orientation of the carbon fiber tube 180°on a weekly basis. An analysis of all 16 weeks of data is presented in the following chapter.

5.2 Analysis Code

We designed analysis code to convert raw TDC and QDC values into meaningful quantities and perform the positronium analysis cuts. These two processes are explained in the following sections.

5.2.1 Pre-processing of raw TDC and QDC values

We converted the raw TDC values to nanoseconds and standardized the values between the individual channels using the procedure explained in this section. First, it is important to recall that the CAEN 775 is not capable of measuring time periods shorter than 14 ns [95]. For this reason, we inserted a delay between the common start and stop for every channel of about 30 ns. This delay is created via a 20 ns delay chip and approximately 10 feet of ribbon cable. The inherent delay for each channel was determined by fitting the peak at the beginning of every bar's timing spectrum. Our timing resolution was about 2 ns. We converted this and all other raw TDC values to nanoseconds by scaling by a factor

of 0.297 [95], using the CAEN prescription, since the full scale range of the TDC was set to 1.2 µs. We subtracted this value off all recorded time values in that channel to obtain an absolute recorded time that can be compared between channels. Two examples of raw timing spectra can be seen in fig 5.2 and fig 5.3. In both of these figures, the very narrow peak on the far left is the start signal. We know this because its converted time is approximately 30 ns. In fig 5.3, there is a second, broader peak that occurs between 60-70 ns. This is about twice the duration of the initial peak, so we suspect that there is some reflection occurring as a result of impedance mismatches in the cable connections. This occurs in the majority of TDC channels. We even saw this feature when only the PMTs for a single bar were powered on (fig 5.4). Under these circumstances, we would expect to see only a single, sharp, 'start signal' peak on the far left, but it is clear from fig 5.4 that that is not necessarily the case.

Dealing with the raw QDC values required a different approach. First, we omitted raw QDC values below 100 and above 3840 from the analysis. The cap at 3840 was due to the fact that the sliding scale was enabled on the QDCs, rendering all values above 3840 unreliable [96]. An example of the raw QDC spectra for different channels can be seen in fig 5.9. For QDC values that survived this cut, we then used the energy reconstruction method described in section 3.3 to calculate the energy associated with a given bar.

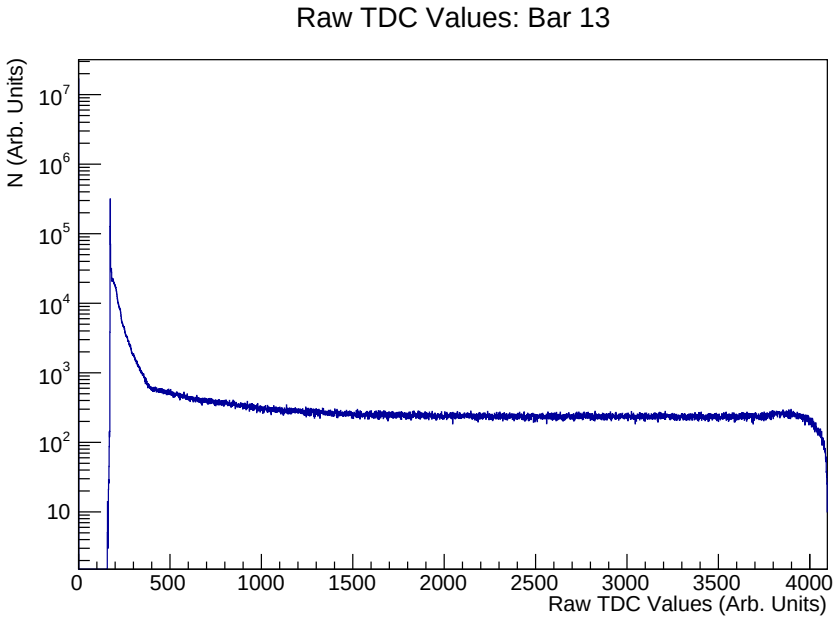

Figure 5.2: Raw TDC values from bar 13 acquired during data-taking. The front PMT only triggers the TDC. The sharp peak at the left was used as the 'start time' that accounts for the inherent delay in the channel. This data was acquired with all PMTs powered on.

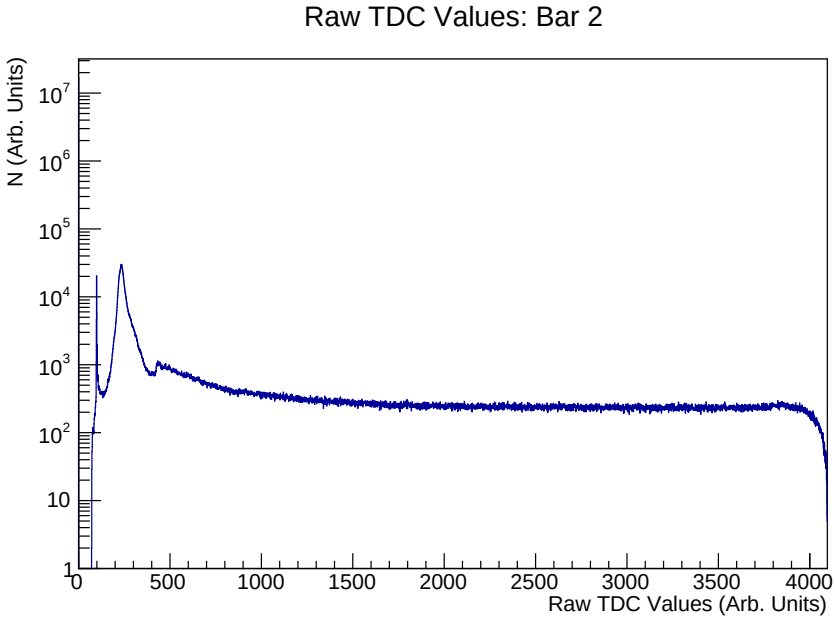

Figure 5.3: Raw TDC values from bar 2. The front PMT only triggers the TDC. In this channel, two separate peaks appear; the first peak on the far left is our 'start peak'. This data was acquired with all PMTs powered on.

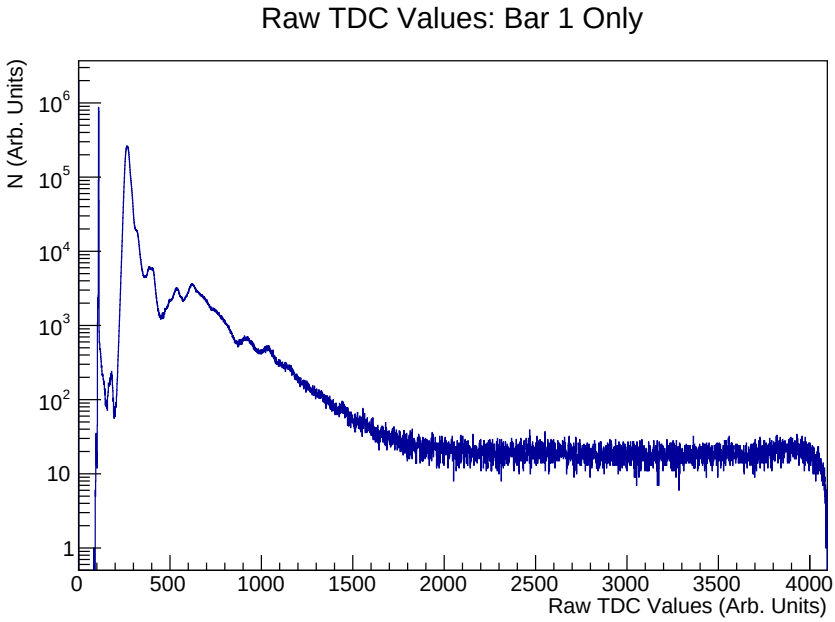

Figure 5.4: Raw TDC values from bar 1. The front PMT only triggers the TDC. In this channel, multiple separate peaks appear. This data was acquired with only PMT 1F powered on. Under these circumstances, we expect to see a single, narrow, peak, but the existence of data over a broad spectrum confirms our theory that some reflections are occurring along the TDC signal path.

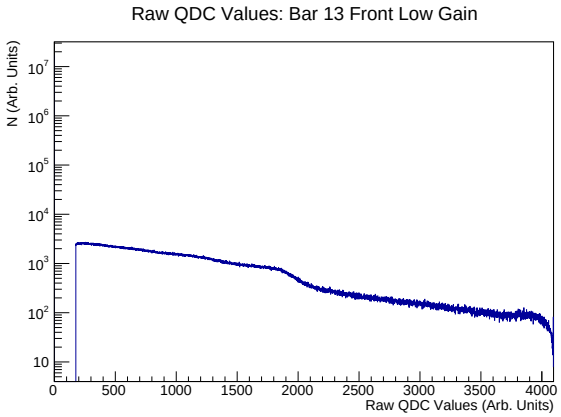

Figure 5.5: Raw QDC values from the front PMT's low gain channel for bar 13.

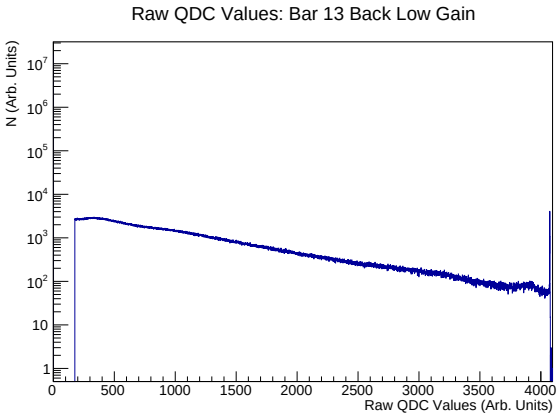

Figure 5.6: Raw QDC values from the back PMT's low gain channel for bar 13.

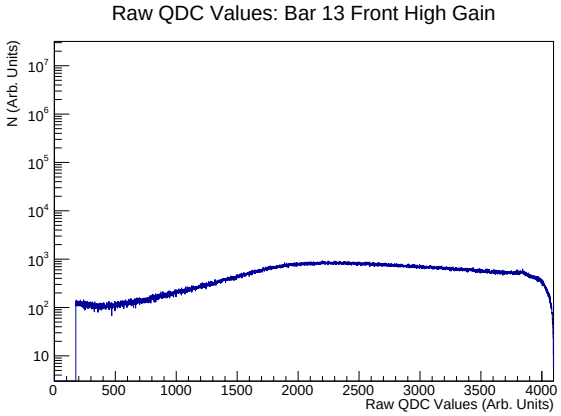

Figure 5.7: Raw QDC values from the front PMT's high gain channel for bar 13.

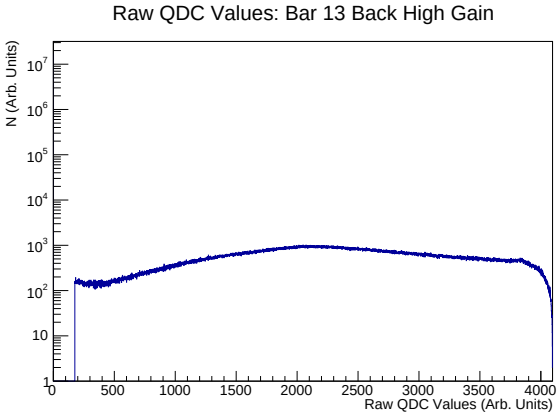

Figure 5.8: Raw QDC values from the back PMT's high gain channel for bar 13.

Figure 5.9: Raw QDC data from all channels for bar 13.

5.2.2 Positronium Analysis Cuts

We applied several cuts to isolate our o-Ps data set from the rest of our data. These analysis cuts can be seen in Table 5.1. In this section, we motivate these analysis cuts and describe their effect on the data. We later demonstrate evidence for positronium detection using the novel technique of tagging on the 1.27 MeV gamma ray and present an analysis of our systematics.

Our first analysis cut excluded all events except those with three or four interactions in the bars. A "four"-bar event accounts for the start signal and all o-Ps gamma rays, whereas a "three"-bar event accounts for the start signal and just two of the o-Ps gamma rays. Presumably, a "three"-bar event excludes the $\vec{k_3}$ gamma ray most of the time due to detector thresholds, but that is not necessarily always the case. It is possible that the $\vec{k_1}$ and $\vec{k_2}$ gamma rays go undetected if they exit the detector without interacting in the NaI(Tl) bars. Events that pass this analysis cut (cut 1 in Table 5.1) account for about 31% of the total number of events. This cut helped exclude events where the $\vec{k_1}$ or $\vec{k_2}$ gamma rays Compton scattered, as well as high energy cosmic rays passing through the detector. A histogram of the number of bars hit can be seen in fig 5.10.

Using the remaining data, we then sorted the gamma rays according to their hit time. This enabled us to identify the so-called 'start signal', which we define as the gamma ray with the earliest occurring time in a given event. Following this, we made a cut on the hit time and energy of the start signal. We required the start signal energy to be in a range from 1.1 MeV-1.6 MeV, since the signal of interest is the 1.27 MeV gamma ray. Likewise, we required the start time to be in a range between 0-40 ns. A 2D histogram of the start time and energy, generated after the cut on the number of bars, can be seen in fig 5.11. This cut helps remove pile-up events and events where the 1.27 MeV gamma ray escaped the APEX array.

After the determination of the start signal, we sorted the remaining gamma rays according to their energy. This enabled us to identify the $\vec{k_1}$, $\vec{k_2}$, and, in the event of a four bar

Cut	**Analysis Cut Name**	**Analysis Cut**
1	Number of bars (N_B)	$2 < N_B < 5$
2	Start Time (T_S)	0 ns $< T_S <$ 40 ns
3	Start Energy (E_S)	1100 keV $< E_S <$ 1600 keV
4	k_1 energy (E_1) and k_2 energy (E_2)	330 keV $< E_1 <$ 511 keV 250 keV $< E_2 <$ 511 keV
5	Difference between $\vec{k_1}$ and $\vec{k_2}$ hit times (ΔT_{12})	$\Delta T_{12} <$ 15 ns
6	Azimuthal Angle (α)	110°$< \alpha <$ 180°
7	Bar Cut	Omit bar 22
8	Z position cut 1	-22.5 cm $< z_1 <$ 22.5 cm -22.5 cm $< z_2 <$ 22.5 cm
9	Z position cut 2	Upper Bound (Center): $z_2 <$ -z_1+20 Lower Bound (Center): $z_2 >$ -0.75*z_1-12.5 Upper Bound (Shift): $z_2 <$ -0.33*z_1+16.7 Lower Bound (Shift): $z_2 >$ -z_1-22.0
10	Difference between $\vec{k_1}$ and $\vec{k_2}$ energies (ΔE_{12})	$\Delta E_{12} <$ 200 keV
11	Average of $\vec{k_1}$ and $\vec{k_2}$ hit times ($T_{avg} = \frac{T_1+T_2}{2}$)	20 ns $< t_{avg} <$ 600 ns

Table 5.1: Table showing the list of analysis cuts. Cut 9 depends on the data set which is used. 'Center' refers to data acquired at the center of the array, whereas 'Shift' refers to data acquired 14 cm towards the front of the array.

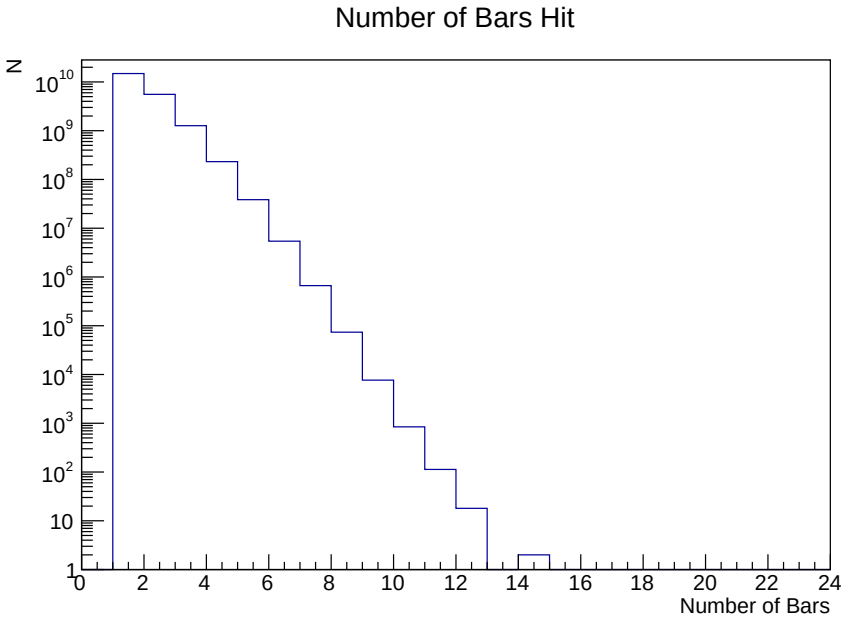

Figure 5.10: Histogram of the number of bars hit in the APEX. We make a cut such that the number of bars is greater than two and less than five. No analysis cuts were made prior to the creation of this histogram.

interaction, $\vec{k_3}$. The relative energy distributions of $\vec{k_1}$ and $\vec{k_2}$ can be seen in fig 5.14. We determined the timing of the $\vec{k_1}$ and $\vec{k_2}$ gamma rays by subtracting the hit time associated with the start signal from the absolute $\vec{k_1}$ and $\vec{k_2}$ hit times. Fig 5.12 shows the $\vec{k_1}$ gamma ray energy and time distribution, and fig 5.13 shows the $\vec{k_2}$ gamma ray energy and time distribution.

The proper identification of the ordering of the gamma ray energies was critical to this experiment. While it is certainly possible to compute alternative CPT-violating observables, such as $\left(\vec{S}\cdot\vec{k_2}\times\vec{k_3}\right)$ or $\left(\vec{S}\cdot\vec{k_1}\times\vec{k_3}\right)$, it is important to remain consistent. In our case, there were a few factors that led to misordered gamma rays, including imperfect energy resolution (addressed in later sections), and missing gamma rays (either below threshold, escaping the detector, or saturating a bar). We assumed that the majority of "three"-bar events omit the $\vec{k_3}$ gamma ray since about 32% of the $\vec{k_3}$ energy spectrum does not exceed our detector thresholds. Still, it is not impossible for us to have missed $\vec{k_1}$ and $\vec{k_2}$ gamma rays due to limited solid angle coverage. We therefore implemented a cut (four in Table 5.1) on the

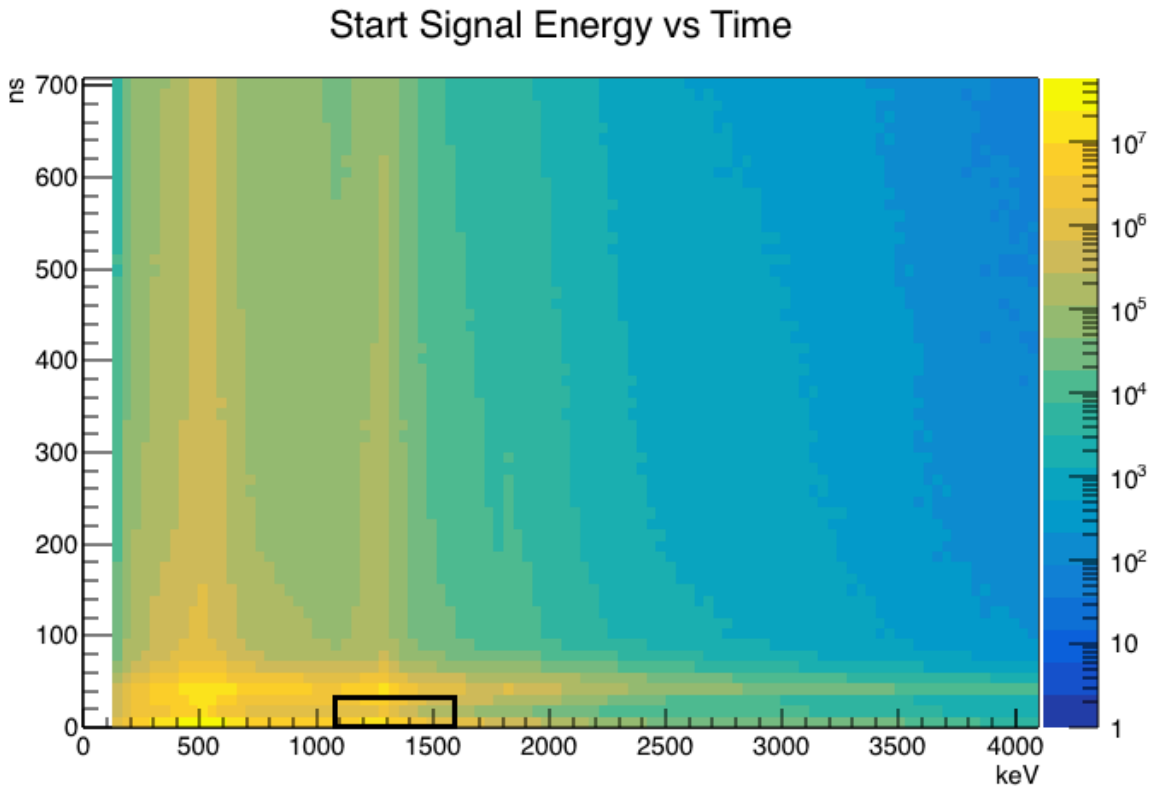

Figure 5.11: 2D histogram of the start signal energy vs time. The only cut before this was a requirement that more than two bars and less than five bars were hit. We accepted events with start times in the range of 0 ns to 40 ns and energies in the range of 1.1-1.6 MeV. The cut is shown bounded by a black box on the histogram.

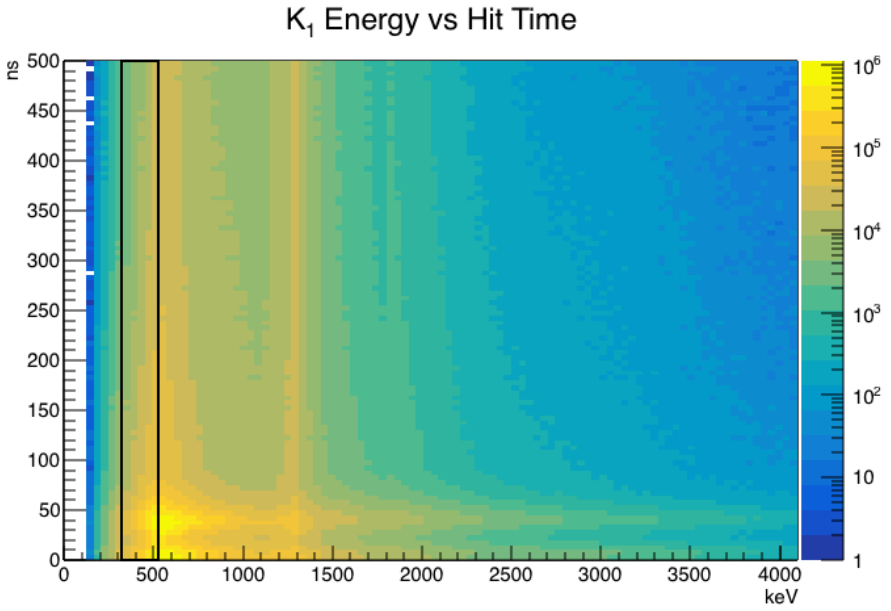

Figure 5.12: $\vec{k_1}$ gamma ray energy vs hit time. This histogram was generated after the cut on the number of bars and the cut on the start signal time and energy. The black box shows the allowed $\vec{k_1}$ gamma ray energy range.

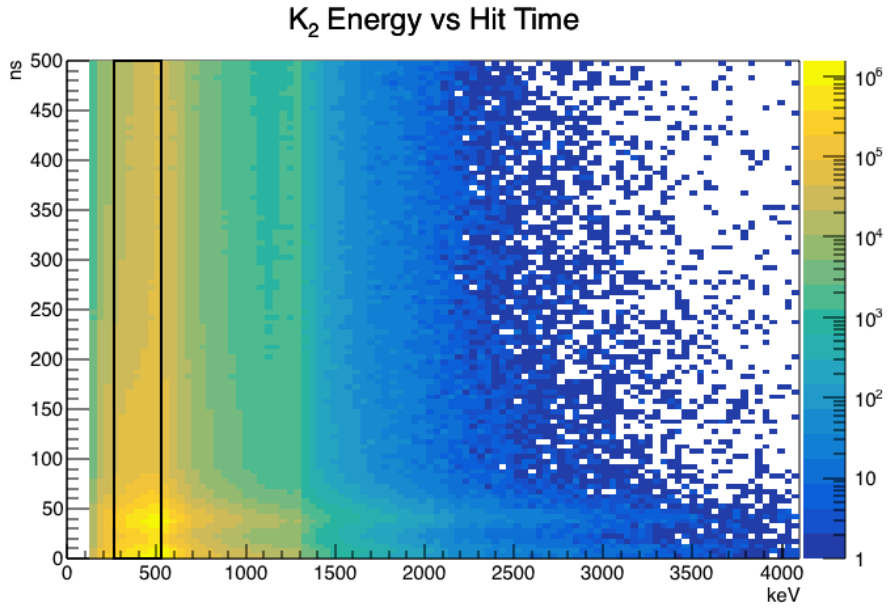

Figure 5.13: $\vec{k_2}$ gamma ray energy vs hit time. This histogram was generated after the cut on the number of bars and the cut on the start signal time and energy. The black box shows the allowed $\vec{k_2}$ gamma ray energy range.

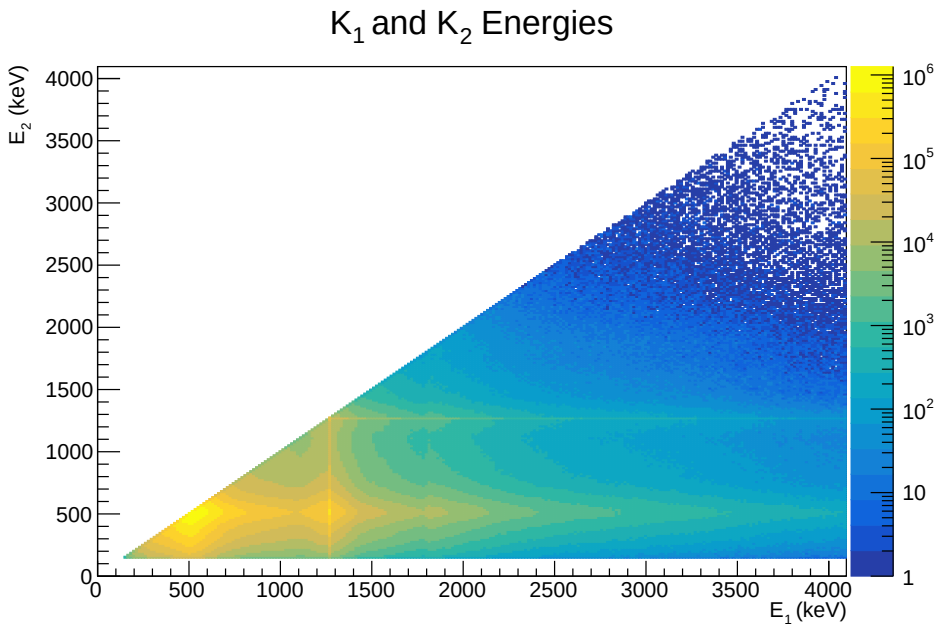

Figure 5.14: 2D histogram of the energies of the $\vec{k_1}$ gamma ray vs the $\vec{k_2}$ gamma ray. This histogram was generated after the cut on the number of bars and the cut on the start signal time and energy.

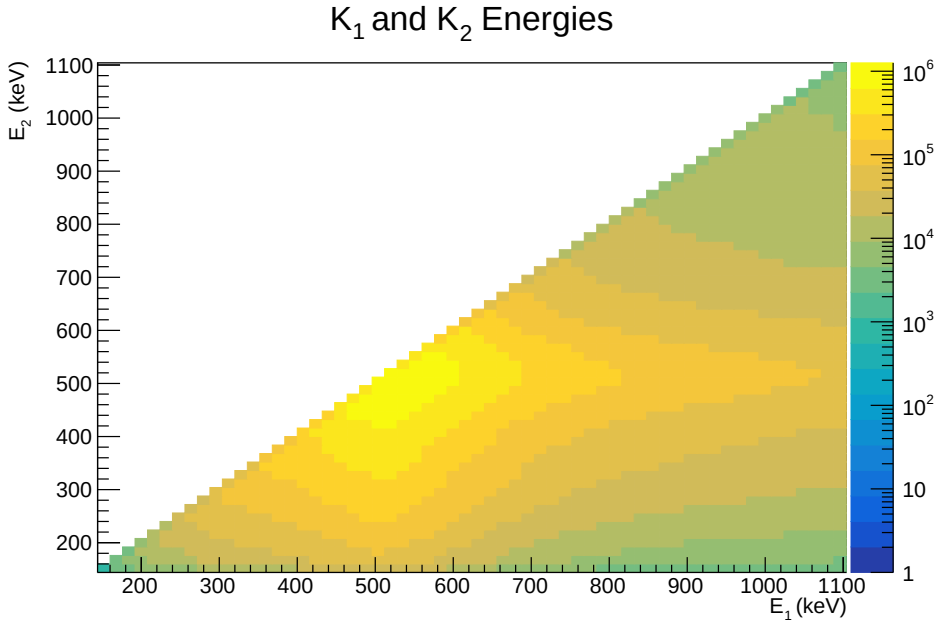

Figure 5.15: 2D histogram of the energies of the $\vec{k_1}$ gamma ray vs the $\vec{k_2}$ gamma ray (zoom of fig 5.14). This histogram was generated after the cut on the number of bars and the cut on the start signal time and energy.

absolute energies of the $\vec{k_1}$ and $\vec{k_2}$ gamma rays to reduce the number of events in which $\vec{k_2}$ and $\vec{k_3}$ are mistaken for $\vec{k_1}$ and $\vec{k_2}$. We restricted the possible energy ranges of the $\vec{k_1}$ and $\vec{k_2}$ gamma rays such that 330 keV $< E_1 <$ 511 keV and 250 keV $< E_2 <$ 511 keV, where E_1 is the energy of the $\vec{k_1}$ gamma ray and E_2 is the energy of the $\vec{k_2}$ gamma ray. A histogram of the $\vec{k_1}$ and $\vec{k_2}$ energy distributions can be seen in fig 5.16. This histogram can be directly compared to the simulated and theoretical $\vec{k_1}$ and $\vec{k_2}$ energy distributions in figs 1.2, 1.3, 4.8, and 4.9. We also include a histogram of the $\vec{k_1}$ and $\vec{k_2}$ energy spectra (shown in fig 5.17) after all of the analysis cuts in Table 5.1, except the cut on E_1 and E_2, to give an idea of its effect on the data.

The energies of the o-Ps gamma rays provided a powerful handle on our data set. As such, we appraised two more tools at our disposal: the sum of and difference between the $\vec{k_1}$ and $\vec{k_2}$ gamma ray energies. Our idea was that these parameters could reduce the inevitable pile-up that comes with the usage of a 10 µCi source and a 1 µs gate. One effect of pile-up would be the contamination of our data set with scattered back-to-back gamma rays from p-Ps decays that appear to have hit times characteristic of o-Ps. We know that the sum of all three gamma rays ($\vec{k_1}$, $\vec{k_2}$, $\vec{k_3}$) should equal 1022 keV, therefore the sum of $\vec{k_1}$ and $\vec{k_2}$ energies should be less than 1022 keV. We implemented this cut in our analysis, but it proved to be redundant with the earlier cut on the individual energies of the $\vec{k_1}$ and $\vec{k_2}$ energies. Still, we examined the effect of a cut on ΔE_{12}. Since the maximum value for the $\vec{k_1}$ gamma ray energy is 511 keV, and the minimum value for the $\vec{k_2}$ gamma ray energy is 250 keV, the difference between the $\vec{k_1}$ and $\vec{k_2}$ energies should not exceed 261 keV. Furthermore, the $\vec{k_3}$ energy spectrum actually overlaps part of the $\vec{k_2}$ energy spectrum, with the $\vec{k_3}$ distribution ending at 330 keV. In order to omit this part of the $\vec{k_3}$ spectrum from our analysis and decrease the chances of flipping $\vec{k_2}$ and $\vec{k_3}$, we implemented a cut such that $\Delta E_{12} <$ 200 keV. This is tabulated as cut eleven in Table 5.1. A histogram of the sum of the $\vec{k_1}$ and $\vec{k_2}$ energies can be seen in fig 5.20 and a histogram of the difference between the $\vec{k_1}$ and $\vec{k_2}$ energies can be seen in fig 5.19.

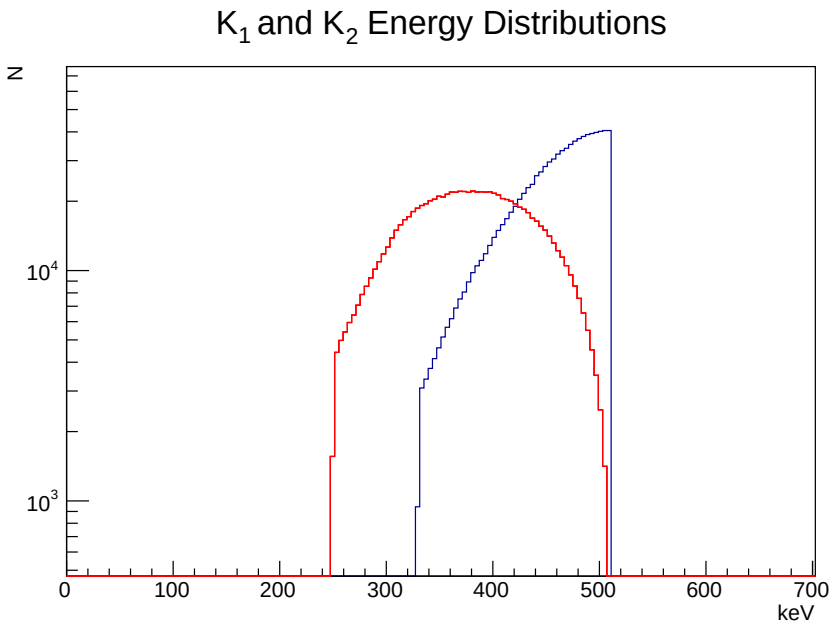

Figure 5.16: Histogram of the $\vec{k_1}$ and $\vec{k_2}$ gamma ray energies after the implementation of all analysis cuts from Table 5.1. The $\vec{k_2}$ energy distribution is shown in red and the $\vec{k_1}$ energy distribution is shown in blue.

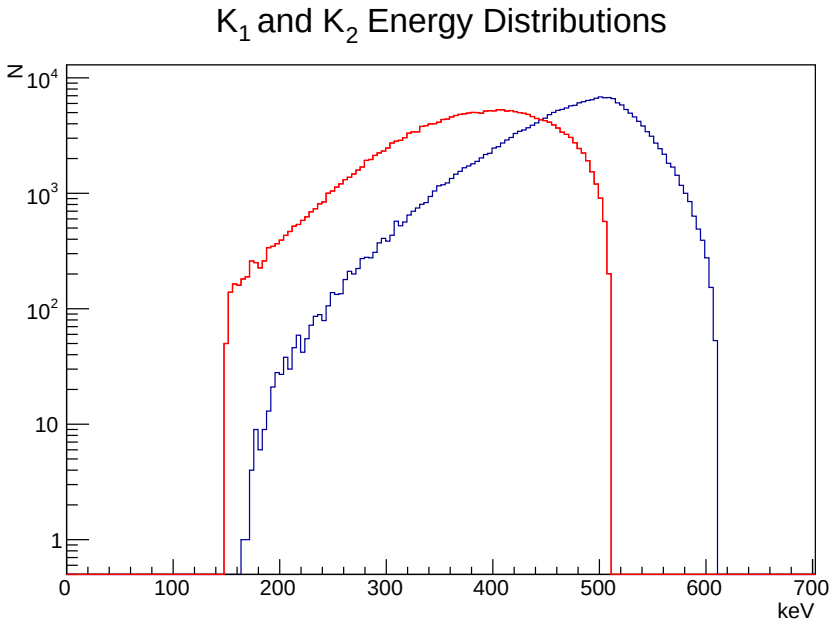

Figure 5.17: Histogram of the $\vec{k_1}$ and $\vec{k_2}$ gamma ray energies after the implementation of all analysis cuts, except for the cut on the individual $\vec{k_1}$ and $\vec{k_2}$ energies. Again, the $\vec{k_2}$ energy distribution is shown in red and the $\vec{k_1}$ energy distribution is shown in blue.

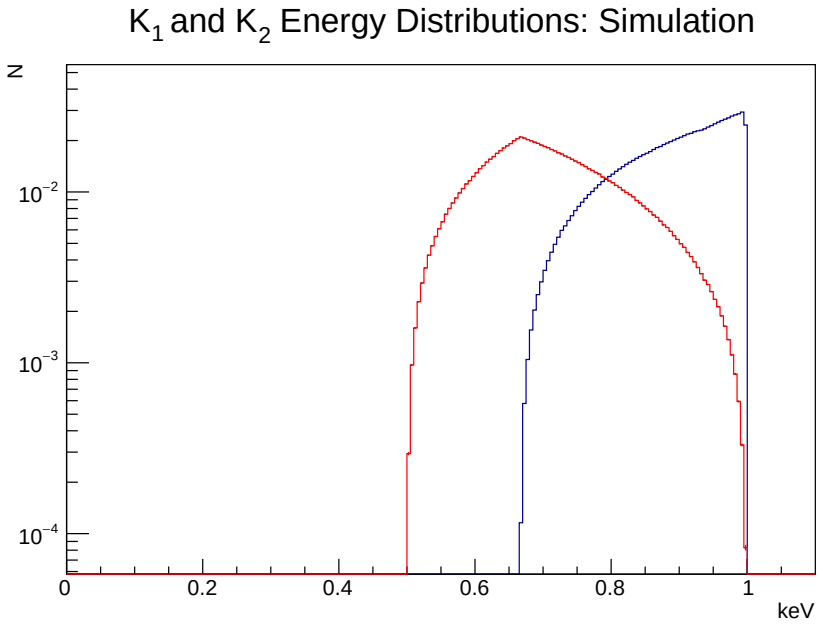

Figure 5.18: Histogram of the $\vec{k_1}$ and $\vec{k_2}$ gamma ray energies from the Ps generator simulation. This can be directly compared to figs 5.16 and 5.16.

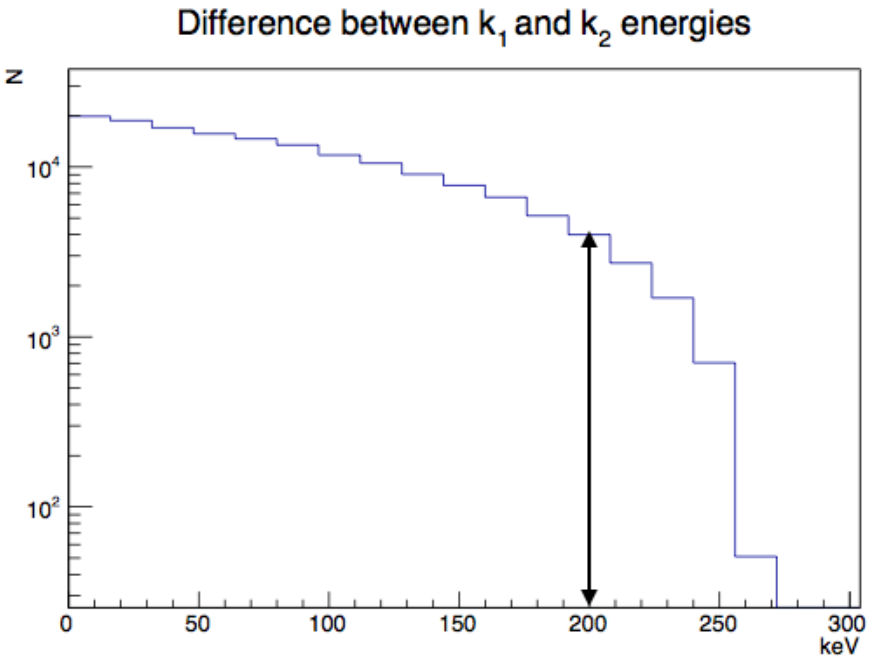

Figure 5.19: Histogram of the difference between the $\vec{k_1}$ and $\vec{k_2}$ gamma ray energies. This histogram was generated after all analysis cuts in Table 5.1, except for the cut on ΔE_{12}

.

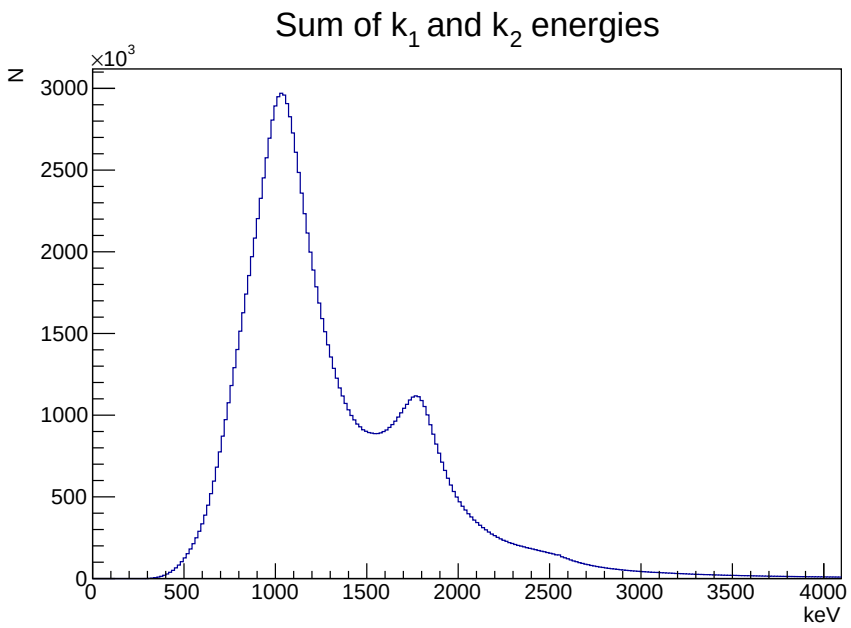

Figure 5.20: Histogram of the sum of the $\vec{k_1}$ and $\vec{k_2}$ energies. A cut was made of this histogram to isolate the o-Ps events. We retained all events less than 1022 keV. This plot was generated after analysis cut three in Table 5.1.

Another cut that we imposed on our data set was a cut on the azimuthal angle (cut 6 in Table 5.1). We know from theory that the angle between the $\vec{k_1}$ and $\vec{k_2}$ gamma rays, ψ, ranges from about 110° to 180°. The azimuthal angle, which is the projection of the angle ψ onto the xy-plane of APEX, is defined as the angle between the $\vec{k_1}$ and $\vec{k_2}$ bars. We therefore applied a cut on the azimuthal angle such that we retain all events that have an azimuthal angle between 110° and 180°. A histogram of the azimuthal angle can be seen in fig 5.24. The application of such a cut reduced Compton scattered events that may contaminate our data set.

We and previous APEX users observed that interactions close to the ends of the NaI(Tl) bars were unreliable due to attenuation [93]. We therefore included a cut on the z position of the $\vec{k_1}$ and $\vec{k_2}$ gamma rays such that -22.5 cm $< z <$22.5 cm. This ensured we included no interactions within 5 cm of the ends of the bars. Furthermore, we implemented a cut that accounted for the kinematics of positronium decay: an upper and lower bound on the plot of z_1 versus z_2, as shown in fig 5.25. This cut was dependent on the data set; a different

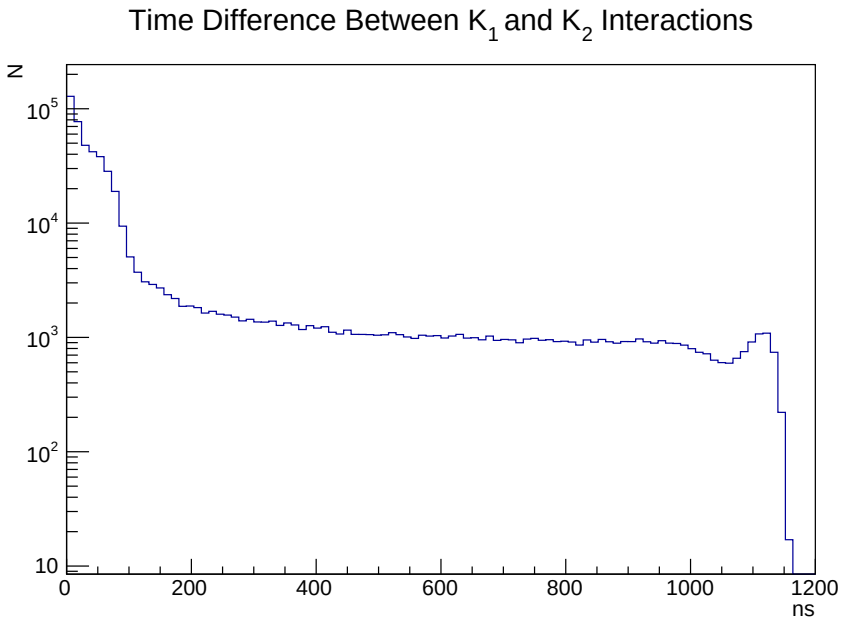

Figure 5.21: Histogram of the time difference between the $\vec{k_1}$ and $\vec{k_2}$ bars. We retained all events that had a hit time difference less than 15 ns. The above histogram was generated by imposing all analysis cuts except the cut on the timing difference between $\vec{k_1}$ and $\vec{k_2}$.

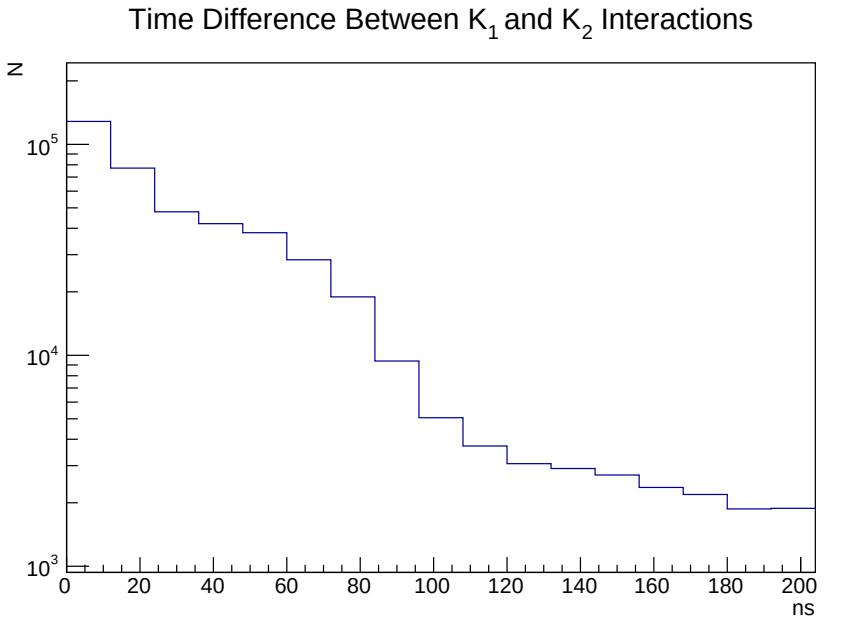

Figure 5.22: Enlarged histogram of the time difference between the $\vec{k_1}$ and $\vec{k_2}$ bars (fig 5.22), showing the region between 0-200 ns. We believe the should from about 15-100 ns is a result of pile-up events.

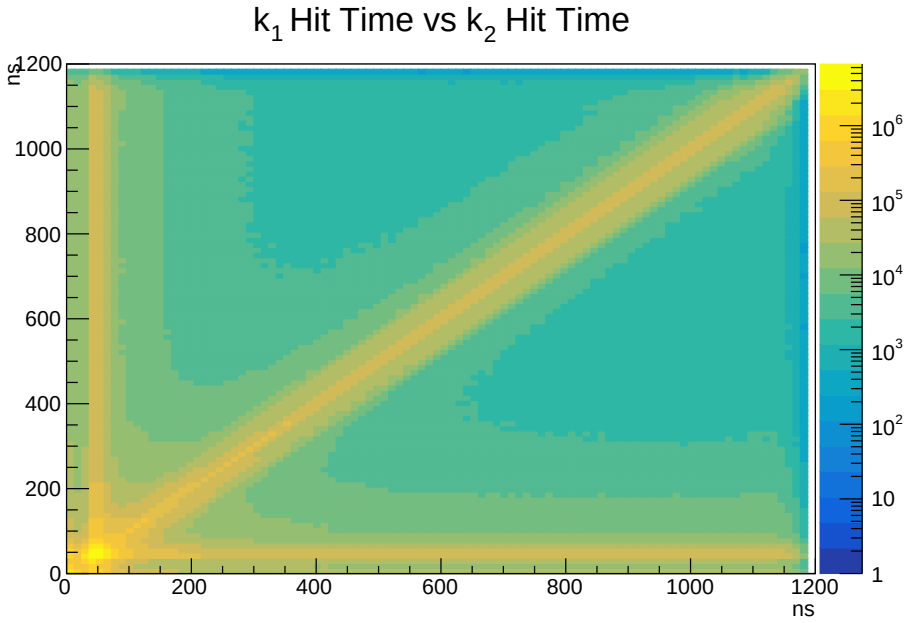

Figure 5.23: 2D visualization of the hit times for the $\vec{k_1}$ and $\vec{k_2}$ gamma rays. We are interested in simultaneous hit times for $\vec{k_1}$ and $\vec{k_2}$, which corresponds to the diagonal yellow band. This plot was generated after the cut on the number of bars and the cut on the start time and energy.

cut was applied to data acquired at the center of the array as opposed to 14 cm towards the front of the array in order to capture events with the correct kinematics. Such a cut also reduced Compton scattered events. These z position cuts are identified in Table 5.1 as cuts 8-9.

In order to qualify as a 'good' o-Ps event, the $\vec{k_1}$ and $\vec{k_2}$ hit times had to occur simultaneously. This motivated us to apply a cut such that the difference between the $\vec{k_1}$ and $\vec{k_2}$ hit times was no more than 15 ns (cut 5 in Table 5.1). A histogram of the difference between the hit times of $\vec{k_1}$ and $\vec{k_2}$ can be seen in fig 5.22. Additionally, a 2D representation of the $\vec{k_1}$ and $\vec{k_2}$ hit times can be seen in fig 5.23. The events of interest occur in the diagonal yellow band.

We made one final cut to isolate our o-Ps data: a cut on the average time of $\vec{k_1}$ and $\vec{k_2}$ such that this time was between 20 and 600 ns. We deduced that events beyond 600 ns were background only by comparing two 'timing spectra' (t_{avg} plots). The first such spectrum

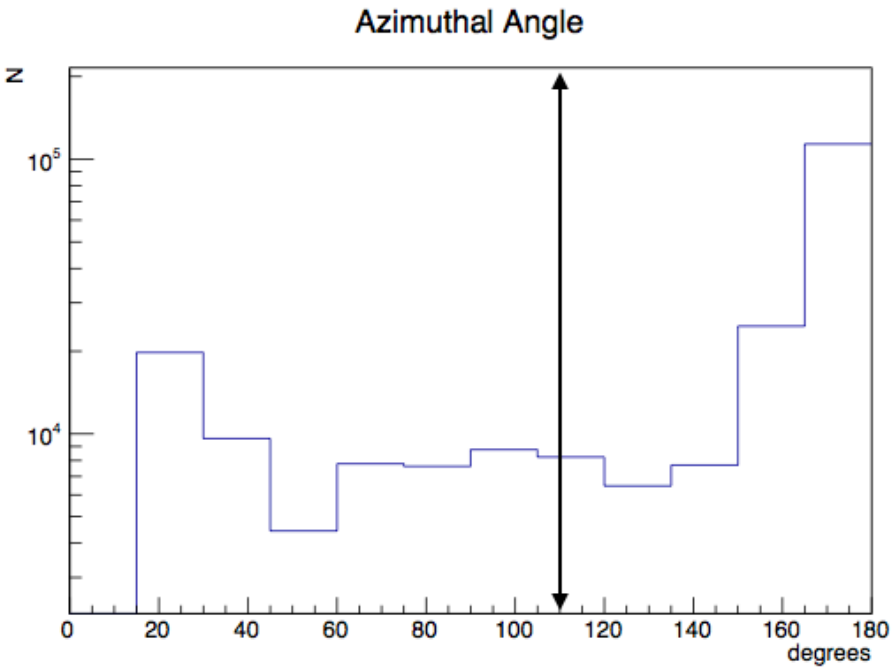

Figure 5.24: Histogram of the azimuthal angle (ψ) between $\vec{k_1}$ and $\vec{k_2}$ gamma rays. It is discretized into 15 degree segments because the APEX array is discretized into 24 NaI(Tl) bars. The angular distribution for ψ was shown in previous chapters, and ranges from about 110 to slightly less than 180 degrees for o-Ps (everything to the right on the black arrow). This plot was generated with all cuts listed in Table 5.1, except the cut on the number of bars and the cut on the azimuthal angle.

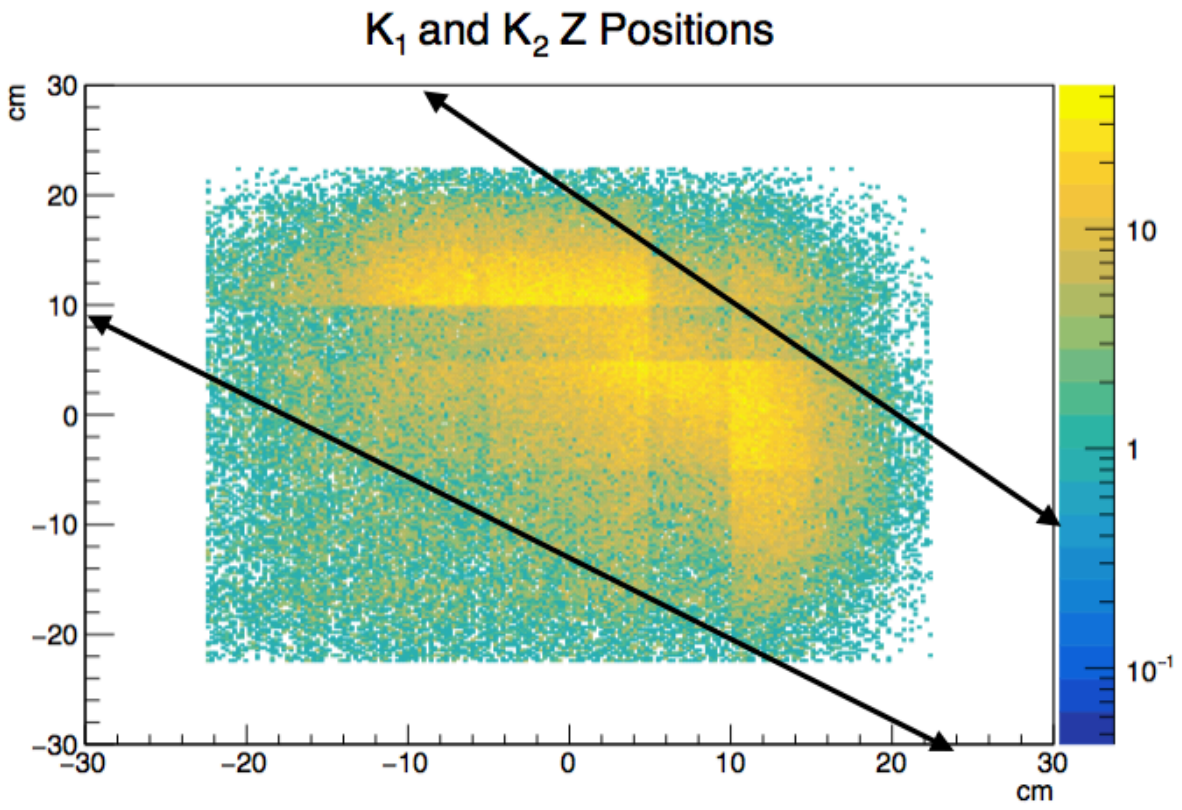

Figure 5.25: 2D histogram of the $\vec{k_1}$ and $\vec{k_2}$ z positions. We know the $\vec{k_1}$ and $\vec{k_2}$ gamma rays emitted in o-Ps decay are approximately back-to-back, and so should be distributed along a line in the z_1-z_2 parameter space. We exclude events external to the black bounds in order to moit events that are kinematically inconsistent with o-Ps decay. The data shown were acquired when the source was shifted towards the front of the APEX array. All analysis cuts except the cut of interest (on the z position), were applied to this histogram. The yellow bands are a result of the fact that the energy calibration is performed along different z positions along the length of the bar.

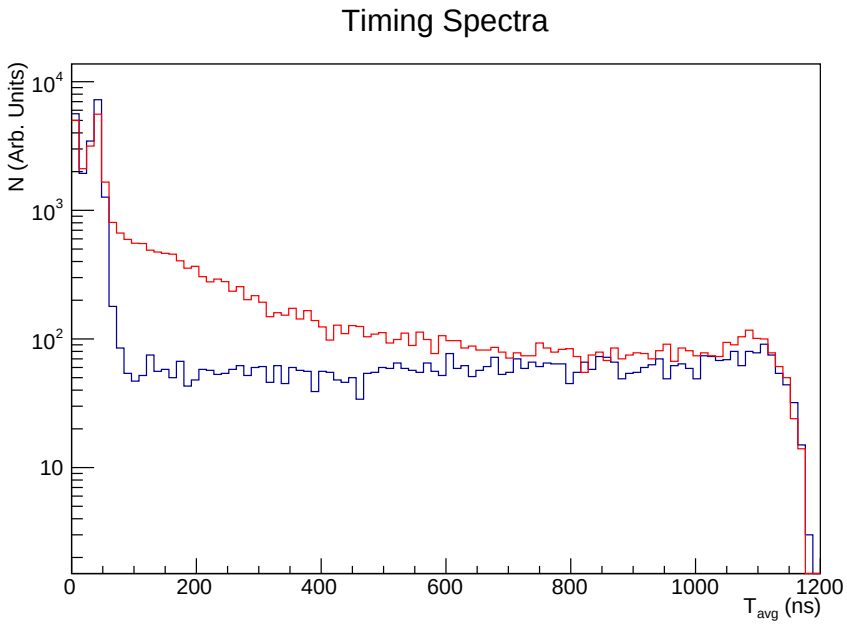

Figure 5.26: Timing spectrum comparing o-Ps and background data.

was comprised of data acquired with only a ^{22}Na button source, whereas the second was comprised of data acquired with the thin film [91] source adjacent to a piece of aerogel ("o-Ps data"). This can be seen in fig 5.26. At approximately 600 ns, the two spectra meet, confirming the hypothesis that we have a flat background in our data that is not removed by the cuts in Table 5.1. To identify this flat background, we ran a series of tests, generating several cut parameter plots using 'background-only' data (events between 600 and 1200 ns). We concluded that the background is pile-up, with the most compelling evidence coming from the fact that the energy spectra of the $\vec{k_1}$ and $\vec{k_2}$ gamma rays are indistinguishable from those generated with the 'signal' data (between 0 and 600 ns). A plot of the $\vec{k_1}$ versus $\vec{k_2}$ gamma ray energies using 'background-only' data can be seen in fig 5.27.

After applying all analysis cuts, we then calculated our CPT-violating observable by reconstructing the momenta of the $\vec{k_1}$ and $\vec{k_2}$ gamma rays using their respective bars, and the energy deposition inside the bars. This allowed us to determine our asymmetry parameter. We elaborate on this in subsequent sections.

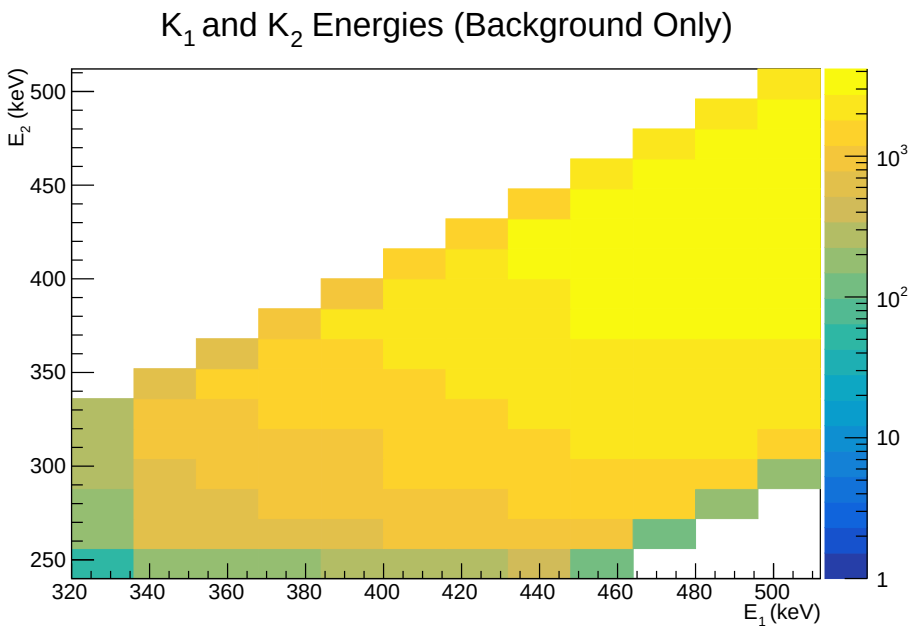

Figure 5.27: Energy distribution of $\vec{k_1}$ and $\vec{k_2}$ gamma rays using background data only (events with 600 ns $< t_{avg} <$ 1200 ns).

5.3 Positronium Detection

We were able to confirm our ability to detect positronium by generating a timing spectrum so that the positronium mean lifetime was clearly evident. Additionally, we were able to demonstrate that this lifetime changed depending on the gas that was present in the aerogel. This information is presented in fig 5.28, which shows the average of the $\vec{k_1}$ and $\vec{k_2}$ hit times. The blue histogram is data taken with a ^{22}Na source and no aerogel. The gray histogram is data taken with a ^{22}Na source and aerogel in air. The red histogram is data taken with a ^{22}Na source and aerogel in nitrogen. The gray and red histograms were fit with an exponential and flat background in ROOT [103]. The gray curve (air) was fit in a region from 80-500 ns and yielded a mean lifetime of 77±12 ns. The red curve (nitrogen) was fit in a region from 50-600 ns and yielded a mean lifetime of 126± 18 ns. These results are consistent with the measurements made by a previous group of the mean lifetime of o-Ps in air of 80.1±2.6 ns and in nitrogen of 129.1±1.8 ns [1].

We only show up to 600 ns in fig 5.28, but a flat background persists up to 1200 ns. We

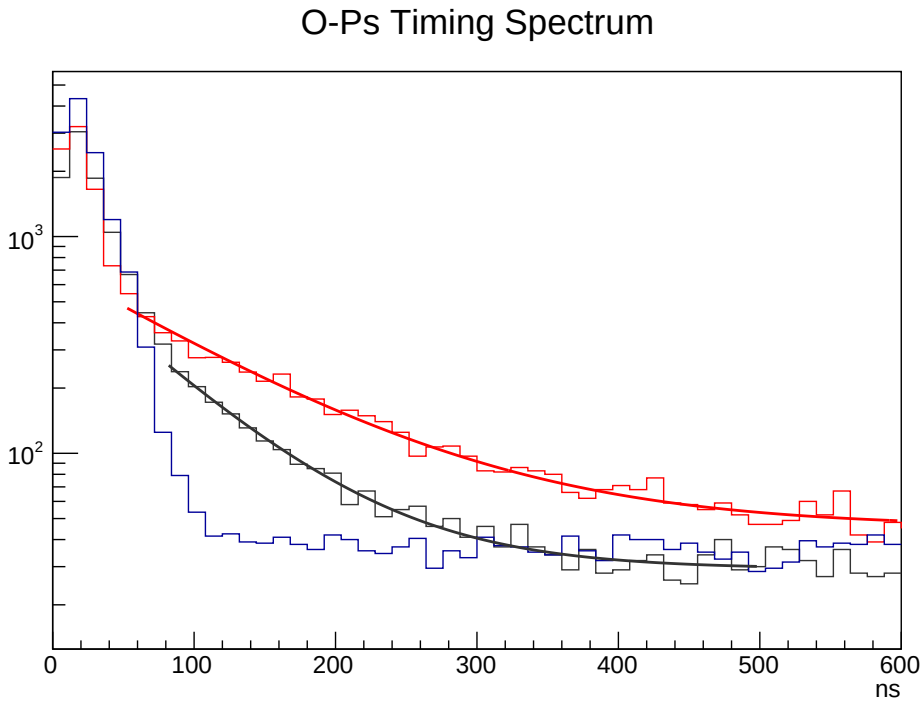

Figure 5.28: Shown above is data taken with the aerogel (red) and data taken without the aerogel (blue). When the aerogel was removed from the source holder, it was replaced with a thin, 0.5 mm aluminum plate, identical to the one in the back of the source. This provides some support for the kapton foil. Data was taken with nitrogen flowing through the tube. The tube was purged for two hours before data was taken. An exponential+background fit was performed using ROOT [103], and a mean lifetime of 125±18 ns was measured. This is consistent with the results of another research group that measured a mean lifetime of 129.1±1.8 ns for o-Ps in nitrogen [66]

.

concluded that this background is the result of pile-up, as the energy distributions of the $\vec{k_1}$ and $\vec{k_2}$ gamma rays are indistinguishable from those of o-Ps. We discuss how the background reduces our sensitivity in later sections.

5.4 Calculating the Asymmetry Parameter

A histogram of our CPT-violating observable, $(\vec{S}\cdot\vec{k_1}\times\vec{k_2})$, is shown in fig 5.29. To calculate the total asymmetry, we subtracted the number of negative events from the number of positive events in this histogram, and normalized by the total number of events:

$$A = \frac{N_+ + N_-}{N_+ + N_-}. \tag{5.1}$$

We calculated this separately for data taken with the source oriented towards the front of the array (A_F) and for data taken with the source oriented towards the back of the array (A_B). The final asymmetry was then calculated by subtracting the two values to cancel out systematics:

$$A = A_F - A_B. \tag{5.2}$$

After the implementation of all analysis cuts in Table 5.1, we obtained the asymmetry values outlined in Table 5.2. Both A_F and A_B should be consistent with zero if no CPT-violating interactions or systematics are present. Subtracting A_F from A_B should cancel this and many other systematics that would exist if only one orientation were used. Nevertheless, we observed an asymmetry with the full dataset (the third entry in 5.2) at a level significantly above previous measurements. We believe that this asymmetry is attributable to one or more unidentified systematics and explain this in the following sections. In Table 5.2, we decoupled several data sets to see if we could isolate the source of the observed asymmetry. These can be seen in the other entries of Table 5.2. These data sets include:

1. Centered data: This refers to data acquired with the source located at the center of the array

2. Shifted data: This refers to data acquired with the source located 14 cm towards the from of the array (measured from the center).

3. 4 bar only: This refers to data with 4 bar interactions only.

4. Calibration Function 1: This refers to data that excluded all events containing interactions calibrated using calibration functions > 1, as explained in Table 3.2

5. Calibration Function 1-5: This refers to data that excluded all events containing interactions calibrated using calibration functions > 5, as explained in Table 3.2. This category is significant because it includes only events for which data was present on all four channels.

We also calculated the asymmetry for combinations of the above data sets. For example, 'Centered, 4 bar only, Calibration Function 1' refers to data acquired with the source at the center of the array, wherein we used only 4 bar events and calibration function 1 to calculate the asymmetry parameter. Data sets labeled with '4 bar only, Calibration Function 1' use the most stringent set of analysis cuts.

In the following chapter, we explain possible causes for these systematics and run through a series of diagnostic tests that we performed in an attempt to isolate the problem.

Data Set	A_F	A_B	A
Centered All Data	-0.0457±0.0013	-0.0451±0.0013	-0.0006±0.0009
Shifted All Data	-0.0070±0.0010	-0.0141±0.0010	0.0071±0.0007
Net All Data	-0.0215±0.0008	-0.0262±0.0008	0.0047±0.0006
Centered (4 bar only)	-0.0116±0.0060	-0.0079±0.0058	-0.0038±0.0042
Shifted (4 bar only)	-0.0142±0.0050	-0.0074±0.0051	-0.0067±0.0036
Net (4 bar only)	-0.0131±0.0038	-0.0076±0.0038	-0.0055±0.0027
Centered Calibration Functions 1-5	-0.0601±0.0022	-0.0591±0.0019	-0.0010±0.0014
Shifted Calibration Functions 1-5	-0.0193±0.0025	-0.0190±0.0025	-0.0008±0.0018
Net Calibration Functions 1-5	-0.0422±0.0016	-0.0447±0.0015	0.0025±0.0011
Centered Calibration Function 1	-0.0570±0.0060	-0.0602±0.0057	0.0032±0.0041
Shifted Calibration Function 1	-0.0405±0.0037	-0.0317±0.0038	-0.0088±0.0026
Net Calibration Function 1	-0.0450±0.0031	-0.0403±0.0031	-0.0047±0.0022
Centered (4 bar only) Calibration Function 1	-0.0602±0.0314	-0.0103±0.0282	-0.0499±0.0210
Shifted (4 bar only) Calibration Function 1	-0.0194±0.0191	-0.0363±0.0202	0.0169±0.0139
Net (4 bar only) Calibration Function 1	-0.0304±0.0163	-0.0275±0.0164	-0.0029±0.0116

Table 5.2: This table delineates our results, with several subsets of the data set decoupled so as to check for variations of the asymmetry between them. Uncertainties are statistical only.

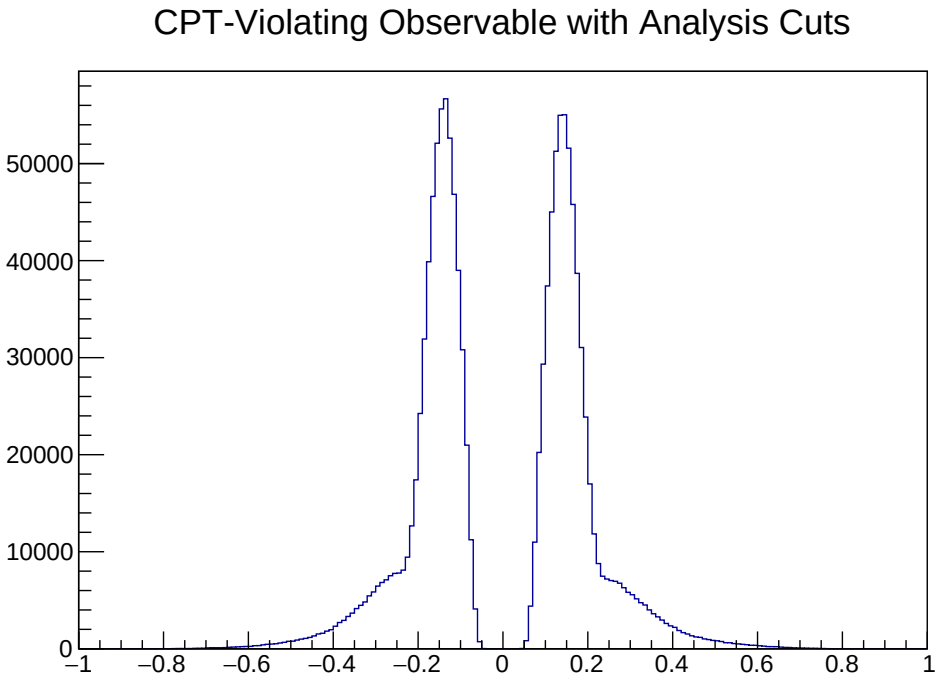

Figure 5.29: Histogram of $(\vec{S} \cdot \vec{k_1} \times \vec{k_2})$. The gap in the center is due to our energy thresholds (150 keV) and the exclusion of back-to-back gamma rays due to an inability to determine their handedness.

5.5 Asymmetry Diagnostics

Any true CPT-violating signal would demonstrate certain qualities as evidence of its authenticity. For example, the signal should not vary as a function of the location or the energy of the gamma ray interactions within the array. Should the CPT-violating asymmetry vary as a function of such a parameter, then the asymmetry is caused by a systematic.

With this in mind, we generated several plots of the asymmetry term as a function of the following cut parameters:

1. E_1: Energy of the $\vec{k_1}$ gamma ray.
2. E_2: Energy of the $\vec{k_2}$ gamma ray.
3. ΔE_{12}: Energy difference between the $\vec{k_1}$ and $\vec{k_2}$ gamma rays.
4. $E_1 + E_2$: Sum of the $\vec{k_1}$ and $\vec{k_2}$ gamma ray energies.
5. T_1: Hit time of the $\vec{k_1}$ gamma ray.
6. T_2: Hit time of the $\vec{k_2}$ gamma ray.
7. T_{avg}: Average of the $\vec{k_1}$ and $\vec{k_2}$ hit times.
8. ΔT_{12}: Timing difference between the $\vec{k_1}$ and $\vec{k_2}$ gamma ray hits.
9. Z_1: Z position of the $\vec{k_1}$ gamma ray.
10. Z_2: Z position of the $\vec{k_2}$ gamma ray.
11. α: Azimuthal angle between $\vec{k_1}$ and $\vec{k_2}$.

It is possible, too, that the data acquired at the center of APEX is subjected to different effects than the data acquired near the front of APEX. We therefore performed these asymmetry diagnostics on both sets of data separately. We generated the diagnostic plots

in this section after applying one of the most stringent set of analysis cuts, the fifteenth entry in Table 5.2, the rationale being that we could isolate an individual systematic before examining a larger portion of the full data set.

5.5.1 Energy Dependence

Our first diagnostic involved examining any energy-dependent effects on the asymmetry parameter. The $\vec{k_1}$ energy ranges from 330 keV to 511 keV, peaking at 511 keV. Figs 5.30 and 5.31 show the asymmetry as a function of $\vec{k_1}$ energy over this range for the centered and shifted data sets, respectively. Although an overall asymmetry is apparent, we observed no remarkable trend as a function of E_1. Likewise, the energy of the $\vec{k_2}$ gamma ray ranges from 250 to 511 keV, peaking at approximately 350 keV. Figs 5.32 and 5.33 show the asymmetry plotted as a function of the $\vec{k_2}$ gamma ray for the centered and shifted data sets, respectively. There is no section of the spectrum which results in an asymmetry that is consistent with zero.

Two other energy parameters of importance are the sum of the $\vec{k_1}$ and $\vec{k_2}$ energies as well as the difference between the $\vec{k_1}$ and $\vec{k_2}$ energies. Figs 5.34 and 5.35 show the asymmetry as a function of the difference between the two gamma ray energies and figs 5.36 and 5.37 show the asymmetry as a function of the sum of the two gamma ray energies. The asymmetry does not display a consistent pattern across the centered and shifted data sets when plotted as a function of the sum of E_1 and E_2. On the other hand, the asymmetry is more exaggerated as ΔE_{12} increases. Events for which 40keV$<\Delta E_{12}<$140keV are consistent with zero, but this would not be a well-justified analysis cut.

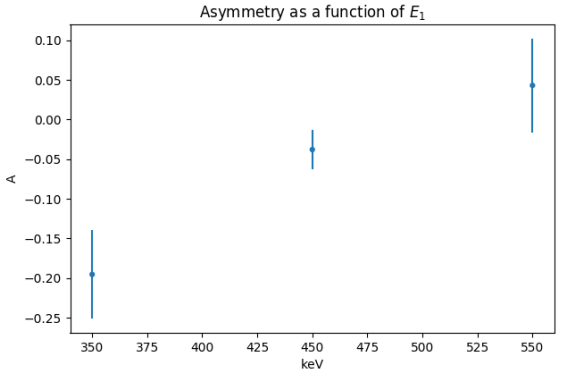

Figure 5.30: Asymmetry vs E_1 (Center).

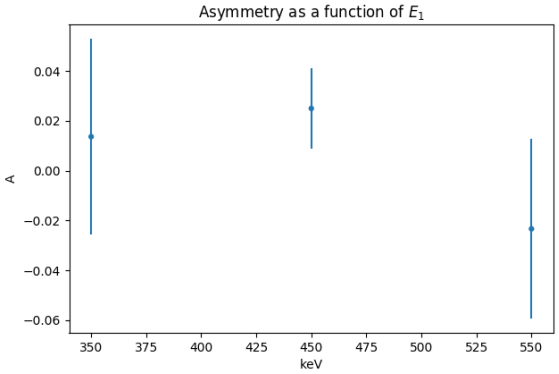

Figure 5.31: Asymmetry vs E_1 (Shift).

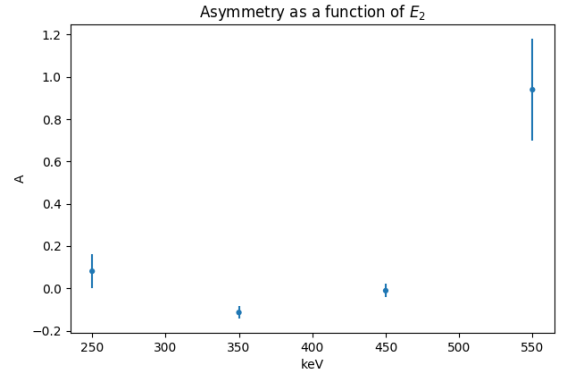

Figure 5.32: Asymmetry vs E_2 (Center).

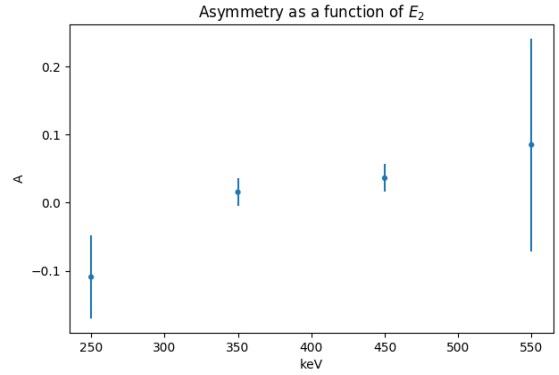

Figure 5.33: Asymmetry vs E_2 (Shift).

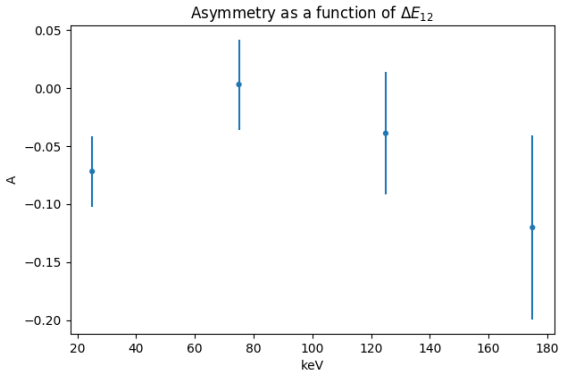

Figure 5.34: Asymmetry vs ΔE_{12} (Centered).

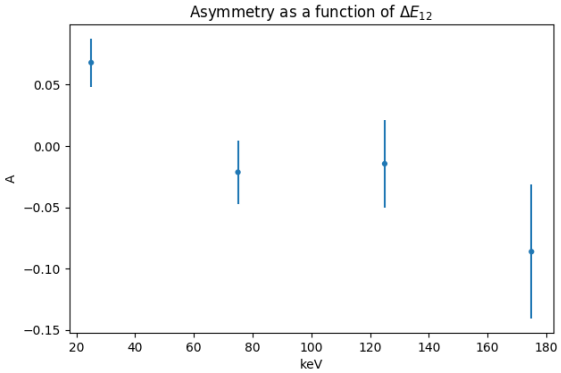

Figure 5.35: Asymmetry vs ΔE_{12} (Shifted).

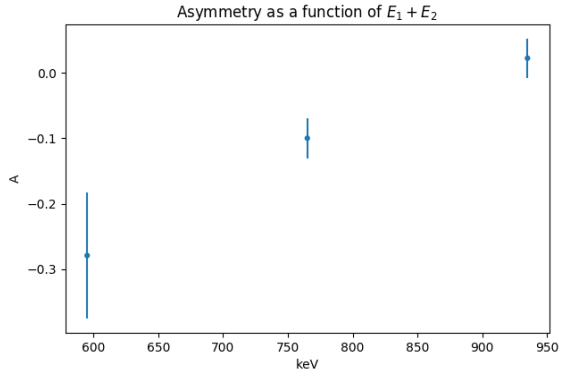

Figure 5.36: Asymmetry vs $E_1 + E_2$ (Centered).

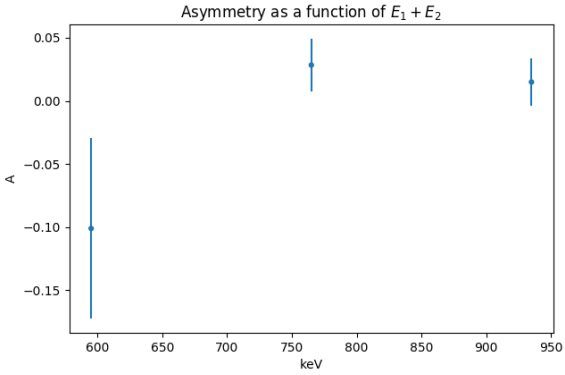

Figure 5.37: Asymmetry vs $E_1 + E_2$ (Shifted).

Figure 5.38: Asymmetry as a function of ΔE_{12} and $E_1 + E_2$

5.5.2 Timing Dependence

Additionally, we considered the possibility that the asymmetry may have some dependence on the timing parameters, including the hit times of the $\vec{k_1}$ and $\vec{k_2}$ gamma rays, the average of and difference between these hit times. Below, we plot the asymmetry as a function of these timing parameters. Figs 5.39 and 5.40 show the asymmetry as a function of the hit time of the $\vec{k_1}$ gamma ray and figs 5.41 and 5.42 show the asymmetry as a function of the hit time of the $\vec{k_2}$ gamma ray. In fig 5.39, one data point stands out between 300-400 ns, although it is not clear what would cause this. Additionally, the first two data points (< 200 ns), exhibit a statistically significant asymmetry, though again, the reason remains unclear. The first two data points in 5.41 also display a statistically significant asymmetry. No clear pattern emerges, however, across all plots that would point to an underlying cause of the asymmetry or justify further analysis cuts.

Figs 5.44 and 5.45 depict the asymmetry as a function of the average of the $\vec{k_1}$ and $\vec{k_2}$ hit times, whereas fig 5.46 and 5.47 display the asymmetry as a function of the difference between the $\vec{k_1}$ and $\vec{k_2}$ hit times. A statistically significant asymmetry in the first two data points of fig 5.44 appears between 0-200 ns.

Fig 5.46 has an asymmetry that appears with decreasing ΔT_{12}, whereas fig 5.47 shows no clear asymmetry as a function of ΔT_{12}. Overall, we observe no clear trends as a function of any of the timing parameters that hint at the underlying cause of the total asymmetry.

Although the asymmetry does fluctuate with the various timing parameters, we did not discern an obvious time-dependence from these plots. This motivated us to see if we could localize the asymmetry within the array by looking at the asymmetry as a function of z position and bar number, as in the following section.

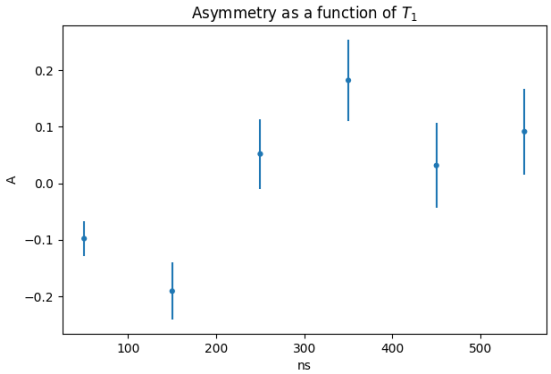

Figure 5.39: Asymmetry vs T_1 (Center).

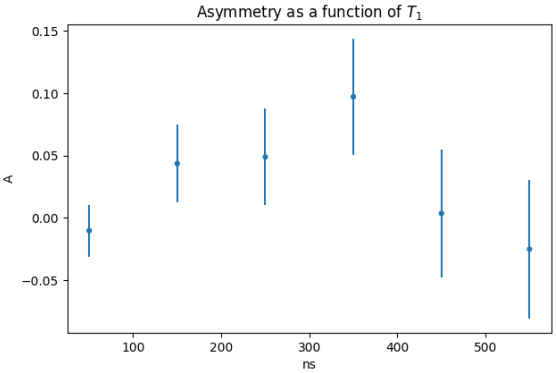

Figure 5.40: Asymmetry vs T_1 (Shift).

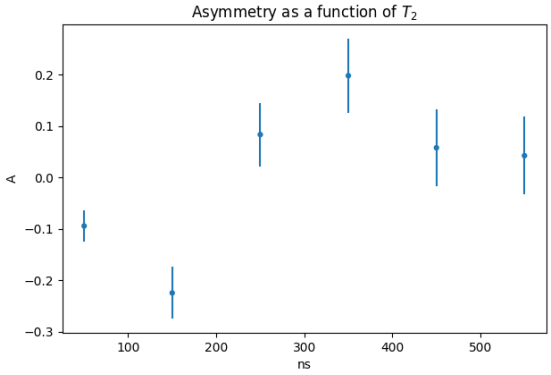

Figure 5.41: Asymmetry vs T_2 (Center).

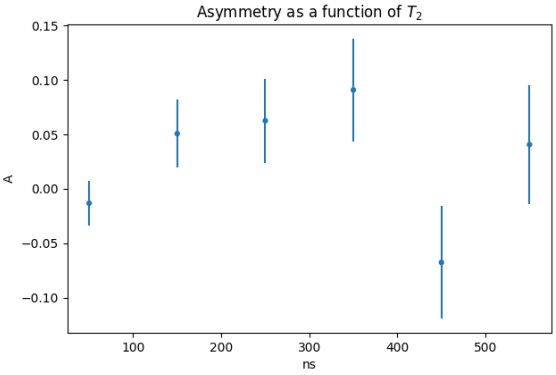

Figure 5.42: Asymmetry vs T_2 (Shift).

Figure 5.43: Asymmetry as a function of T_1 and T_2

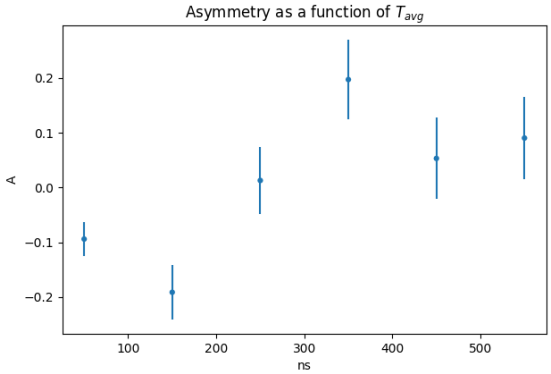

Figure 5.44: Asymmetry vs T_{avg} (Centered).

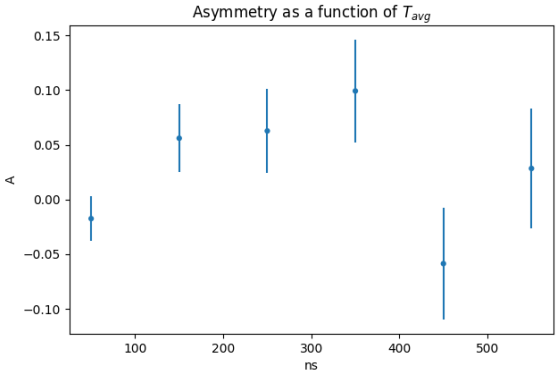

Figure 5.45: Asymmetry vs T_{avg} (Shifted).

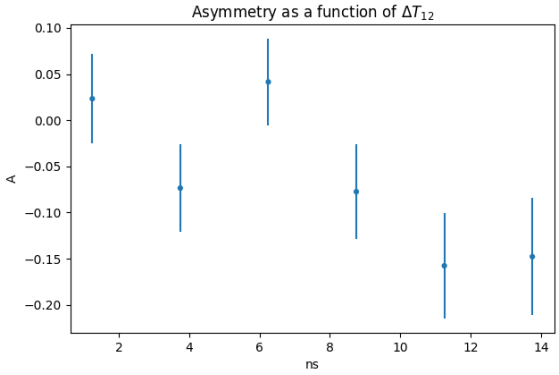

Figure 5.46: Asymmetry vs ΔT_{12} (Centered).

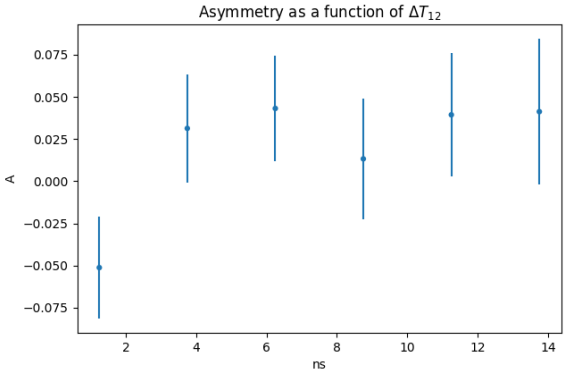

Figure 5.47: Asymmetry vs ΔT_{12} (Shifted).

Figure 5.48: Asymmetry vs Timing Parameters

5.5.3 Position Dependence

The physical location of gamma ray interactions within the APEX array should have no bearing on the asymmetry term. Should such a correlation exist, it might point to experimental systematics. The first test we ran checked if the asymmetry term varied as a function of the z position. We plotted the asymmetry as a function of z_1 and z_2, the z position of the $\vec{k_1}$ and $\vec{k_2}$ gamma ray interactions, respectively. A z-dependent asymmetry parameter might indicate issues along the length of the bar. Figs 5.49 and 5.50 show the asymmetry as a function of z_1 (with centered and shifted data sets, respectively), and figs 5.51 and 5.52 show the asymmetry as a function of z_2 (with the centered and shifted data sets, respectively). As a reminder, these plots were generated using 'Calibration Function 1' only, which, by definition, restricts the z position range to between -5 and 5 cm. Overall, a net asymmetry appears to exist independent of the z position, and so this does not preclude issues related to other dimensions of the array, such as problems with individual bars or specific DAQ channels.

With this in mind, we looked for an association between the asymmetry and calibration functions described in Table 3.2. A relationship between the asymmetry and the calibration functions could indicate an issue with the calibration. One possibility is that certain calibration functions are more susceptible to the effects of noise near threshold. For example, noise might dominate events with only three viable channels as opposed to four. In principle, the noise should cancel when the source holder is flipped 180°, unless the noise is time-dependent. Time-dependent noise could generate a fake asymmetry in which A_F does not negate A_B.

For the full analysis (the first entry in Table 5.2), we used all of the calibration functions described in Table 3.2 to determine the energy of the interactions. A histogram showing the number of events which fall into each category of calibration function can be seen in fig 5.56. 21% of all interactions events are determined via calibration functions 1-5 (4 channel events). The remaining 79% of events use other calibration functions, which may warrant investigation.

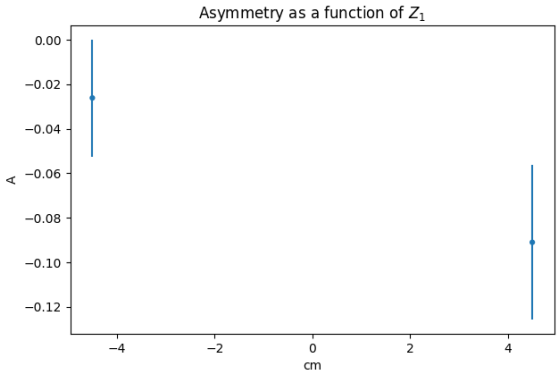

Figure 5.49: Asymmetry vs Z_1 (Centered).

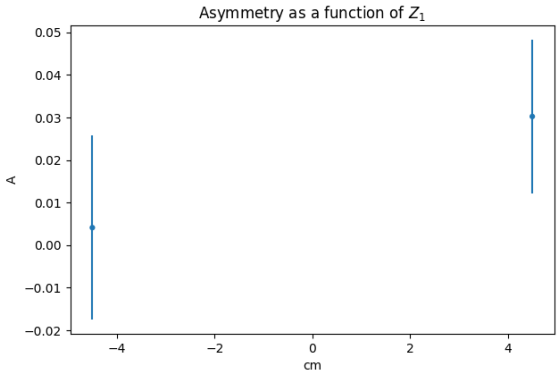

Figure 5.50: Asymmetry vs Z_1 (Shifted).

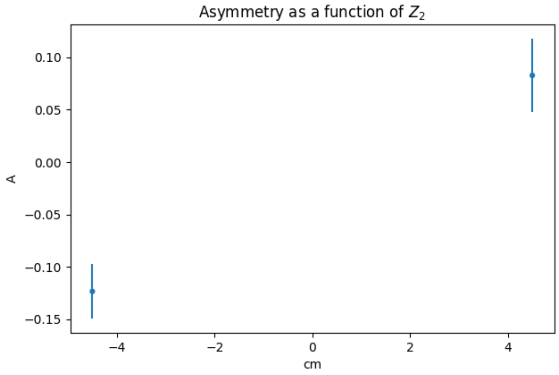

Figure 5.51: Asymmetry vs Z_2 (Centered).

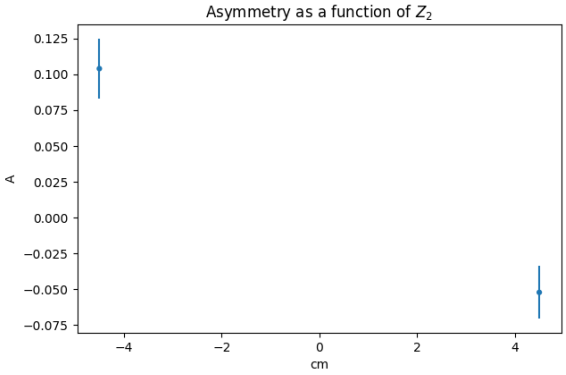

Figure 5.52: Asymmetry vs Z_2 (Shifted).

Figure 5.53: Asymmetry vs Z Parameters

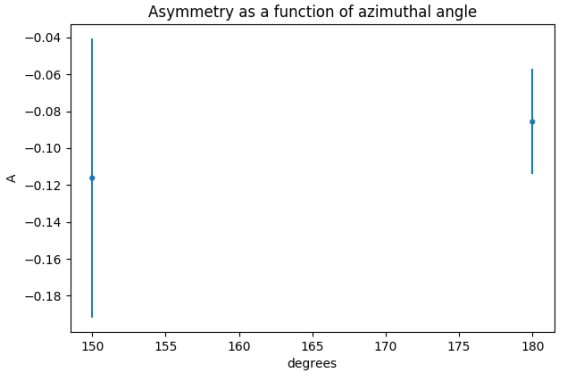

Figure 5.54: Asymmetry vs α (Centered).

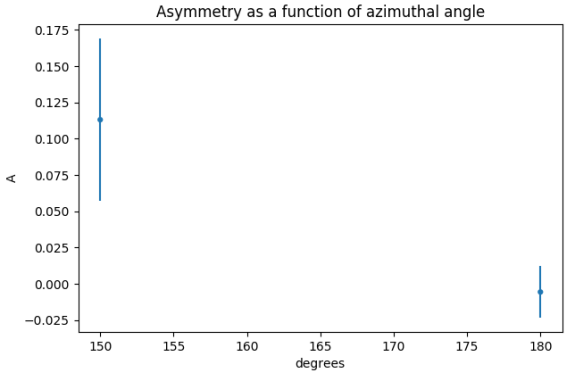

Figure 5.55: Asymmetry vs α (Shifted).

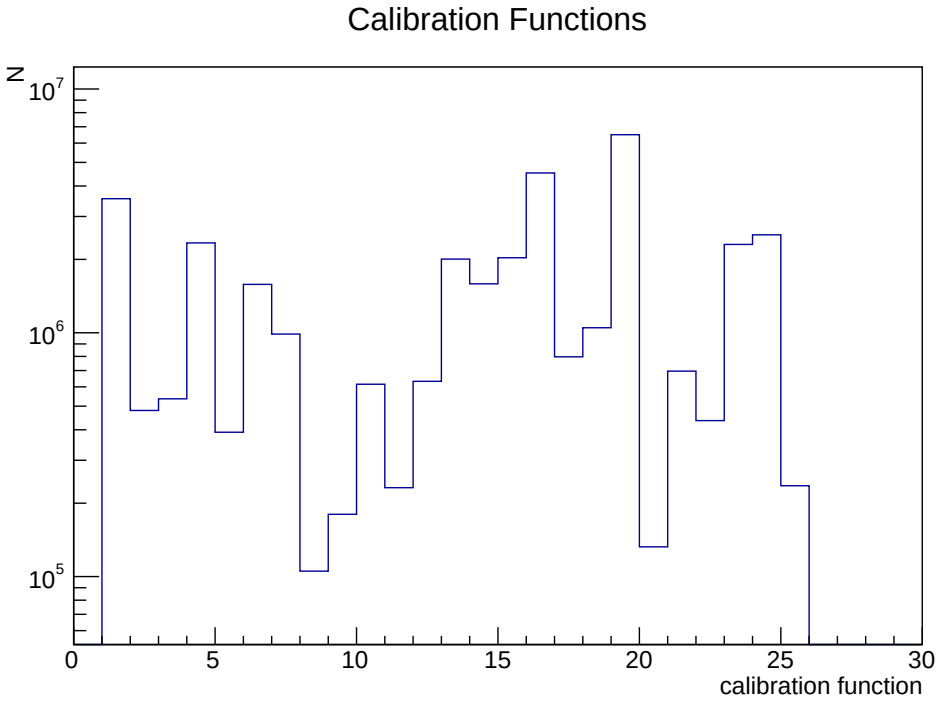

Figure 5.56: Histogram of the number of calibration functions used in the analysis.

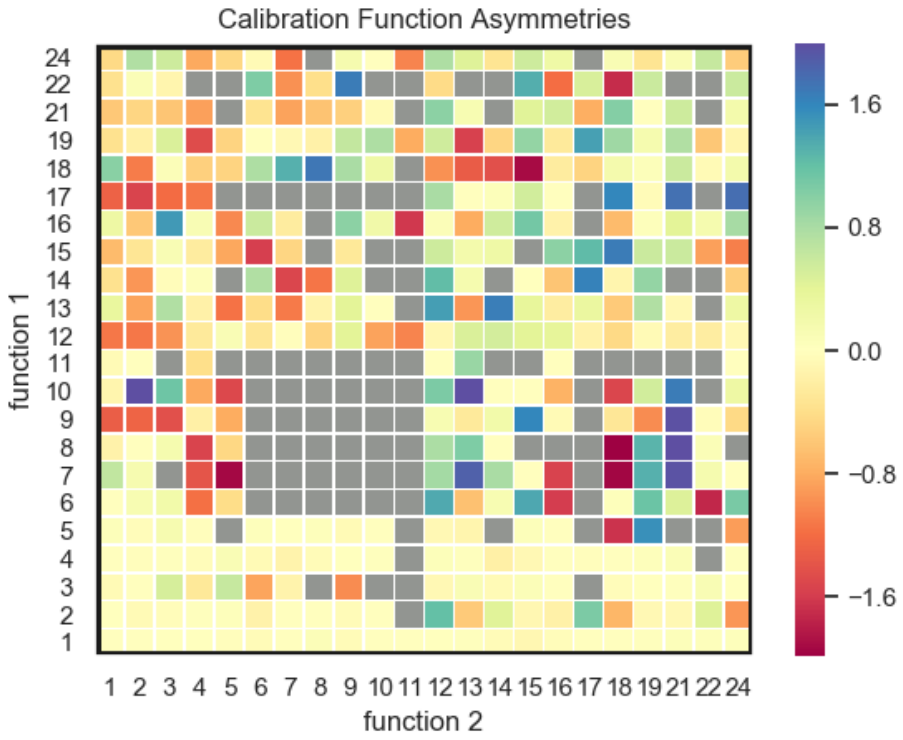

Figure 5.57: Calibration functions for $\vec{k_1}$ and $\vec{k_2}$. The numbers on the x and y axes correspond to the functions from the plot in Table 3.2. Gray patches mean there was no data from those calibration functions after all of the analysis cuts had been applied.

We plotted the asymmetry as a function of the calibration functions used to determine the energies for $\vec{k_1}$ and $\vec{k_2}$. Fig 5.57 is a 2D representation of the asymmetry versus the $\vec{k_1}$ ("function 1") and $\vec{k_2}$ ("function 2") calibration functions. A true asymmetry would exist at the same level (within the statistical uncertainty), regardless of the calibration function that is used. It is clear from fig 5.57 that larger asymmetries exist for calibration functions greater than 5. These are our three- and two-channel events. To determine whether or not an asymmetry is uniformly distributed amongst the calibration functions, we also generated a 1D histogram of all of the asymmetries represented in the 2D plot. This can be seen in fig 5.58. While there are a few outliers, there also appears to be an overall systematic shift. Therefore, identifying the source of the asymmetry is more than a matter of troubleshooting individual calibration functions.

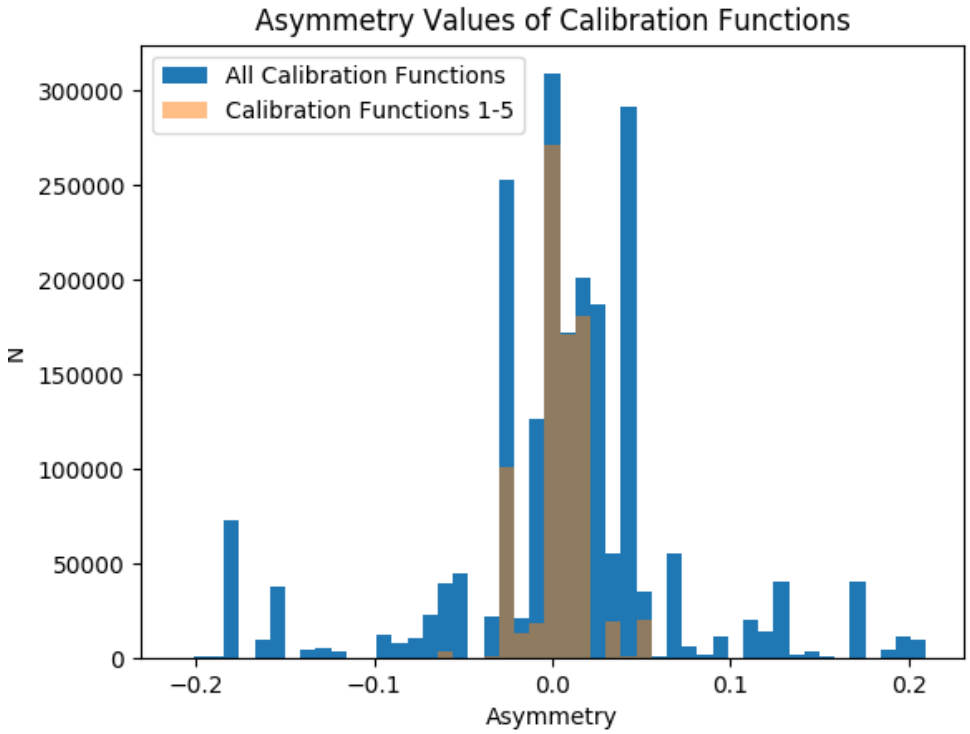

Figure 5.58: Histogram showing the asymmetry values as a function of the $\vec{k_1}$ and $\vec{k_2}$ calibration functions. An overall shift in the positive or negative direction of this histogram would provide more evidence to support the idea that we are seeing a true CPT-violating asymmetry. Outliers in either direction would lend support to the idea that the asymmetry we are seeing derives from a unidentified systematic.

We used a similar approach to investigate if individual NaI(Tl) bars were causing the asymmetry. One could imagine that defects in the NaI(Tl), issues with PMTs, or noise pertaining to specific DAQ channels may unequally affect certain bars and therefore cause a fake asymmetry. Again, any true signal would present itself in all of the bars at the same level (within the statistical uncertainty). Fig 5.59 shows a 2D plot of the asymmetry as a function of the two bars in which $\vec{k_1}$ and $\vec{k_2}$ are detected. In this plot, the asymmetry is calculated for each pair of bars, call them a and b, which have a fixed orientation relative to each other in the array. Suppose that when $\vec{k_1}$ interacts in bar a and $\vec{k_2}$ interacts in bar b (call this (a,b)), $\left(\vec{S}\cdot\vec{k_1}\times\vec{k_2}\right)$ is positive, contributing to N_+ in our asymmetry calculation. The corollary of this is that when $\vec{k_1}$ interacts in bar b and $\vec{k_2}$ bar interacts in bar a (call this (b,a)), the handedness is flipped, and so $\left(\vec{S}\cdot\vec{k_1}\times\vec{k_2}\right)$ is negative, contributing to N_- is our asymmetry calculation. For a given pair of bars, we tally the N_+ and N_- events, then calculate the asymmetry. We plot this asymmetry in fig 5.59 as a function of a and b, where the asymmetry is identical for points (a,b) and (b,a). We also calculate the 1D histogram of the asymmetries shown in fig 5.59 to determine whether or not there is a net asymmetry that is uniformly distributed throughout the bars. This can be seen in fig 5.60. While we did observe an overall shift in the asymmetry, we do not believe this is proof of CPT-violation in the absence of other evidence.

Our search for the underlying cause of the observed asymmetry was more thorough than discussed in this section. In addition to the above plots, we generated diagnostic plots of all cut parameters for several more data sets. These include data using 'Calibration Function 1' only (entries 10 and 11 in 5.2) and, separately, data using '4 bar events' only (entries 4 and 5 in 5.2). We also included the asymmetry diagnostic plots for the least stringent set of cuts (entries 2 and 3 in Table 5.2). These plots can be found in the appendix.

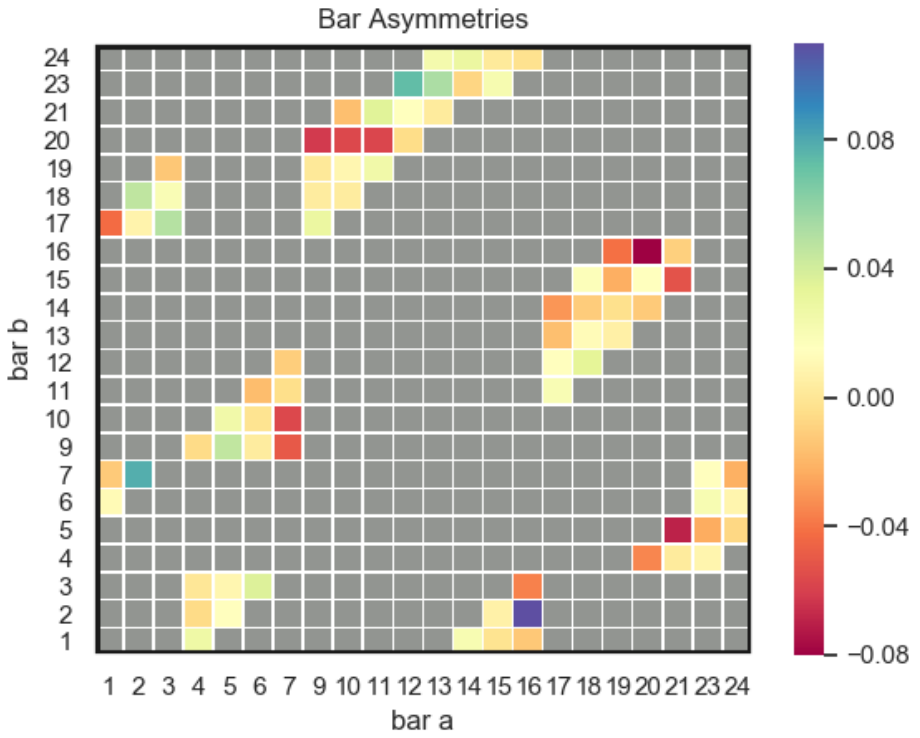

Figure 5.59: Asymmetries as a function of the two bars. There is no correspondence between the axes and the gamma ray associated with the bar. Rather, this plot is meant to show asymmetries associated with pairs of bars. The asymmetry for $\vec{k_1}$ interacting in bar 9 and $\vec{k_2}$ interacting in bar 13 is the same as the asymmetry for $\vec{k_2}$ interacting in bar 9 and $\vec{k_1}$ interacting in bar 13, for example. Gray patches are bar combinations that were excluded due to cuts on the azimuthal angle.

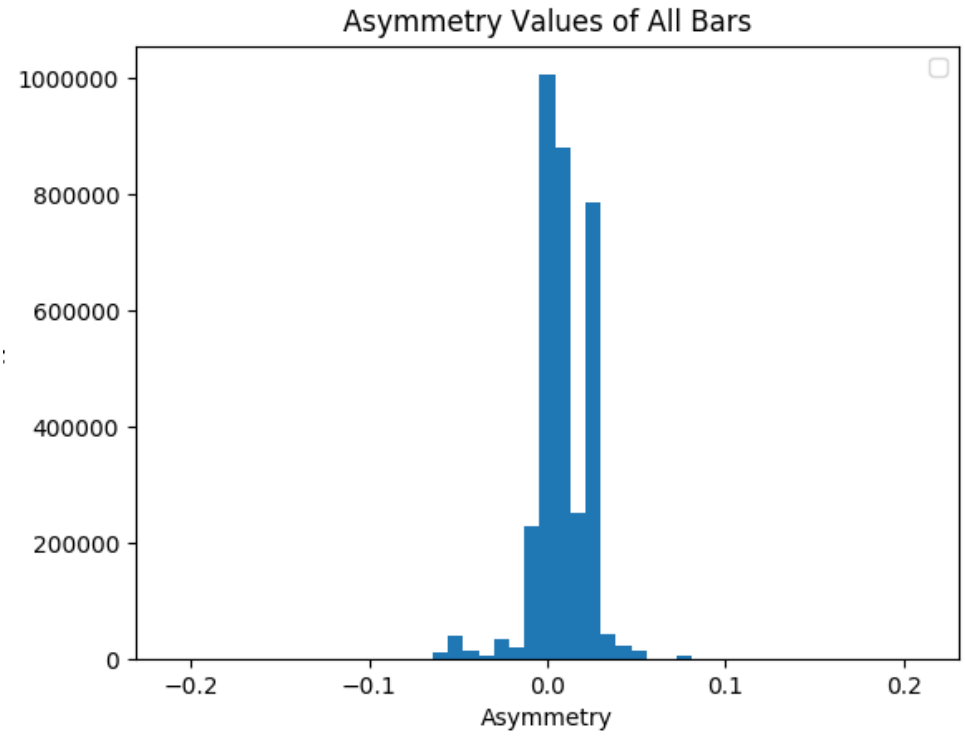

Figure 5.60: Histogram of all asymmetry values for different pairs of bars. Again, a net shift in the direction of this histogram may be indicative of a true asymmetry, when considered with other factors. An overall shift in the positive or negative direction of this histogram would provide more evidence to support the idea that we are seeing a true CPT-violating asymmetry. Outliers in either direction would lend support to the idea that the asymmetry we are seeing derives from a unidentified systematic.While we see an overall shift in the positive direction, this would have to exist in the context of other evidence for a real CPT-violating asymmetry.

5.6 Sensitivity Overview

In calculating our limit, we must consider several effects that reduce our overall sensitivity. These effects include a reduction in our sensitivity due to background, and the fact that not all of the o-Ps is polarized along the positive z-axis. In this section, we calculate the CPT-violating amplitude, C, which is equal to our raw asymmetry value multiplied by a factor that accounts for our limitations in sensitivity. In doing so, we set a limit on the CPT-violating amplitudes, C_1, as was presented by [1].

5.6.1 Sensitivity Corrections

First, our sensitivity is diminished by the fact that not all o-Ps have their spin oriented perfectly in the z-direction. A number of factors contribute to fact that we cannot guarantee perfect alignment of the spin for all o-Ps events. First, not all of the positrons from the ^{22}Na are aligned along the z-direction immediately upon emission. According to the V-A theory of weak interactions, the polarization of the positrons is related to their velocity by $\langle P \rangle = \frac{\langle v \rangle}{c}$ [110]. For positrons emitted by ^{22}Na, 67% of the positrons are polarized along the z-axis [1]. Additionally, some of the positrons are somewhat depolarized as they interact in the aerogel; approximately 90% of the positrons stay polarized in the z-direction [1] [110]. Of the fraction of positrons that retain a z-axis polarization, only a subset of them transfer

Percent polarized along z upon emission	67%±1%
Percent unaffected by aerogel interactions	90%±1%
Percent that transfer polarization to o-Ps	67%±1%
Percent that are emitted in $+z$ direction	50%±5%

Table 5.3: List of effects that impact the percentage of o-Ps events that retain z spin polarization.

that same polarization on to the o-Ps (67%) [1]. The magnitude of the source polarization is further minimized because we are only accepting positrons oriented in the $+z$ direction within a solid angle of 2π [1], as the aerogel is flush against only one side of the source. The product of these values gives the factor by which we must scale our uncertainty, resulting in an overall reduction in sensitivity by a factor of 5.00 ± 0.02. A list of these factors is outlined in Table 5.3.

Next, we must consider the impact of our background on our sensitivity. In an ideal case, the true asymmetry, A_T, would consist of a pure sample of o-Ps events, and could be written as:

$$A_T = \frac{N_{T+} - N_{T-}}{N_{T+} + N_{T-}}, \tag{5.3}$$

where N_{T+} is the number of true o-Ps events for which $(\vec{S}\cdot\vec{k_1}\times\vec{k_2})$ is positive and N_{T-} is the number of true o-Ps events for which $(\vec{S}\cdot\vec{k_1}\times\vec{k_2})$ is negative. With our background, our sensitivity to the asymmetry is reduced. The measured asymmetry term, A_M, is then actually:

$$A_M = \frac{N_{T+} - N_{T-} + N_{B+} - N_{B-}}{N_{T+} + N_{T-} + N_{B+} + N_{B-}}. \tag{5.4}$$

This can be simplified as:

$$A_M = \frac{N_T A_T - N_B A_B}{N_{total}}, \tag{5.5}$$

where N_T is the total number of o-Ps events, A_T is the asymmetry due to only o-Ps events, N_B is the total number of background events, A_{BG} is the asymmetry due to only background events, and N_{total} is the total number of o-Ps plus background events. Solving for A_T, we obtain:

$$A_T = \frac{A_M N_{total} + A_{BG} N_B}{N_{total} - N_B}. \tag{5.6}$$

We know that $N_B = f_B * N_{total}$, where f_B is the fraction of the events that are background due to pile-up. We estimate this fraction by comparing our o-Ps data set to a run with a ^{22}Na button source. We estimate this fraction to be 15% by integrating the number of events in the 'background' region (from 600-1200 ns), as compared to the number of events in the 'signal' regions (from 20-600 ns).

This means that our true o-Ps asymmetry is actually:

$$A_T = \frac{A_M N_{total} + 0.15 A_{BG} N_{total}}{0.85 N_{total}}. \tag{5.7}$$

We calculate A_{BG} using the same events that pass our analysis cuts, in our regular analysis, save the timing cut. Instead, we place a timing cut such that the average of the $\vec{k_1}$ and $\vec{k_2}$ hit times is between 600 and 1200 ns. This data is exclusively background data, and the time interval is approximately of the same length. We present a table in the same style as Table 5.2, in which we calculate the asymmetry parameters for the same subsets of data, this time using the 'background' data (data with average hit times between 600-1200 ns). Inserting these values into equation 5.7, we see that the reduction in sensitivity as a result of any asymmetry present in the background data is very small. We therefore can assume that the contribution of A_{BG} to the asymmetry is negligible, and the measured asymmetry need only be scaled by a factor of $\frac{1}{0.85}$, or 1.18 to obtain the true asymmetry to account for pile-up. We estimate the error on this value to be no more than 10%.

Because our energy resolution is limited, the $\vec{k_1}$ and $\vec{k_2}$ energies sometimes flip in our reconstruction. One can calculate how this affects the asymmetry parameter as follows. The asymmetry can be written in terms of the number of 'good' events, in which the energies of $\vec{k_1}$ and $\vec{k_2}$ gamma rays are reconstructed such that the ordering is correct, N_g, and the number of 'bad' events, in which the energies of the $\vec{k_1}$ and $\vec{k_2}$ gamma rays are reconstructed such that the ordering is incorrect, N_b. These events can be further split into N_{g+}, or 'good' events that yield $(\vec{S}\cdot\vec{k_1}\times\vec{k_2})$ positive, and N_{g-}, or 'good' events that yield $(\vec{S}\cdot\vec{k_1}\times\vec{k_2})$ negative. Similarly, the 'bad' events can be split into N_{b+} and N_{b-}. This means that our

Data Set	A_F	A_B	A_{BG}
Centered All Data	-0.0322±0.0035	-0.0389±0.0034	0.0067±0.0024
Shifted All Data	-0.0250±0.0026	-0.0305±0.0026	0.0055±0.0018
Net All Data	-0.0276±0.0021	-0.0336±0.0020	0.0060±0.0015
Centered (4 bar only)	-0.0074±0.0110	-0.0258±0.0106	0.0183±0.0076
Shifted (4 bar only)	-0.0085±0.0086	-0.0181±0.0087	0.0096±0.0061
Net (4 bar only)	-0.0081±0.0068	-0.0212±0.0067	0.0131±0.0048
Centered Calibration Function 1	-0.0681±0.0163	-0.0626±0.0159	-0.0055±0.0114
Shifted Calibration Function 1	-0.0606±0.0100	-0.0524±0.0102	-0.0081±0.0071
Net Calibration Function 1	-0.0626±0.0085	-0.0554±0.0086	-0.0072±0.0061
Centered (4 bar only) Calibration Function 1	-0.0546±0.0523	-0.0386±0.0491	-0.0160±0.0358
Shifted (4 bar only) Calibration Function 1	-0.0881±0.0330	-0.0817±0.0339	-0.0064±0.0236
Net (4 bar only) Calibration Function 1	-0.0786±0.0279	-0.0678±0.0279	-0.0108±0.0197

Table 5.4: This table delineates the asymmetries as measured using the background data, decoupled in the same sense as Table 5.2.

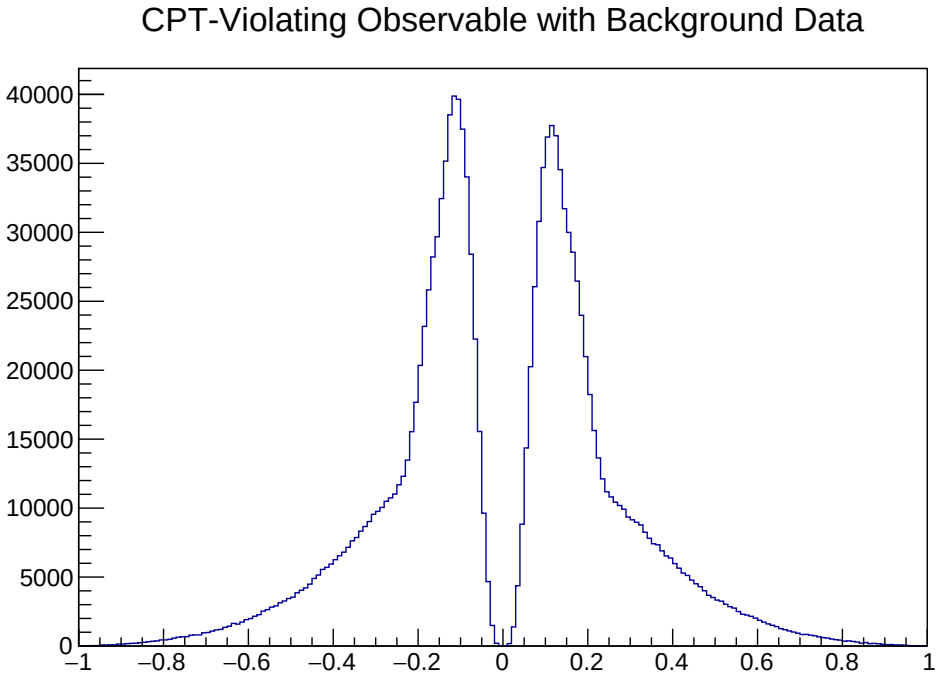

Figure 5.61: The CPT-violating asymmetry term computed using background-only data.

total, measured asymmetry, A_M, can be written as:

$$A_M = \frac{N_{g+} - N_{g-} + N_{b+} - N_{b-}}{N_{g+} + N_{g-} + N_{b+} + N_{b-}}, \tag{5.8}$$

which can be rewritten as:

$$A_M = \frac{N_{g+} + N_{b-} - (N_{g-} + N_{b+})}{N_{g+} + N_{g-} + N_{b+} + N_{b-}.} \tag{5.9}$$

If there is some fraction of 'good' events that yield $(\vec{S}\cdot\vec{k_1}\times\vec{k_2})$ positive, then we can rewrite N_{g+} in terms of this probability, p, times the total number of $(\vec{S}\cdot\vec{k_1}\times\vec{k_2})$ positive events, and likewise for N_{b-}. Therefore, our asymmetry term can be written as:

$$A_M = \frac{pN_+ + (1-p)N_- - pN_- - (1-p)N_+}{N_+ + N_-}. \tag{5.10}$$

Grouping terms, we get:

$$A_M = \frac{(2p-1)N_+ - (2p-1)N_-}{N_+ + N_-}. \tag{5.11}$$

Therefore, the true asymmetry can be written in terms of the measured asymmetry as:

$$A_M = (2p-1)A_T, \tag{5.12}$$

where

$$A_T = \frac{N_+ - N_-}{N_+ + N_-}. \tag{5.13}$$

And so, to obtain the true asymmetry, we must multiply our measured asymmetry by a factor of $\frac{1}{2p-1}$. Using our data, we determined the number of events for which $(\vec{S}\cdot\vec{k_1}\times\vec{k_2})$ is positive and the number of events for which $(\vec{S}\cdot\vec{k_1}\times\vec{k_2})$ is negative for each pair of bars in our array. We fed this information and the energy resolution to a simulation to calculate the value for p. We determined that the finite detector resolution diminishes our sensitivity by a factor of about 1.5±0.15. A plot showing the number of events for each bar combination that yields $(\vec{S}\cdot\vec{k_1}\times\vec{k_2})$ positive (negative) can be seen in fig 5.62 (fig 5.63). These plots were used to weight the bars according to their contribution to the asymmetry in order to determine the value for p.

To calculate the CPT-violating amplitude, we must multiply our raw asymmetry term by the factor of 5.00±0.02×1.5±0.15×1.18±0.12 = 8.85±0.14, accounting for the spin-polarization sensitivity reduction, the background sensitivity reduction, and the energy resolution sensitivity reduction. The results are displayed in Table 5.5. These results can be directly compared to the CPT-violating amplitudes (with a weighting factor of one) set in [1]. Despite numerous attempts to isolate the source of the asymmetry, we are left questioning its origins. If the asymmetry is a result of CPT-violation in o-Ps, it would contradict Vetter's result, which measured no CPT-violation at the level of 0.0026±0.0031 [1]. This

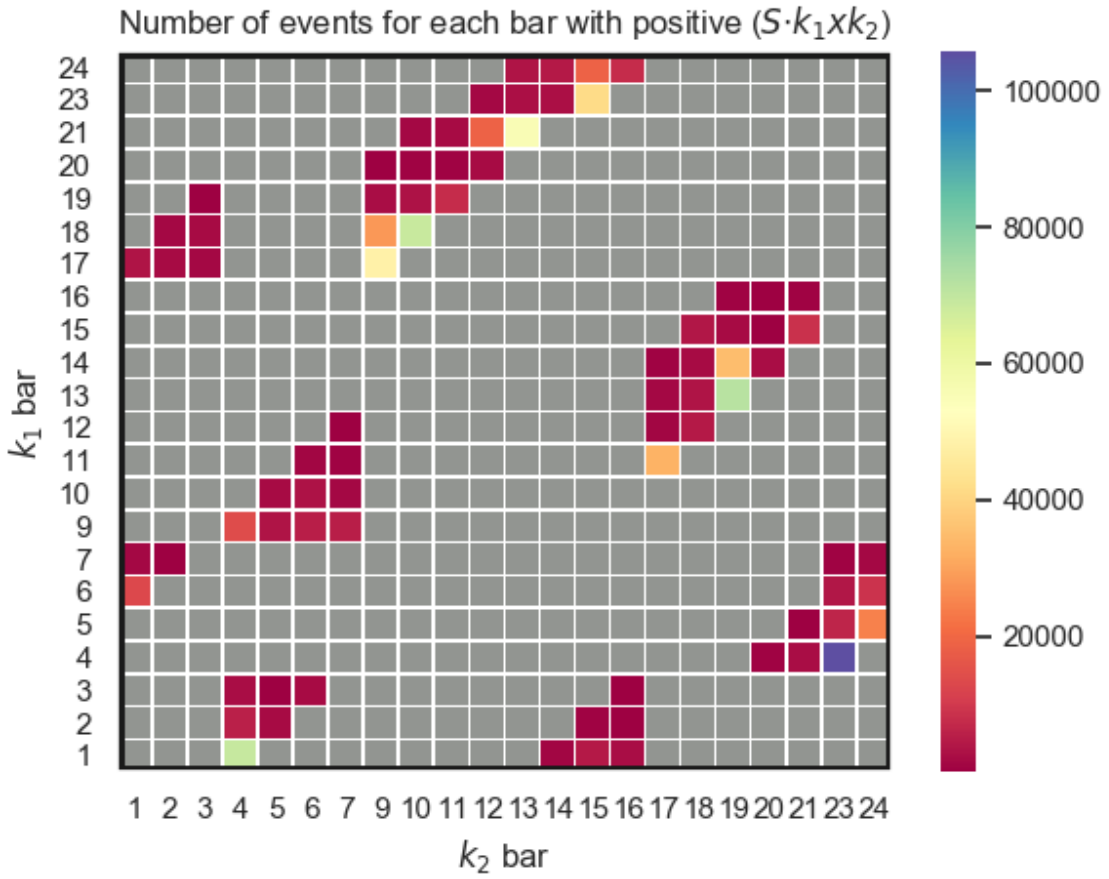

Figure 5.62: Number of events for the bars associated with $\vec{k_1}$ and $\vec{k_2}$ that yield a positive CPT-violating observable term, $(\vec{S} \cdot \vec{k_1} \times \vec{k_2})$. This information was used to weight the bars according to their contribution to our overall measurement. This is how we calculated p, which determines the probability that we swap $\vec{k_1}$ and $\vec{k_2}$.

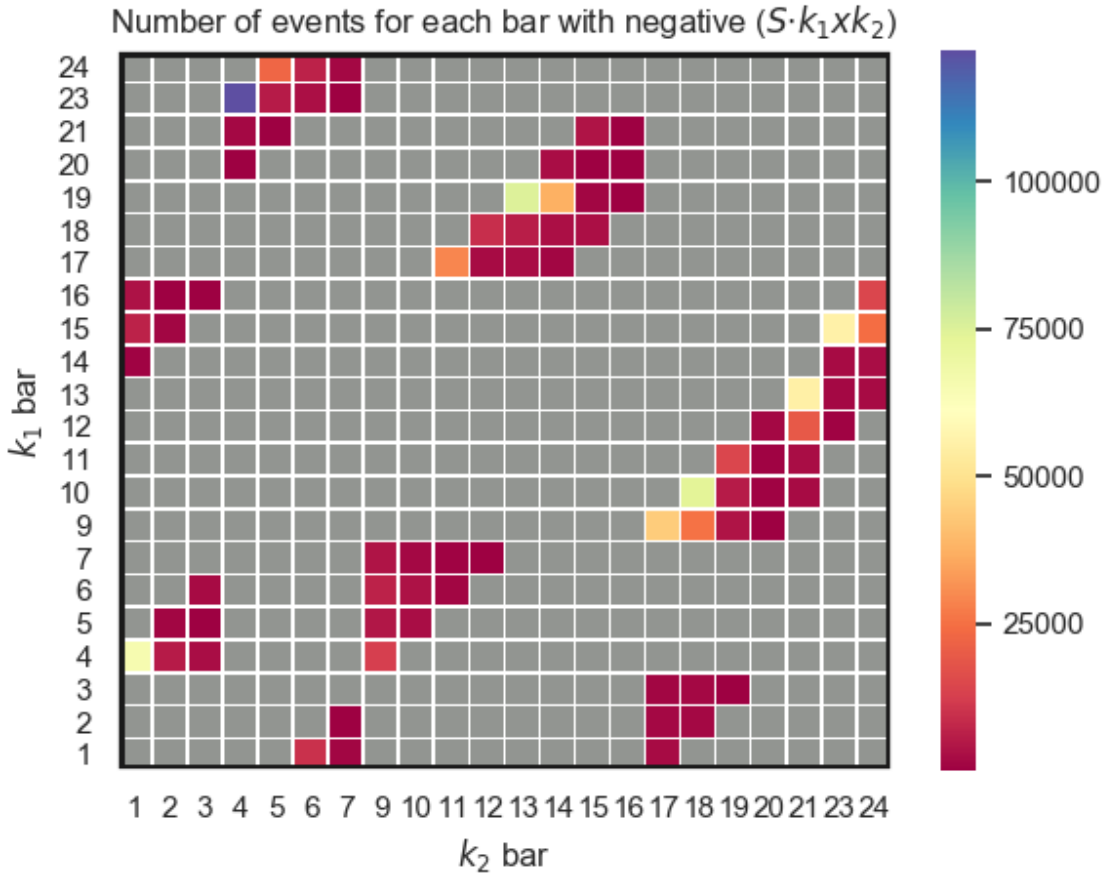

Figure 5.63: Number of events for the bars associated with $\vec{k_1}$ and $\vec{k_2}$ that yield a negative CPT-violating observable term, $(\vec{S} \cdot \vec{k_1} \times \vec{k_2})$. This is how we calculated p, which determines the probability that we swap $\vec{k_1}$ and $\vec{k_2}$.

is certainly a possibility that we cannot rule out, but a much more extensive series of tests would be required to make such a claim. One observation suggests that the asymmetry is in fact, a systematic error: the most stringent set of cuts in Table 5.2 (the final entry) results in an asymmetry that is consistent with zero. It is also important to note that, for some subsets of the data, our result also contradicts the result by Ref [87], which set a limit at the 2.3% level in searching for CPT-violation in o-Ps.

In the next chapter, we identify several improvements and address further lines of inquiry that could be made regarding the asymmetry we observed.

Data Set	C_1
Centered All Data	-0.0053±0.0080
Shifted All Data	0.0628±0.0062
Net All Data	0.0416±0.0053
Centered (4 bar only)	-0.0336±0.0372
Shifted (4 bar only)	-0.0593±0.0319
Net (4 bar only)	-0.0487±0.0234
Centered Calibration Function 1-5	-0.0089±0.0124
Shifted Calibration Function 1-5	-0.0071±0.0160
Net Calibration Function 1-5	0.0221±0.0097
Centered Calibration Function 1	0.0283±0.0363
Shifted Calibration Function 1	-0.0779±0.0230
Net Calibration Function 1	-0.0416±0.0195
Centered (4 bar only) Calibration Function 1	-0.4416±0.0186
Shifted (4 bar only) Calibration Function 1	0.1496±0.1230
Net (4 bar only) Calibration Function 1	-0.0257±0.1027

Table 5.5: This table presents our calculation of C_1, our CPT-violating amplitude, which is directly comparable to the result presented in ref. [1]. C_1 has a weighting factor of one.

CHAPTER 6: Conclusion

6.1 Suggestions for Future Improvement

There are a number of intriguing paths that, if pursued, could help us resolve the questions that arise from our measurement. In this chapter, we highlight several aspects of CALIOPE that warrant further study. Of highest importance is to understand the source of the observed asymmetry. In order to claim evidence of CPT-violation, there are a number of possibilities that would need to be eliminated. There are already a number of clues that point to an unidentified systematic as the cause of this asymmetry. The most salient of such clues is the fact that there are as-yet unexplained outliers in the plots of the asymmetry as a function of various parameters. These would need to be better characterized and understood before making any claims of CPT-violation.

We demonstrated in our Monte Carlo simulation that it is possible to fabricate a false asymmetry when there is an azimuthal gradient in the bar thresholds with the source oriented in one direction only. The propensity to generate a fake asymmetry would likely be compounded by the fact that the thresholds also vary as a function of the z position for individual bars. This would mean that even small displacements in the x, y, and z position of the carbon fiber tube between source flips could induce a fake asymmetry, since A_F and A_B would no longer cancel. Though care was taken to align the carbon fiber tube with respect to APEX, we estimate that the offset could be, at worst 1 cm in the x direction due to jostling of the aluminum channel at the top of the array between source flips. Furthermore, it is possible that the z position was off by, at most, 0.5 cm, especially for data acquired with the source shifted towards the front of the array. This configuration necessitated pulling the carbon fiber tube forward by 14 cm and measuring that distance with a ruler. During

this process, we noted that it was also possible to compress the tube somewhat and so the measured distance could vary depending on the tension in the tube. Other refinements to the simulation would likely be beneficial, such as better characterizing bar thresholds and simulating the effect of pile-up.

In earlier chapters, we explained several challenges to performing the energy calibration and reconstruction with the APEX array. It is possible there are better approaches that may enable us to improve our energy resolution. Furthermore, experimenting with alternative techniques may reveal problems with our current method. Identifying the root cause of the large asymmetries in calibration functions 6-24 would be a good starting point. One possibility is that there is a time-dependent noise source that disproportionately impacts these calibration functions. A time-dependent noise source would cause a fake asymmetry if it varied on a timescale of weeks, which is how frequently we rotate the source holder.

The energy reconstruction could be further improved by developing a more robust understanding of individual detector thresholds. We have shown in previous chapters that we have reason to believe our nonzero front and back asymmetry parameters, A_F and A_B, are a result of varying detector thresholds that break the azimuthal symmetry. Minimizing this effect may enable us to improve the overall measurement. Furthermore, it would be worthwhile to perform the energy calibration with finer discretization of the NaI(Tl) bars, as it would enhance our sensitivity. The difficulty here lies in the fact that this would entail fitting several thousand histograms, a process which we were not able to automate easily due to noise at low energies. This is partially attributable to the fact that we split each PMT signal into high and low gain channels. In addition to complicating the analysis, it cut the signal in half and diminished our sensitivity to low energy gammas. As a result, we had to run the PMTs very close to or at their maximum operating voltages. This likely exacerbated nonlinear effects near the ends of the NaI(Tl) bars. Previous APEX users [93] did not split the signal, and were therefore able to efficiently automate this process.

A number of adjustments to the physical DAQ would help improve our overall sensitivity,

but would require more resources. First, we faced several issues pertaining to the TDC. Notably, we were limited by the fact that we did not have enough TDC channels to connect both front and back PMTs to the TDC. This effectively cut our number of statistics in half. A second TDC would enable us to provide all PMTs with a TDC channel. Additionally, the TDC timing spectra exhibited unexpected features. In the absence of other PMT data, a single PMT should register a single, sharp peak. Instead, we observed the appearance of multiple peaks in the timing spectrum, which seems to be indicative of issues related to impedance matching. A likely source of this problem is the connectors to our delay boards. While we do not see an obvious way that this could create a fake asymmetry, it would be worth adjusting, as it likely cuts into our sensitivity by creating a number of events that are discarded from the analysis. An alternative option to the TDC adjustments would be to use digitizers in lieu of TDCs and QDCs. This was an idea that we considered briefly in 2014, going so far as to demonstrate the feasibility of timing and energy reconstruction techniques using digitizers with the APEX array. Digitizers would enable us to retain information about the shape of the waveform and therefore potentially perform a more thorough analysis. This would likely enhance our sensitivity, but it would have to be reconciled with the higher electronics cost.

It may also be worthwhile to keep the approaches of the previous such searches in mind. For example, it would be interesting to perform the experiment with ^{68}Ge, as achieved in [1]. As discussed in [1], a true CPT-violating signal would scale differently with the different sources. While the complex geometry of the Gammasphere partially motivated their use of an alternative source, it is possible that our experiment may still benefit from this extra check. Moreover, tagging on the positron with scintillator as it is emitted by the ^{22}Na could potentially be advantageous, as it may reduce some of the background. This would require some modifications to the source holder, including space for plastic scintillator between the kapton foil and aerogel as well as some sort of feed-through for optical fiber. An external PMT would need to be incorporated into the DAQ which would serve as our start signal.

6.2 Concluding Remarks

CPT-symmetry is a well-established feature of the Standard Model and any indication of its violation would have profound ramifications in particle physics community. In undertaking a search for CPT-violation, we are cognizant of the fact that previous searches have turned up empty-handed. At our current level of sensitivity, a discovery of CPT-violation would be inconsistent with previous searches. Therefore, a comprehensive analysis of all systematics must be developed before making any claims.

In conclusion, we have conclusively identified o-Ps using the APEX array, demonstrating that tagging on the 1.27 MeV gamma ray is a viable technique for detecting o-Ps. In addition, we have shown that a search for CPT-violation in o-Ps is feasible, but would require extended systematics studies to be competitive with previous searches.

APPENDIX: ASYMMETRY DIAGNOSTIC PLOTS

Here we present extra asymmetry diagnostic plots that were not included in the thesis. Figs 5.30-5.55 show the asymmetry plotted as a function of various cut parameters, using only calibration function 1 (but both 3 and 4 bar events).

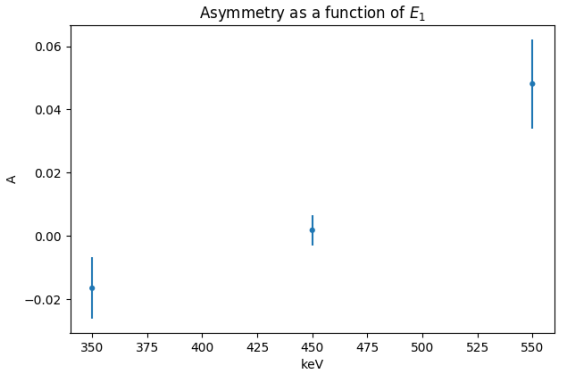

Figure 1: Asymmetry vs E_1 (Center).

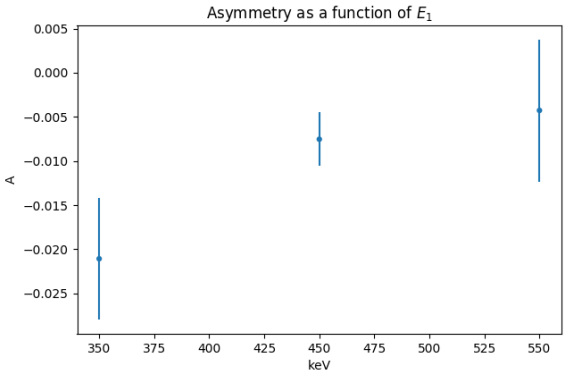

Figure 2: Asymmetry vs E_1 (Shift).

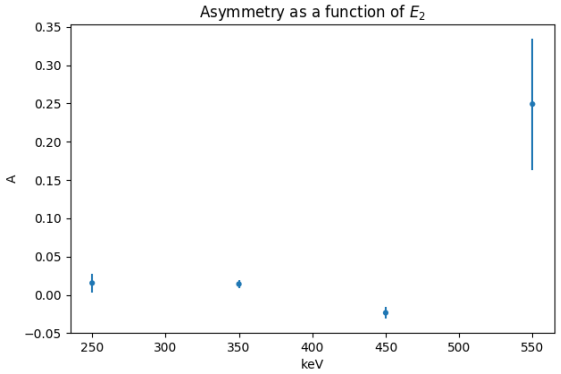

Figure 3: Asymmetry vs E_2 (Center).

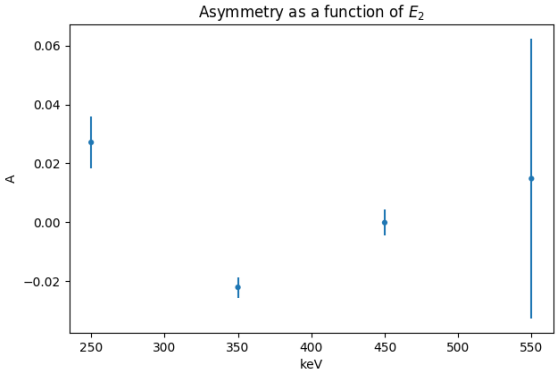

Figure 4: Asymmetry vs E_2 (Shift).

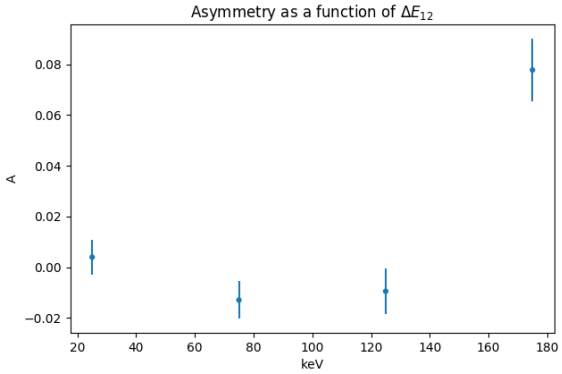

Figure 5: Asymmetry vs ΔE_{12} (Centered).

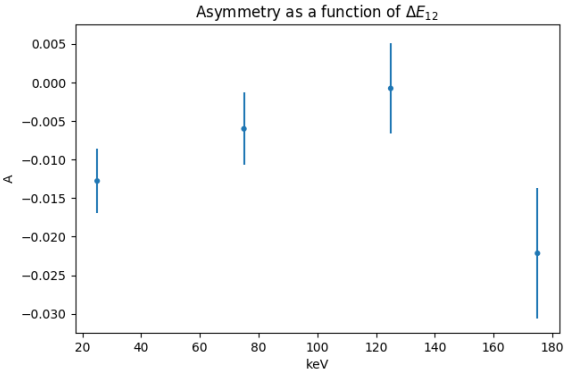

Figure 6: Asymmetry vs ΔE_{12} (Shifted).

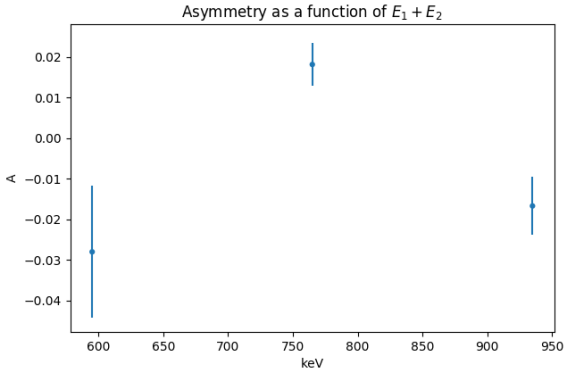

Figure 7: Asymmetry vs ΔE_{12} (Centered).

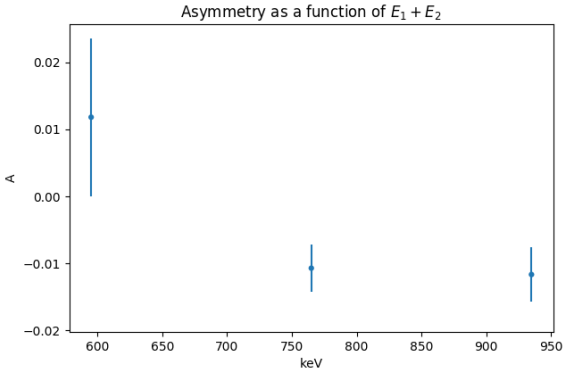

Figure 8: Asymmetry vs ΔE_{12} (Shifted).

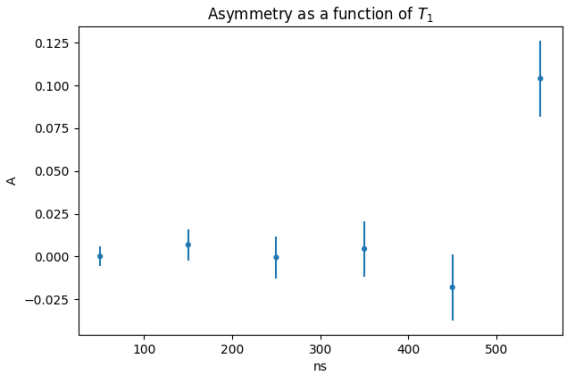

Figure 9: Asymmetry vs T_1 (Center).

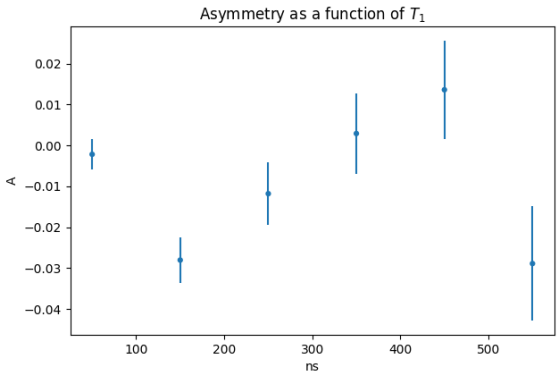

Figure 10: Asymmetry vs T_1 (Shift).

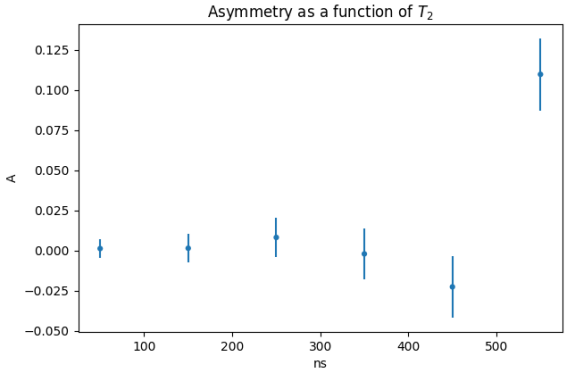

Figure 11: Asymmetry vs T_2 (Center).

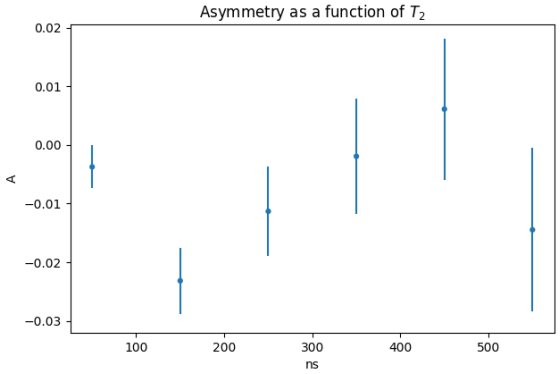

Figure 12: Asymmetry vs T_2 (Shift).

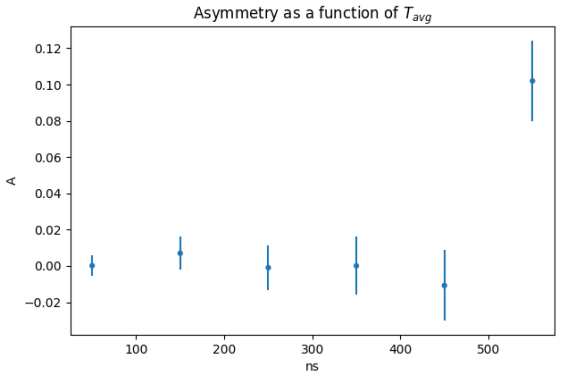

Figure 13: Asymmetry vs T_{avg} (Centered).

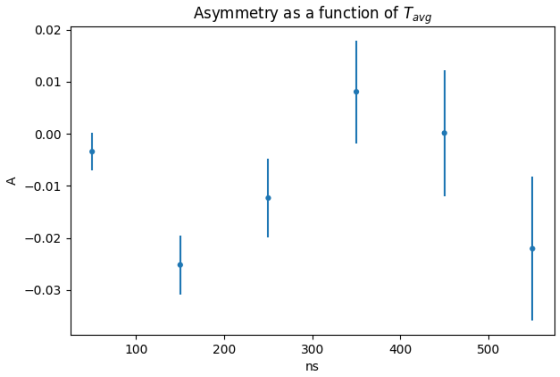

Figure 14: Asymmetry vs T_{avg} (Shifted).

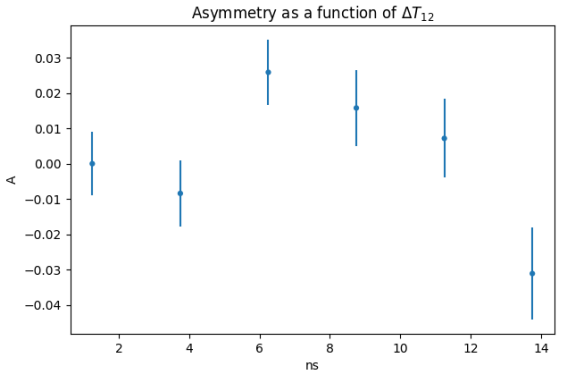

Figure 15: Asymmetry vs ΔT_{12} (Centered).

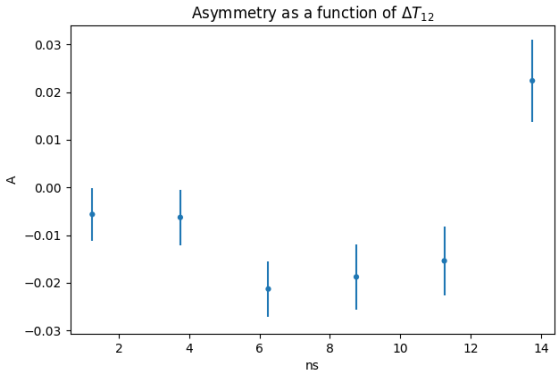

Figure 16: Asymmetry vs ΔT_{12} (Shifted).

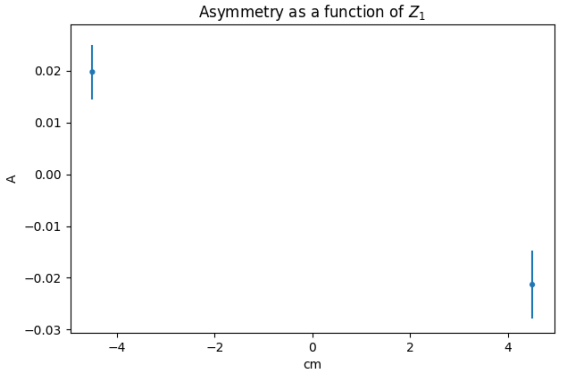

Figure 17: Asymmetry vs Z_1 (Centered).

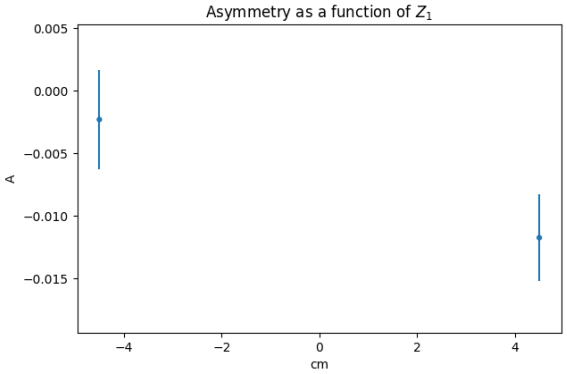

Figure 18: Asymmetry vs Z_1 (Shifted).

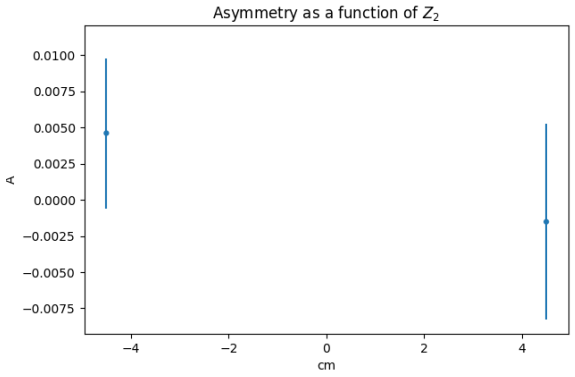

Figure 19: Asymmetry vs Z_2 (Centered).

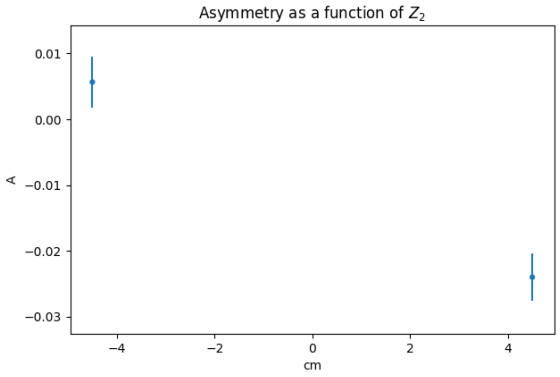

Figure 20: Asymmetry vs Z_2 (Shifted).

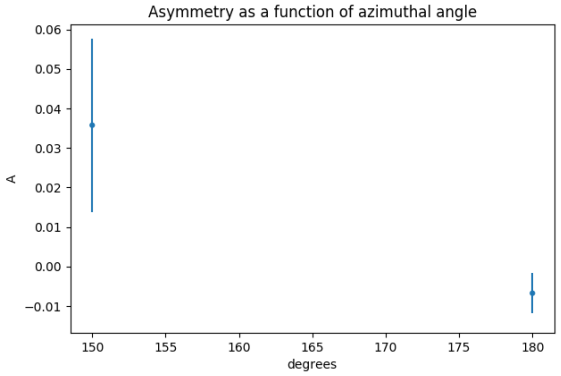

Figure 21: Asymmetry vs α (Center).

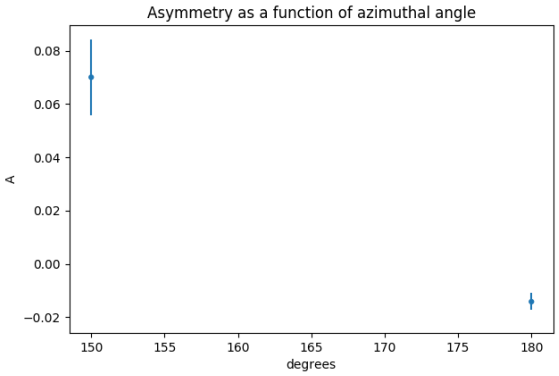

Figure 22: Asymmetry vs α (Shift).

Figs 23-44 show the asymmetry plotted as a function of various cut parameters, using only 4 bar events.

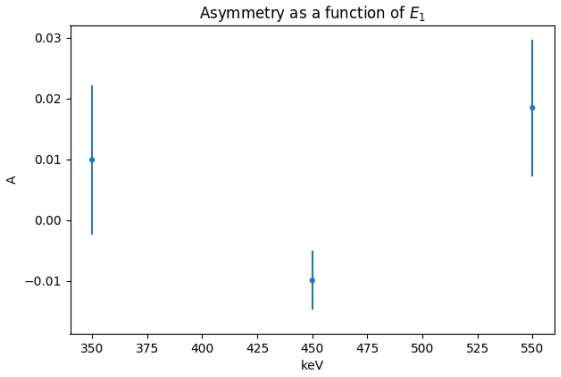

Figure 23: Asymmetry vs E_1 (Center).

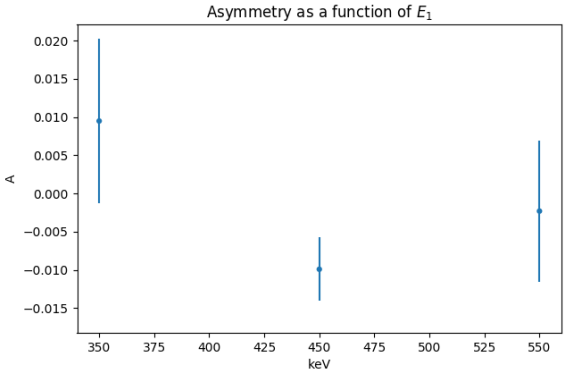

Figure 24: Asymmetry vs E_1 (Shift).

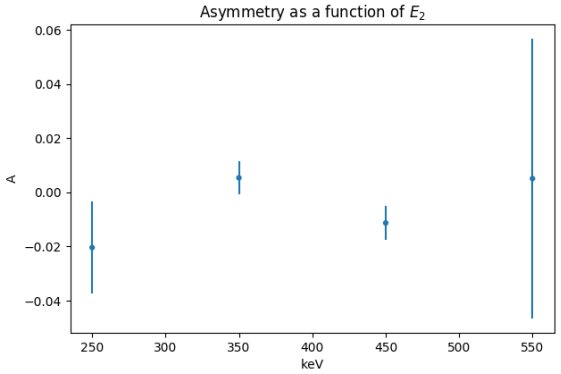

Figure 25: Asymmetry vs E_2 (Center).

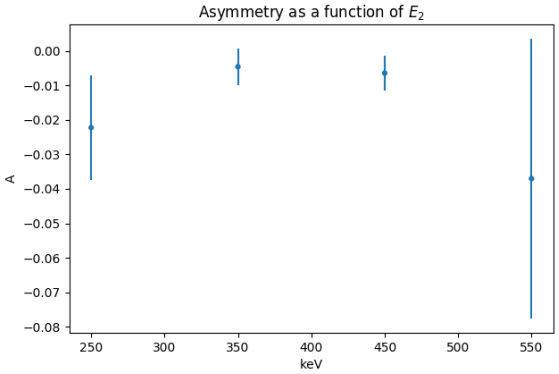

Figure 26: Asymmetry vs E_2 (Shift).

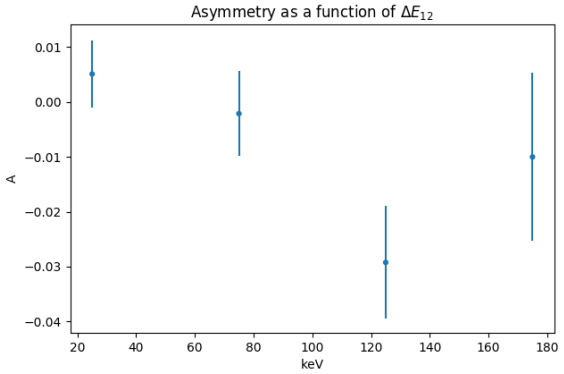

Figure 27: Asymmetry vs ΔE_{12} (Centered).

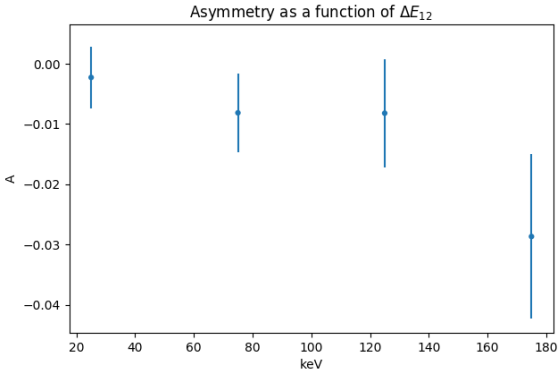

Figure 28: Asymmetry vs ΔE_{12} (Shifted).

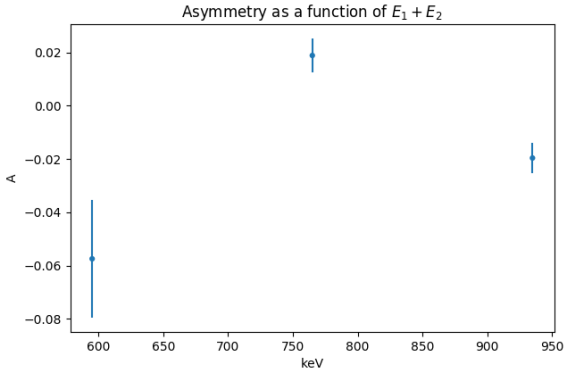

Figure 29: Asymmetry vs ΔE_{12} (Centered).

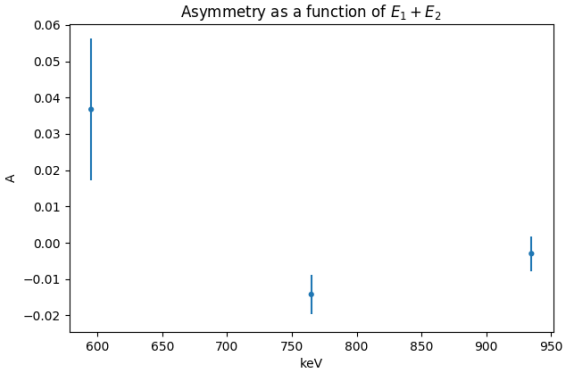

Figure 30: Asymmetry vs ΔE_{12} (Shifted).

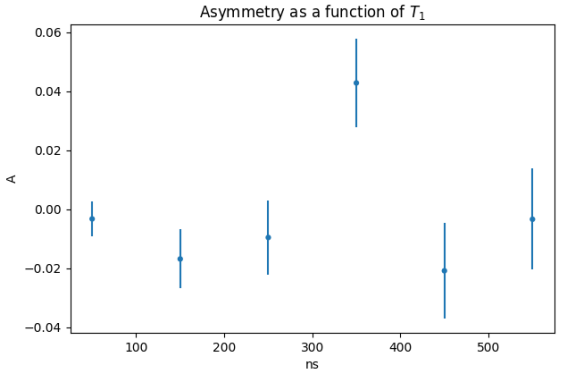

Figure 31: Asymmetry vs T_1 (Center).

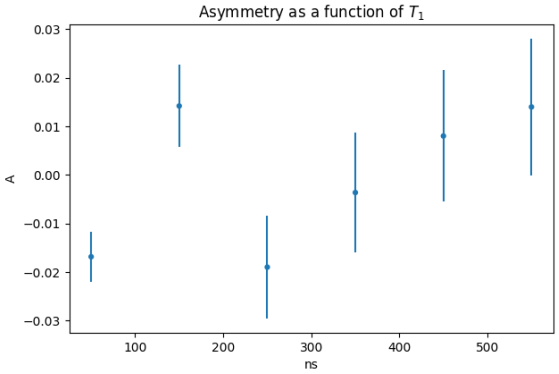

Figure 32: Asymmetry vs T_1 (Shift).

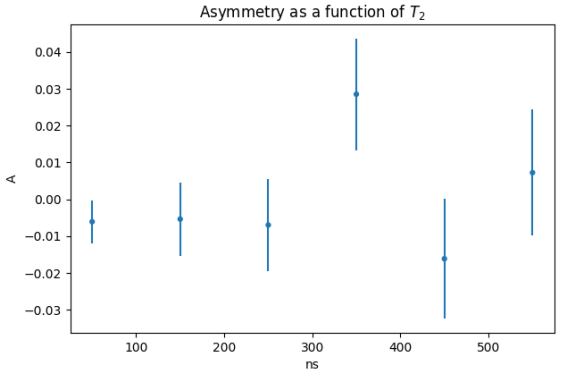

Figure 33: Asymmetry vs T_2 (Center).

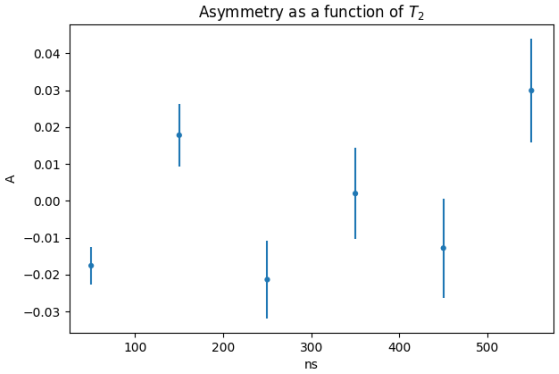

Figure 34: Asymmetry vs T_2 (Shift).

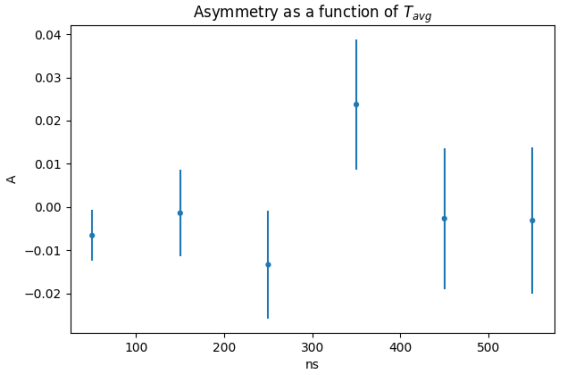

Figure 35: Asymmetry vs T_{avg} (Centered).

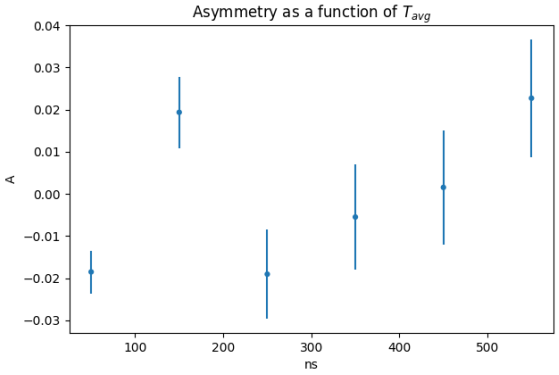

Figure 36: Asymmetry vs T_{avg} (Shifted).

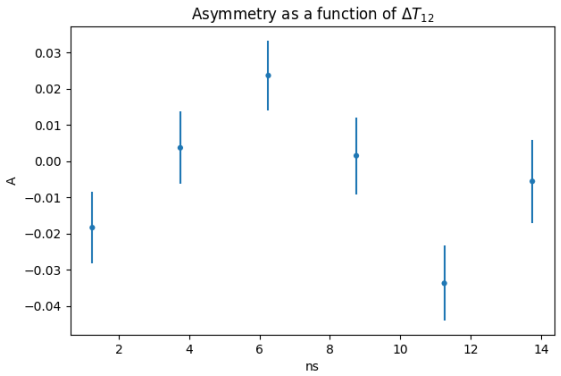

Figure 37: Asymmetry vs ΔT_{12} (Centered).

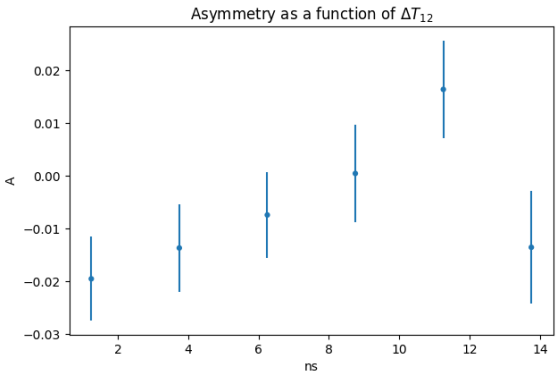

Figure 38: Asymmetry vs ΔT_{12} (Shifted).

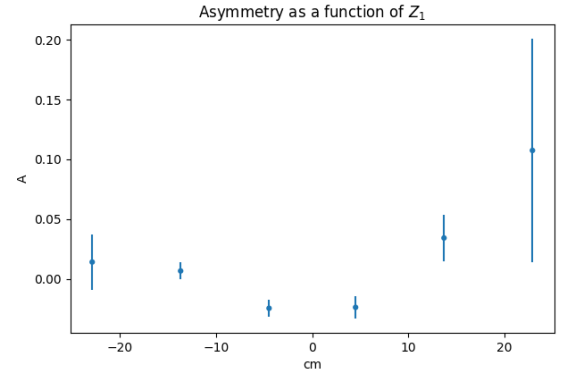

Figure 39: Asymmetry vs Z_1 (Centered).

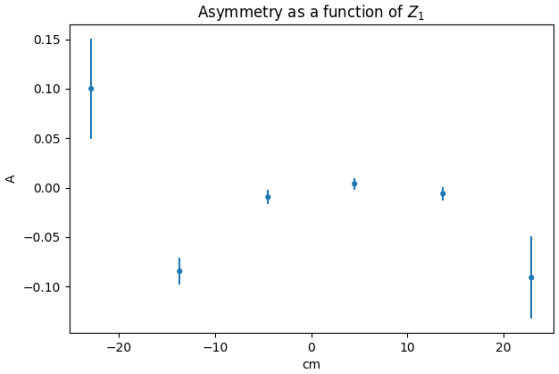

Figure 40: Asymmetry vs Z_1 (Shifted).

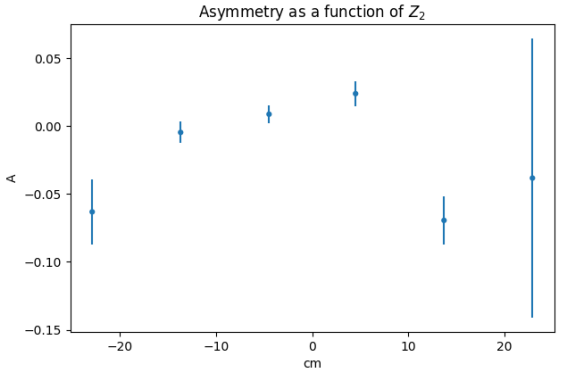

Figure 41: Asymmetry vs Z_2 (Centered).

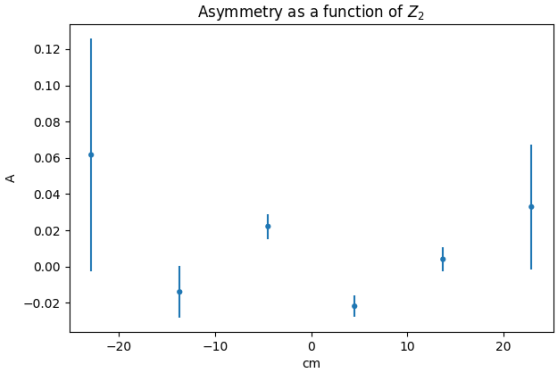

Figure 42: Asymmetry vs Z_2 (Shifted).

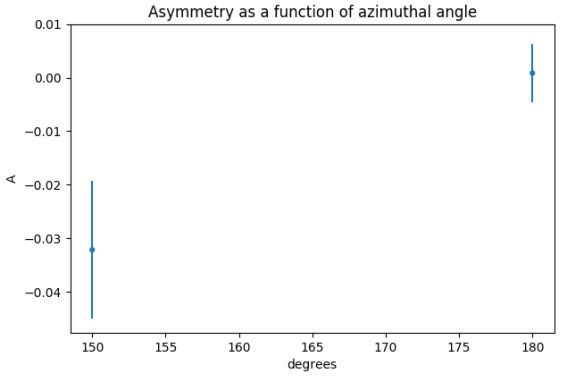

Figure 43: Asymmetry vs α (Center).

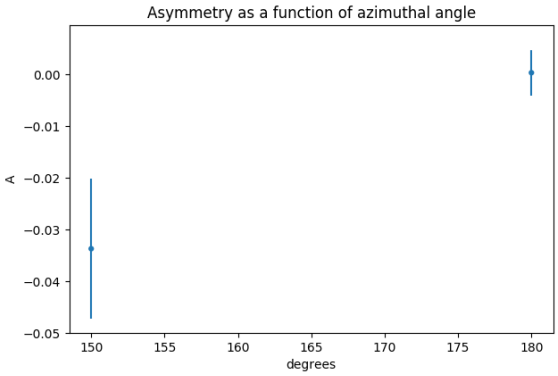

Figure 44: Asymmetry vs α (Shift).

Figs 45-66 show the asymmetry plotted as a function of various cut parameters, using all available data.

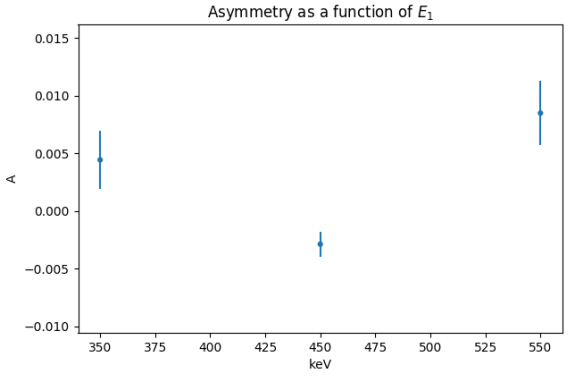

Figure 45: Asymmetry vs E_1 (Center).

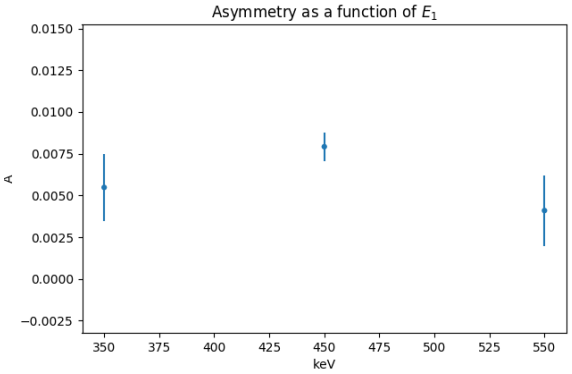

Figure 46: Asymmetry vs E_1 (Shift).

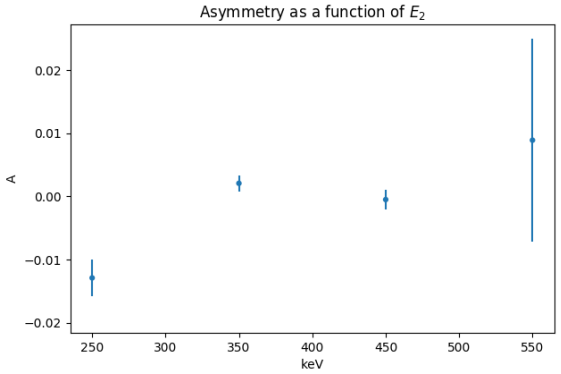

Figure 47: Asymmetry vs E_2 (Center).

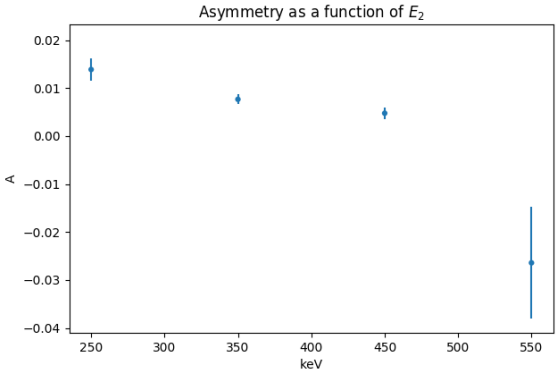

Figure 48: Asymmetry vs E_2 (Shift).

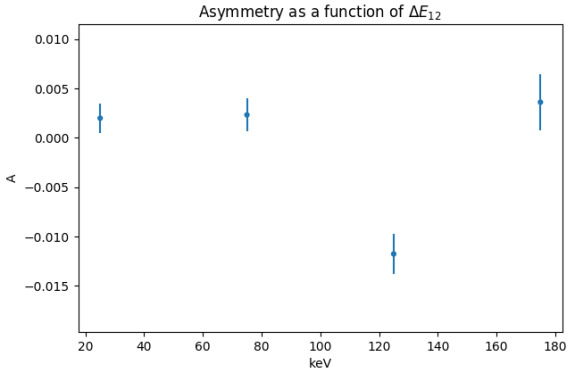

Figure 49: Asymmetry vs ΔE_{12} (Centered).

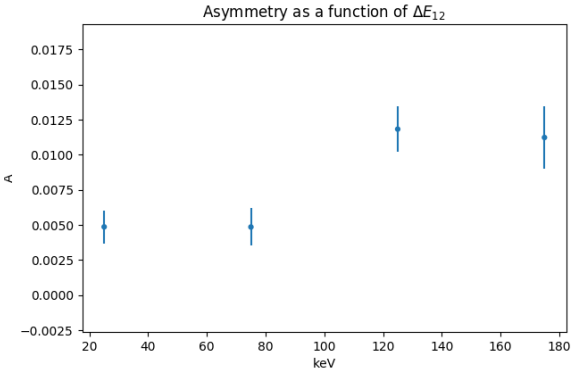

Figure 50: Asymmetry vs ΔE_{12} (Shifted).

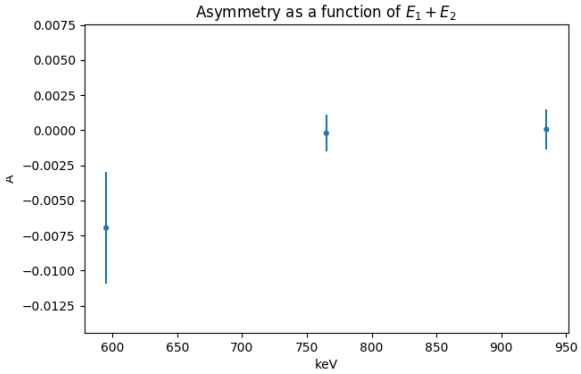

Figure 51: Asymmetry vs ΔE_{12} (Centered).

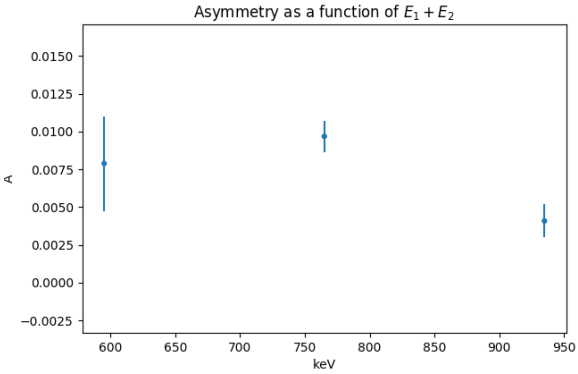

Figure 52: Asymmetry vs ΔE_{12} (Shifted).

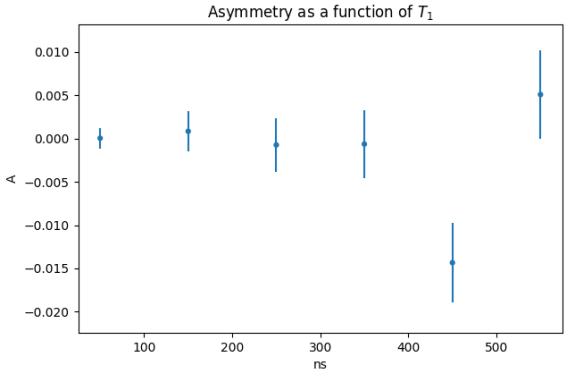

Figure 53: Asymmetry vs T_1 (Center).

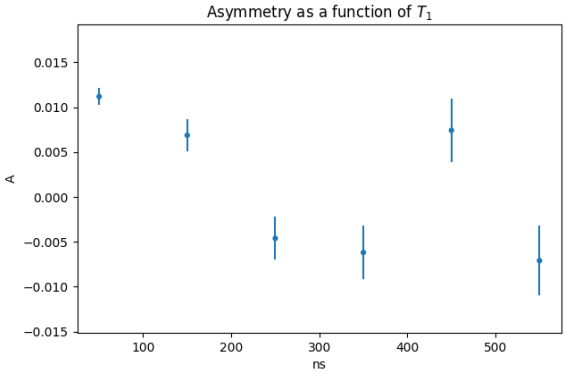

Figure 54: Asymmetry vs T_1 (Shift).

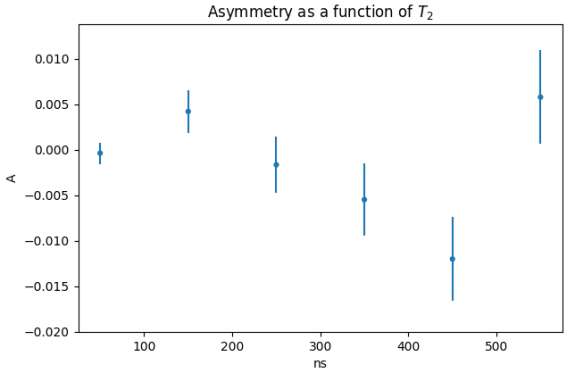

Figure 55: Asymmetry vs T_2 (Center).

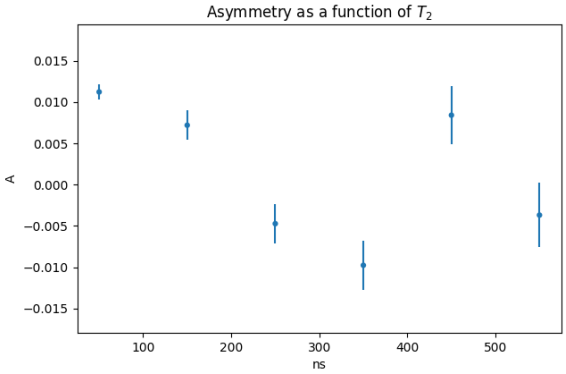

Figure 56: Asymmetry vs T_2 (Shift).

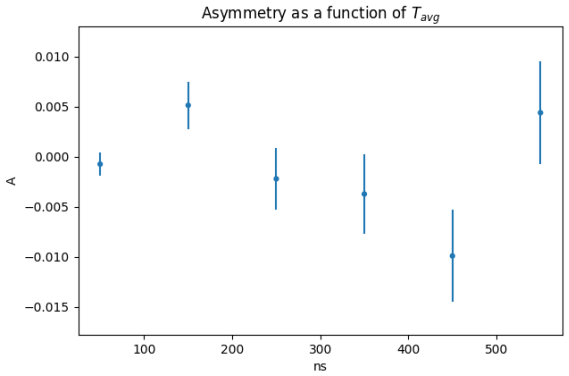

Figure 57: Asymmetry vs T_{avg} (Centered).

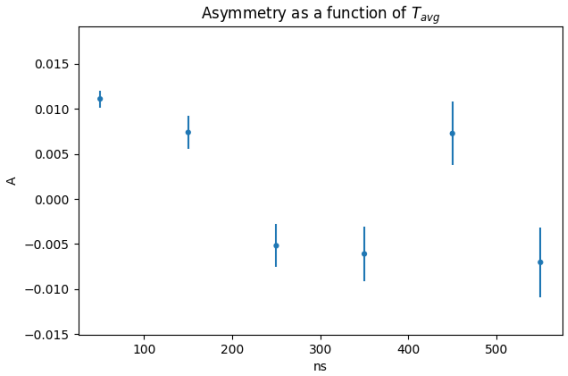

Figure 58: Asymmetry vs T_{avg} (Shifted).

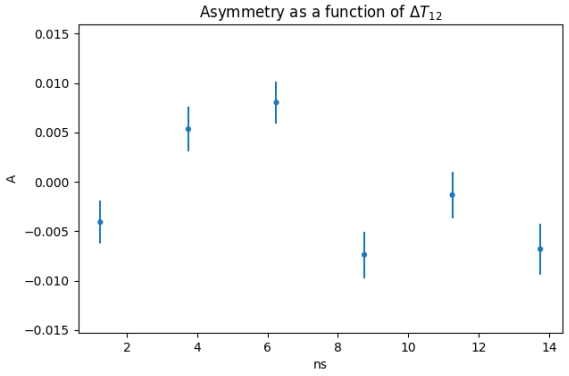

Figure 59: Asymmetry vs ΔT_{12} (Centered).

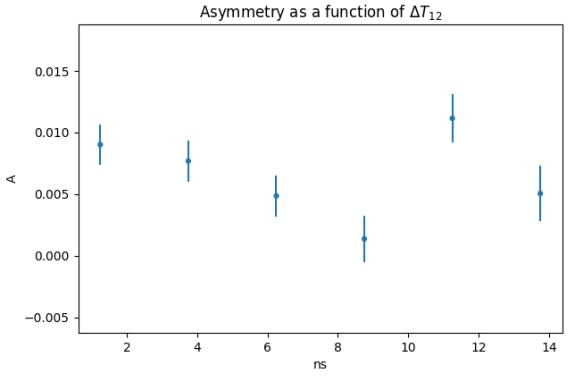

Figure 60: Asymmetry vs ΔT_{12} (Shifted).

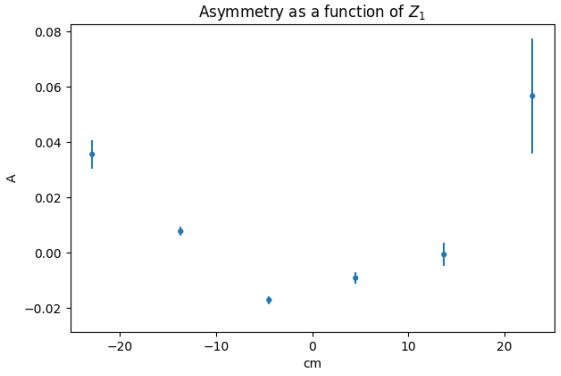

Figure 61: Asymmetry vs Z_1 (Centered).

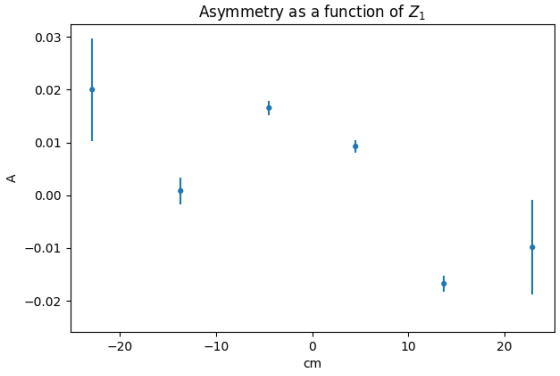

Figure 62: Asymmetry vs Z_1 (Shifted).

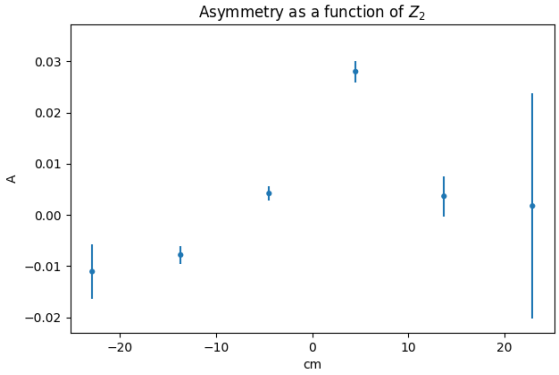

Figure 63: Asymmetry vs Z_2 (Centered).

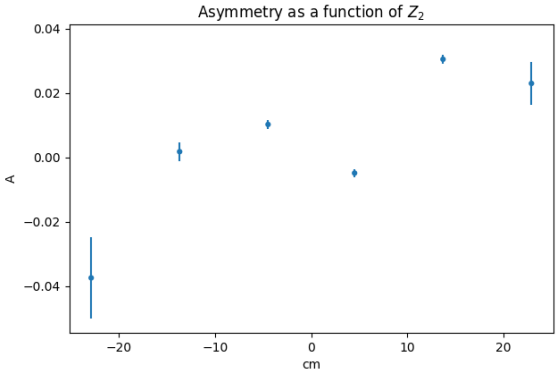

Figure 64: Asymmetry vs Z_2 (Shifted).

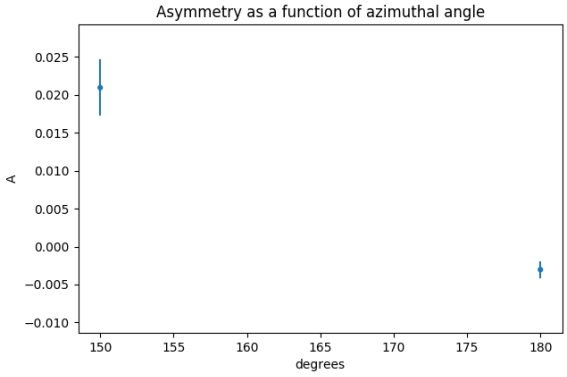

Figure 65: Asymmetry vs α (Center).

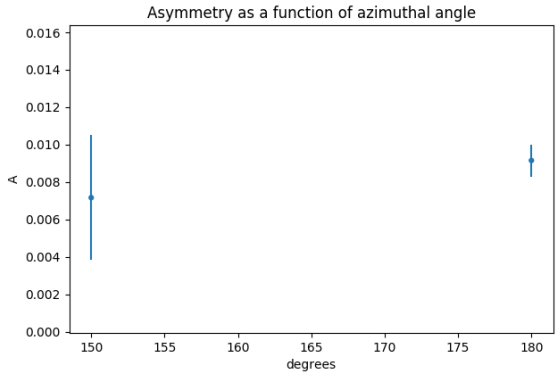

Figure 66: Asymmetry vs α (Shift).

BIBLIOGRAPHY

[1] P. Vetter and S. J Freedman, "Search for CPT-Odd Decays of Positronium," *Physical review letters* **91** (12, 2003) 263401.

[2] A. Ore and J. L. Powell, "Three-Photon Annihilation of an Electron-Positron Pair," *Phys. Rev.* **75** (Jun, 1949) 1696–1699. http://link.aps.org/doi/10.1103/PhysRev.75.1696.

[3] E. P. Wigner, "On the Conservation Laws of Quantum Mechanics," 1927.

[4] E. Wigner, "Ueber die Operation der Zeitumkehr in der Quantenmechanik," *Nachrichten von der Gesellschaft der Wissenschaften zu Gttingen, Mathematisch-Physikalische Klasse* **1932** (1932) 546–559. http://eudml.org/doc/59401.

[5] "Quantised singularities in the electromagnetic field,," *Proceedings of the Royal Society of London A: Mathematical, Physical and Engineering Sciences* **133** no. 821, (1931) 60–72, http://rspa.royalsocietypublishing.org/content/133/821/60.full.pdf. http://rspa.royalsocietypublishing.org/content/133/821/60.

[6] W. Pauli, *Exclusion Principle, Lorentz Group and Reflection of Space-Time and Charge*, pp. 459–479. Vieweg+Teubner Verlag, Wiesbaden, 1988. https://doi.org/10.1007/978-3-322-90270-2_41.

[7] G. Luders, "On the Equivalence of Invariance under Time Reversal and under Particle-Antiparticle Conjugation for Relativistic Field Theories," *Kong. Dan. Vid. Sel. Mat. Fys. Med.* **28N5** no. 5, (1954) 1–17.

[8] **E731** Collaboration, L. K. Gibbons *et al.*, "CP and CPT symmetry test from the two pion decays of the neutral kaon with the Fermilab E731 detector," *Phys. Rev.* **D55** (1997) 6625–6715.

[9] R. S. Van Dyck, P. B. Schwinberg, and H. G. Dehmelt, "New high-precision comparison of electron and positron g factors," *Phys. Rev. Lett.* **59** (Jul, 1987) 26–29. https://link.aps.org/doi/10.1103/PhysRevLett.59.26.

[10] **KTeV** Collaboration, A. Alavi-Harati *et al.*, "Measurements of direct CP violation, CPT symmetry, and other parameters in the neutral kaon system," *Phys. Rev.* **D67** (2003) 012005, arXiv:hep-ex/0208007 [hep-ex]. [Erratum: Phys. Rev.D70,079904(2004)].

[11] "A measurement of the phases of the CP-violating amplitudes in K0 decays and a test of CPT invariance," *Physics Letters B* **237** no. 2, (1990) 303 – 312.

[12] **CDF** Collaboration, T. Aaltonen *et al.*, "Measurement of the mass difference between top and antitop quarks," *Phys. Rev.* **D87** no. 5, (2013) 052013, arXiv:1210.6131 [hep-ex].

[13] **KLOE** Collaboration, F. Ambrosino *et al.*, "First observation of quantum interference in the process $\phi \to K(S)K(L) \to \pi^+\pi^-\pi^+\pi^-$: A Test of quantum mechanics and CPT symmetry," *Phys. Lett.* **B642** (2006) 315–321, arXiv:hep-ex/0607027 [hep-ex].

[14] **KTeV** Collaboration, E. Abouzaid *et al.*, "Precise Measurements of Direct CP Violation, CPT Symmetry, and Other Parameters in the Neutral Kaon System," *Phys. Rev.* **D83** (2011) 092001, arXiv:1011.0127 [hep-ex].

[15] J. M. Link *et al.*, "Charm System Tests of CPT and Lorentz Invariance with FOCUS," *Phys. Lett.* **B556** (2003) 7–13, arXiv:hep-ex/0208034 [hep-ex].

[16] **Belle** Collaboration, N. C. Hastings *et al.*, "Studies of B0 - anti-B0 mixing properties with inclusive dilepton events," *Phys. Rev.* **D67** (2003) 052004, arXiv:hep-ex/0212033 [hep-ex].

[17] **BaBar** Collaboration, B. Aubert *et al.*, "Limits on the decay rate difference of neutral$-B$ mesons and on CP, T, and CPT violation in $B^0\overline{B}^0$ oscillations," *Phys. Rev.* **D70** (2004) 012007, arXiv:hep-ex/0403002 [hep-ex].

[18] **BaBar** Collaboration, B. Aubert *et al.*, "Search for T, CP and CPT violation in B0 anti-B0 mMixing with inclusive dilepton events," *Phys. Rev. Lett.* **96** (2006) 251802, arXiv:hep-ex/0603053 [hep-ex].

[19] **BaBar** Collaboration, B. Aubert *et al.*, "Search for CPT and Lorentz violation in B0 - anti-B0 oscillations with dilepton events," *Phys. Rev. Lett.* **100** (2008) 131802, arXiv:0711.2713 [hep-ex].

[20] A. Kostelecky and R. Van Kooten, "CPT violation and B-meson oscillations," *Phys. Rev.* **D82** (2010) 101702, arXiv:1007.5312 [hep-ph].

[21] T. Higuchi *et al.*, "Search for Time-Dependent CPT Violation in Hadronic and Semileptonic B Decays," *Phys. Rev.* **D85** (2012) 071105, arXiv:1203.0930 [hep-ex].

[22] **D0** Collaboration, V. M. Abazov *et al.*, "Search for Violation of CPT and Lorentz Invariance in B_s^0 Meson Oscillations," *Phys. Rev. Lett.* **115** no. 16, (2015) 161601, arXiv:1506.04123 [hep-ex]. [Addendum: Phys. Rev. Lett.116,no.1,019901(2016)].

[23] **BaBar** Collaboration, J. P. Lees *et al.*, "Tests of CPT symmetry in $B^0 - \overline{B}^0$ mixing and in $B^0 \to c\bar{c}K^0$ decays," *Phys. Rev.* **D94** no. 1, (2016) 011101, arXiv:1605.04545 [hep-ex].

[24] **LHCb** Collaboration, R. Aaij *et al.*, "Search for violations of Lorentz invariance and CPT symmetry in $B^0_{(s)}$ mixing," *Phys. Rev. Lett.* **116** no. 24, (2016) 241601, arXiv:1603.04804 [hep-ex].

[25] R. Brown, U. Camerini, P. H. Fowler, H. Muirhead, C. F. Powell, and D. M. Ritson, "Observations with Electron-Sensitive Plates Exposed to Cosmic Radiation*,".

[26] R. W. Birge, J. R. Peterson, D. H. Stork, and M. N. Whitehead, "Mass Values of the K Mesons," *Phys. Rev.* **100** (Oct, 1955) 430–431. https://link.aps.org/doi/10.1103/PhysRev.100.430.

[27] L. W. Alvarez, F. S. Crawford, M. L. Good, and M. L. Stevenson, "Lifetime of K Mesons," *Phys. Rev.* **101** (Jan, 1956) 503–505. https://link.aps.org/doi/10.1103/PhysRev.101.503.

[28] T. D. Lee and C. N. Yang, "Question of Parity Conservation in Weak Interactions," *Phys. Rev.* **104** (Oct, 1956) 254–258. http://link.aps.org/doi/10.1103/PhysRev.104.254.

[29] C. S. Wu, E. Ambler, R. W. Hayward, D. D. Hoppes, and R. P. Hudson, "Experimental Test of Parity Conservation in Beta Decay," *Phys. Rev.* **105** (Feb, 1957) 1413–1415. http://link.aps.org/doi/10.1103/PhysRev.105.1413.

[30] J. H. Christenson, J. W. Cronin, V. L. Fitch, and R. Turlay, "Evidence for the 2π Decay of the K_2^0 Meson," *Phys. Rev. Lett.* **13** (Jul, 1964) 138–140. http://link.aps.org/doi/10.1103/PhysRevLett.13.138.

[31] B. e. a. Aubert, "Observation of *CP* Violation in the B^0 Meson System," *Phys. Rev. Lett.* **87** (Aug, 2001) 091801. http://link.aps.org/doi/10.1103/PhysRevLett.87.091801.

[32] A. D. Sakharov, "Violation of CP in variance, C asymmetry, and baryon asymmetry of the universe," *Soviet Physics Uspekhi* **34** no. 5, (1991) 392. http://stacks.iop.org/0038-5670/34/i=5/a=A08.

[33] A. Riotto, "Theories of baryogenesis," in *Proceedings, Summer School in High-energy physics and cosmology: Trieste, Italy, June 29-July 17, 1998*, pp. 326–436. 1998. arXiv:hep-ph/9807454 [hep-ph].

[34] **Particle Data Group** Collaboration, M. Tanabashi, K. Hagiwara, K. Hikasa, K. Nakamura, Y. Sumino, F. Takahashi, J. Tanaka, K. Agashe, G. Aielli, C. Amsler, M. Antonelli, D. M. Asner, H. Baer, S. Banerjee, R. M. Barnett, T. Basaglia, C. W. Bauer, J. J. Beatty, V. I. Belousov, J. Beringer, S. Bethke, A. Bettini, H. Bichsel, O. Biebel, K. M. Black, E. Blucher, O. Buchmuller, V. Burkert, M. A. Bychkov, R. N. Cahn, M. Carena, A. Ceccucci, A. Cerri, D. Chakraborty, M.-C. Chen, R. S. Chivukula, G. Cowan, O. Dahl, G. D'Ambrosio, T. Damour, D. de Florian, A. de Gouvêa, T. DeGrand, P. de Jong, G. Dissertori, B. A. Dobrescu, M. D'Onofrio, M. Doser, M. Drees, H. K. Dreiner, D. A. Dwyer, P. Eerola, S. Eidelman, J. Ellis, J. Erler, V. V. Ezhela, W. Fetscher, B. D. Fields, R. Firestone, B. Foster, A. Freitas, H. Gallagher, L. Garren, H.-J. Gerber, G. Gerbier, T. Gershon, Y. Gershtein, T. Gherghetta, A. A. Godizov, M. Goodman, C. Grab, A. V. Gritsan, C. Grojean, D. E. Groom, M. Grünewald, A. Gurtu, T. Gutsche, H. E. Haber, C. Hanhart, S. Hashimoto, Y. Hayato, K. G. Hayes, A. Hebecker, S. Heinemeyer, B. Heltsley, J. J. Hernández-Rey, J. Hisano, A. Höcker, J. Holder, A. Holtkamp, T. Hyodo, K. D. Irwin, K. F. Johnson, M. Kado, M. Karliner, U. F. Katz, S. R. Klein, E. Klempt, R. V. Kowalewski, F. Krauss, M. Kreps, B. Krusche, Y. V. Kuyanov, Y. Kwon, O. Lahav, J. Laiho, J. Lesgourgues, A. Liddle, Z. Ligeti, C.-J. Lin, C. Lippmann,

T. M. Liss, L. Littenberg, K. S. Lugovsky, S. B. Lugovsky, A. Lusiani, Y. Makida, F. Maltoni, T. Mannel, A. V. Manohar, W. J. Marciano, A. D. Martin, A. Masoni, J. Matthews, U.-G. Meißner, D. Milstead, R. E. Mitchell, K. Mönig, P. Molaro, F. Moortgat, M. Moskovic, H. Murayama, M. Narain, P. Nason, S. Navas, M. Neubert, P. Nevski, Y. Nir, K. A. Olive, S. Pagan Griso, J. Parsons, C. Patrignani, J. A. Peacock, M. Pennington, S. T. Petcov, V. A. Petrov, E. Pianori, A. Piepke, A. Pomarol, A. Quadt, J. Rademacker, G. Raffelt, B. N. Ratcliff, P. Richardson, A. Ringwald, S. Roesler, S. Rolli, A. Romaniouk, L. J. Rosenberg, J. L. Rosner, G. Rybka, R. A. Ryutin, C. T. Sachrajda, Y. Sakai, G. P. Salam, S. Sarkar, F. Sauli, O. Schneider, K. Scholberg, A. J. Schwartz, D. Scott, V. Sharma, S. R. Sharpe, T. Shutt, M. Silari, T. Sjöstrand, P. Skands, T. Skwarnicki, J. G. Smith, G. F. Smoot, S. Spanier, H. Spieler, C. Spiering, A. Stahl, S. L. Stone, T. Sumiyoshi, M. J. Syphers, K. Terashi, J. Terning, U. Thoma, R. S. Thorne, L. Tiator, M. Titov, N. P. Tkachenko, N. A. Törnqvist, D. R. Tovey, G. Valencia, R. Van de Water, N. Varelas, G. Venanzoni, L. Verde, M. G. Vincter, P. Vogel, A. Vogt, S. P. Wakely, W. Walkowiak, C. W. Walter, D. Wands, D. R. Ward, M. O. Wascko, G. Weiglein, D. H. Weinberg, E. J. Weinberg, M. White, L. R. Wiencke, S. Willocq, C. G. Wohl, J. Womersley, C. L. Woody, R. L. Workman, W.-M. Yao, G. P. Zeller, O. V. Zenin, R.-Y. Zhu, S.-L. Zhu, F. Zimmermann, P. A. Zyla, J. Anderson, L. Fuller, V. S. Lugovsky, and P. Schaffner, "Review of Particle Physics," *Phys. Rev. D* **98** (Aug, 2018) 030001. https://link.aps.org/doi/10.1103/PhysRevD.98.030001.

[35] E. Kolb and M. Turner, *The Early Universe*. Frontiers in physics. Addison-Wesley, 1990. https://books.google.com/books?id=CHDFQgAACAAJ.

[36] G. W. S. Hou, "Source of CP Violation for the Baryon Asymmetry of the Universe," *Int. J. Mod. Phys.* **D20** (2011) 1521–1532, arXiv:1101.2161 [hep-ph].

[37] M. Hartz, "T2K Neutrino Oscillation Results with Data up to 2017 Summer." KEK Seminar for New T2K Results, 2017.

[38] K. Abe, R. Akutsu, A. Ali, J. Amey, C. Andreopoulos, L. Anthony, M. Antonova, S. Aoki, A. Ariga, Y. Ashida, and et al., "Search for CP violation in Neutrino and Antineutrino Oscillations by the T2K experiment with 2.2×10^{21} protons on target," *ArXiv e-prints* (July, 2018) , arXiv:1807.07891 [hep-ex].

[39] M. Sanchez, "NOvA Results and Prospects," June, 2018. https://doi.org/10.5281/zenodo.1286758.

[40] "LBNE collaboration." http://lbne.fnal.gov/. Accessed: 2015-03-25.

[41] **Hyper-Kamiokande** Collaboration, K. Abe *et al.*, "Physics potentials with the second Hyper-Kamiokande detector in Korea," *PTEP* **2018** no. 6, (2018) 063C01, arXiv:1611.06118 [hep-ex].

[42] D. Hanneke, S. Fogwell, and G. Gabrielse, "New Measurement of the Electron Magnetic Moment and the Fine Structure Constant," *Phys. Rev. Lett.* **100** (Mar, 2008) 120801. http://link.aps.org/doi/10.1103/PhysRevLett.100.120801.

[43] **Muon (g-2)** Collaboration, G. W. Bennett *et al.*, "An Improved Limit on the Muon Electric Dipole Moment," *Phys. Rev.* **D80** (2009) 052008, arXiv:0811.1207 [hep-ex].

[44] K. Inami, K. Abe, K. Abe, R. Abe, T. Abe, I. Adachi, H. Aihara, M. Akatsu, Y. Asano, T. Aso, V. Aulchenko, T. Aushev, A. Bakich, Y. Ban, E. Banas, P. Behera, I. Bizjak, A. Bondar, T. Browder, P. Chang, Y. Chao, B. Cheon, R. Chistov, Y. Choi, Y. Choi, L. Dong, S. Eidelman, V. Eiges, Y. Enari, C. Fukunaga, N. Gabyshev, A. Garmash, T. Gershon, B. Golob, C. Hagner, F. Handa, T. Hara, H. Hayashii, M. Hazumi, I. Higuchi, T. Higuchi, T. Hokuue, Y. Hoshi, W.-S. Hou, H.-C. Huang, T. Igaki, T. Iijima, A. Ishikawa, H. Ishino, R. Itoh, H. Iwasaki, H. Jang, J. Kang, J. Kang, N. Katayama, H. Kawai, Y. Kawakami, N. Kawamura, T. Kawasaki, H. Kichimi, H. Kim, H. Kim, J. Kim, S. Kim, S. Korpar, P. Krokovny, R. Kulasiri, A. Kuzmin, Y.-J. Kwon, J. Lange, G. Leder, S. Lee, J. Li, D. Liventsev, R.-S. Lu, J. MacNaughton, F. Mandl, T. Matsuishi, S. Matsumoto, T. Matsumoto, W. Mitaroff, H. Miyake, H. Miyata, T. Nagamine, Y. Nagasaka, T. Nakadaira, E. Nakano, M. Nakao, J. Nam, S. Nishida, T. Nozaki, S. Ogawa, T. Ohshima, T. Okabe, S. Okuno, S. Olsen, W. Ostrowicz, H. Ozaki, P. Pakhlov, H. Park, K. Park, L. Peak, J.-P. Perroud, L. Piilonen, K. Rybicki, H. Sagawa, S. Saitoh, Y. Sakai, M. Satapathy, O. Schneider, S. Semenov, K. Senyo, M. Sevior, H. Shibuya, B. Shwartz, V. Sidorov, J. Singh, N. Soni, S. Stani, M. Stari, A. Sugi, A. Sugiyama, K. Sumisawa, T. Sumiyoshi, S. Suzuki, S. Suzuki, T. Takahashi, F. Takasaki, K. Tamai, N. Tamura, J. Tanaka, M. Tanaka, G. Taylor, Y. Teramoto, S. Tokuda, T. Tomura, T. Tsuboyama, T. Tsukamoto, S. Uehara, Y. Unno, S. Uno, G. Varner, K. Varvell, C. Wang, Y. Watanabe, B. Yabsley, Y. Yamada, A. Yamaguchi, Y. Yamashita, Y. Yusa, Z. Zhang, V. Zhilich, and D. ontar, "Search for the electric dipole moment of the lepton," *Physics Letters B* **551** no. 1, (2003) 16 – 26. http://www.sciencedirect.com/science/article/pii/S0370269302029842.

[45] S. Hoogerheide, J. C. Dorr, E. Novitski, and G. Gabrielse, "High efficiency positron accumulation for high-precision magnetic moment experiments," *Review of Scientific Instruments* **86** (05, 2015) 053301.

[46] G. Gabrielse, A. Khabbaz, D. S. Hall, C. Heimann, H. Kalinowsky, and W. Jhe, "Precision Mass Spectroscopy of the Antiproton and Proton Using Simultaneously Trapped Particles," *Phys. Rev. Lett.* **82** (Apr, 1999) 3198–3201. https://link.aps.org/doi/10.1103/PhysRevLett.82.3198.

[47] D. Colladay and V. A. Kostelecký, "CPT," *Phys. Rev. D* **55** (Jun, 1997) 6760–6774. https://link.aps.org/doi/10.1103/PhysRevD.55.6760.

[48] D. Colladay and V. A. Kostelecký, "Lorentz-violating extension of the standard model," *Phys. Rev. D* **58** (Oct, 1998) 116002. https://link.aps.org/doi/10.1103/PhysRevD.58.116002.

[49] C. D. Anderson, "The Positive Electron," *Phys. Rev.* **43** (Mar, 1933) 491–494. https://link.aps.org/doi/10.1103/PhysRev.43.491.

[50] S. Mohorovičić, "Möglichkeit neuer Elemente und ihre Bedeutung für die Astrophysik," *Astronomische Nachrichten* **253** (Nov., 1934) 93.

[51] A. E. Ruark, "Positronium," *Phys. Rev.* **68** (Dec, 1945) 278–278. https://link.aps.org/doi/10.1103/PhysRev.68.278.

[52] J. A. Wheeler, "Polyelectrons," *Annals of the New York Academy of Sciences* **48** no. 3, (1946) 219–238. http://dx.doi.org/10.1111/j.1749-6632.1946.tb31764.x.

[53] J. Pirenne, "The proper field and the interaction of Dirac particles. IIII," *Arch. Sci. phys. nat* **28** (1946) 233–272.

[54] J. Pirenne, "J. Pirenne, Arch. sci. phys. et nat. 29, 207 (1947)," *Arch. sci. phys. et nat.* **29** (1947) 207.

[55] M. Deutsch, "Evidence for the Formation of Positronium in Gases," *Phys. Rev.* **82** (May, 1951) 455–456. http://link.aps.org/doi/10.1103/PhysRev.82.455.

[56] A. Ore and J. L. Powell, "Three-Photon Annihilation of an Electron-Positron Pair," *Phys. Rev.* **75** (Jun, 1949) 1696–1699. https://link.aps.org/doi/10.1103/PhysRev.75.1696.

[57] M. Perkal and W. Walters, "Positron annihilation in synthetic zeolites 4A and 13X," *The Journal of Chemical Physics* **53** no. 1, (1970) 190–198.

[58] S. Chuang and S. Tao, "Study of various properties of silica gel by positron annihilation," *The Journal of Chemical Physics* **54** no. 11, (1971) 4902–4907.

[59] Y. Ito, T. Yamashina, and M. Nagasaka, "Structure of porous vycor glass and its adsorption characteristics of waterAn application of positron annihilation method," *Applied physics* **6** no. 3, (1975) 323–326.

[60] Y. Nagashima, M. Kakimoto, T. Hyodo, K. Fujiwara, A. Ichimura, T. Chang, J. Deng, T. Akahane, T. Chiba, K. Suzuki, B. T. A. McKee, and A. T. Stewart, "Thermalization of free positronium atoms by collisions with silica-powder grains, aerogel grains, and gas molecules," *Phys. Rev. A* **52** (Jul, 1995) 258–265. https://link.aps.org/doi/10.1103/PhysRevA.52.258.

[61] R. Yu, K. Ito, K. Hirata, W. Zheng, and Y. Kobayashi, "Effects of coexistent pores and paramagnetic defects on positron annihilation in silicon oxide thin films," *Journal of applied physics* **93** no. 6, (2003) 3340–3344.

[62] S. Eijt, A. van Veen, C. Falub, R. E. Galindo, H. Schut, P. Mijnarends, F. de Theije, and A. Balkenende, "Depth-selective 2D-ACAR studies on low-k dielectric thin films," *Radiation Physics and Chemistry* **68** no. 3-4, (2003) 357–362.

[63] K. Venkateswaran, K. Cheng, and Y. Jean, "Application of positron annihilation to study the surface properties of porous resins," *The Journal of Physical Chemistry* **88** no. 12, (1984) 2465–2469.

[64] M. Petkov, C. Wang, M. Weber, K. Lynn, and K. Rodbell, "Positron annihilation techniques suited for porosity characterization of thin films," *The Journal of Physical Chemistry B* **107** no. 12, (2003) 2725–2734.

[65] Y. Kobayashi, K. Ito, T. Oka, and K. Hirata, "Positronium chemistry in porous materials," *Radiation Physics and Chemistry* **76** no. 2, (2007) 224 – 230. http://www.sciencedirect.com/science/article/pii/S0969806X06001496. Proceedings of the 8th International Workshop on Positron and Positronium Chemistry.

[66] P. Crivelli, *New Search for Invisible Decays of o-Ps.* PhD thesis, ETH Zurich, 2006.

[67] R. BEERS and V. HUGHES, "ANNIHILATION RATE OF ORTHOPOSITRONIUM," in *BULLETIN OF THE AMERICAN PHYSICAL SOCIETY*, vol. 13, p. 633, AMER INST PHYSICS CIRCULATION FULFILLMENT DIV, 500 SUNNYSIDE BLVD, WOODBURY, NY 11797-2999. 1968.

[68] P. G. Coleman, T. C. Griffith, G. R. Heyland, and T. L. Killeen, "Positron lifetime spectra for the noble gases," *Journal of Physics B: Atomic and Molecular Physics* **8** no. 10, (1975) 1734. http://stacks.iop.org/0022-3700/8/i=10/a=021.

[69] V. Hughes, "Plenarvortrag Physikertagung 37th," in *Physik Verlab*, p. 123. Physik 1973, 1973.

[70] M. A. Stroscio and J. M. Holt, "Radiative corrections to the decay rate of orthopositronium," *Phys. Rev. A* **10** (Sep, 1974) 749–755. https://link.aps.org/doi/10.1103/PhysRevA.10.749.

[71] D. W. Gidley, K. A. Marko, and A. Rich, "Precision Measurement of the Decay Rate of Orthopositronium in SiO_2 Powders," *Phys. Rev. Lett.* **36** (Feb, 1976) 395–398. https://link.aps.org/doi/10.1103/PhysRevLett.36.395.

[72] D. Gidley, "DW Gidley, PW Zitzewitz, KA Marko and A. Rich, Phys. Rev. Lett. 37, 729 (1976).," *Phys. Rev. Lett.* **37** (1976) 729.

[73] T. Griffith and G. Heyland, "The mean lifetime of orthopositronium in vacuum," *Nature (London)* **269** no. 5624, (1977) 109–112.

[74] W. Caswell, "WE Caswell, GP Lepage, and J. Sapirstein, Phys. Rev. Lett. 38, 488 (1977).," *Phys. Rev. Lett.* **38** (1977) 488.

[75] D. W. Gidley and P. Zitzewitz, "Measurement of the vacuum decay rate of orthopositronium formed in an MgO-lined cavity,".

[76] D. Gidley, A. Rich, P. Zitzewitz, and D. Paul, "New experimental value for the orthopositronium decay rate," *Physical Review Letters* **40** no. 12, (1978) 737.

[77] W. E. Caswell and G. P. Lepage, "O (α 2 ln (α- 1)) corrections in positronium: Hyperfine splitting and decay rate," *Physical Review A* **20** no. 1, (1979) 36.

[78] C. I. Westbrook, D. W. Gidley, R. S. Conti, and A. Rich, "Precision measurement of the orthopositronium vacuum decay rate using the gas technique," *Phys. Rev. A* **40** (Nov, 1989) 5489–5499. https://link.aps.org/doi/10.1103/PhysRevA.40.5489.

[79] J. S. Nico, D. W. Gidley, A. Rich, and P. W. Zitzewitz, "Precision measurement of the orthopositronium decay rate using the vacuum technique," *Phys. Rev. Lett.* **65** (Sep, 1990) 1344–1347. https://link.aps.org/doi/10.1103/PhysRevLett.65.1344.

[80] S. Asai, S. Orito, and N. Shinohara, "New measurement of the orthopositronium decay rate," *Physics Letters B* **357** no. 3, (1995) 475 – 480. http://www.sciencedirect.com/science/article/pii/0370269395009169.

[81] O. Jinnouchi, S. Asai, and T. Kobayashi, "Measurement of orthopositronium decay rate using SiO(2) powder: Integration of thermalization into time spectrum fitting procedure," *Submitted to: Eur. Phys. J. D* (2000) , arXiv:hep-ex/0011011 [hep-ex].

[82] R. S. Vallery, P. W. Zitzewitz, and D. W. Gidley, "Resolution of the Orthopositronium-Lifetime Puzzle," *Phys. Rev. Lett.* **90** (May, 2003) 203402. https://link.aps.org/doi/10.1103/PhysRevLett.90.203402.

[83] S. Asai, S. Orito, T. Sanuki, M. Yasuda, and T. Yokoi, "Direct search for orthopositronium decay into two photons," *Phys. Rev. Lett.* **66** (Mar, 1991) 1298–1301. https://link.aps.org/doi/10.1103/PhysRevLett.66.1298.

[84] T. Mitsui, R. Fujimoto, Y. Ishisaki, Y. Ueda, Y. Yamazaki, S. Asai, and S. Orito, "Search for invisible decay of orthopositronium," *Phys. Rev. Lett.* **70** (Apr, 1993) 2265–2268. https://link.aps.org/doi/10.1103/PhysRevLett.70.2265.

[85] S. Asai, S. Orito, K. Yoshimura, and T. Haga, "Search for long-lived neutral bosons in orthopositronium decay," *Phys. Rev. Lett.* **66** (May, 1991) 2440–2443. https://link.aps.org/doi/10.1103/PhysRevLett.66.2440.

[86] W. Bernreuther and O. Nachtmann, "Weak Interaction Effects in Positronium," *Z.Phys.* **C11** (1981) 235.

[87] B. K. Arbic, S. Hatamian, M. Skalsey, J. Van House, and W. Zheng, "Angular-correlation test of CPT in polarized positronium," *Phys. Rev. A* **37** (May, 1988) 3189–3194. https://link.aps.org/doi/10.1103/PhysRevA.37.3189.

[88] P. A. VETTER, "EXPERIMENTAL TESTS OF FUNDAMENTAL SYMMETRIES IN POSITRONIUM ANNIHILATION," *International Journal of Modern Physics A* **19** no. 23, (2004) 3865–3878, https://doi.org/10.1142/S0217751X04020130. https://doi.org/10.1142/S0217751X04020130.

[89] W. Bernreuther, U. Low, J. Ma, and O. Nachtmann, "How to Test CP, T and CPT Invariance in the Three Photon Decay of Polarized s Wave Triplet Positronium," *Z.Phys.* **C41** (1988) 143.

[90] D. Mercer, D. Mikolas, J. Yurkon, S. M. Austin, D. B. in, S. Gaff, E. Kashy, D. Kataria, J. Winfield, R. Betts, D. Henderson, A. Hallin, M. Liu, and F. Wolfs, "A large solid-angle array for heavy ions from {APEX}," *Nuclear Instruments and Methods in Physics Research Section A: Accel erators, Spectrometers, Detectors and Associated Equipment* **350** no. 3, (1994) 491 – 502. http://www.sciencedirect.com/science/article/pii/0168900294912491.

[91] "Eckert & Ziegler." http://www.ezag.com, 2017.

[92] "Marketech International." https://mkt-intl.com/. Accessed: 2018-10-13.

[93] S. M. Daigle, *Low Energy Proton Capture Study of the* $^{14}N(p,\gamma)^{15}O$ *Reaction*. PhD thesis, University of North Carolina, Chapel Hill, 2013.

[94] "National Nuclear Data Center." https://www.nndc.bnl.gov/. Accessed: 2018-10-14.

[95] *Technical Information Manual MOD. V775 series*.

[96] *Technical Information Manual MOD. V862 series*.

[97] Motorola, "MVME 5100 Datasheet," tech. rep.

[98] E. Jastrzembski, "VME Trigger Interface," tech. rep., Jefferson Lab, 1997. https://userweb.jlab.org/~brads/Manuals/Hardware/JLab/VmeTIRManual_v2.pdf.

[99] *Technical Information Manual MOD. V812 series*.

[100] J. Lab, "Coda." https://coda.jlab.org/drupal/.

[101] J. Lab, "Aram Teymurazyan.".

[102] B. B. A. S. Ahmad, I., "A new look at positron production from heavy-ion collisions: Results from apex," tech. rep., Argonne National Lab, 1995. http://inis.iaea.org/search/search.aspx?orig_q=RN:27054874.

[103] R. Brun and F. Rademakers, "ROOT An object oriented data analysis framework," *Nuclear Instruments and Methods in Physics Research Section A: Accelerators, Spectrometers, Detectors and Associated Equipment* **389** no. 1, (1997) 81 – 86. http://www.sciencedirect.com/science/article/pii/S016890029700048X. New Computing Techniques in Physics Research V.

[104] S. Agostinelli, J. Allison, K. Amako, J. Apostolakis, H. Araujo, P. Arce, M. Asai, D. Axen, S. Banerjee, G. Barrand, F. Behner, L. Bellagamba, J. Boudreau, L. Broglia, A. Brunengo, H. Burkhardt, S. Chauvie, J. Chuma, R. Chytracek, G. Cooperman, G. Cosmo, P. Degtyarenko, A. Dell'Acqua, G. Depaola, D. Dietrich, R. Enami, A. Feliciello, C. Ferguson, H. Fesefeldt, G. Folger, F. Foppiano, A. Forti, S. Garelli, S. Giani, R. Giannitrapani, D. Gibin, J. G. Cadenas, I. Gonzlez, G. G. Abril, G. Greeniaus, W. Greiner, V. Grichine, A. Grossheim, S. Guatelli, P. Gumplinger, R. Hamatsu, K. Hashimoto, H. Hasui, A. Heikkinen, A. Howard, V. Ivanchenko, A. Johnson, F. Jones, J. Kallenbach, N. Kanaya, M. Kawabata, Y. Kawabata, M. Kawaguti, S. Kelner, P. Kent, A. Kimura, T. Kodama, R. Kokoulin, M. Kossov, H. Kurashige, E. Lamanna, T. Lampn, V. Lara, V. Lefebure, F. Lei, M. Liendl, W. Lockman, F. Longo, S. Magni, M. Maire, E. Medernach, K. Minamimoto, P. M. de Freitas, Y. Morita, K. Murakami, M. Nagamatu, R. Nartallo, P. Nieminen, T. Nishimura, K. Ohtsubo, M. Okamura, S. O'Neale, Y. Oohata, K. Paech, J. Perl, A. Pfeiffer, M. Pia, F. Ranjard, A. Rybin, S. Sadilov, E. D. Salvo, G. Santin, T. Sasaki, N. Savvas, Y. Sawada, S. Scherer,

S. Sei, V. Sirotenko, D. Smith, N. Starkov, H. Stoecker, J. Sulkimo, M. Takahata, S. Tanaka, E. Tcherniaev, E. S. Tehrani, M. Tropeano, P. Truscott, H. Uno, L. Urban, P. Urban, M. Verderi, A. Walkden, W. Wander, H. Weber, J. Wellisch, T. Wenaus, D. Williams, D. Wright, T. Yamada, H. Yoshida, and D. Zschiesche, "Geant4 a simulation toolkit," *Nuclear Instruments and Methods in Physics Research Section A: Accelerators, Spectrometers, Detectors and Associated Equipment* **506** (2003) 250 – 303.

[105] `https://github.com/TeamCALIOPE/`.

[106] R. Ferragut, A. Calloni, A. Dupasquier, G. Consolati, F. Quasso, M. G. Giammarchi, D. Trezzi, W. E. L. Ravelli, M. P. Petkov, S. M. Jones, B. Wang, O. M. Yaghi, B. Jasinska, N. Chiodini, and A. Paleari, "Positronium formation in porous materials for antihydrogen production," *Journal of Physics: Conference Series* **225** no. 1, (2010) 012007. `http://stacks.iop.org/1742-6596/225/i=1/a=012007`.

[107] W. A. A.R.P.A. Jahan Zed, *Gamma Shielding by Aluminum*. PhD thesis, Pakistan Atomic Energy Commission, 2010.

[108] `https://its.unc.edu/rc-services/longleaf-cluster/`.

[109] "VNC." `https://www.realvnc.com/en/connect/download/vnc/linux/`. Accessed: 2015-03-25.

[110] . Jinfeng, . Masami, . Ryosuke, . Tachishige, . Mitsuhiro, and TetsuroKumita, "Study on Spin Precession of Polarized Slow Positrons in Solids," *Japanese Journal of Applied Physics* **36** no. 6R, (1997) 3764. `http://stacks.iop.org/1347-4065/36/i=6R/a=3764`.